ADDIS ABABA UNIVERSITY

ADDIS ABABA INSTITUTE OF TECHNOLOGY (AAiT)

SCHOOL OF CHEMICAL AND BIO ENGINEERING

COUPLING BIO-ELECTRO HETERO-FENTON OXIDATION PROCESSES FOR TEXTILE WASTEWATER TREATMENT

❖

Mr. Redae Nuguse (Ph.D. student)

A PhD Dissertation submitted to the School of Chemical and Bio Engineering, Addis Ababa Institute of Technology (AAiT), Addis Ababa University

❖

December 2023, Addis Ababa, Ethiopia

ADDIS ABABA UNIVERSITY

ADDIS ABABA INSTITUTE OF TECHNOLOGY

SCHOOL OF CHEMICAL AND BIO ENGINEERING

This is to certify that the PhD dissertation performed by **Mr. Redae Nuguse** entitled "***Coupling Bio-electro Hetero-Fenton Oxidation Processes for Textile Wastewater Treatment***" and submitted in partial fulfillment of the requirements for award of the Degree of DOCTOR OF PHILOSOPHY in Chemical Engineering (Environmental Engineering) complies with the university regulations and meets the accepted standards with respect to originality and quality.

Approved by:

Supervisor	Signature	Date
1. Hyunook Kim (Professor):		24-12-23
2. Joon Wun Kang (Professor):		25-12-23
3. Shimelis Kebede (Ph.D.):		

Examiners	Signature	Date
1. Hern Kim (Professor):		26-12-23
2. Zenamarkos Bantie (Ph.D.):		30-12-2023

Dean of the school	Signature	Date
1. Shimelis Kebede (Ph.D.):		

Declaration

I hereby declare that the dissertation titled ***"Coupling Bio-electro Hetero-Fenton Oxidation Processes for Textile Wastewater Treatment"*** is an original piece of work completed after I registered for the Doctor of Philosophy program at the Addis Ababa Institute of Technology (AAiT), School of Chemical and Bio Engineering. To the best of my knowledge, not previously published or written by someone else and previously included in any thesis or dissertation submitted to any other institution for a degree, diploma, or other credentials has ever been included in the dissertation. The rights of the participants have been acknowledged or cited, and I have attempted to identify all potential risks while doing this research. I have also received the required ethical and/or safety permits.

Name student	Signature	Date
Mr. Redae Nuguse Berhe:	Redae	20-12-23

Abstract

Discharging colored industrial wastewater effluents into natural water bodies is one of the main sources of environmental contamination globally and locally. The textile industry is one of the main water consuming and wastewater producing industries that needs serious attention. Conventional industrial textile wastewater treatments are not designed to treat emerging organic dyes (EODs). These compounds mainly remain unaffected even after the secondary biological treatment processes. Advanced oxidation processes (AOPs) are thought to be a successful and promising method of removing EODs. These processes rely on in situ liberation of reactive oxygen species (ROS), which have an active role in the degrading of EODs. The integration of wastewater treatment systems, which calls for knowledge in interdisciplinary domains, is a current focus. Although integrating wastewater treatment systems are challenging endeavors in the field of wastewater technology, various coupled systems have been developed. For example, systems such as bio-electrochemical system (BES) and electro-Fenton systems (EFS) for oxidation combine biological and electrochemical processes. The objective of the study was to combine the high oxidation power of EFS and cost-effectiveness of BES to oxidize textile wastewater effluents. Hence, a coupled system of BES-EFS oxidation system was developed in four phases to optimize the treatment process and offer a potential solution to oxidize EODs.

To begin, different sized Fe_3O_4 nanoparticles (INPs) were synthesized using modified co-precipitation method. The synthesized INPs (C, S, and M) possessed an average hydrodynamic diameter of 23, 17 and 48 nm with a saturation magnetization of 76 ± 2.4, 79 ± 2.6 and 66 ± 2.8 emu g^{-1} respectively and fluidized microelectrodes were prepared from each INPs (C, S, and M). The fluidized electrodes were tested for catalytic degradation of Acid orange 7 and 89.4 ± 1.7%, 93.2 ± 1.5% and 83.7 ± 2.3% degradation efficiency was determined respectively. On a second phase, a carbon felt (CF) was activated to synthesize activated functional cathode (ACF). The cathode was checked to have carboxyl functional groups (-C =O-OH) to drive H_2O_2 generation during EF oxidation. The selectivity of ACF toward H_2O_2 generation, i.e., two electron oxygen reduction reaction (2e-ORR) was estimated to be more than 89 ± 3.1%. Over 40-min of EF reaction test and 94.3 ± 1.7% removal efficiency for Congo red (CR) was achieved. Similarly, total organic carbon (TOC) and mineralization current efficiency were achieved as 82.7 ± 2.8% and 58 ± 2% over 40-min, respectively. The chemical quenching, LC-MS and IC analysis confirmed the role of $\cdot OH$ and $O_2^{-\cdot}$ radicals in CR degradation into NO_3^- and SO_4^{2-} ions. On third phase, functional composite electrode (Fe_3O_4/CNT/ACF) was synthesized and characterized. Fe_3O_4 and carbon

nanotubes (CNTs) were used as surface modifiers, i.e., to ease charge-transfer by forming multilayered channels and to enhance the thermal and structural strength of the electrode respectively. Using Fe_3O_4/CNT/ACF cathode, 93.7 ± 3.7% methylene blue (MB) removal was obtained within 1 h, following 2.7×10^{-2} M^{-1} min^{-1} pseudo-second-order rate kinetics. Based on TOC analysis, 57.8 ± 2.9% of MB could be mineralized. On fourth phase, a four-electrode-based coupled BEF system with ACF and iron strips as cathode and anode of BES and polarizable Fe_3O_4@ACF and iron strip as cathode and anode of EFS was developed. Methyl orange (MO) was used as a model pollutant for oxidation. After stabilization of the BES about 275.23 ± 9.4 mW cm^{-2} power density was generated, which could drive the EFS. At 20 mg L^{-1} of MO concentration, an external resistance of 100 Ω, a catholyte pH of 3.5, and an aeration rate of 300 mL min^{-1}, 82.5 ± 4.3% removal efficiency was achieved over 40 hours. Simultaneously, sewage wastewater was oxidized and accompanied with TOC, COD and NH_4^+-N removal efficiencies of 67.4 ± 3.6%, 71.2 ± 3.8% and 69.3 ± 3.7%, respectively. The results showed that the coupled BES-EFS system achieved satisfactory MO oxidation efficiency, indicating the synergistic effect of combining these two systems.

Finally, the BES-EFS system was assessed for actual textile wastewater degradation which showed to be an effective system for industrial applications. Thus, the overall study provides an insight for an innovative mechanism of well-performing and easily recyclable composite electrodes and stable BEF system for degradation of recalcitrant EODs.

Keywords: *Advanced oxidation process; Bio-electro-Fenton; Cathode synthesis; Dye degradation; Electro-Fenton oxidation; Magnetic nanoparticles; Wastewater Treatment*

Acknowledgement

I want to begin by thanking **Almighty God** for providing me the stamina, fortitude, and patience required to finish my PhD dissertation at the difficult time of Tigray war.

Second, I would like to express my deepest gratitude to **Professor Hyunook Kim** for letting me part of his incredible research lab to perform all my research activities. I do not have enough words to mention all that they did for me. However, I do appreciate their material and monetary assistance as well as their continuous supervision and follow-up. Without their support, this success would be impossible. I really appreciate their patience and the way they have been treating me to develop my analysis over the past two years.

Third, I want to thank **Professor Joon Wun Kang** for all their support, encouragement, and assistance in arranging my research trip to Korea possible. Throughout my study term, I appreciate their guidance to be hard worker and top-notch researcher in AOPs, which has kept me moving forward. I would also like to thank **Shimelis Kebede (Ph.D.)** for all his guidance, motivation, and assistance with my PhD study. Since I have begun my lab work, they have been on my side in every activity. I appreciate their viewpoints, comments and advice on my dissertation activities and papers.

Fourth, I would like to express my sincere to my colleagues at Water Energy-Nexus laboratory at the University of Seoul, Korea, particularly **Monu Verma (Ph.D.)** and **Ingyu Lee (Ph.D.)**, for their ongoing support and direction. I also want to thank all staff members of the Chemical and Bio Engineering School, specifically, **Brook Tesfamichael** (**Ph.D.**) and **Berhanu Assefa** (**Ph.D.**) for their constrictive comments and valuable recommendations of the dissertation.

Finally, I want to thank my parents for their unwavering support during every stage of my life. I have no words to adequately express my gratitude to my father **Prest Nuguse Berhe** and mother my **W/ro Lielt Berhe**. This success would not have been possible without their assistance and encouragement. I want to tell them how much I adore them. I want to express that this dissertation is devoted to my parents.

Wish you all the best!

(1) Published Papers

i. **R.N. Berhe**, S.K. Kassahun, J.W. Kang, M. Verma, H. Kim, Synthesis of Fe_3O_4/CNT/ACF Cathode-based Electro-Fenton System for Efficient Mineralization of Methylene Blue Dye: Kinetics and Mechanism. Journal of Environmental Chemical Engineering 10 (6), (2022) 108672, Impact factor of 7.968. https://doi.org/10.1016/j.jece.2022.108672.

ii. **R.N. Berhe**, S.K. Kassahun, J.W. Kang, Ingyu Lee, M. Verma, H. Kim, Performance evaluation of Fe_3O_4@ACF-supported bio-electro Fenton system for simultaneous sewage treatment and methyl orange degradation. Materials Today Communications (2023), 106331, Impact factor of 3.662. https://doi.org/10.1016/j.mtcomm.2023.106331.

(2) Under Review Papers

iii. **R.N. Berhe**, S.K. Kassahun, J.W. Kang, M. Verma, H. Kim, Synthesis of magnetite nanoparticles for fluidized electrocatalytic degradation of acid orange dye *in situ* and stepwise mechanism.

iv. **R.N. Berhe**, S.K. Kassahun, J.W. Kang, H. Kim, Homogeneous Fe^{2+}-Enhanced Oxidation of Real Textile Wastewater Using Carboxylic-Group-Saturated Carbon Felt Cathode: Electro Kinetics and Degradation.

Table of Contents

List of Figures

List of Tables

Acronyms

2e-ORR	*Two Electron Oxygen Reduction reaction*
4e-ORR	*Four Electron Oxygen Reduction reaction*
ACF	*Activated Carbon Felt*
AO7	*Acid Orang 7 or Acid orange II*
AOP	*Advanced Oxidation Process*
ATZ	*Atrazine*
BEF	*Bio-electro-Fenton*
BEHF	*Bio-electro Heterogeneous Fenton*
BES	*Biological Electrochemical System*
BOD	*Biological Oxygen Demand*
CMC	*Carboxymethyl cellulose*
CNT	*Carbon Nanotubes*
COD	*Chemical Oxygen Demand*
CR	*Congo red*
CV	*Cyclic Voltammetry*
DS	*Dissolved Solids*
E_0	*Standard Electrode Potential*
EAOP	*Electrochemical Advanced Oxidation*
EC	*Electrocoagulation*
EDX	*Energy Dispersive x-ray*
EF	*Electro-Fenton*
EFS	*Electro Fenton System*
EIS	*Electrochemical Impedance Spectrometry*
eV	*Electron Volt*
Hetero-EF	*Heterogeneous Electro-Fenton*
INPs	*Iron nanoparticles*
HRT	*Hydraulic Retention Time*
LSV	*Linear Swept Voltammetry*
MB	*Methylene Blue*
MEC	*Microbial Electrolysis Cell*
MFC	*Microbial Fuel Cell*

MO	*Methyl Orange*
NF	*Nanofiltered*
PC	*Peroxi-coagulation*
PEF	*Photo Electro-Fenton*
PEM	*Proton Exchange Membrane*
PFC	*Photo-catalytic Fuel Cell*
PPCP	*Pharmaceuticals and Personal Care Product*
PVA	*Polyvinyl Alcohol*
RB5	*Reactive Blue 5*
RhB	*Rhodamine B*
RR	*Oxygen Reduction Reaction*
SEM	*Scanning Electron Microscopy*
SHE	*Standard Hydrogen Electrode*
SMX	*Sulfamethoxazole*
SS	*Suspended Solids*
TDS	*Total Dissolved Solids*
TEM	*Transmission Electron Microscope*
TOC	*Total Organic Carbon*
TSS	*Total Suspended Solids*
UF	*Ultrafiltered*
UV	*Ultraviolet light*
XPS	*X-ray photoelectron Spectroscopy*
XRD	*X-ray Diffraction Spectroscopy*

Frequently Used Parameters

Parameter	***Units***
Concentration, C	$mg\ L^{-1}$
Temperature, T	^{0}C
Flowrate, F	$m^{3}\ h^{-1}$
Resistance, R	Ω
Rate of reaction, r	$M\ min^{-1}$
Rotation speed of electrodes, ω	*RPM*

Frequently Used Elements

Elements	***Symbols***
Iron	*Fe*
Sulfur	*S*
Chlorine	*Cl*
Oxygen	O_2
Nitrogen	N_2
Ozone	O_3

Oxygen Reactive Species

Free radicals	***Symbols***
Hydroxyl	$\cdot OH$
Hydro peroxyl	$HO_2^{\cdot}$
Superoxide ion	$O_2^{\cdot -}$

Frequently Used Constants

Constants	*Values and units*
Faradays, f	*96,485.3 C mol^{-1}*
Ideal gas constant, R	*8.3144 L kPa K^{-1} mol^{-1}*
Diffusion coefficient of oxygen, D	*2.47×10^{-5} m^2 s^{-1}*
kinematic viscosity of water, v	*1×10^{-2} $m^2 s^{-1}$*
concentration of oxygen, C	*1.67×10^{-9} mol L^{-1}*

Model Dye Contaminants

Dyes (Contaminant)	***Molecular formula***	***Mass (g mol^{-1})***
Acid orange 7/II	$C_{16}H_{11}N_2NaO_4S$	350.32
Congo red	$C_{32}H_{22}N_3Na_2O_6S_2$	696.66
Methylene blue	$C_{16}H_{18}ClN_3S$	319.85
Methyl orange	$C_{14}H_{14}N_3NaO_3S$	327.34

CHAPTER 1

1. INTRODUCTION

Billions of tons of wastewater are produced every year worldwide from domestic use in large cities, industrial sites and agricultural sectors [1]. Environmental pollution, specifically water contamination by varieties of organic and inorganic chemicals, has become a serious global issue due to the increment of population and industrialization [2]. It is well known that the wastewater contains large amounts of synthetic organic pollutants, including industrial chemicals, pesticides, dyes [3], pharmaceuticals and personal care products (PPCPs), acids, alkalis, hydrogen peroxide, starch, surfactants, dispersing agents and soaps of metals which are released daily into many types of wastewaters and enter into natural water bodies [4–6]. Consequently, water and environmental pollution remains a pervasive threat with water quality being merely a concept reflecting the kind and quantity of contaminants contained within it [5,6]. Due to rapid development of textile dyeing and finishing industry, water pollution from refractory organic pollutants has been problematically increasing. To treat industrial textile wastewater, different treatment technology options have been developed such as physical, chemical, and biological treatment processes. Conventional physicochemical methods such as coagulation, adsorption and membrane filtration have been used for many years. However, they require high energy and chemical consumption [7]. Although biological methods show cost-competitive, less sludge production and producing non-hazardous metabolites, they are insufficient for rate of removal and longer time for emerging organic contaminants [8].

Advanced oxidation processes (AOPs) are defined as a process that involves the use of free hydroxyl radical (·OH) in aqueous solution which are produced by different means such as chemical, photochemical, or electrochemical reactions to promote the oxidation of organic compounds present in wastewater. They are developed to replace the traditional way of wastewater treatment processes. Hydroxyl radicals are one of the strongest oxidants (E_0 = 2.8 eV) after Fluorine (E_0 = 3.0 eV) and can react 10^6–10^{12} times faster than ozone (O_3) depending on the substrate to be degraded, which capable of oxidizing recalcitrant organic compounds to CO_2, H_2O and inorganic ions [9–16]. Fenton process is one of the AOPs developed for textile

wastewater treatment, however, its working pH ranges and continuous supply of chemicals hinders its industrial application [17]. Electro Fenton (EF) is developed to resolve the continuous supply of chemicals in classical Fenton process and bio-electro Fenton (BEF) oxidation process is again developed to minimize the energy consumption of the electro Fenton's oxidation process. Ozonation process can be classified as an AOP process, since it can generate ·OH radicals initiated by hydroxyl ion (OH^-) at alkaline pH [18]. Fenton's oxidation, EF oxidation and BEF oxidation increase the pH value of the wastewater, whereas ozonation process decreases the pH value of the wastewater due to the accumulation and elimination of OH^- ions buffer conditions.

Combining treatment methods could increase the success of oxidation and mineralization. For better organic degradation performance in wastewater treatment, for instance, ozone is combined with H_2O_2, UV, catalysts, and the Fenton system with UV and titanium oxide, as well as with various heterogeneous catalyst supports, particularly with metal and semiconductor elements. Bio-electro Fenton oxidation was created for practical textile wastewater treatment applications by fusing the expertise of interdisciplinary domains such as environmental engineering, bio-electrochemistry, and material science. The main objective of the study was to combine an electro-Fenton oxidation system with a bio-electrochemical system for practical wastewater treatment. The shortcomings of classic biological treatment systems, electro-Fenton oxidation systems, and Fenton oxidation systems were overcome by the integrated system.

1.1. Problem Statement and Identified Gaps

Ethiopia is home to many textile businesses that lack an effective wastewater treatment system. They frequently discharge wastewater that is greater in concentrations of physical, chemical, and organic contaminants than is permitted to open land and rivers. It also seriously contaminates agriculture; therefore, its effects go beyond just contaminating the air, water, and land. Unwarily, farmers who live close to industrial areas (like the Aka textile industry) use wastewater effluent to grow vegetables [19]. It is well known that some vegetables, particularly cabbages, have the capacity to extract heavy metals and accumulate on their leaves. In the end, vegetables with high concentrations of organic carcinogens, notably heavy metals, would be marketed to the population, which could be harmful to human health. The agricultural sector is specifically aggravated using significant volumes of dyestuffs in the dyeing process of textile manufacturers and the discharge of wastewater to waterways.

Physical-chemical, biological, or combined treatment methods have been developed with varied degrees of therapeutic efficiency. The biological treatment options are very cumbersome and frequently convert the organic contaminants into other intermediates that may assemble in the environment. Moreover, physicochemical treatment methods are frequently ineffective in terms of energy use and environmental safety. Another easy approach is to treat wastewater from the textile sector using chlorine and ozone, however this option cannot fully oxidize the dyes. Ozonation is a potential approach for treating textile wastewater, but as it reacts with OH^-, it becomes less effective, producing $O_2^{\cdot -}$ and $HO_2^{\cdot}$, which prevents the degradation of organic contaminants [20]. Furthermore, a larger dose restricts its use in industry. The current state of the art in advanced oxidation techniques (Fenton's mechanism) for the treatment of emerging pollutants in textile wastewater was reviewed. The alkaline character of textile industry effluents makes it difficult to treat them effectively using Fenton, electro Fenton, biological systems, or ozonation method because of pH range, energy requirements, and chemical consumption respectively.

1.2. Objective of the Study

1.2.1. General Objectives

The goal of the study was to combine a bio-electrochemical system with an electro-Fenton system to create a bio-electro hetero Fenton oxidation method for the treatment of textile effluent.

1.2.2. Specific Objectives

The subsequent specific objectives were completed to achieve the overall objective.

- Different size-controlled heterogeneous magnetic nanoparticles (MNPs, Fe_3O_4) using different iron salt precursor solutions, i.e., $FeCl_3.6H_2O$, $FeSO_4 \cdot 7H_2O$, $FeCl_2.6H_2O$, $Fe_2(SO_4)_3.6H_2O$ were synthesized and characterized.
- Carbon felt (CF) based electrodes were activated, their surface morphology and electrochemical functionality were characterized and evaluated.
- MNPs-ACF based various composite functional cathode electrodes (such as ACF, Fe_3O_4/ACF, Fe_3O_4/CNT/CF and Fe_3O_4/CNT/ACF) were prepared and their degradation capability was evaluated.

- A coupled system of bio-electrochemical system (BES) and electro-Fenton system (EFS) was developed and evaluated in degrading organic textile dyes. The coupled system was based on the idea described in (Fig. 1.1). BES was developed by inoculating activated sludge from a wastewater treatment facility to ascertain the ideal voltage output in an open-circuit voltage.
- For each mentioned above, the degradation kinetics, the effects of major operational parameters such as solution pH, initial dye concentration, applied current (voltage), catalyst dosage, and rate of *in situ* H_2O_2 generation were investigated.
- The model equations were developed and the optimum value of the operating parameters for maximum percentage of target contaminant degradation were identified.

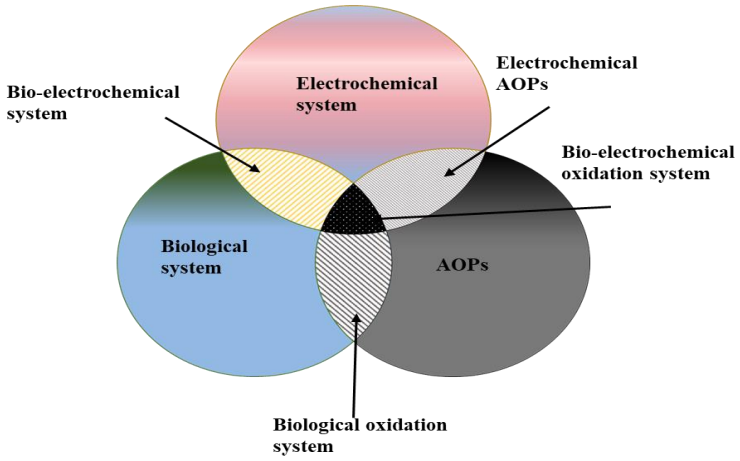

Figure 1.1: Interaction of multi-disciplinary fields

1.3. Scope of the Study

The scope of the study included material synthesis (including Fe_3O_4 and composite electrodes), evaluation of the synthesized materials for electro-Fenton dye degradation, development of an open circuit bio-electrochemical system, coupled system development (bio-electro Fenton oxidation) and implementation of the system for simultaneous municipal wastewater and textile dye degradation applications. Potential variables like the amount of Fe_3O_4 used in the EF process, the capability and durability of the composite electrodes to be recycled and reused, the applied potential, the number of contaminants present, the solution's pH, stability of the system and the production of H_2O_2 were all carefully examined.

1.4. Significance of the Study

The coupling of bio-electro and hetero-Fenton oxidation processes is significant because it has the potential to address important sustainability and environmental issues. Wastewater from the textile sector is notorious for having a complicated composition that includes organic contaminants, heavy metals, and colors. Thus, the study discusses the substantial issues of textile wastewater that could harm the ecosystems and water bodies. The study offers a novel, multidisciplinary method for treating wastewater. In comparison to conventional treatment techniques, this unique combination may increase the efficiency of contaminant removal by utilizing both biological and chemical mechanisms. The capacity of the coupled system for enhanced treatment performance is highlighted by the synergistic effects that have been observed. This could result in fast treatment time, higher removal rates of contaminants, and an overall improvement in treatment efficiency in an environmentally friendly way.

The focus of the study was on textile wastewater treatment methods. Textile industries are the main stakeholders to take advantage of the research for implementing a more effective and sustainable technique of treating wastewater. The coupled bio-electro hetero-Fenton system has the potential to save operating costs, assist industries comply with environmental requirements, and enhance their environmental impact overall. Adopting a successful wastewater treatment strategy can result in better water quality near to the textile industry, which can benefit the community. Apart from the main target, the research can be advantageous for regulatory agencies that supervise environmental standards and wastewater discharge rules. Moreover, the research could be beneficial for businesses that specialize in water treatment technologies. This may result in the development of more sustainable and effective solutions for a wider range of sectors. The system could contribute a significant insight into wastewater treatment processes to the academic and research community. Similarly, the research could be useful for governmental bodies and policy makers. Because the research supports initiatives to promote cleaner industrial practices and is in line with sustainability goals. The study establishes a foundation for further research and developments in the field of environmental engineering, in addition to contributing to the corpus of information already available in the field. Essentially, the study could have a good knock-on impact that would help not just the immediate parties involved in treating textile wastewater but also more general environmental objectives and sustainable development.

1.5. Structure of the Study

To help readers gain a general grasp of the study, the performed activities were arranged sequentially into seven chapters. **Chapter 1** gives the overview of the study including the research area, research gaps, and objectives of the research. A thorough literature review on Fenton, electro-Fenton, and bio-Fenton processes is presented in **Chapter 2** with a focus on wastewater textile wastewater oxidation. The key topics of **Chapter 3** are synthesis of MNPs and their detailed characterization, including their morphology and electrochemical properties as well as their physical and crystallite structure. Here AO7 oxidation was tested in Fenton oxidation system. The topics of CF activation, carbonyl functional group formation, and characterization are covered in **Chapter 4**. Electro Fenton oxidation system which is the modification of Fenton oxidation system was used to oxidize CR. **Chapter 5** focused on synthesis and characterization of composite electrodes, such as CNT/ACF, Fe_3O_4/ACF, Fe_3O_4/CNT/ACF and Fe_3O_4@ACF. Here, the EF system was also employed for MB degradation and operating parameters such as pH, initial MB concentration and applied voltage were thoroughly examined. **Chapter 6** presents the experimental set up of bio-electrochemical system (BES), EF system (EFS) and coupled BES-EFS, i.e., bio-electro-Fenton (BEF) system. The power generation and stability of the system were analyzed. Moreover, oxidizing capability of the system on simultaneous sewage and MO over various operational parameters were evaluated. **Chapter 7** summarizes the overall analysis and activities conducted in this dissertation. Furthermore, it points out some remarkable areas where future work based on the overall finding of this study can be carried out.

CHAPTER 2

2. LITRATURE SURVAY

2.1. Magnetic nanoparticles (MNPs)

MNPs have rapidly gained recognition as promising materials for wastewater treatment applications. MNPs have a high specific surface area to volume ratio, numerous surface functional groups, which enable them functioning in chelating agents to achieve selectivity, and high-speed of random motion, which leads to rapid electro catalytic oxidation, [19–22]. Currently,, many NPs have been reported for wastewater treatment application, including graphene oxide nanoparticles (GONPs), carbon nanotubes (CNT), ZnO, TiO_2, Al_2O_3, CeO_2, MgO, and MnO_2 [23–25]. However, these NPs generally exhibit poor magnetic separation and reusability, which limit their practical applications for wastewater application [19]. Consequently, MNPs have to date attracted high attention in the field of nanoscience and nanotechnology due to their high saturation magnetization, high specific surface area, eco-friendliness, low cost, and as an abundant source of iron material [23,25]. Particularly, Fe_3O_4 have numerous applications in different fields such as electro catalysis, sensor images, energy, magnetic resonance, drug delivery systems, and separation applications [25,26]. Noteworthily, Fe_3O_4 in addition to exhibiting efficient separation procedures through an external magnetic field application without using centrifugation, it is an excellent reusable, making highly attractive for water and wastewater treatment application [20,21]. Besides, some adsorbent including Fe_3O_4@SiO_2, rGO@Fe_3O_4, cellolose@Fe_3O_4, and polymer-based Fe_3O4 have been utilized for adsorption of eco-toxic metals [19,22]. Nevertheless, these composite materials cause a loss of nature of magnetization and size reduction occurred in Fe_3O_4, which hinders the separation process applying an external magnetic field due to poor randomization [25].

Interparticle gaps, which offer a high specific surface area and more active sites while strengthening the magnetic property to obtain greater effectiveness for the removal of contaminants, appear to help hierarchical cluster nanostructures overcome these disadvantages [26]. Fe_3O_4 has been prepared by various procedures, including sono-chemical, coprecipitation

method, microwave-assisted technique, high-energy ball mill, sol-gel method, and solvothermal procedures. Employing toxic solvents, poor crystallinity, and complicated procedures make the methods limited. Figure 2.1 shows SEM images of different MNPs [27].

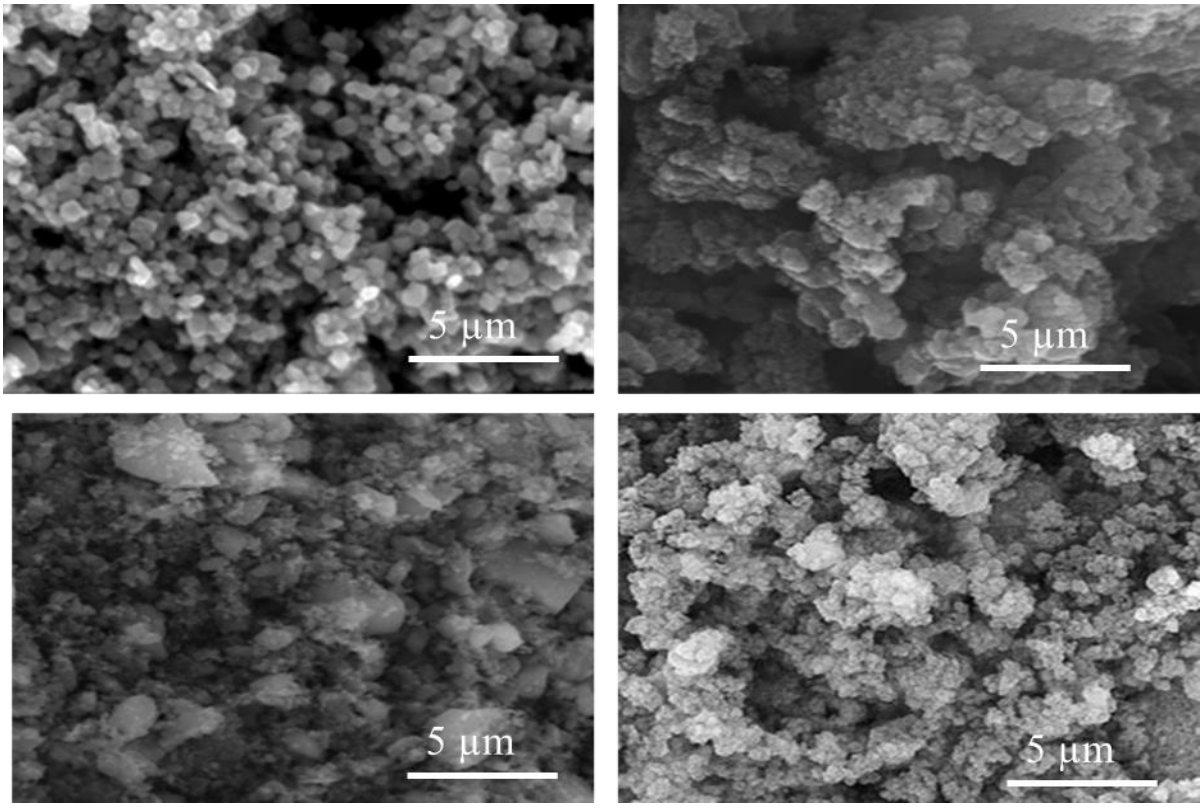

Figure 2.1: Some examples of SEM images of MNPs from different literature

2.1.1. Magnetic Nanoparticles (MNPs) and Synthesis Methods

To synthesize MNPs, numerous efforts have been applied towards developing new and novel methods of preparation [20]. Precise MNP surface functionalization is an essential parameter as it may affect the electrochemical properties, surface stability and contaminant removal efficiency. generally, MNPs synthesis could be classified to three techniques, i.e., (1) physical methods, such as mechanical milling, electron beam lithography, gas-phase deposition, vapor deposition and patterning and electrical explosion, (2) chemical methods, like spray pyrolysis, laser pyrolysis, co-precipitation, thermal decomposition, microemulsion, Hydrothermal, /solvothermal and sol-gel, and (3) biological or microbial methods [22]. The physical methods are based on the top-down strategy, i.e., synthesis starts from bulk material and depleting to generate NPs [19,22]. Whereas, chemical and biological methods follow a bottom-up approach,

where the atoms/molecules are assembled which forms different sizes of NPs [20,22]. The most common methods are physical and chemical methods are presented in Fig. 2.2 below.

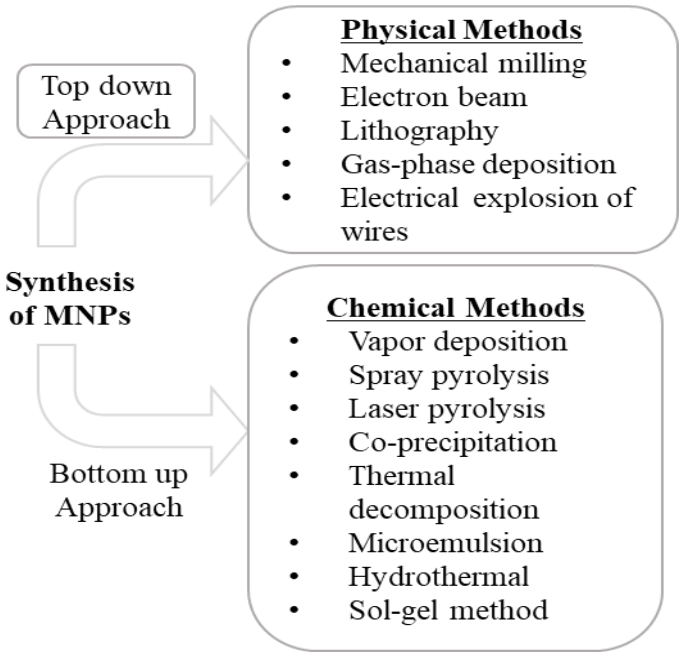

Figure 2.2: Methods of MNPs synthesis

2.1.2. Properties of MNPs and Characterization

MNPs overcome physiological and cellular barriers to reach their target, and their reusability, regeneration, and easy separation offer benefits [28]. The size, shape, and composition of MNPs also influence their magnetic properties, with size reduction leading to excellent magnetism and shape supporting inhomogeneity [29]. The reliability and validity of characterization techniques are essential for determining the most efficient synthesis process, which may enhance the target-specific capacity of MNPs. Techniques like field-emission scanning electron microscopy and high-resolution transmission electron microscopy are used to characterize MNP size and shape.

MNPs are defined by their crystallinity and purity, and their structure can be determined using techniques like infrared spectroscopy, thermal analysis, and X-ray diffraction. Researchers have also investigated the structure of composite NPs using techniques like thermogravimetric and differential thermogravimetric analysis. Thermodynamic stability and surface charge are crucial for determining the efficiency of surface modifications in MNPs with organic or inorganic pollutants in wastewater. The wettability of particles and the interaction between

particles in the aqueous medium determine the ability of MNPs to be dispersed or aggregated, helping estimate their ability to remove contaminants from water and wastewater samples. Magnetic properties of MNPs are essential for estimating their stability, efficiency, separation, recovery, and recyclability. MNPs exhibit permanent magnetization even after being removed from a magnetic field, while paramagnetic particles do not.

2.1.3. Mechanisms of Contaminant Removal Using MNPs

Rapid industrialization and population growth lead to the release of contaminants in wastewater, including organic and inorganic pollutants [22,30]. Untreated wastewater poses environmental risks, endangering aquatic species, and affecting the food chain and human health [31]. Eco-friendly nanomaterials have been developed for efficient remediation and removal. MNPs have four major removal mechanisms: adsorption, filtration, transformation, and catalysis. Adsorption involves binding pollutants to the adsorbent surface, followed by movement and binding [32].

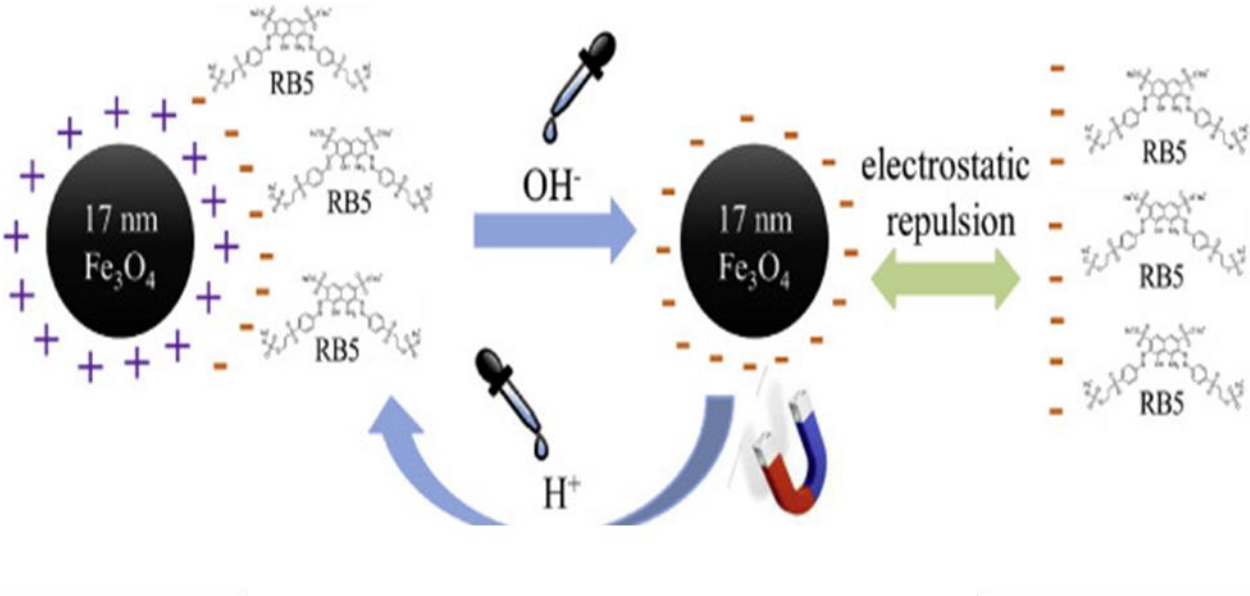

Figure 2.3: Description of the mechanisms of MNPs for Reactive blue Fenton oxidation

MNPs have higher surface areas, nano-sized pores, and magnetic properties for adsorption. Filtration plays a significant role in water and wastewater treatment, including membrane filtration. Nanofiltration using MNPs is a membrane separation technique with high permeation rates and lower pressure requirements. It provides selectivity towards contaminants due to anthropogenic activities [33]. Photocatalysis is an inexpensive method for removing pollutants

from water and wastewater using MNPs [34]. This technique uses a semiconductor material as a catalyst medium, creating electron-hole pairs that produce reactive oxidizing and reducing agents and radicals in wastewater [35]. Nanostructured semiconductor materials are more suitable for wastewater treatment due to their higher surface-volume ratio compared to traditional photocatalysts. The redox reactions lead to the speciation of metals in wastewater, reducing metal toxicity and achieving a stable oxidation state [36]. Figure 2.3 above describes the mechanism of MNPs [37].

2.1.4. Removal of Organic Pollutants Using MNPs

Organic contaminants in wastewater pose a significant threat to aquatic life and human health. Conventional wastewater treatment methods struggle to remove these pollutants, leading to the development of MNPs for wastewater treatment [38]. Fe-MNPs, prepared via a novel ion-thermal synthesis, have been found to be highly stable and efficient. Poly(ethylenimine) (PEI) coated MNPs have been proven to remove various contaminants, reducing turbidity, color, total nitrogen, and microbial content [22,35,39]. A sustainable and eco-friendly method for copper doped Fe_3O_4 MNPs was also developed, enhancing H_2O_2 activation ability. Research on the removal of colored wastewater is crucial due to dyes' long-term effects on photosynthesis. Kaolinite-supported nanoscale zero-valent iron (K-nZVI) can effectively remove over 97% of crystal violet, with a removal efficiency of over 99.9%. Betaine-modified magnetic iron oxide nanoparticles (BMNPs) can also be used for degradation of methylene blue (MB) dye. Fe_3O_4 MNPs produced by co-precipitation using glutaraldehyde have been studied for the removal of direct green azo dyes, reactive red azo dyes, and a mixture of both. A low-cost and selective adsorbent was prepared by grafting poly (ionic liquid) onto silicon coated Fe_3O_4. The increasing use of pharmaceutical and personal care products has led to concerns about the environmental impact of pharmaceutically active compounds (PhACs). Researchers have developed novel adsorbents using 2-D graphene oxide and graphite carbon nitride for wastewater treatment. These adsorbents can remove toxic tetracycline antibiotic and methylene blue dye, allowing for recovery and reuse [40]. Additionally, an amino-modified magnetic nano-adsorbent was developed for methylparaben removal. The efficiency of contaminant removal using MNPs is high, with magnetic nano-sorption being the most suitable mechanism.

2.2. Carbon Felts Electrodes

Carbon Felt (CF) is a popular choice for electrodes due to its good electronic conduction, high surface area, and low cost [41–43]. Other carbon-based materials like vitreous carbon, carbon sponge, carbon fiber, and carbon paper have limitations, such as cost and rigidity. CF is chosen for its commercial availability and tenacity [42,43]. However, CF has limitations due to its hydrophobic surface and poor kinetics for reduction and oxidation reactions. Modification methods have been adopted to enhance electrochemical activity of CF (Fig. 2.4).

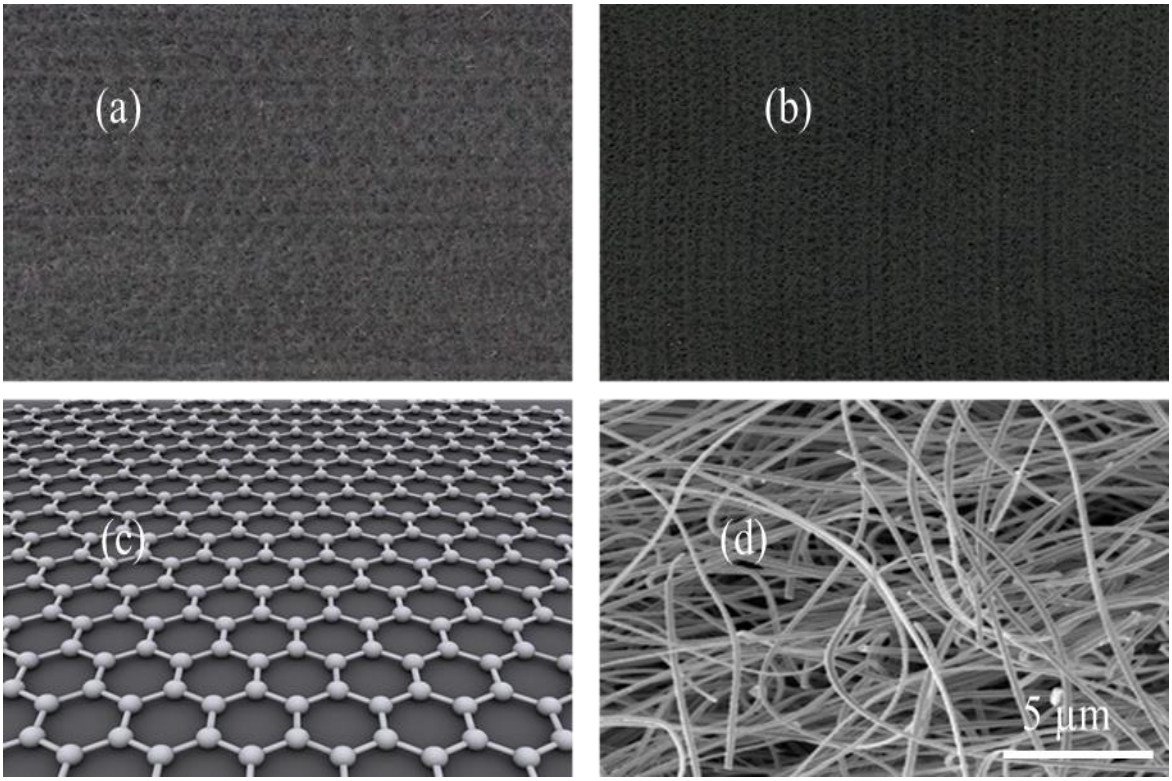

Figure 2.4: Images of pristine carbon felt

Images of pristine carbon felt (a and b), carbon structure (c) and under SEM (d)

Carbon-based electrodes have been used in environmental remediation and wastewater treatment through electrochemical advanced oxidation processes. Modification methods, such as metal deposition and functional group addition, have been explored to improve catalytic properties and conductivity [44]. CF are also used as cathode materials for removing persistent organic pollutants (POPs) in aqueous mediums. CF electrodes offer advantages like nontoxicity, good stability, conductivity, and chemical resistance. However, understanding CF and selecting suitable modification methods for various demands requires deeper research [43,45].

2.2.1. Manufacturing Method of CF Material

Common precursors for graphite or carbon felts include polyacrylonitrile (PAN) and rayon, a regenerated cellulose. The manufacturing process involves needle-punching and graphitizing, with the latter being prepared via thermal treatment. Graphite felt (GF) is produced by graphitizing carbon, with processing temperatures ranging from 1200-1600 ^{0}C for carbon and 2000-2600 ^{0}C for graphite [46]. The precursors and processing parameters can influence the graphitization stage rendering different carbon and graphite felts as presented in Table 2.1.

Table 2.1: Physical properties of carbon and graphite felts [67,71,72].

Property	**Carbon felt**		**Graphite felt**	
	PAN	**Rayon**	**PAN**	**Rayon**
Bulk density (g cm $^{-3}$)	0.15	0.08-0.11	0.10	0.08
Carbon content (%)	95.6	>98.5	>99.5	>99.8
Tensile strength (MPa)	0.19	0.132	0.12	0.10
Process temperature (^{0}C)	1520	1401	2400	2200-2500

There are numerous grades of carbon or graphite felts from various sources, with significant variations in properties [49]. For example, GF-based on rayon has a higher resistivity than PAN-based felt, and CF has higher electro-catalytic activity due to higher CeOH and quaternary nitrogen groups and defect sites [50]. The differences in precursors, manufacturing factors, and processing procedures significantly affect the properties of the produced felt materials.

2.2.2. Modification Methods of CF

Different modification techniques of CF have been utilized for many years. The most common modification methods are plasma treatment, thermal treatment, chemical treatment, graphene-based modification, carbon nanotube-based modification and metallic modification. Plasma treatment improves the wettability of commercial carbon fibers by enhancing electrochemical reactivity through the growth of oxygen-containing functional groups or nitrogen doping [51]. This process is controlled by time, power, and oxygen pressure. X-ray photoelectron spectroscopy (XPS) shows that the plasma treatment process favors the formation of phenolic groups. However, the process only increases the number of functional groups on felt and not

significantly the surface area. Oxygen-containing functional groups and nitrogenous groups can also improve electrocatalytic activity of carbon electrode materials for redox reactions, increasing the basicity of carbon and electrical conductivity [52,53]. Thermal treatment is a method for felt modification that improves the electrochemical properties and hydrophilicity of felt electrodes. Studies have shown that PAN-based felts have higher electrical conductivity and better oxidation resistance compared to rayon-based felts. Nitrogen-doped GF electrodes show higher electrochemical performance due to increased electrical conductivity, active site amount, and improved wettability.

The surface area of modified felts can also be improved, with a 13.44% increase in surface area compared to bare PAN-CF [54]. Additionally, thermal treatment can increase the surface area of commercial CF by 700 times and improve the crystalline average size due to selective etching of amorphous carbon [40,54]. However, chemical treatment of CF involves using chemicals like nitric acid or sulfuric acid to activate the surface of felt materials[55]. This results in felts with chemisorbed oxygen on the surface, which can be used as electrodes. The increased electrochemical performance is due to the increased concentration of CeO and C=O functional groups on the surface. Combining thermal and chemical treatments can improve the electrochemical behavior of the felts. Electrochemical oxidization can also be used to grow functional groups on felt electrodes. This method has been successfully applied to improve the properties of different felts, including graphite and graphite [55,56]. Graphene is a popular material for materials science and condensed matter physics due to its electrical, physical, thermal, optical, high specific surface area, and mechanical properties [57]. It has been used for electrochemical activity of electrodes, with methods like dip-coating, constant potential technique, and electrophoretic deposition. For example, reducing graphene oxide (rGO) on CF has been coated, resulting in higher current density and better conductivity.

Carbon nanotubes (CNTs) are used to modify felt electrodes due to their mechanical flexibility, electrical and thermal conductivities, and large surface area. Coating single-walled carbon nanotubes (SWCNTs) with CF and drying them at 80 °C for 5 hours improves catalytic performance. CNTs can also be grown directly on felt surfaces using chemical vapor deposition (CVD) methods [58]. The small size of CNTs increases electrochemical surface area and improves electrode performance. CNTs/CF electrodes can also be obtained by growing CNTs on cobalt and manganese metallic particles [59]. CVD is an efficient technique for growing MWCNTs on CF substrates. The CNTs with high aspect ratio were grown from iron sites,

enhancing mechanical strength and electrical conductivity. The CNTs loading allowed for a surface area of 150 m^2 g^{-1} with a 98% weight intake. Other CNTs/CF electrodes were prepared using methanol decomposition on metallic catalysts. The CNTs on the CF electrode have a bamboo-like structure [60]. Metallic modification enhances the electro-conductivity of carbon felt electrode materials by coating metal on the fibers through impregnation with metallic ions like Pt^{4+}, Pd^{2+}, Au^{4+}, Mn^{2+}, Te^{4+}, In^{3+}, and Ir^{3+} [61]. The amount of metal on the fiber surface can vary depending on the method and treatment time. However, the high cost of noble metal catalysts limits their commercial application. Studies have focused on less expensive metals, such as electrochemical deposition of PbO_2 on graphite fibres, electrodeposition of MnO_2 on the CF surface, and thermal deposition of $Fe(CO)_5$. These metals act as catalysts, improving the electrochemical activity of the modified electrode. Iron-doping increases electron transfer efficiency in microbial fuel cells (MFCs), resulting in lower internal resistance and higher power generation [61,62].

2.2.3. Characterization of CF Electrodes

Carbon and graphite felts are frequently seen beneath long smooth fibres dispersed randomly with homogeneous large void spaces between them in Scanning Electron Microscopy (SEM) images. Each fiber has a cylinder-like shape with shallow grooves along its long axis, formed by melting together thinner fibers lengthwise. The addition or removal of thinner sheets from the original can alter the thickness of the three-dimensional felt electrode. Fibers have a distinct geometrical shape that sets them apart from other materials, resulting in a wide range of structural and physical parameter values.

2.3. Textile Wastewater Treatments

One of the problems associated with textile industries is unacceptable effluents, especially dyes, which are difficult to degrade with the traditional physicochemical and biological treatment processes [5]. Although membrane separation and adsorption are efficient processes, they are not capable of ultimately mineralizing antibiotics and their efficiency is noticeably reduced by the presence of certain organic contaminants [63]. Moreover, dye effluent/waste cannot be degraded with the help of primary treatment involving coagulation and flocculation and secondary treatments which encompasses activated sludge process [64]. Biological treatment technologies are environmentally-friendly and cost-effective which are often applied for municipal and industrial wastewater treatments [7,65].

Figure 2.5: Different textile wastewater effluents from different sources

Dyes comprise of chromophores, responsible for color and the auxochromes, responsible for chromophore and give enhanced affinity (to attach) toward the fibers. Dyes are classified by their chemical structure (azo dye, anthraquinone, triphenylmethane, phthalocyanine, indigo, and sulfur), their solubility (acid, mordant, metal complex, direct, basic, and reactive dyes, and insolubility (azoic, sulfur, vat and disperse). Fundamental chemical structure of dye contains chromophores such as -C=C-, -C=O, -N=N-, -NO_2, -C=N and a functional group attached with auxochromes such as halogens, -CO_2H, -COR, -SO_3H, -CH_3CO-, -CH_3, and -NH_2. Currently, azo dyes, which belong to various applicative groups of dyes, are the most used colorants up to 70% of all dyes used in the textile industry. Azo dyes undergo cleavage of the azo bond anaerobically which results in the formation of aromatic amines and at the same time the disappearance of color [66–68]. Dyes are stable in aquatic environment and are not completely degraded in the conventional wastewater treatment plants and discharge to natural streams leads to environmental contamination in terms of the breakdown of dyes into toxic products, aesthetic, light penetration issues, mutagenicity, carcinogenicity effects on aquatic life in the receiving water bodies [69]. Figure 2.5 above presents different textile wastewater effluents with complex color characteristics. Table 2.2 presents the comparison of biological treatment with other methods in textile wastewaters.

Table 2.2: Comparison of biological treatment with other methods in textile wastewaters [5,7,66,70–75].

Physical/ chemical	Components	Advantage	Disadvantage
Conventional methods	Coagulation/ flocculation, Adsorption, Membrane technologies, Oxidation, Ozonation	Effective, cheap, easy to handle and available, operated without phase changes or chemical conditioning, (pressure) in membranes, low operational cost, and low energy consumption in ion exchange	High sludge production, high energy cost, short half-life, excess use of chemicals, high cost of chemicals and results secondary pollution, formation of unwanted by-products, long contact time requirement
Biological	Enzyme/ Whole cell	Eco-friendly, cost-competitive Less sludge production, producing non-hazardous metabolites, requires less water consumption optimal operating time.	Require a large area with low digestion rates (days or weeks) Diurnal variation as well as toxicity of some chemicals Less flexibility in design and operation

Aromatic amines may also undergo autoxidation aerobically and turn into colored molecules [75]. Nevertheless, it would be of great interest to find out to what extent dyes are degraded biologically and what remains in the effluent after treatment. Therefore these amines, although colorless which are toxic and mutagenic and it is necessary to degrade them further, possibly into carbon dioxide and water [70]. Dyes might be either toxic or hard to degrade with microorganisms in which only 47% of 87 of dyestuff are biodegradable. They also have an impact on aquatic life due to low light penetration and oxygen consumption. Coagulants such as aluminum chloride, ferrous sulphate, aluminum sulphate, ferric chloride and hydrated lime are the most extensively used coagulant for sludge conditioning and dewatering in coagulation processes at lower temperatures and a broader pH range that adsorb negatively charged natural particles resulting in charge neutralization. However, they produce activated sludge which is very hazardous.

Mineralization of dyes, organic compounds and hence the toxicity of the wastewater generated by textile industry and dye manufacturing industries is a main challenge and an ecological

concern. The effluent produced by textile industries contains a large amount of acid, dyes, alkalis, surfactants, and metals soaps. Typical textile industry wastewater is characterized by high ranges of pH, color, total dissolved solids (TDS), total suspended solids (TSS), total solid (TS), chloride, biological oxygen demand (BOD), chemical oxygen demand (BOD), heavy metals and sodium [67,76]. Hence, understanding of the characteristics (composition and components) of the emerging real textile wastewater is ecologically worth selecting the best treatment technology available. Although characteristics textile effluents are highly variable depending on the processed fabrics, types of processes, types of machines used, type and amount of chemicals used and season of the processing year, Table 2.3 represents the general characteristics of textile wastewater effluents. The effluent produced by textile industries contain a large amount of acid, dyes, alkalis, hydrogen peroxide (H_2O_2) [8], surfactants and metals soaps [67,76]. Understanding the characteristics of the emerging real textile wastewater is ecologically worth for selecting the best treatment technology available.

Table 2.3: Characteristics of most textile and dyeing industry wastewater [64,70,77,78]**.**

Parameters (mg/L)	**Values**	**Parameters (mg/L)**	**Values**
pH	7.0−9.0	TDS	2,900−3,100
BOD	80−6,000	Chloride	1000−1600
COD	150−12,000	Color (Pt-Co)	50−2500
TSS	15−8,000	TKN	70−80

Despite the use of sophisticated and modern technologies, the textile industry is among the highest water-consuming industries and discharge large amount of wastewater to water bodies. Around 100−350 liters of fresh water are required to process 1 kilogram of textile material and 200−250 m^3 water is used per ton of cotton cloth [8]. Hence, almost 20% of the pollution of freshwater comes from textile industries [79]. Table 2.4 describes the processing steps, water consumption and effluents generated in textile industry. Among the textile processing steps, the dying process contributes the highest colored wastewater. There are different processing steps involved in textile industry which consumes a large amount of freshwater [68] and the wastewaters generated are estimated as shown in Table 2.3. Textile effluents contain not only

textile dyes, but also several auxiliary chemicals and inhibitory compounds with serious environmental impacts [80].

Table 2.4: Processing steps, water consumption and effluents generated in textile industry.

Textile Processing Units	Types of effluent compounds	Nature of the composition of effluents	Amount of water discharged (L/Kg)	References
Sizing	Starch, waxes, carboxymethyl cellulose (CMC), polyvinyl alcohol (PVA), wetting agents.	High in BOD, COD Starch,	3−6	[68,81]
De-sizing	Starch, CMC, PVA, fats, waxes, pectin	High in BOD, COD, SS, DS	26−43	[68,81]
Bleaching	Sodium hypochlorite, Cl_2, phosphate, NaOH, H_2O_2, acids, surfactants, $NaSiO_3$, short cotton fiber	High alkalinity, high SS	3−124	[68,81]
Mercerizing	Sodium hydroxide, cotton wax	High pH, low BOD, TDS,	232−308	[68,81,82]
Dyeing	Dyestuffs urea, reducing agents, oxidizing agents, acetic acid, detergents, wetting agents	Strongly colored, high BOD, TDS, low SS, heavy metals	8−300	[68,81,82]
Printing	Pastes, urea, starches, gums, oils, binders, acids, Thickeners, cross-linkers, reducing agents, alkali	Highly colored, high BOD, oily appearance, SS slightly alkaline, low BOD	8−300	[30,68,81,82]
Finishing	Resins, waxes, chlorinated compounds, Acetate,	SS, low BOD	5−250	[68,81–83]

2.4. Advanced Oxidation Processes (AOPs)

AOPs are a viable alternative for the removal of non-biodegradable recalcitrant contaminants and attract a widespread attention in the last few years due to their tremendous choice in the mineralization of recalcitrant pollutants [78]. Among different types of AOPs, ozonation is used for oxidation of several textile dyes and chemical organic compounds [84]. Globally it is estimated that around 10,000 commercial synthetic dyes are well known. They are employed for oxidation of various organic contaminants in polluted water and wastewater. Different types of AOPs were discussed by different researchers for wastewater treatment and grouped into two general categories namely; non-photochemical and photochemical AOPs based on generation of ·OH in absence of light either by ozonation/Fenton's reaction or presence of UV light along with O_3, H_2O_2 and/or Fe^{+2} to generate reactive ·OH by Sharma et al. [85]. Similarly Paździor et al. [3] catagorized AOPs into five catagories as described in the Table 2.5 [86].

Table 2.5: Categories of different types of AOPs [119,120, 121,113]

Fenton based	**O_3 based**	**Photo-catalytic**	**EAOPs**
Fenton	O_3	TiO_2/UV	Electrochemical
Photo-Fenton	O_3/UV	TiO_2/VIS	EF
Photo-Fenton/TiO_2	O_3/H_2O_2	TiO_2+ doping/UV	
	O_3/H_2O_2/UV	Semiconductors/UV	EF like
	O_3/catalysis	Calcined/ Semiconductors/UV	Micro-cell electrolysis
Sono-Fenton			Advanced EC
Fenton like			

O_3-based processes were intensively studied for textile wastewater and wastewater treatments of dyes removal and decolorization [30]. Since dyes were intentionally designed to resist degradation and conventional biological wastewater treatment methods are ineffective in removing the color of textile dyes. The combination of H_2O_2 and Fe^{2+} is referred to as Fenton's reagent and considered as one of the AOPs, however it has limited application for industrial wastewater. There are operational parameters that can affect Fenton's reaction. Fenton's reagent and pH are usually considered the most critical parameters. Excess concentration of H_2O_2 and Fe^{2+} can lead to scavenging of ·OH and converted to less reactive $HO_2^{\bullet}$ and Fe^{3+}. S.

Scienze stated two main limitations which are linked to Fe^{2+} regeneration and the possible formation of oxalic acid ($H_2C_2O_4$) which is poisonous and persistent in wastewater treatment which attributes to ferrioxalate species that inhibit conventional Fenton's reaction to take place.

Although the process is cost and energy intensive, textile wastewater treatment involving ozone oxidation has been performed by different researchers. Ozone is a powerful oxidant for water and wastewater. Ozone is an effective agent for reducing the color of all dyestuff textile wastewater except non-soluble disperse and vat dyes which react slowly and take longer time [87]. It is transformed to generate ·OH during decomposition and reacts with various kinds of O_3-resistant organics rapidly. Though the normal rate of O_3 transforming to ·OH is slow at acidic and neutral conditions due to the lack of hydroxide ions (OH^- initiator), it is suitable alternative for textile wastewater treatments as their pH is higher. If the wastewater to be treated has a pH > 8 and precipitation of calcium carbonate is not of concern ozonation might be a promising process [86].

Elimination of color from textile wastewater is both immediate and long-term interest to textile industries and to limit the discharge of color from textile manufacturing plants. However, AOPs are not cost-effective in terms of chemical consumption (Fenton's processes), energy demand (photo irradiated AOPs), expensive catalysts (EAOPs), side reactions and a possible yield of sub-active by-products, they are potential alternative replacing the conventional wastewater treatments technologies. Fenton's oxidation method is one of the AOPs, which attracts much attention by its strong mineralization ability for organic recalcitrant pollutants. Despite the high efficiency of Fenton reaction, the process is limited by the acidic pH, chemical consumption and the formation of high amount of sludge in the coagulation step [88]. High chemical consumption (H_2O_2) in classical Fenton process is minimized by EF process in which H_2O_2 is produced in-situ spontaneously and it is highly efficient, convenient operation and environment-friendly. EAOPs of wastewater involves both recycling/decomposing where cells and electrodes are designed to minimize power consumptions [7]. It is more effective for removing recalcitrant organic dyes from industrial effluents compared to the classical Fenton process.

EF is one of the most applied EAOPs, and widely investigated for the mineralization of organic and bio-recalcitrant contaminants present in textile wastewater. Electrochemical treatments are advantageous comparing to classical Fenton's process, However, EF treatments are much more

costly and energy intensive utilizes an expensive electrodes with high energy consumption [7] which seriously hinders their application. Combining EF process with Bio-EAOPs would be a promising alternative solution [84] which shows several advantages over classical and electro-chemical Fenton's process. Bio-electrochemical system (BES) is developed to optimize the advantages of both biological and EAOPs. BES extracts electrical energy from organic pollutants trough microbial metabolism where electrons are constantly generated by electro-active microbes leading to the synthesis of chemicals, mineralization of contaminants and conversion to different types of energy forms to make it more productive in the anode [89] and are consumed by electron acceptors in the cathode [4,90]. BEF is a suitable technology to solve problems of energy and environmental aspects by breaking the chemical bonds of organic compounds into electrical energy through the catalytic reactions of microorganisms under aerobic conditions. Recently, various bioreactors of BES have emerged such as single-chambered BES, dual-chambered BES, and BES-based integrated systems. Extensive and meaningful investigation on BES can contribute to treat organic contaminants of textile wastewaters, to produce electricity as energy source for EF process to occur.

2.4.1. Classical Fenton Process

Since Fenton's mechanism is emerged as one of the most effective AOPs and widely applied for removal of various organic contaminants from wastewater through direct reaction of ferrous ion (Fe^{2+}) with H_2O_2 to generate ·OH, the primary oxidant in Fenton reagent. The combination of H_2O_2 and Fe^{2+} is referred to as Fenton reagent. Its oxidative mechanism is related to its characteristic of electrophilic, high reactivity and non-selectivity [89]. When the Fenton process is carried out without using high temperature or pressure and working with conventional equipment, the best results are obtained at acidic pH and catalyst/oxidant ratio 1.5. Moreover, it is linked with high reagent dosage and accumulation of Fe^{3+} ions in real life wastewater applications. The generation of ·OH terminates as soon as all the initial Fe^{2+} ions are oxidized to Fe^{3+} ions [78]. Fenton oxidation involves a catalytic decomposition of H_2O_2 by ferrous iron (Fe^{2+}) to produce ·OH under acidic conditions according to Eqn. 2.1 with rate constant ($k = 63\ M^{-1}\ s^{-1}$) [91]. Figure 2.6 shows the Fenton degradation mechanism.

$$Fe^{2+} + H_2O_2 \rightarrow Fe^{3+} + \cdot OH + OH^- \qquad (2.1)$$

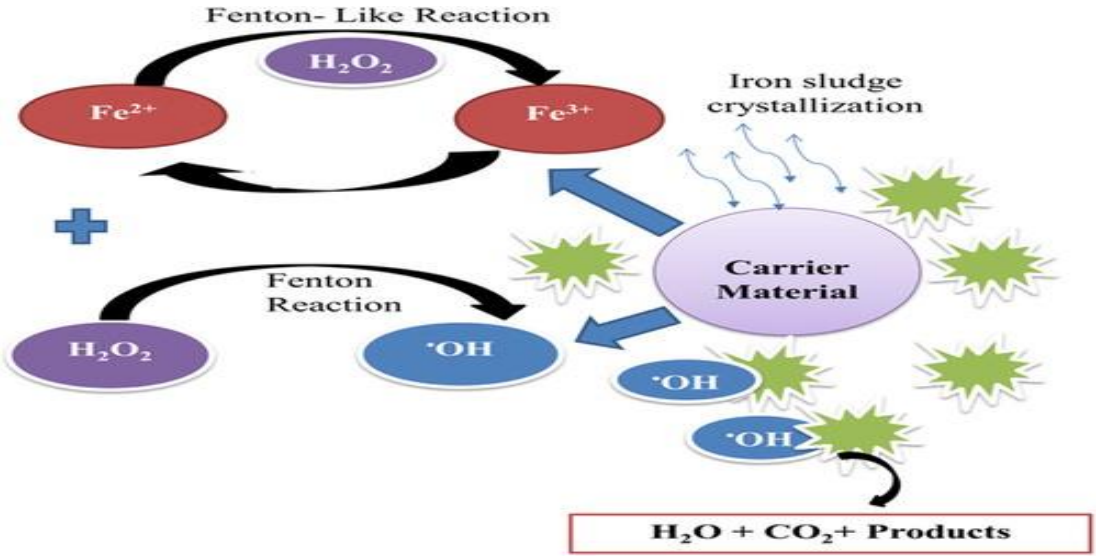

Figure 2.6: Fenton reaction mechanisms

Thus, the Fenton's reaction alone is not capable of further mineralizing the organic compounds because of iron ion depletion [89]. But through Fenton-like reaction, Fe^{3+} can also react with H_2O_2 according to Eqn. 2.2 and Eqn. 2.4, recycling $Fe^{2+}$and thus supporting to continue the Fenton's process [17]. ·OH can interact with organic compounds or Fenton's catalyst through, hydroxyl addition hydrogen abstraction and electron transfer [78]. Hydroxyl addition occurs with organic compounds having an aromatic system or carbon-carbon multiple bonds (Eqn. 2.5). Hydrogen abstraction occurs with unsaturated organic compounds (Eqn. 2.6) whereas electron transfer occurs when •HO interacts with inorganic ions (Eqn. 2.7) [76].

$$Fe^{3+} + H_2O_2 \rightarrow FeOOH^{2+} + H^+ \quad (2.2)$$

$$FeOOH^{2+} \rightarrow HO_2^{\cdot} + Fe^{2+} \quad (2.3)$$

$$Fe^{3+} + HO_2^{\cdot} \rightarrow Fe^{2+} + H^+ + O_2 \quad (2.4)$$

$$\cdot OH + R \rightarrow R(OH) \quad (2.5)$$

$$\cdot OH + RH \rightarrow R^{\bullet} + H_2O \quad (2.6)$$

$$\cdot OH + Fe^{2+} \rightarrow Fe^{3+} + OH^- \quad (2.7)$$

Fe^{2+} regeneration from reaction Eqn. 2.2 is very slow ($k = 2.7\times10^{-3}\ s^{-1}$), however, Fe^{2+} can be regenerated more rapidly by the reduction of Fe^{3+} with $HO_2^{\bullet}$ from Eqn. 2.4 ($k = 2\times10^{3}\ M^{-1}\ s^{-1}$),

with an organic radical $R^{\bullet}$ from Eqn. 2.8 ($k = 10^7–10^8\ M^{-1}\ s^{-1}$) and/or superoxide ion ($O_2^{\bullet-}$) from Eqn. 2.9 ($k = 5\times10^7\ M^{-1}\ s^{-1}$) as well as $HO_2^{\bullet}$ with reaction rate ($k = 2.7\times10^{-3}\ M^{-1}\ s^{-1}$) and $O_2^{\bullet-}$ with reaction rate (pK = 4.8) are produced by Eqn. 2.10 and 2.11, respectively.

$$Fe^{3+} + R^{\bullet} \rightarrow Fe^{2+} + R^{+} \quad (2.8)$$

$$Fe^{3+} + O_2^{\cdot-} \rightarrow Fe^{2+} + O_2 \quad (2.9)$$

$$HO_2^{\cdot} \leftrightarrow H^{+} + O_2^{\cdot-} \quad (2.10)$$

$$H_2O_2 + \cdot OH \rightarrow HO_2^{\cdot} + H_2O \quad (2.11)$$

Fenton's reaction is limited by the acidic pH, chemical consumption and the formation of high amount of sludge in the coagulation step [88]. High chemical consumption in classical Fenton's process is minimized by EF process in which H_2O_2 is produced in-situ spontaneously and it is highly efficient, convenient operation and environment-friendly [92]. EF has attracted great attention in the field of wastewater treatment because of its good environmental compatibility, high efficiency, and convenient operation as well as H_2O_2 and Fe^{2+} can be electro-generated continuously at the cathode which reduces reagent transportation and storage [93] and reduces formation of metal sludge which are commonly encountered in classical Fenton's process [94]. EF is limited by H_2O_2 production [87,90] according to Eqn. 2.15 in acidic media or Eqn. 2.16 in neutral media and decomposed by external added Fe^{2+} to form ·OH (Eqn. 2.19) to degrade persistent organic pollutants according to Eqn. 2.20 and 2.21 [95].

$$O_2 + 2H^{+} + 2e^{-} \rightarrow H_2O_2 \quad (2.15)$$

$$O_2 + 2H_2O + 2e^{-} \rightarrow H_2O_2 + 2OH^{-} \quad (2.16)$$

$$O_2 + 4H^{+} + 4e^{-} \rightarrow 2H_2O \quad (2.17)$$

$$O_2 + 2H_2O + 4e^{-} \rightarrow 4OH^{-} \quad (2.18)$$

$$H_2O_2 + Fe^{2+} \rightarrow \cdot OH + 2OH^{-} + Fe^{3+} \quad (2.19)$$

$$\text{Pollutants} + \cdot OH \rightarrow \text{intermidates} \quad (2.20)$$

$$\text{Intermidates} \rightarrow CO_2 + 2H_2 \quad (2.21)$$

2.4.2. Electro-Fenton Process

Application of EAOP technology has emerged as a promising alternative for Fenton's oxidation, which utilizes electron for in-situ generation of Fenton's reagent. H_2O_2 is continuously generated at the cathode. In a typical process, air/O_2 is continuously supplied to the cathode, where the generation of H_2O_2 is induced by a two-electron reduction of O_2 in acidic medium. The addition of Fe^{2+} results in the catalytic decomposition of H_2O_2 to generate ·OH based on Fenton's reaction. It is clear that some of the limitations of the classical Fenton's oxidation are minimized [78]. Several studies have focused on the development of efficient cathode materials for H_2O_2 electro-generation in the EF process. To enhance the production rate of H_2O_2, anodic loss pathways, which significantly reduce the overall H_2O_2 production rate, should be inhibited. Lim and Ho [96] observed organic electron donors enhance the electrochemical production of H_2O_2, while simultaneously undergoing oxidative degradation. The observed positive effect of organic electron donors on the electrochemical production of H_2O_2 was due to a preferential adsorption of organic substrates on the TiO_2 outer layer of the anode [87,97]. Figure 2.7 shows different electro Fenton oxidation compartment setups.

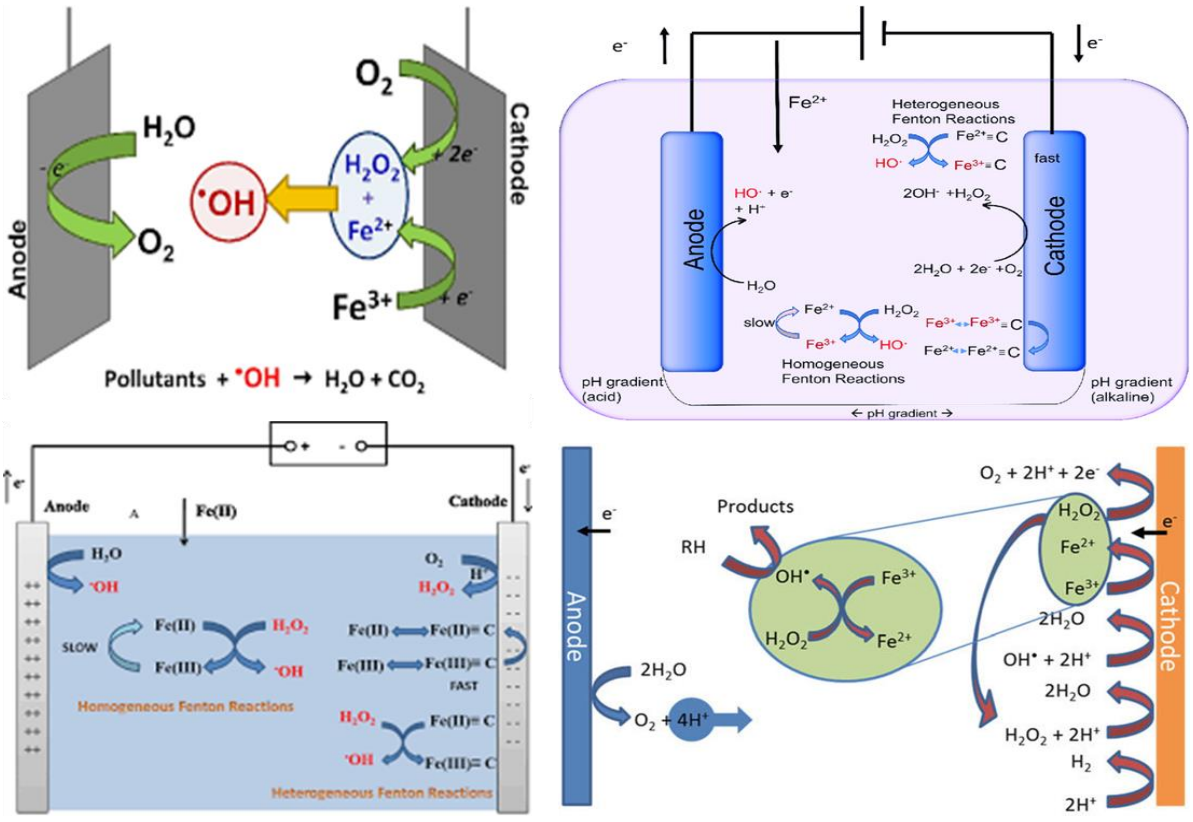

Figure 2.7: Different electro Fenton process set-ups and mechanisms

Cathodic material and its performance are a key factor for H_2O_2 generation in EF reaction for H_2O_2 yield, current efficiency, and energy consumption. Carbon materials show high electrical conductivity, no toxicity, low costs, and high catalytic activity during H_2O_2 decomposition and high stability in ORR processes including graphite, activated carbon fiber materials, carbon sponges, ordered mesoporous carbon and carbon aerogels. The large specific surface area of porous carbon provides many active sites for electrochemical reactions. Yu et al. [98] developed hierarchically porous carbon modified active carbon fiber (ACF-HPC electrode) as an effective cathode used in electro-Fenton in ORR process and obtained the H_2O_2 concentrations increase from 111.8 mg L^{-1} to 160.4 mg L^{-1} at pH 3, from 143.4 mg L^{-1} to 227.4 mg L^{-1} at pH 7 (the highest H_2O_2 production rate of 11.05 mg h^{-1} cm^{-2}) and from 80.4 mg L^{-1} to 142.4 mg L^{-1} at pH 9 when the current density varied from 16 mA cm^{-2} to 24 mA cm^{-2} respectively. Similarly Zhou et al. [99] synthesized activated carbon/stainless steel mesh (ACSS) composite cathode, where SS mesh distributes current and AC supports H_2O_2 electro-generation and organic compounds adsorption. Currently there are metal oxide modified cathodes that have become the most efficient materials for oxygen reduction via two electron oxygen reduction and H_2O_2 production electrochemically in cathode surface. H_2O_2 is widely used in many fields, especially in chemical industry and environmental protection due to its strong oxidizing property that degrades organic compounds to only oxygen and water and no hazardous residuals production. Although accurate measurement of the electro-generated H_2O_2 in the cathode is useful, real-time detection of the generated H_2O_2 within the electro-chemical reactor is difficult. Cho et al. [100] determined H_2O_2 production using various chemical methods such as titanium oxalate, titanium tetrachloride and cobalt (II) ion that form colored complexes with H_2O_2.

2.4.3. Heterogeneous-Electro-Fenton Process

In heterogeneous Fenton's oxidation Fe^{2+} is immobilized within the structure or pores of supported catalysts as iron oxide, generation of ferric oxide, loss of catalysts and pH effect will be minimized. However mass transfer limitations may affect the effectiveness of the process, there is a possibility of iron leaching, which can induce homogeneous Fenton's reaction which contribute to the removal of the pollutants. The process involves two complex processes i.e., chemical reactions between ·OH and organic pollutants and physical processes that occur at the surface of the heterogeneous catalysts during mineralization of organic pollutants. H_2O_2 may react with leached iron in the solution or iron species at the surface of the catalysts, leading

to the production of ·OH. The organic pollutants and ·OH may be adsorbed at the surface of the catalyst through chemisorption [78]. Even if goethite (αFeOOH) and magnetite (Fe_3O_4) are the most applied catalysts, Fe_3O_4 based nanoparticles are extensively being investigated as heterogeneous catalysts. Figure 2.8 describes different heterogenous electro Fenton oxidation.

Iron based metal-organic frameworks N-containing ligands are a kind of porous materials prepared from metal ions and organic ligands for preparing various kinds bi-functional catalyst via a simple carbonization process to facilitate electron transfer and electrochemical H_2O_2 generation. Cao et al. [101] prepared iron oxide (FeOx) nanoparticles embedded nitrogen-doped hierarchically porous carbon (FeOx/NHPC) by carbonization. The authors investigated the hetero-EF activity of FeOx/NHPC750 catalyst by mineralization of phenol, sulfamethoxazole, atrazine, rhodamine B and 2, 4-di-chlorophenol at pH 6. The removal of phenol by adsorption effect (25%) and electro-catalysis (EC) (43%) were compared to phenol removal efficiency by hetero-EF process on FeOx/NHPC750 (99%) within 120 min, with pseudo-first order kinetic constant of phenol degradation 0.034 min^{-1}. Table 2.6 summarizes different potential operational factors in Fenton related reactions.

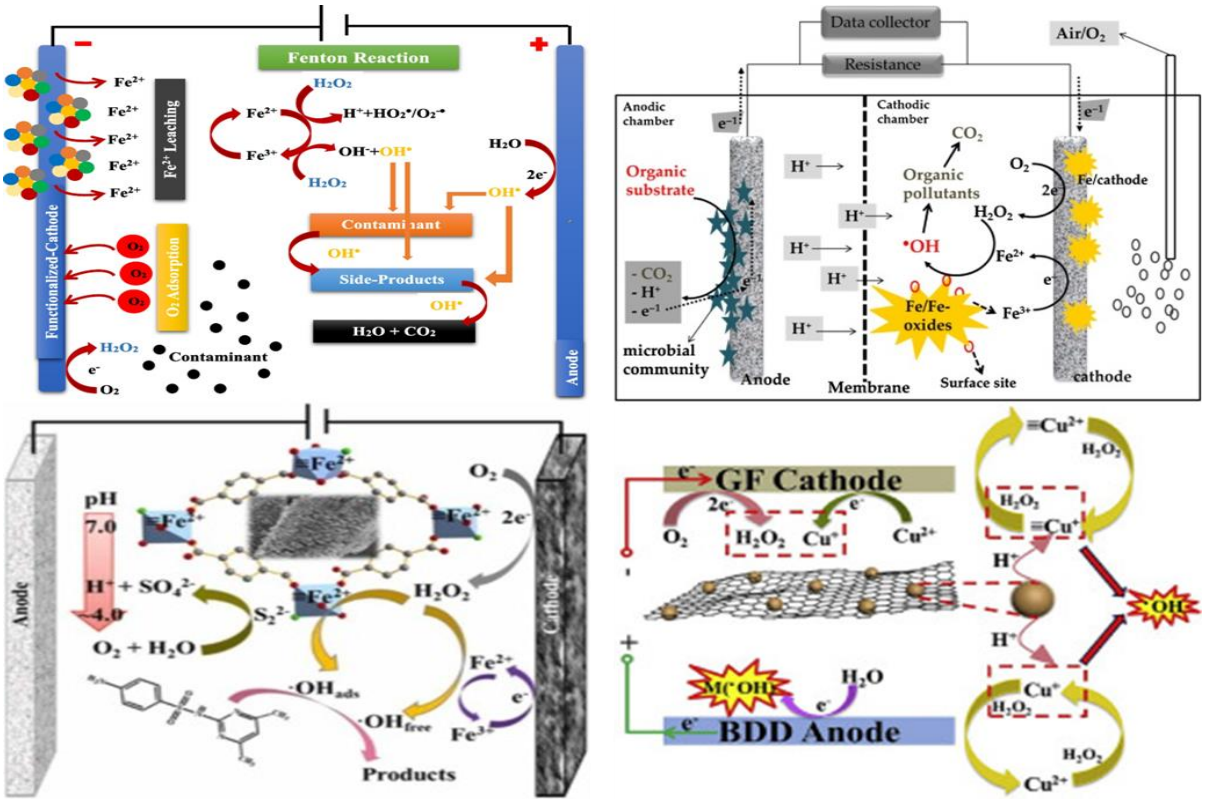

Figure 2.8: Different heterogeneous Electro Fenton set-ups and mechanisms

Table 2.6: Summery of potential operational factors in Fenton related reactions

Parameters	Operational effects	Ref.
Pollutant concentration	Increasing the initial pollutant concentration, decolorization rate increased. This can be related to the increased amount of dye molecules exposed to the Fenton's reaction. Also, this causes the ·OH radicals to be used in the desired reactions and increases the rates of dye decolorization.	[2]
Reaction time	The rate of decomposition reaction increases with an increase the duration or residence time of a reaction, while keeping all other factors constants	
Reaction temperature	High temperature can promote oxidation rate and enhance Fenton's reaction. The positive effect of higher temperature can be attributed to more efficient consumption of H_2O_2, which results in higher generation of ·OH, however the optimal operational temperature ranges between 20−40 °C	
Solution pH	At low solution pH, scavenging of ·OH by excess H^+, formation of $[Fe(H_2O)]^{2+}$, prevent the interaction between Fe^{3+} and H_2O_2 and evolution of H_2 occurred. At high solution pH, deficiency of H^+, which hampers ·OH formation, decomposition of H_2O_2 and precipitation of Fe^{3+} as iron OH^- leading to the production of excessive sludge	[102]
Fenton's reagent	Excess concentration of H_2O_2 and Fe^{2+} can lead to scavenging of ·OH converted to less reactive $HO_2^{\bullet}$ and Fe^{3+} residue	[103]
Nature of reaction matrix	Presence of organic/inorganic compounds in wastewater can result in scavenging effect on ·OH. Inorganic compounds such as NaCl, Na_2CO_3 and Na_2SO_3 are found in various concentrations in real wastewaters and can react with ·OH decreasing the performance Fenton's oxidation.	[104]

Table 2.7: Literature survey for various case studies related to EF and Hetero-EF

Modified cathode	Target pollutant	Mineralization (%)	Decolorization (%)	Reactor volume	Pollutant concentration	Ref
Flyash augmented Fe_3O_4	Benzoic acid	84.7	−	100 ml	50 mg L^{-1}	[93]
CF/GO/AQS	Rhodamine B	89.9	95	10 ml	20 µmol L^{-1}	[90]
Fe^{2+}/OA/CaO_2	Methyl Orange (MO)	99	−	100 ml	0.15−0.5 mg L^{-1}	[105]
CNTs-nafion/NF/PTFE	Atenolol	~100		250 ml	20 mg L^{-1}	[106]
GO / PEDOT	MB	97.9	−	200 ml	94.2 mg L^{-1}	[107]
$FeVO_4$@BiOCl	p-nitro-phenol (PNP)	~100	−	110 ml	20 mg L^{-1}	[108]
MgO supported by zeolite	Recalcitrant wastewater	78	−	500 ml	−	[109]
Sodium vermiculite	Ponceau SS diazo dye	84.1	−	130 ml	0.15 mg L^{-1}	[110]
Selenite $Bi_{25}FeO_{40}$	levo floxacin	91.1	−	250 ml	5 mg L^{-1}	[111]
Dimethyl silicon oil (DMS)	fungicide-flutriafol	~100	48.88	250 ml	100 mg L^{-1}	[112]
Graphite	Methylene Blue	74	99	20 L	20 mg L^{-1}	[103]
Fe@Fe_2O_3/NCF	Estrogen	81	−	150 ml	20 µmg L^{-1}	[113]
SrM-NPs	Antibiotics	85.9-88.2	74.8-87.2	250 ml	10 mg L^{-1}	[114]
CNT and γ-FeOOH	Orange II	~100	−	151.2 ml	0.1 mg L^{-1}	[115]

To address the challenges of classical Fenton, heterogeneous Fenton's process was employed because of coexistence of both Fe^{2+} and Fe^{3+}, magnetic nature, large number of active sites, reusable nature, and non-toxicity of the catalyst. Therefore, careful selection of catalyst/support material is needed to fit the aforementioned characteristics of Hetero-EF catalysts [110]. Thus to propose a material as potential heterogeneous catalyst or functionalized cathodic materials, it is obvious that extensive investigations are required to determine the experimental conditions range in which the materials can exhibit catalytic activity and stability, extent of leaching, interaction of support with the H_2O_2 and the environmental compatibility of the solid catalyst support [78]. Table 2.7 provides detailed literature survey for various EF case studies.

Table 2.8: The main factors and conditions that affect BEF reaction process.

Parameters	**Operational effects**	**Ref.**
Microbial concentration	Rate of H_2O_2 generation and pollutant degradation increases with increasing microbial concentration of anodic chamber.	[104]
Electrode nature	Electrodes contact with the microbial population and the effluents that provide suitable electrical conductivity, corrosion resistance and biocompatibility.	[116]
Power density	More power generated, the reduction of oxygen in the cathodic compartment will increase, leading to increased generation of H_2O_2, which will participate in the Fenton's reaction to generate ·OH, and thus higher degradation of organic materials.	[117]
Mass transfer limitations	Diffusion-controlled process results in complex steps of electron transfer, which in turn lead to multiple reaction kinetics to be considered in these types of systems and some limitations related to mass transfer.	[118]
Substrate concentration	H_2O_2, production is proportional to the substrate concentration in the reaction medium, up to certain a limit, where the maximum rate of reaction is achieved according to Michaelis-Menten model for the enzymatic kinetics.	[119]

2.4.4. Bio-Electro-Fenton Process

BEF systems are promising methods for treatment of persistent organic pollutants from many sources of wastewaters [69]. They are complex linked compartments and elements, which are affected by various conditions that should be taken into account while designing BEF in degrading recalcitrant organic pollutants from textile wastewater effluents [2,116]. The right choice of electrodes to be used as anode and cathode is the first factor that makes BEF system more successful [104]. Table 2.8 lists the main operational parameters of BEF systems.

Table 2.9: Lists of different bio-electrochemical systems.

BES	Volume	Microbial inoculum	Anodic dominant microbes	Ref
MEC	400 ml	Potato and dairy wastewater	Geobacteraceae	[7]
MFC	280 ml	Biogas digestate	Geovibrio and purple non-sulfur bacteria	[120]
MFC	28 ml	activated sludge	metabolically active bacteria	[121]
MFC	250 ml	Wastewater	Acinetobacter, Azospirillum and Comamonas	[114]
MFC	200 ml	Wastewater	Saprospiraceae and Caldilineaceae	[122]
MFC	70 ml	20ml, mixed anaerobic sludge	–	[123]
MFC	2000 mL	20g/L, Mixed anaerobic sludge	Chlorella species	[124]
MFC	45 m^3	150ml, activated sludge	Proteobacteria (47%) and Bacteroidetes (18%),	[125]
MEC	300 ml	Activated sludge	Geobacter	[126]

The rapid development of advanced materials has led to the invention of some emerging functional materials, which can be potentially applied as suitable substrates and/or dispersants for catalysts in environmental remediation. BES which use microorganisms to facilitate oxidation/reduction processes through the release/capture of electrons from an electrode have drawn increasing attention in recent years as an emerging technology [127]. BES combines microbiology with electrochemistry used for several applications such as electricity generation

(microbial fuel cell, MFC), hydrogen production (microbial electrolysis cells, MEC), value-added chemical synthesis (microbial electro-synthesis, MES), desalination (microbial desalination cell, MDC), and removing contaminants (microbial remediation cell, MRC). Table 2.9 provides detailed literature survey for various BEF case studies (Fig.2.9).

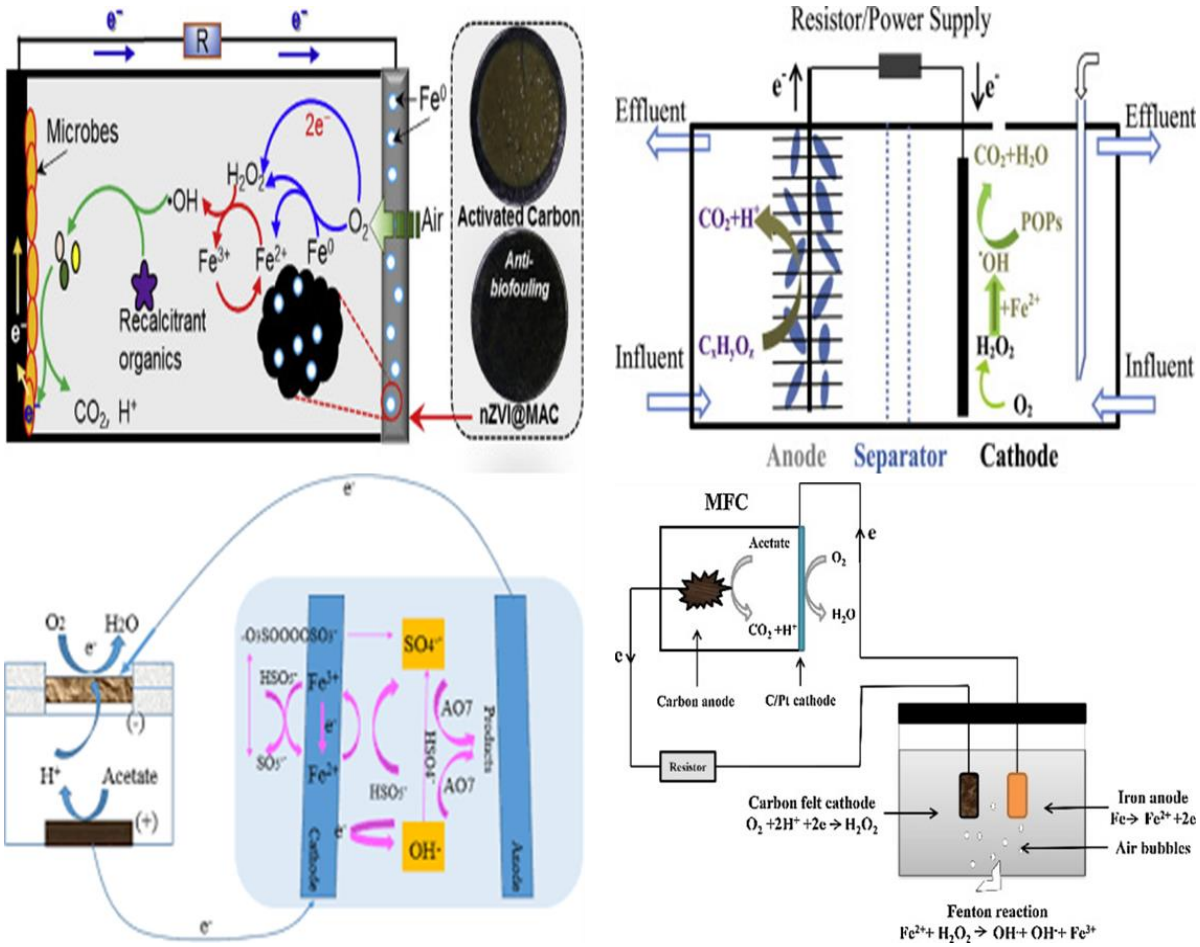

Figure 2.9: Different bio-electro Fenton set-ups and mechanisms

Deng et al. [128] demonstrated magnetic recyclable $CoFe_2O_4$@PPy prepared by in-situ Fenton's oxidization polymerization with advanced photo-Fenton's performance for Methylene blue, Methyl orange and Rhodamine B (RhB) and their result showed that decolorization rates reached nearly 100% in the photo-degradation of 10 mg L^{-1} RhB after 2 h visible-light irradiation RhB at wavelength range of 200−650 nm scan and only low toxicity small molecules are detected by LC-MS. They demonstrated that the peak at 553 nm was decreasing, and the peak at 259 nm, 310 nm, and 320 nm gradually disappeared, indicated that the aromatic chain, N-position ethyl group and conjugated structure in the RhB molecule were gradually destroyed during the reaction resulting in small organic molecules. *Dai et al.* [7]

noticed that the effect of sulfide concentration on sulfide oxidation and no effect was observed when the sulfide concentration was increased from 120 to 180 mg L^{-1} (greater than 95% sulfide removal was achieved). However, it was obviously affected when the sulfide concentration was substantially increased to 360 mg L^{-1}. The degradation efficiency of Congo Red azo dye increased with the increase in aqueous sulfide concentration from 120 mg L^{-1} to 360 mg L^{-1}. Besides a sulfide concentration of 178.0 mg S L^{-1} was beneficial for bacterial growth and sulfide oxidation under anaerobic conditions in MFCs. Schematic illustration of the working principle of typical BEF system and chemical reactions that takes place on the system.

Zou et al. [103] conducted a scaling-up of BEF system for methylene blue (MB) removal and concluded the decolorization and mineralization efficiency of MB with concentration of 20 mg L^{-1} were 99% and 74% with retention time of 28 h respectively. Authors checked the system performance with varied catholyte pH and observed drop of decolorization efficiency, TOC removal efficiency, K_{app} and K_{TOC} of MB when pH increased from 2 to 8 and achieved maximum removal efficiency at pH 2 (99%, 89%, 0.68 h^{-1} and 0.22 h^{-1}) and they underlined that, regardless of the initial cathodic pH, pH was increased with increasing operational time in the cathode. Besides they investigated the effect of initial Fe^{2+} concentration (0.05, 0.1, 0.2, 0.5 and 1 mM) on MB mineralization with set of define parameters (20 mg L^{-1} of MB, pH of 2, Na_2SO4 of 50 mM, applied voltage of 0.4 V, and aeration rate of 350 mL min^{-1}) and concluded a rapid decolorization (95% at 6 h and 99% at 28 h), TOC removal efficiency (89% at 28 h and K_{app} of 0.68 h^{-1}) were obtained with initial Fe^{2+} concentration of 0.2 mM.

The power consumption in the EF process mainly contributes to its operating costs and it is very attractive and challenging to develop an energy-saving EF system with the BEF concept using bioelectrons to drive an EF process by properly configuring a MFC. Mai & Li [129] developed MFC driven BEF process for Orange II, a model azo dye degradation that is widely used in a in textile industries using shewanella discolorations in anaerobic anode and aerated cathode dual-chamber equipped with a carbon nanotube (CNT)/γ-FeOOH composite cathode for in-situ generation of H_2O_2 and Fe^{2+} at neutral pH by direct electro-reduction of γ-FeOOH to adsorbed Fe^{2+}. They investigated the effect of cathode composition on the power output in MFCs. The power density curves of four MFCs operated with different cathode compositions. A maximum power density of 312 mW m^{-2} was obtained at a current density of 0.90 mAm^{-2} with CNT/γ-FeOOH ration of 1:2 in MFCs in 100 mM PBS at pH 7.0. Figure 2.10 different BEF system for contaminant degradation.

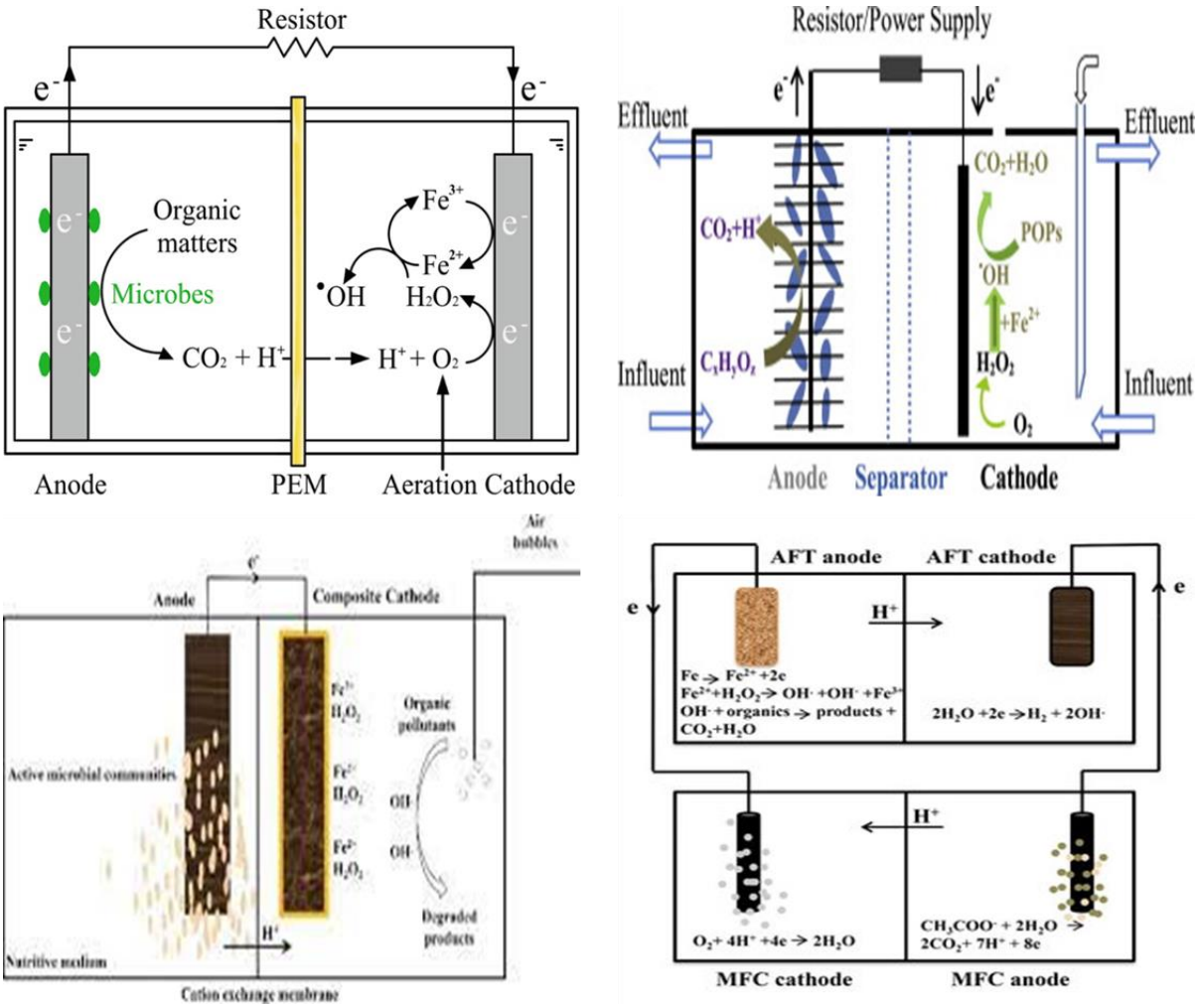

Figure 2.10: Different membrane separated bio-electro Fenton set-ups.

A detailed literature survey was conducted regarding ozonation, EF, BEF and their mechanisms of wastewater and textile wastewater decolorization, degradation and mineralization. Their degradation and decolorization mechanism dependence on operating pH condition, reaction time, initial concentration of the model contaminant, concentration ratio of H_2O_2/Fe^{2+}, nature of the cathode material and its surface area as well as microbial concentration and their characteristics. Drawbacks of Fenton's oxidation was discussed, including high chemical consumption, instability of the Fenton's reagent, parasitic reactions and loss of oxidant, difficulty in optimizing the reagent concentrations and the necessity to neutralize the treated wastewater before disposal. Real textile effluents contain carbonates, bicarbonates, chlorides, and bromides in addition to dyes that reduce the degradation efficiency of the dyes by scavenging the oxidizing agents. The reviews covered the fundamentals of ozonation, Fenton's oxidation electro Fenton and bio-electro Fenton's oxidation, focusing on the major limitations

and the recent progress towards addressing them. Figure 2.11 shows the advantages of BEF process for real wastewater application.

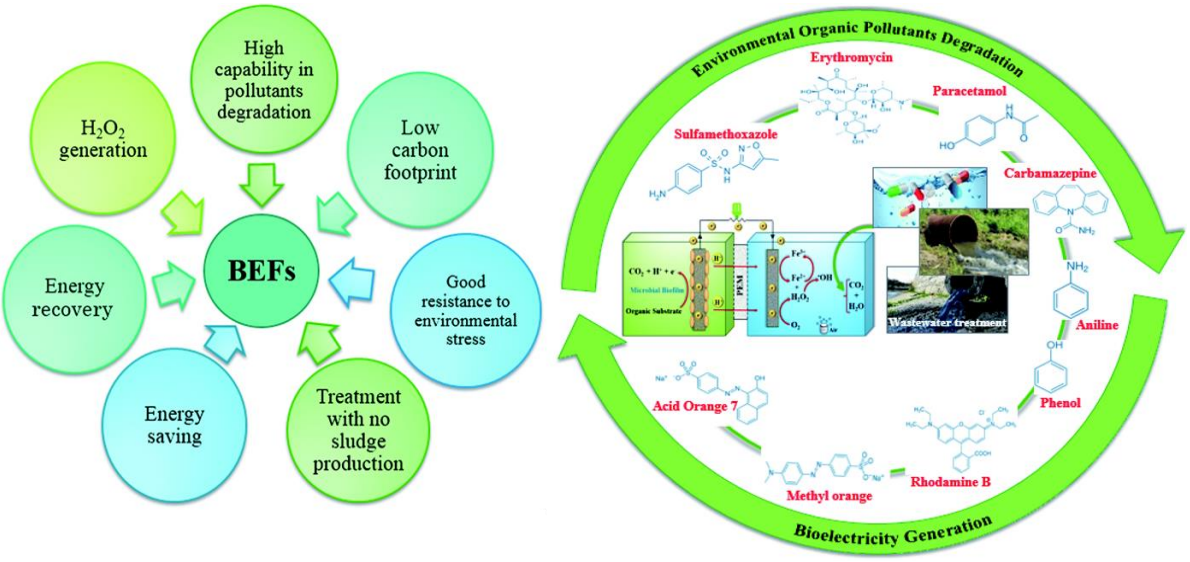

Figure 2.11: Advantages of bio-electro Fenton processes

2.4.5. Ozone Based AOPs

O_3 is a powerful oxidant that can react directly with organic compounds as an electrophile under acidic conditions and a complex chain radical mechanism under alkaline pH conditions, which rapidly decomposes to produce ·OH [3]. O_3-based AOPs were intensively studied for textile wastewater treatments [30]. Since dyes were intentionally designed to resist degradation, the conventional biological wastewater treatment methods were ineffective. Rate of disintegration of O_3 in water decreases as pH decreases, which is disadvantageous for textile wastewater [18] whose pH > 8. To date, attention has been given to catalytic ozonation due to its great capability to efficiently eliminate harmful organic pollutants at mild temperatures. Ozonation process can be applied alone or in combination with UV light, catalyst, ultrasound or activated carbon to treat textile wastewater [64].

Comparing to non-catalytic ozonation, catalytic ozonation has an effective degradation efficiency [130]. It is important to optimize the applied O_3 dose and ozonation time to achieve a maximum biodegradability of the specific pollutant. [3,92]. Unlike Fenton's process, ozonation process doesn't increase the volume of wastewater and sludge production [92]. Mechanisms involved in initiating formation of radicals include ozonation at elevated pH and combinations of O_3/H_2O_2, O_3/UV, and O_3/catalysts. The reaction involving O_3 and the $O_2^{\cdot-}$

creates an ozonide anion radical ($O_3^{\cdot}$) and releasing ·OH. But the reaction has its own limitation that cannot be applied to acidic conditions since O_3 initiation is restricted by OH^- initiator to produce $HO_2^{\cdot}$ and $O_2^{\cdot -}$, subsequently produce ·OH according Eqn. 2.22 [85]. Wastewater matrix, pH of the solution, temperature, organic matter and alkalinity are the main parameters that affect the stability of O_3.

$$O_3 + OH^- \rightarrow HO_2^- + O_2 \text{ and } O_3 + HO_2^- \rightarrow \cdot OH + O_2^{\cdot -} + O_2 \qquad (2.22)$$

The combination of O_3 and H_2O_2 is known as peroxone. This process involves the generation of the conjugate base of H_2O_2 i.e., HO_2^- which reacts with O_3 resulting in formation ·OH radical by the following reactions, Eqn. 2.23–25 [85].

$$H_2O_2 \rightarrow HO_2^- + H^+ + e^- \qquad (2.23)$$

$$HO_2^- + O_3 \rightarrow HO_2^{\cdot} + O_3^{\cdot -} \qquad (2.24)$$

$$O_3 + H_2O_2 \rightarrow 2 \cdot OH + O_3^{\cdot -} \qquad (2.25)$$

$$O_3 + 2H^+ + 2e^- \rightarrow O_2 + H_2O \qquad (2.26)$$

Although ozonation leads to the formation of partial oxidation products such as organic acids, aldehydes, and ketones, it doesn't yield complete mineralization to CO_2 and H_2O. Furthermore, ozonation enhances the biodegradability of textile wastewater (BOD/COD ratio) by a factor of up to 6.8-fold [64,131]. Generally AOPs lead to high capital and operating costs and reduced efficacy in natural waters due to ·OH scavenging, they are more often being employed owing to the ability of ·OH to degrade bio-recalcitrant pollutants [92]. Hassaan & Nemr [131] and Sharma *et al.* [85] reported the rate of disintegration of O_3 in water raised as pH increased. The authors clarified that at pH 10, the half-life of O_3 in water became less than one minute. They determined that reaction of OH^- and O_3 led to formation of $O_2^{\cdot -}$ and hydroperoxyl radical ($HO_2^{\cdot}$). The initiation of this reaction, however, is quite slow with a second-order rate constant of 70 $M^{-1}\ s^{-1}$ [86].

S. Yuan *et al.* [132] reviewed several articles on catalytic ozonation of dyes and stated variation in pH showed only slight effect on removing Orange 4, but exerted a significant impact on TOC removal (86%) with complete elimination of the compound within 21 min by Cu@SBA-

15 as heterogeneous catalyst in the presence of O_3 (5 gm^{-3}) and TOC elimination efficiency was reduced to 48.4% at pH 3.0, which may be attributed to self-decomposition rate of O_3 rather than converting to reactive ·OH. Fe_2O_3/Al_2O_3@SBA-15 was found to have an excellent performance for the mineralization (90%) of ibuprofen during catalytic ozonation within 60 min [121]. The heterogeneous catalysts act as electron acceptor and reducing O_3 to form ·OH or catalyzing O_3 decomposition directly with the formation of ·OH. Different studies were performed on varying textile wastewater (COD between 186 and 5720 mg O_2 L^{-1}), with a wide range of chemical doses. A single ozonation was generally implemented to industrial textile wastewater treatment. The O_3 dose to the initial COD ratio was usually in the range 0.5−2.5 gO_3 gO_2^{-1} (for applied doses) or 0.07−0.8 gO_3 gO_2^{-1} (for absorbed doses) [133]. The ozonation was effective, an increase of the applied O_3 dose above 1.7 gO_3 gO_2^{-1} did not improve COD removal in decolorization (above 80% in most cases. The obtained COD removals varied between 5 and 37%.

Somensi *et al*. [134] investigated decolorization and mineralization efficiency of pre-treated textile wastewater using O_3. They demonstrated that ozonation process was more effective in degrading and decolorizing of textile wastewater dyes under alkaline pH than acidic pH and the average efficiencies for color removal were 40.6% for pH 3.0 and 67.5% for pH 9.1. After 240 min of pre-ozonation the values of COD decreased by 25.5 and 18.7% for pH 9.1 and pH 3.0, respectively. However, they mentioned ozonation efficiency was influenced by the dye structure and solubility, reactive dyes are very soluble in water, and thus O_3 could easily react with them. Ozonation was enhanced by metallic ions including Pb^{+}, Cu^{2+}, Zn^{2+}, Fe^{2+}, Ti^{2+}, and Mn^{2+} and Fe^{2+} is most widely used because it could be removed easily and cause low damage to water body. Some organic compound contaminants are O_3-resistant for degradation such as atrazine (ATZ). However, ·OH generated from O_3 decomposition can react with various kinds of organics contaminants. Forexample Zhou *et al*. [135] conducted a novel AOPs using iron electrodes and O_3 for ATZ mineralization in an open electrolytic cell containing 500 mL ATZ solution of 5 µM at a certain pH (5.6). In their report using iron electrodes, they found electrocoagulation (EC/O_3) had 87% mineralization efficiency in 10 min compared to 27% ozonation alone with rate constant 125 M^{-1} s^{-1}. Only 6% removal of ATZ was achieved by electrocoagulation alone.

Hassan & Hawkyard [136] investigated decolorization of aqueous Fenton process and found it to be effective at a wide pH ranges and in alkaline conditions Ferral, derived from natural clay

sources, which contains 2% ferric sulfate and 6% aluminum sulfate + H_2O_2 achieved better color removal than $Fe_2(SO_4)_3$ + H_2O_2 in the ozonation process. The authors found that color removal was 64% (O_3-only process, 44%) and 49% in the Ferral + H_2O_2 and ferric sulfate + H_2O_2 catalyzed ozonation processes respectively at pH 8.2 comparing without O_3 was 10% and 3% respectively. In the case of Ferral-catalyzed ozonation more dye molecules underwent an oxidation reaction rather than with ferric sulfate-catalyzed ozonation. Similarly, Coca *et al.* [137] carried out a decolorization kinetics study of molasses wastewater by chemical oxidation with O_3 in a 2 L jacketed stirred reactor connected to an O_3 generator with mass flow of 1.7 $gO_3\ h^{-1}$. They evaluated that the decolorization rate constant was 0.6×10^7–$3.8\times10^7\ M^{-1}\ s^{-1}$, depending on the stirring rate and the inlet gas flow at pH 8.7 and 25 ℃. Authors determined mass transfer parameters in ozonation process such as O_3 solubility, O_3 decomposition rates and the volumetric mass transfer coefficient of O_3 in the liquid phase at the same time kinetic parameters, such as the stoichiometric coefficient, the ozonation rate constant and the regime of O_3 absorption were studied.

Jung *et al.* [10] studied an ozonation mineralization of diethyl phthalate (DEP) in a cylindrical, semi-batch reactor and the intermediates of the ozonation process were identified by GC/MS. The O_3 decay pattern in DEP solution was with 1mg L^{-1} (corresponding to 20.8µM) O_3dose at pH 3 and 7. The O_3 mineralization in DEP solution at pH 3 showed low O_3 decay rate (only 3.6−6.3% of depletion, $k_o = 0.01\ min^{-1}$). However, at pH 7, the O_3 injected in the DEP solution ($k_o = 0.23\ min^{-1}$) degraded rapidly ($k_o = 0.02\ min^{-1}$). Consequently, O_3 decay by DEP addition at pH 7 was believed to be responsible for the formation of intermediates via DEP oxidation. It was also reviewed by Asghar *et al.* [64] that COD removal of direct dye stuff in wastewater at pH 6.5 was 23.3% after 2 h of ozonation which increased to 65.0% when pH value increased to 12 and time required for decolorizing direct dye stuff reduced to 59.6% when pH increased from 2 to 12. It has been reported that energy consumption for ozonation of Congo red dye increases linearly and to achieve 80% TOC removal, 528 $kWhm^{-3}$ power was consumed which was 254 $kWhm^{-3}$ for EAOPs.

Waktole *et al*. [138] carried out treatment of anthraquinone dye textile wastewater using anaerobic dynamic membrane bioreactor and O_3 generator with mass flow rate 120 mg $O_3\ h^{-1}$ (0.33 g O_3 was required to completely oxidize 0.25 g dye Remazol Brilliant Blue R (RBBR) under neutral pH of the reactor (7.0-7.2). Accordingly, the amount of O_3 required to partially oxidize 0.25 g L^{-1} RBBR will be 0.17 g. They notice that stable COD removal efficiency of >

93.0%, and color removal of > 96.7% were achieved and the total suspended solid rejection by the dynamic layer was > 98.8% and observed that Proteobacteria, Aminicenantes, Spirochaetae, Bacteroidetes, Firmicutes, Thermotogae, Chloroflexi, and Euryarchaeota were top phyla in microbial community. Su *et al*. [139] developed a simultaneous combination of ozonation and biodegradation for enhancing tetracycline decomposition and toxicity elimination. Authors tried to shift from the traditional way of sequential combination of ozonation and biodegradation, the process took place simultaneously in a single bioreactor.

Although ozonation was an environmentally sound process, their result showed that the optimum ozonation and O_3 oxidation efficiency was restricted only to alkaline condition (pH ~8.1−11). Despite no sludge formation, non-hazardios and ease of operation, ozonation is restricted to complete decolorization rather than mineralization. The process was an appropriate technology for textile wastewater treatment under alkaline pH. But intensive energy requirement for O_3 generation, pH sensitivity, mass transfer limitations and high rate of O_3 consumption were challenging for industrial applications. Consequently, ozonation process needs a further investigation to combine with other technologies that can minimize the aformentioned challenges which could be applicable for all industrial wastewater treatment processes. Ozonation process for azo dye complete oxidation was inefficient due to its high molecular weight and complex structure [120].

Generally, from textile wastewater treatment literatures, the value of mineralization rate constant was lower than the decolorization rate constant because azo dye mineralization was more difficult to degrade due to its high molecular weight and complex structure. Poor treatment performance of the Fenton oxidation processes was observed when the initial pH was above 4, and the pH increased quickly and reached above 11 at 28 h and brought several impacts to the system. The generated H_2O_2 could decompose into O_2 and H_2O when pH exceed 5, higher pH caused the formation of $Fe(OH)_3$ precipitate by Fe^{3+} species, which may reduce the Fe^{3+}/Fe^{2+} recycling process.

2.5. Summary of Literature Review

An extremely complex matrix can be used to describe textile wastewater, according to the literature review that was conducted. In addition to color, other indicators of contamination could include salinity, alkalinity, a low BOD/COD ratio, and the presence of hazardous chemicals. Additionally, the parameters of the wastewater vary greatly among the reviews

examined. Different AOPs based textile wastewater treatment systems were reviewed such as Fenton based, photocatalytic, EAOPs and ozone based AOPs. The Fenton process and ozone based AOPs were shown to be the most effective in terms of cost. They are also simple to use and practicable. It is recommended that the Fenton process for wastewater with an acidic pH, such as effluents from the processing of wool or the dyeing of polyester, taking into mind the fundamental drawback of the Fenton process, namely the requirement to maintain pH 3. For wastewater from dye-houses that use mostly reactive dyes, ozone-based procedures might be the most cost-effective option. The extremely alkaline reactive dye effluents contain inorganic species that function as radical scavengers and negatively affect the Fenton process more so than the ozonation process. Numerous studies have been conducted on the treatment of textile wastewater using light irradiation, but it is important to keep in mind that the textile wastewater's strong color and turbidity make it nearly hard for light to penetrate to the medium's deeper layers. The majority of the photo-AOPs were thereby distinguished from the other AOPs by having much higher operational costs. The solar photo-AOPs are inexpensive to operate, but they require a sizable surface area and consistent solar light irradiance. The use of an electron beam radiation was also carried out at full-scale, however it was utilized as a stand-alone treatment to improve biodegradability while removing very little pollution.

It is considered that biological processes are substantially more affordable than chemical oxidation. The complex microorganism consortium biodegradation process was scaled up and applied in industrial settings, primarily as activated sludge or, much less frequently, as a biofilm. Even though certain papers are devoted to the research of monoculture bacterial or fungal textile wastewater therapy, they have little practical value despite offering valuable information for scholarly objectives. The low operating costs that biological processes provide are one of its key advantages; yet, running a biological process in sterile conditions necessitates more energy and specialized equipment, which results in greater investment and operating expenses.

The review has demonstrated potential advantages that both AOPs and biological approaches have in the treatment of textile wastewater, especially when the procedures are combined. Overall, combination treatment was more efficient than individual methods. In the case of the Fenton and ozone-based procedures, the application of AOPs to the biotreated textile wastewater led to lower operational costs. The pretreatment or posttreatment of AOPs is unquestionably more appropriate for textile wastewater treatment. Particularly in the order of AOPs before applying bioprocesses, the systems presented were not entirely optimized. It is

recommended that biodegradation should be used as a pretreatment considering the textile effluents' existence of both biodegradable and bio-recalcitrant organic components. Before creating any system, preliminary experiments including textile wastewater biodegradability and/or toxicity should be conducted locally.

It is also possible to think about using the electrochemical oxidation found in AOPs for industrial purposes. The operational expenses of electrochemical oxidation (EO) are significant for wastewater that lacks sufficient electrolytes, though. For EO to be effective, ohmic resistance must be kept low in the reaction mixture, which calls for a high salt content. It might be advised for segregated dye-bath effluents that have a high salt level. Promising techniques for the treatment of persistent organic pollutants from textile wastewater sources include bio-Fenton (BF) and bio-electro-Fenton (BEF). They have been shown to be effective in several pollutant degradation processes, as well as in lowering costs and enhancing workplace safety. The biomaterials are employed in the BF process to manufacture H_2O_2 in-situ, which lowers the risk of stocking and transporting.

The main benefit for the BEF, however, is the generation of electricity from microbial activity, which offers a suitable solution for the significant power consumption in electro-Fenton-based systems without sacrificing the effectiveness of organic pollutant degradation. To drive Fenton's reaction in the cathodic compartments, these systems' low power density generated in the anodic compartments presents their biggest hurdle. Additionally, there are also concerns about the longevity and stability of these systems. The system's efficiency should be improved, more sustainable cathode materials should be produced, and new techniques for producing bio-anodes should be developed to increase the power density produced by the microbial population, so more research should be done to be able to use these methods on industrial scales.

CHAPTER 3

3. MAGNETIC NANOPARTICLES AND FLUIDIZED ELECTRODES

3.1. INTRODUCTION

Over a few decades, synthesis of nano-sized catalysts has been one of the hottest research areas in academia and industry. One of the most studied nanoparticles for water treatment applications is Fe_3O_4 nano-spheres (INPs) as catalysts, due to its high surface area to volume ratio, and good biocompatibility [140,141]. It can be easily recyclable with its magnetism in the outer layer [142] and its catalytic character facilitates it to react with multiple recalcitrant organic compounds which makes it a promising heterogeneous catalyst for water and wastewater treatment applications [143,144]. In fact, it has been applied to the surface of an electrode as an active catalyst (e.g., Fenton reagent) [143]; the electrode is integrated into an electro-chemical advanced oxidation processes [93,144].

Apart from Fenton process, electro Fenton (EF) has a capacity of a continuous hydrogen peroxide (H_2O_2) regeneration at the cathode surface [90,93], i.e., reducing sludge formation [94,144]. Subsequently, the H_2O_2 could be oxidized to hydroxyl radicals (·OH) [92] and the ·OH radicals in turn could react with recalcitrant organic compounds. Though EF favors in acidic conditions (at pH value of 2-4), the working pH range become wider in nano-sized heterogeneous catalysts [78]. Due to their unique properties, such as high saturation magnetization, biocompatibility, and stability, INPs are applied for biomedical applications (i.e., electrochemical sensors, cancer treatment, or medical imaging), catalysis (i.e., in wastewater application), supercapacitors (energy storage). The electrochemical behavior is thus the first step toward the assessment of the potential effectiveness of the material. Different types of nano-sized catalysts synthesizing methods, e.g., thermo-chemical [145], ultrasonic-chemical [145,146], wet-chemical [147,148], hydrothermal co-precipitation [147], etc. have been employed by different researchers. Among the methods, the chemical co-precipitation has been widely used due to its simplicity and operation temperature (i.e., 70-95 ^{0}C) [143]. However, it has been known to yield nano-sized catalysts with low magnetism, high

polydispersity, agglomerating property, and various sizes and shapes [149]. Besides synthesis of pure and uniform size nano-sized catalysts is a challenging task in chemical co-precipitation method [150]. Thermodynamically, purity and size of nanoparticles can be easily improved by oxidizing unstable Fe_2O_3 to stable magnetic nanoparticles at the ambient temperature during chemical co-precipitation process [151]. In addition, systematic monitoring of nuclei formation is required to control the size and shape of nano-sized catalysts [152].

Effect of iron salt precursors on size distribution of nano-sized catalysts has been investigated. Bhavani *et al*. [153] synthesized larger magnetic nanoparticles using iron sulfate salts than iron chloride salts. Indicated that the size of the particles could be affected by iron salt precursors. Yazdani and Seddigh [154] determined that the size of the particles could be controlled by ionic strength of anions. During co-precipitation methods, increasing the stirring intensity tends to decrease the size of the particles. Various reducing agents such as NH_4OH [155], KOH [146], NaOH [20,156], urea [156], and $(C_2H_5)_4NOH$ [157] have their own effect on size of the particles. Weaker reducing agents were used to produce smaller size and better magnetization particles. However, size, shape, and purity of nanoparticles varies as the particle-synthesis procedure varies [20,157]. Similarly, order of iron complex formation during co-precipitation method, affect size and shape distribution of the particles. The solution with ferric salt began to produce $Fe(OH)_3$ precipitates in acidic conditions (at pH~2-4). Under the condition, it is hard to precipitate $Fe(OH)_2$ [21]. Nevertheless, $Fe(OH)_2$ precipitates in alkaline condition (at pH~7.5-8) which was not favorable for $Fe(OH)_3$ precipitation. In fact, magnetic nanoparticles were formed as a result of co-precipitation of $Fe(OH)_2$ and $Fe(OH)_3$ at pH 8-11 [158]. In addition to $Fe(OH)_3$ precipitate, ferric ions in solution can also form different iron complexes in acidic conditions (pH 3-5); such as, $[Fe(H_2O)_6]^{3+}$, $[Fe(H_2O)_5]^{2+}$, $[FeC1_2(H_2O)_4]^{+}$ and $[FeC1_4]^{-}$ [159]. At low iron salt concentration, $[Fe(H_2O)_6]^{3+}$ dominated the system. Improper preparation of iron salt solution could lead to the production of more $Fe_6(OH)_{12}CO_3$ and poorly crystalline $Fe_{10}O_{14}(OH)_2$ [149] which could hinder the production of magnetic nanoparticles with uniform size distribution.

Environmental pollution caused by the textile industry has received an increasing amount of attention within the last decade reported that more than 10,000 t of dyes are consumed per year in the textile industry, in which 10-15% are released to the environment as wastewater. Moreover, the dyebath and rinsing processes discharge a large portion of textile wastewater with high temperatures of 50-80 °C. At a rate of 60 -70% consumption, the azo

dyes are known as the most consumed dyes in the textile industry. Acid Orange 7 (AO7, $C_{16}H_{11}N_2NaO_4S$), also named as Orange II, is a widely used azo dye that appears in manufacturing wastewater disposed of from the textile, food, and cosmetic industries [160].

Synthetic dyes are extensively used in many industrial fields, such as dyestuffs, textile, paper, and plastics. It is estimated that there are around 100,000 commercially available dyes with over 7×10^5 tons of dyestuff produced annually. Synthetic dyes exhibit considerable structural diversity, and are classified as azo, anthraquinone, sulfur, indigo, triphenylmethyl, and phthalocyanine derivatives. Most synthetic dyes currently used in the industry are azo dyes and their derivatives. Because they are highly stable during washing, lightfast and not susceptible to degradation under natural conditions [161]. Azo dyes contain one or more azo bonds (-N=N-) as chromophore groups linked to aromatic structures with functional groups such as –OH, and $-SO_3H$.

Most dyes are non-biodegradable, hinder sunlight penetration and inhibit the photosynthesis process and increase the chemical and the biological demand for oxygen. Therefore, water ecosystems are disturbed. In aqueous solution, the negatively charged anionic azo dyes exist over a broad pH range. Anionic mono azo dyes and their metal salts are widely used on dyeing papers and leather, or as pigments [32]. Among mono azo dyes Acid orange 7 (AO7) is also known as 2-naphtanol orange and orange II, is one of the most popular azo dyes used in leather dyeing, paper coloration, cosmetics, and personal care products. AO7 is also well known, inexpensive and dyes rather quickly in weak acidic solution [25]. Because of these properties, it is extensively used for dying a variety of materials such as nylon, aluminum, detergents, cosmetics, wool, and silk. It is highly toxic, and its ingestion can cause eye, skin, mucous membrane, and upper respiratory tract irritations; severe headaches; dizziness; nausea; and loss of bone marrow leading to anemia. Like most other azo dyes in textile industries, AO7 is being discharged in considerable amounts into water streams.

In this paper, the co-precipitation method was modified in solution preparation method for size and shape controlled INPs synthesis. (1) effect of salt precursors, solution activity and solution mixing procedure on size distribution and nuclei-formation of Fe_3O_4 nanoparticles (INPs) were investigated using different iron salt precursor solutions (sulfates and chlorides), (2) small sizes and uniform shapes of INPs were synthesized, (3) the INPs were characterized. fluidized iron

nano particle (INP) electrodes were synthesized and their degradation capacity of INPs were evaluated on AO7 dye in electro Fenton process.

3.2. Materials and Methods

3.1.1. Chemicals and Materials

$FeCl_3.6H_2O$ (99% purity), $FeSO_4 \cdot 7H_2O$ (98%), $FeCl_2.6H_2O$ (99% purity), $Fe_2(SO_4)_3.6H_2O$ (99% purity), were purchased from Sigma-Aldrich (Seoul, Korea). AO7 (Appendix 3.1); analytical grade), Scientific-E160-04 iron electrodes (6 cm × 3 cm) were purchased from Sigma-Aldrich (Seoul, Korea). The solution reagents were prepared with a high-purity water-filtering system (resistivity > 18.2 MΩ cm; Seoul, Korea). HCl and NaOH solutions were used for initial pH adjustment when an experiment was performed. All inorganic and organic chemical reagents used in this study were of analytical grade, purchased from Samchun Pure Chemicals (Seoul, Korea), and used as received, i.e., without further purification.

3.1.2. Synthesis of INPs

Fe_3O_4 nano-particles (INPs) were synthesized by modifying the existing co-precipitation method according to our previous report [162]. In a brief, five different solutions, i.e., containing 1.78 g $FeCl_3 \cdot 6H_2O$, 0.96 g $FeCl_2 \cdot 4H_2O$, 1.73 g $Fe_2(SO4)_3 \cdot 6H_2O$, 1.22 g $FeSO_4 \cdot 7H_2O$, and mixture of 0.89 g of $FeCl_3.6H_2O$ and 0.48 g of $FeCl_2.4H_2O$, were prepared and indexed as C_3, C_2, S_3, S_2 and M (i.e., C, S and M stands for chlorides, sulfate and mixture salts solution), respectively. The pH of the solutions was adjusted with 1-mM HCl and 2-mM NaOH. All the solutions were prepared at room temperature and the solutions were heated to 95 ^{0}C for 30 min in the oven while being stirred at 7500 RPM under N_2 atmosphere.

After the solutions were heated, the C_2 solution was mixed to solution C_3 and labeled as solution C. Similarly, solution S_2 was mixed to solution S_3 and labeled as solution S. At the same time, 0.89 g of $FeCl_3.6H_2O$ and 0.48 g of $FeCl_2.4H_2O$ were mixed in 100-mL and then labeled as solution M. For all solutions, the ratio of ferric and ferrous was approximately maintained at 2 and the mixing rate of the solutions were kept constant (i.e., 23-mL min^{-1}) to form uniform size distribution of INPs. After 30-min heating, aqueous ammonia (25 mL, 28 wt.%) was added to the solution in a drop-wise manner using a dropping funnel over 30-min. Then, the solution with precipitates was allowed to cool down to a room temperature.

Subsequently, the supernatant of the solution was discarded and INPs were harvested using an external magnet. After washing with distilled water and ethanol, it was dried at 50 ^{0}C overnight. Finally, a fluidized INPs electrode was prepared by dispersing 1 g in 250 mL deionized water from each INPs and thoroughly stirred for 2.5 h and sonicated for 1 h at 30 kHz.

3.1.3. Physco-chemical Characterization

The pH of Fe_3O_4 co-precipitation (i.e., nuclei formation) as a function of reducing agent (NH_3 solution) was determined using pH meter (Eutech Instruments Pte, Ltd, 6plus pH meter, Singapore). The stability of fluidized INPs electrode dispersion of each INPs was investigated by zeta potential (Zeta nano-sizer, Malvern Instruments Ltd, Malvern, UK) by dispersing 0.2 wt.% of the synthesized INPs in 5-mL of 10 mM KCl solution and ultrasonicating at temperature of 25 ^{0}C [163]. The morphology of the synthesized INPs was analyzed through a field emission scanning electron microscope (FE-SEM, SU8010, Hitachi, Japan) at an operating voltage of 10 KV. The Raman scattering spectra were recorded on a Raman microscope (Horiba, Kyoto, Japan) at an excitation wavelength of 785 nm and 2-W laser energy with a step of 0.02 and acquisition time of 1.0 s step^{-1}. The crystallinity and size of crystallites of the synthesized INPs were characterized using X-ray diffraction spectroscopy (XRD) patterns. The structural information was employed for diffraction pattern comparison to the pattern of standardized plane angles of the substance. To confirm the crystallinity, the obtained results were compared to the Joint Committee on Powder Diffraction Standards of Fe_3O_4. For XRD analysis, an X-ray diffractometer (Rigaku, Tokyo, Japan) was used with Cu Kα (λ = 0.1541 nm) radiation over the 2θ interval of 4-84 with a step of 0.01 at 40 kV and 30 mA. The average size of the synthesized INPs was estimated from the full width at half-maximum of the main XRD peak, using the Scherrer's equation (Eqn. 3.1) and the distance between atomic layers of the crystals was calculated using Bragg's law (Eqn. 3.2) [164]. Interplanar spacing of INP-cubic crystals was calculated using Miller Indices and lattice parameters (Eqn. 3.3).

$$D = \frac{0.9\lambda}{\beta \cos\theta} \quad (3.1)$$

$$d_{hkl} = \frac{n\lambda}{2 \sin\theta_{hkl}} \quad (3.2)$$

$$a = d_{hkl} \times (h^2 + l^2 + k^2)^{1/2} \quad (3.3)$$

where D is the average particle size (nm), λ is the wavelength of Cu Kα radiation, β is the FWHM (radian), θ is the peak position (radians), n is a number (integer), d_{hkl} is the spacing between planes (Å), θ_{hkl} is the angle of the incident X-ray beam (degree) and (hkl) are Miller's indices.

3.1.4. Magnetic Property and Photo-electrochemical Characterization

The ferromagnetic properties of the synthesized INPs were determined using Vibrating-Sample Magnetometer (VSM, LDJ Electronics Inc. Westerville-Ohio, USA) at 25 ^{0}C in the range of sweeping -8000k to 8000 Oe. Hysteresis is the process of gaining of magnetization when the applied field removed [165]. UV-vis reflectance spectra mode (DRS; UV-2600, Shimadzu, Kyoto, Japan) was used to investigate the optical energy gap (E_g^{opt}), i.e., the intrinsic band gap absorption of the synthesized INPs within 300-700 nm [166]. The mobility of electrons from valence band to conduction band can be determined using the Davis and Mott's equation for direct and indirect transition energy gaps (E_g). To determine the UV-Vis's spectrum of each INPs, 0.005 mg of each INPs (C, S, and M) was used for reflectance spectra analysis. Tauc's plot [hν vs $(\alpha h\nu)^n$] was used to estimate the E_g from the optical absorption spectra using Eqn. 3.4 [167].

$$(\alpha h\nu)^n = k(h\nu - E_g) \quad (3.4)$$

where h (Planck constant), ν (photon's frequency), E_g (bandgap energy), k (constant), and α (absorption coefficient), which describes how much light is absorbed by the material of given thickness, n is a factor which depends on the nature of the electron transition and is numerically equal to 2 or 1/2 for direct or indirect transitions, respectively and α(λ) as a function of lambda was calculated from absorption (A) spectrum following Eqn.3. 5, where t is a film thickness [168].

$$a(\lambda) = \frac{2.303 \times A}{t} \quad (3.5)$$

The electrochemical activity of each fluidized INPs electrode was characterized by cyclic voltammetry (CV, CHI660E, Chenhua, China) at 25 mV s^{-1} scanning rate. 10 μL of the fluidized INPs electrode solution was dispersed directly into the electrolyte solution (containing 50 mg L^{-1} Na_2SO_4) and the solution pH was adjusted to 3. A conventional three-electrode system where a platinum mesh was used as the counter electrode, Ag/AgCl as the reference electrode and glassy carbon (3 mm diameter) as the working electrode. Linear sweep

voltammetry (LSV) was performed under the same scan rate from -1.5 to 0 V (vs. Ag/AgCl). The average number of electrons transferred (n) for molecular oxygen reduction reaction were determined from the slope of Levich equation [169] (Eqn. 3.6) at different rotating speed of the electrode. The two-electron oxygen reduction reaction was measured based on H_2O_2 generated at different cell potentials (-1.5 to 0 V) according to Eqn. 3.7.

$$i = 0.62nAFD^{2/3}\nu^{-1/6}C_{i,\delta}\omega^{1/2} \quad (3.6)$$

$$H_2O_2\ generation\ (\%) = \frac{2 \times i_R}{Ni_D + i_R} \times 100 \quad (3.7)$$

where i is limiting current (A), n is number of electrons transferred, F is the Faraday constant (C mol^{-1}), D is the diffusion coefficient of oxygen ($m^2\ s^{-1}$), A is the electrode area (cm^2), ν is the kinematic viscosity of water ($m^2\ s^{-1}$), C is the concentration of oxygen at the electrode surface (mol cm^{-3}), ω is the rotation speed (RPM) of the electrode, *N* is the collection efficiency (27%), and i_R and i_D are the values of the ring and disk current densities at different cell potentials (-1.5 to 0 V).

3.1.5. Determination of Catalytic Activity of Fluidized INPs Electrodes

The catalytic activities of each fluidized INPs electrode (C, S, and M; with 0.3 g L^{-1} dose) were evaluated in 500-mL beaker with a working volume of 250-mL containing 5 mg L^{-1} of AO7 as model contaminant. Both the anode and cathode electrodes were made from iron electrode strips (6 cm × 3 cm) with an effective wettable area of 13.5 cm^2, and connected to DC source (TDP-3010B, TOYOTECH, Seoul, Korea) 2 cm apart. The electrodes were washed several times using ethanol to remove organic and inorganic contaminants. The EF oxidation was performed at 5 mg L^{-1} initial concentration of AO7, pH 3, applied electro-potential of 3 V and 2.5-mL of H_2O_2 as reaction initiator. From each experiment, aliquots of 2.5-mL were taken for analysis and the effect of contact time, reusability of the fluidized INPs electrode was evaluated. The AO7 removal efficiency was monitored by UV-Vis spectroscopy (Shimadzu 1800 UV, Kyoto, Japan) absorbance at 485 nm using Eqn. 3.8 [104]. Chemical quenching method was conducted to determine the oxygen reactive species that involved in degrading of AO7 [170].

$$AO\ 7\ Removal\ Efficiency\ (\%) = \frac{C_0 - C_t}{C_0} \times 100 \quad (3.8)$$

where C_0 and C_t are the concentration of AO7 measured at time 0 and time t, respectively.

At the end of EF reaction, the fluidized INPs electrodes were separated by an external magnet and tested several times for reusability. The remaining solution was checked for residual iron ions using inductively coupled plasma optical emission spectrometry (ICPE-900, Shimadzu, Tokyo, Japan). Finally, liquid chromatography-mass spectrometry (LC-MS, Shimazu, Kyoto, Japan) and ion-exchange chromatography (ICS-90, Thermo Fisher Scientific, Borken, Germany) were used to determine the oxidation intermediate products and inorganic ions (i.e., NO_3^- and SO_4^{2-}) respectively.

3.3. Results and Discussions

3.3.1. Effect of pH on Particle Co-precipitation and Suspension Stability

Following the solution preparation procedures, a series of different iron-water complexes were proposed. When the ferric chloride salt dissolved in distilled water, a cyber yellow color was observed due to unstable octahedral iron complex ($[Fe(H_2O)_6]^{3+}$) which subsequently changed to a stable, insoluble, and neutral bright-yellow color upon the addition of HCl through a series of iron ion complex formation (Eqn. 3.9-3.11) [171]. The iron complex was acting as a strong acid by donating hydrogen ion (deprotonation) to water molecules. Since hydrogen atoms attached to water ligands are positively charged, they could be pulled out in a reaction involving water molecules (C_3, Fig. 3.1a). However, the solution of ferric sulfate was an orange yellow color (S_3, Fig. 3.1a), which subsequently changed to bright yellow upon addition of HCl through continuous stirring.

On the other hand, ferrous chloride solution (C_2, Fig. 3.1a) gave a golden yellow color whereas ferrous sulfate (S_3, Fig. 3.1a) gave white color. After adding NaOH solution to both solutions, their color was changed immediately to deep green color precipitate. In this case, the precipitates were also unstable iron water complexes either in the form of $[Fe(H_2O)_5]^{2+}$ or $[Fe(H_2O)_6]^{3+}$ which could be easily converted to more stable form of iron oxide, (i.e., ferrous hydroxide) by losing a single hydrogen ion (Eqn. 3.13 and 3.14) [172]. In contrast, when C_2 and C_3 as well as S_2 and S_3 were mixed, a brown-orange color was observed (C and S, Fig. 3.1b). Eventually, a black precipitate was formed on addition of reducing agent (i.e., concentrated ammonia solution) (Eqn. 3.15 and M, C, and S, Fig. 3.1b). Further information regarding the color formation was presented in Fig. 3.1a & b. The overall iron ion-water ligand formation was described for both C and S solutions during the modified co-precipitation process at equilibrium. The highly soluble iron ion $[Fe(H_2O)_6]^{3+}$ complex started to precipitate

at pH 3 which then reacted with the existing Fe^{2+} ions in the solution to form INPs. Iron complex formation was the key factor for size distribution of magnetite particles [171,172]. Effect of reducing reagent on co-precipitation and pH variation of solution C, S and M were described in Fig. 3.1c.

$$Fe^{3+} + 6H_2O \leftrightarrow [Fe(H_2O)_5(OH)]^{2+}(aq) + H_3O^+ \quad (3.9)$$

$$[Fe(H_2O)_5(OH)]^{2+}(aq) + H_3O^+ \leftrightarrow [Fe(H_2O)_3(OH)_3]^+(aq) + H_3O^+ \quad (3.10)$$

$$[Fe(H_2O)_3(OH)_3]^+(aq) + H_3O^+ \rightarrow Fe(OH)_3(s) + 3H_2O + 3H^+ \quad (3.11)$$

$$Fe(OH)_3(s) \rightarrow FeOOH(s) + H_2O \quad (3.12)$$

$$Fe^{2+} + 6H_2O \leftrightarrow [Fe(H_2O)_6]^{2+}(aq) \quad (3.13)$$

$$Fe^{2+} + 2OH^- \rightarrow Fe(OH)_2(s) \quad (3.14)$$

$$2FeOOH + Fe(OH)_2 \rightarrow Fe_3O_4 + 2H_2O \quad (3.15)$$

The surface charge of each fluidized INPs electrode was measured using zeta potential as function of pH. As presented in the Fig. 3.1d, the zeta potential of each fluidized INPs electrode as not significant among each fluidized INPs electrodes (C, S and M). Thus, similar conditions could be applied for each fluidized INPs electrode dispersion stability behavior. In nanofluidic theory, zeta potential could be considered stable if the magnitude of zeta potential is higher than 30 mV [163,173]. Furthermore, the higher the magnitude of zeta potential, the higher the stability of the fluidized INPs electrode suspension. This stability resulted from the higher electrostatic repulsion forces between particle suspension, i.e., that could avoid subsequent particle aggregation and sedimentation due to gravitational force. The approximate magnitude of zeta potential values of each fluidized INPs electrodes (C, S, and M) at pH = 7, were 44.1, 41.9 and 36.5 mV respectively. The values indicated that the synthesized particles were in moderate suspension stability. Nano particles with smaller size could have higher zeta potential, i.e., more stable [163].

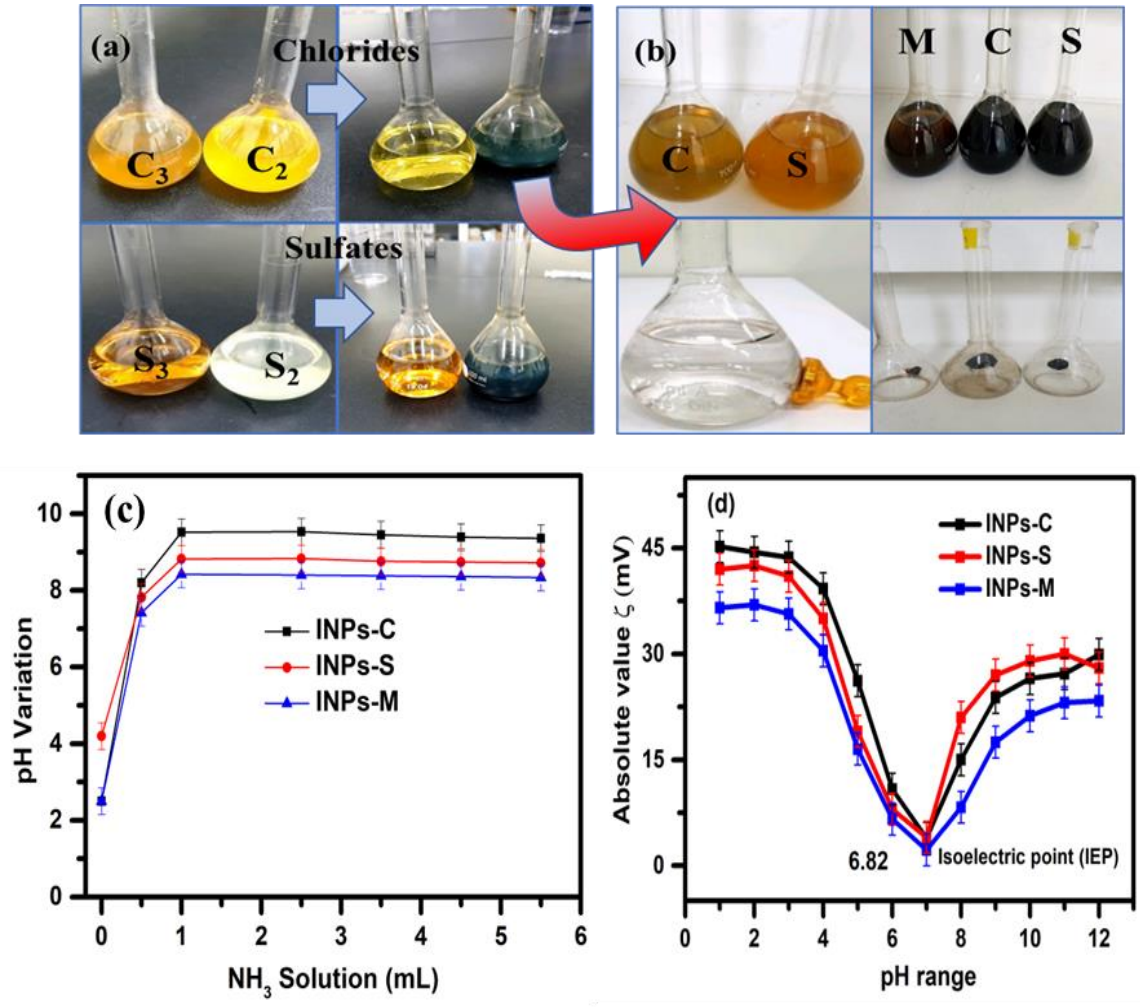

Figure 3.1: *Solution preparation, effect of pH on co-precipitation and suspension stability*

Solution preparation (a); Co-precipitation of INPs (b); pH effect on co-precipitation of INPs (c); and pH effect on of INPs suspension (zeta potential) (d)

3.3.2. Phyco-chemical Characterization of Fluidized INPs Electrode

The FE-SEM analysis was performed to distinguish the morphological structure of the synthesized INPs (C, S and M), and presented in the Fig. 3.2. The average diameter of the INPs were calculated using image j-software (particle image analyzer, FIJI IS JUST) and summarized in Table 3.1. From the FE-SEM images and size distribution histogram analysis, the spherical particle agglomerates were observed due to the surface energy of the particles.

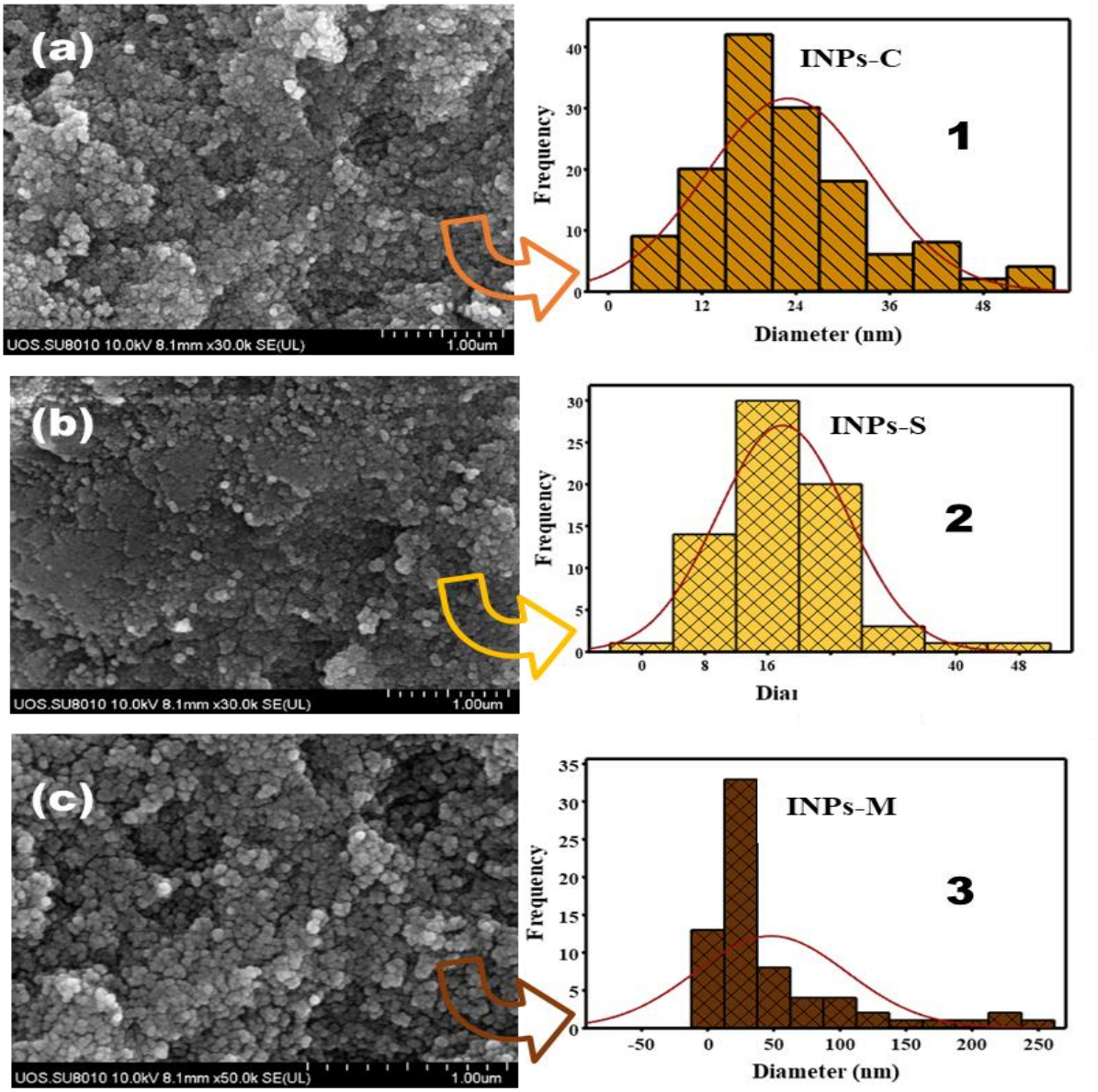

Figure 3.2: *Images of INPs by FE-SEM and their size distributions*

INPs-C (a, 1), INPs-S (a, 2); and INPs-M (a, 3) respectively

Table 3.1: Mean diameter of INPs (C, *S*, and M) using SEM and j-imaging software

INPs	***Total particle count***	***Mean of diameter (nm)***	***SE Mean diameter (nm)***	***StDev (nm)***	***Min. particle (nm)***	***Max. particle (nm)***
C	*569*	*23.02*	*0.895*	*10.6*	*3.1*	*53.4*
S	*575*	*17.93*	*0.988*	*8.3*	*2.9*	*45.2*
M	*570*	*47.94*	*6.850*	*57.4*	*6.2*	*245.7*

Due to high surface energy, more particle agglomerates were observed in INPs-S (Fig. 3.2b,2), comparing to INPs-C (Fig. 3.2a,1) and INPs-M (Fig. 3.2c,3). Since the particles (i.e., INPs-S) possess high surface energy, they tend to aggregate to minimize the surface energy [174]. However, a clear surface boundary was observed between INPs-M particles. The surface morphology of INPs-M consists of larger and irregular agglomerates than the other INPs. Employing suitable synthesis methods contributes to smaller particle size and uniform morphology. The shape of each INPs showed spherical which were in accordance to Ruíz-Baltazar [175].

The structural fingerprint of the synthesized INPs was characterized by Raman Spectroscopic analysis at excitation wavelength of 785 nm and 2 W laser energy to distinguish a multi-phase oxides existing on INPs [176]. The main phases present in the synthesized INPs were identified and presented in Fig. 3.3a. Since Fe_3O_4 possesses five spinel symmetry of A_{1g}, E_g and $3T_{2g}$ and Fe_2O_3 possesses three spinel symmetry of A_{1g}, E_g and T_{2g}, i.e., the most expected Raman active vibrational modes [173,177,178]. Attending to the Raman spectra results for the INPs, five main bands appearing at 219, 400, 487, 601 and 667 cm^{-1}, corresponding to the T_{2g} (1), E_g, T_{2g} (2), T_{2g} (3), and A_{1g} modes of Fe_3O_4, respectively [163,179]. Although both INPs-C (Fig. 3a, black) and INPs-S (Fig. 3.3a, red) followed the same Raman spectra pattern, the vibrational modes of INPs-C were higher than that of INPs-S. This could be due to the size difference, in which smaller particle size would have a stable Raman spectrum. The presence of two narrow intense peaks at around 284 and 875 that correspond to the E_g and A_{1g} phase vibrational mode of Fe_2O_3 receptively. Due to similar structure and facile formation of both phases during co-precipitation process, the band pattern suggested both vibrational phases of Fe_2O_3 and Fe_3O_4 were observed in INPs-M (Fig. 3.3a, blue) [151,179]. Thus, the Raman spectra confirmed the presence of both oxides on INPs-M, considering the very intense A_{1g} band of Fe_3O_4 and the two main bands of Fe_2O_3 were presented, though likely with a different ratio of iron oxide phases. However, modified co-precipitation process offered a great route for synthesis of a single phase Fe_3O_4.

The microstructure of the prepared nano-sized particles was determined using XRD technique and reported in Fig. 3.3b. Several distinct diffraction peaks were clearly observed at 19.2°, 31.3°, 34.9.6°, 43.4°, 57.2°, and 62.7°, and 74.2° which correspond to (111), (220), (311), (400), (511), (440), and (622) lattice planes respectively. The lattice planes correspond to

JCPDF#41-1487, indicating the successful synthesis of Fe_3O_4 particles [180]. However, the highest intensity of the peak was observed at 35.6° which attributed to (311) lattice plane [181].

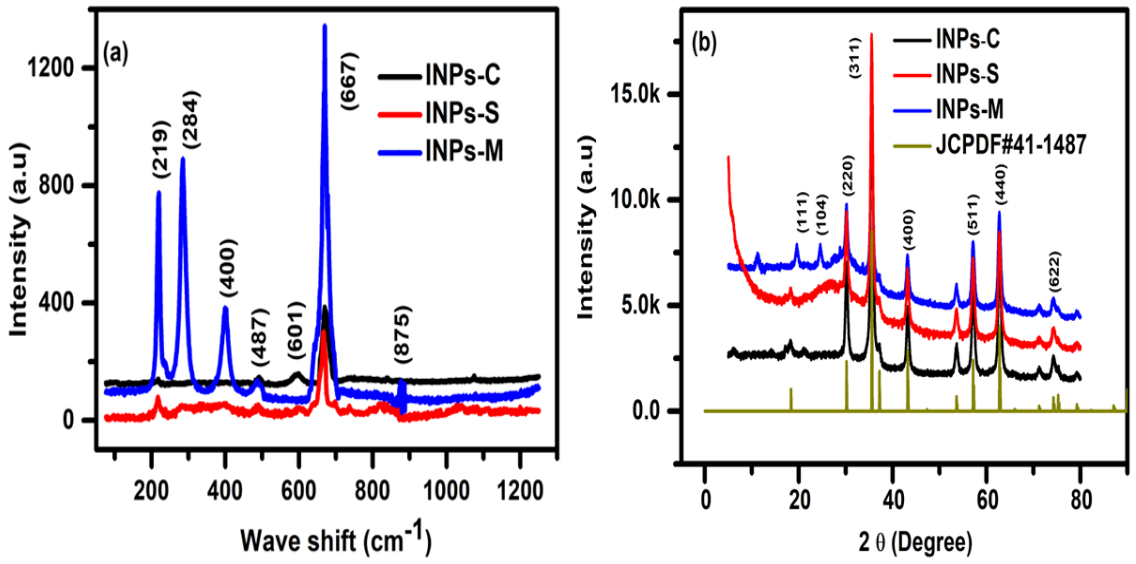

Figure 3.3: *Raman spectral vibrations and XRD diffraction patterns of INPs (C, S and M)*

Ramn vibration of INPs (C, S and M) (a); XRD diffraction patterns of INPs (C, S and M) (b)

The high peak intensity-to-peak width ratio suggested the high crystallinity of the INS clusters. The pattern phases and the peak positions of Fe_2O_3 and Fe_3O_4 are almost the same making them trouble to distinguish their crystallographic structures. However, color difference during co-precipitation process and the XRD pattern deviation of Fe_2O_3 from Fe_3O_4, could make them easily distinguishable [182]. The XRD pattern of INPs-C (Fig. 3b, black) and INPs-S (Fig. 3.3b, red) remained exactly the same to the JCPDF standard pattern (Fig. 3.3b, yellow-green), confirmed that INPs-C and S were supposed to be pure Fe_3O_4 with crystal face of cubic spinel structure [183]. Comparing the XRD pattern of the synthesized particles, INPs-M (Fig. 3.3b, blue) composed of an extra peak around 32.4^0, corresponding to (104) Miller indices which were the characteristic of Fe_2O_3 that indicated the presence of some Fe_2O_3 phases, INPs-M. Coexistence of both Fe_2O_3 and Fe_3O_4 phases could be happen in classical co-precipitation process.

The crystallite size and the lattice parameter of the synthesized INPs were calculated using the Debye-Scherrer's equation and Bragg's law and summarized in the Table 3.2 which were in accordance with the standard (JCPDF#41-1487; parameter) [184,185]. Comparing the sizes of INPs-C and S, Fe_3O_4 synthesized from solution S were smaller due to the solution activity effect

and surface energy of the particles. The iron salt precursor with higher anionic strength, could produce smaller sizes of Fe_3O_4. Here, since the ionic strength of SO_4^{2-} was higher than Cl^-, INPs-S were smaller in size with uniform size distribution. The average crystallite sizes calculated from the XRD, and the average diameter resulted from image j-FE-SEM image analysis were obviously different. It was clear that XRD analysis showed the crystallite size not the particle size [186,187]. The difference was come from the agglomeration and magnetization aggregation of the particles during FE-SEM analysis [174,188].

Table 3.2: Sizes and characteristics of INPs (C, *S,* and M)

INPs	***Lattice constant α (Å)***	***Diameter (nm) SEM***	***Crystal size (nm) XRD***	***d_{hkl} spacing (Å)***	***E_{g1}^{opt} (eV)***	***E_{g2}^{opt} (eV)***	***Magnetization (emu g^{-1})***
C	*80.73*	*41.62*	*10.98*	*24.43*	*2.04*	*2.08*	76 ± 2.4
S	*76.27*	*40.59*	*10.71*	*22.82*	*2.12*	*2.17*	79 ± 2.6
M	*87.58*	*33.31*	*8.79*	*26.71*	*2.14*	*2.18*	66 ± 2.8

3.3.3. Magnetization and Electrochemical characterization Fluidized INPs

The magnetic properties of all INPs were examined using VSM and depicted in Fig. 4a. Although the synthesized INPs (C, S and M) exhibited ferromagnetic characteristics with low intrinsic coercivity [183,189], they behaved differently in a maximum magnetization (Ms, saturation magnetization) values. Each INPs (C, S and M) showed the classical sigmoidal shapes of a typical super ferromagnetic behavior of Fe_3O_4 particles with a narrow hysteresis curve and a small coercive field. Using the law of approach, the absolute value magnetization saturation (M_S) of INPs-C (Fig. 3.4a, black), INPs-S (Fig. 3.4a, red) and INPs-M (Fig. 3.4a, blue) were 76 ± 2.4, 79 ± 2.6 and 66 ± 2.8 emu g^{-1}, respectively.

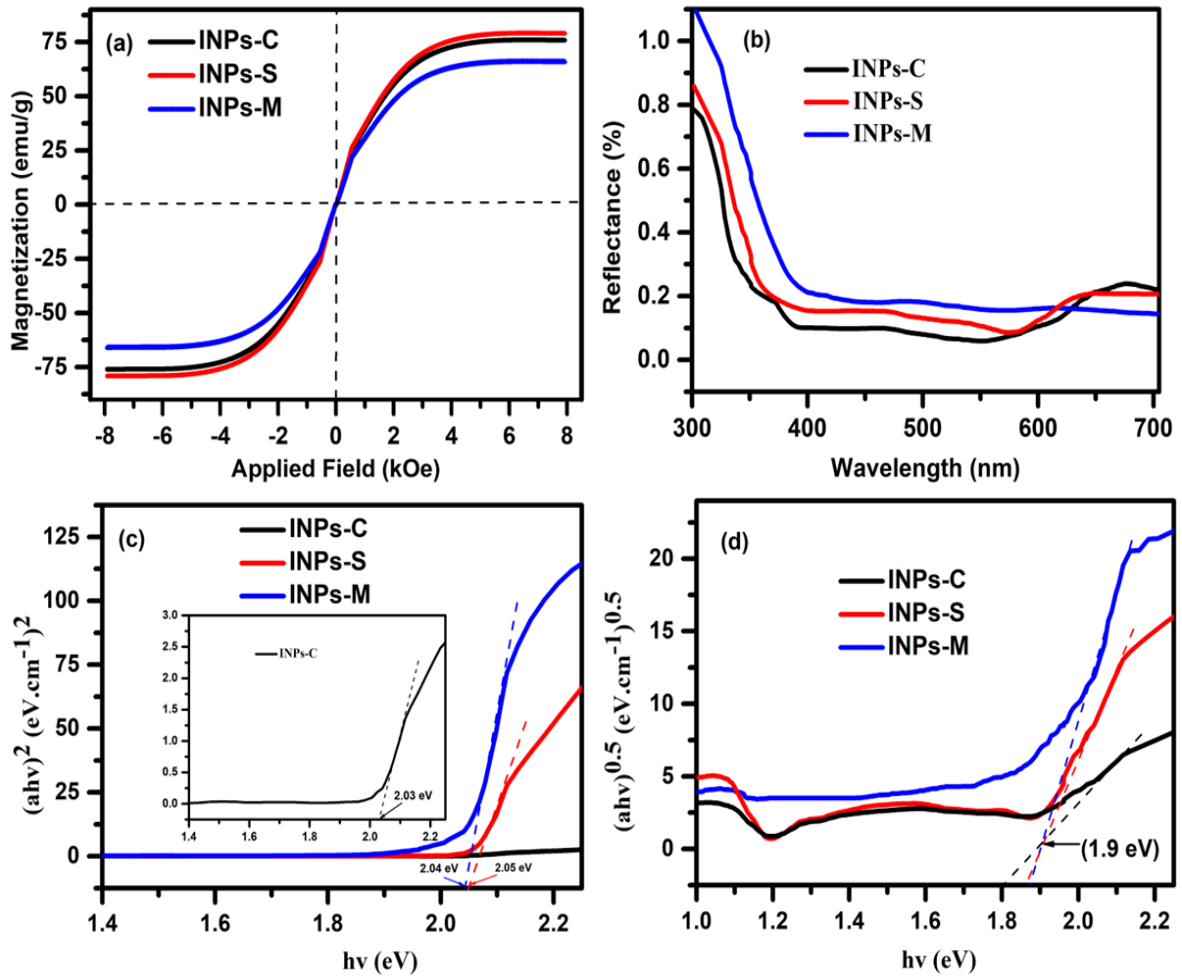

Figure 3.4: *Magnetization and optical characterization*

Magnetization curves of INPs (a); optical characterization of INPs (b); Tauc's plot for direct energy gap of INPs (c); and Tauc's plot for indirect energy gap of INPs (d)

INPs synthesized from iron chloride (INPs-C) possessed less M_s Values than that of iron sulfates (INPs-S), indicating that M_S values were also dependent on phase composition, crystallinity, and particle size [190]. The M_s Values of each INPs confirmed to ease of separation from aqueous media using an external magnet [191]. Although magnetic nanoparticles were not UV-vis active for optical characterization, it was performed to explore the optical properties in its crystalline form and to investigate the correlation between the band gap energy and catalytic behavior of the synthesized INPs [192]. Thus, UV-visible absorption spectra were observed in the visible range which gradually decreased up to around 600 nm (Fig. 3.4b). According to Hong *et al*. and Zhu *et al*. [24,193], magnetic nanoparticles containing iron oxides such as α-Fe_2O_3 or γ-Fe_2O_3 and Fe_2O_3, exhibited higher absorption spectra than pure

Fe_3O_4. The high peak absorbance in INPs-M was associated to dual coexistence of different phases of iron oxides. Moreover, the optical properties of magnetic nanoparticles were affected by the size, quantity, and particle interaction.

As the size of the particles get smaller, the overlapping of orbitals become weaker and give a higher energy gap between valence and conduction bands. Thus, the movement of electrons was restricted resulted in a shift of absorption spectrum toward lower wavelength. Smaller particles absorb higher energy than larger particles, i.e., INPs-S. Hence the absorption peak for smaller particles was observed at lower wavelengths [146,193]. Following the Tauc's Plot for direct energy gap (Fig. 3.4c) and indirect energy gap (Fig. 3.4d), the E_g^{opt} values of each INPs (C, S and M) were estimated. These values could be occur on the same position as reported by Bahadur *et al*. [194]. The values of direct (E_{g1}^{opt}) and indirect (E_{g2}^{opt}) optical energy band gap was in the range of 2.04-2.14 eV and 2.08-2.18 eV, respectively. However, higher values of E_{g2}^{opt} were observed as shown in the Table 3.2 above and similar results were reported by Kouotou *et al.* and Carmona-Carmona *et al.* [192,195].

The electrochemical properties of fluidized INPs electrodes were tested to determine the electrochemical performance in a three-rotating disk electrode system over O_2-saturated solution at 750 RPM rotating speed. Rather than being in continuous contact with the current collector, INPs aggregates were dispersed and stirred the solution to collide on the working electrode and contribute electrochemical reactions. The CV was recorded in fluidized INPs electrode mode, and the potential sweep was run from -1.5 V to 0 vs Ag/AgCl. As described in the Fig. 3.5a, the electrochemical property of each fluidized INPs electrodes exhibited various peak current densities in both oxidation and reduction potential states [196]. Higher oxidation reduction potential was observed by INPs-S due to the intrinsic characteristics of the fluidized aggregates of the particles (Fig. 3.5a, red). Higher reduction potential of 5.70 ± 0.14-mA cm^{-2} at -1.3 V and oxidation potential of 6.67 ± 0.15-mA cm^{-2} at -0.85 V were recorded. However, INPs-M exhibited less oxidation potential (3.63 ± 0.12-mA cm^{-2}) and reduction potential (-2.81 ± 0.1-mA cm^{-2}) at the potential scan of -0.72 V and -1.14 V, respectively (Fig. 3.5a, blue). The result indicates the dependence of electrochemical potential on the size of the fluidized electrodes. Further, linear sweep voltammetry was conducted as described in Fig. 5b, over the same potential scan, and the INPs-S showed the highest negative current density (-7.56 ± 0.2-mA cm^{-2}) at -1.2 V. The high oxygen reduction reaction observed by INPs-S in O_2-saturated solution was attributed to its high surface area to volume ratio which could enhance

the organic contaminant degradation. The rotation speed of the disc electrode enhanced the collision rate of the fluidized electrodes with the working electrode and contributed to high oxygen conversion. Consequently, the convective and diffusive limiting current densities were affected by rotational speed of the electrode and determined using Levich plot [169,197].

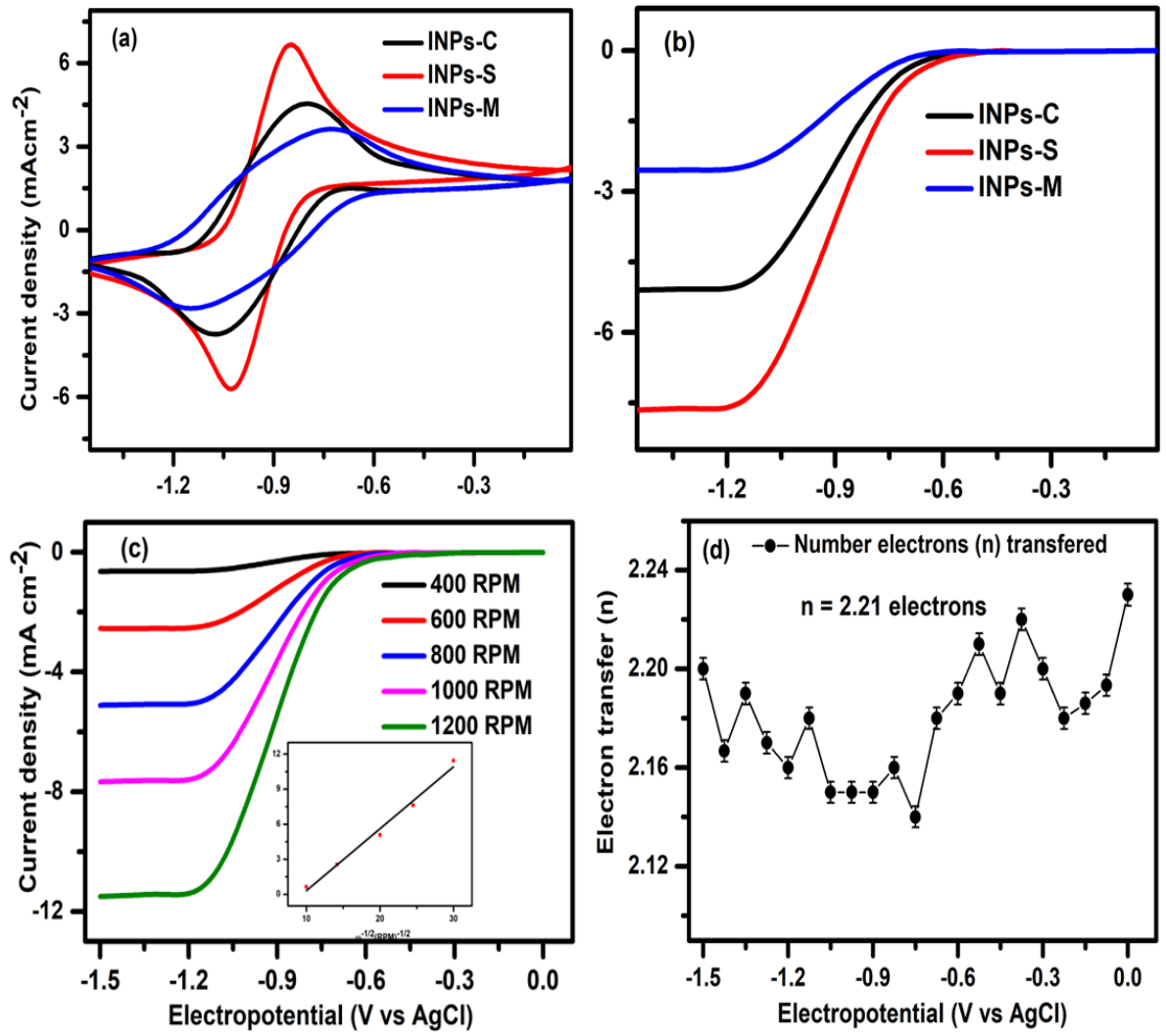

Figure 3.5: *Electrochemical characterization of INPs*

Cyclic voltammetry (CV) of INPs (a); Linear sweep voltammetry (LSV) of INPs (b); Effect of rotating speed of the fluidized electrodes of INPs (c); estimation of electron transfer using INPs-S (d); at scan rate of 25 mV s^{-1}*, potential scan of -1.5 V to 0 vs Ag/AgCl, pH 3 and electrolyte (*Na_2SO_4*, 50 mg* L^{-1}*)*

The sigmoidal curve in Fig. 5c explained the dependence of limiting current on rotational speed. The limiting current density is directly related to rotational speed of the disk electrode. The Levich plot (Fig. 3.5c, insert) described the kinetic contribution of the fluidized INPs electrode

on oxygen reduction reaction. Therefore, using the faraday's constant (F, 96,485.3 C mol^{-1}), diffusion coefficient of oxygen (D, 2.38×10^{-5} m^2 s^{-1}), electrode area (A, 1.1 cm × 0.98 cm), kinematic viscosity of water (ν, 5×10^{-3} m^2 s^{-1}), concentration of oxygen at the electrode surface (C, 1.58×10^{-9} mol L^{-1}) and rotation speed (ω, RPM) at -1.2 V cell potential, the number of electrons transferred were estimated to be 2.21 ± 0.01 [169,198]. The quantity of transferred electrons (2.21 ± 0.01 e) confirmed the shift of the ordinary four electron oxygen conversion to two electron oxygen conversion. Based on Levich plot, the number of transferred electrons could be calculated at various potential (-1.5 to 0 V) (Fig. 3.5d) and the efficiency of the redox reaction was measured based on H_2O_2 generated [169,199]. Thus, more than 92 ± 3.4% H_2O_2 generation was estimated at the same cell potentials (-1.5 to 0 V) (Appendix 3.2).

3.3.4. Catalytic Efficiency of Fluidized INPs on Acid orange Degradation

0.3 g L^{-1} of each fluidized electrode (C, S and M) was mixed with AO7 contaminated solution separately to evaluate their catalytic degradation efficiency holding pH value (~3), AO7 concentration (5 mg L^{-1}), H_2O_2 concentration (2.5-mL) and applied voltage (3 V) constant. Thus, the degradation efficiency of each fluidized INPs electrodes was measured at 485 nm UV absorbance over 40-min reaction time and various values of degradation values were obtained. The degradation value variation of the fluidized INPs electrodes was the result of the intrinsic behavior of the colloidal particles and the structural size of the fluidized INPs aggregates. As described in Fig. 3.6a, INPs-S showed the highest degradation efficiency (approximately 93.2 ± 1.5%, Fig. 3.6a, red) compared to INPs-C (89.4 ± 1.7%, Fig. 3.6a, black) and INPs-M (83.7 ± 2.3%, Fig. 3.6a, blue). Both INPs-S and INPs-C exhibited fast degradation efficiencies over 20-min, whereas INPs-M showed a slow progress over 40-min and attained maximum efficiency at 40-min. The catalytic behavior of the fluidized INPs electrodes could be affected by morphology and crystallites grains of the INPs [192]. Small size nanoparticles have higher surface area to volume ratio which could contribute higher degradation efficiency due to collusion between the particles and the contaminants as explained by Boutemedjet *et al*. [165]. A series of chemical reaction mechanisms of fluidized INPs electrodes (C, S and M) were proposed on EF process (Eqn. 3.16-3.19) [45] for AO7 degradation. Small amounts of H_2O_2 were required for initiation of the reaction mechanism. After several AO7 degradation trials, INPs-S electrodes were adopted for further AO7 degradation analysis.

$$\text{INPs } (Fe_3O_4) + 8H^+ \rightarrow Fe^{2+} + 2Fe^{3+} + 4H_2O \quad (3.16)$$

$$Fe^{2+} + H_2O_2 \rightarrow Fe^{3+} + \cdot OH + OH^- \quad (3.17)$$

$$O_2 + 2H^+ + 2e^- \rightarrow H_2O_2 \quad (3.18)$$

$$\cdot OH + AO7 \rightarrow AO7(\cdot OH) \quad (3.19)$$

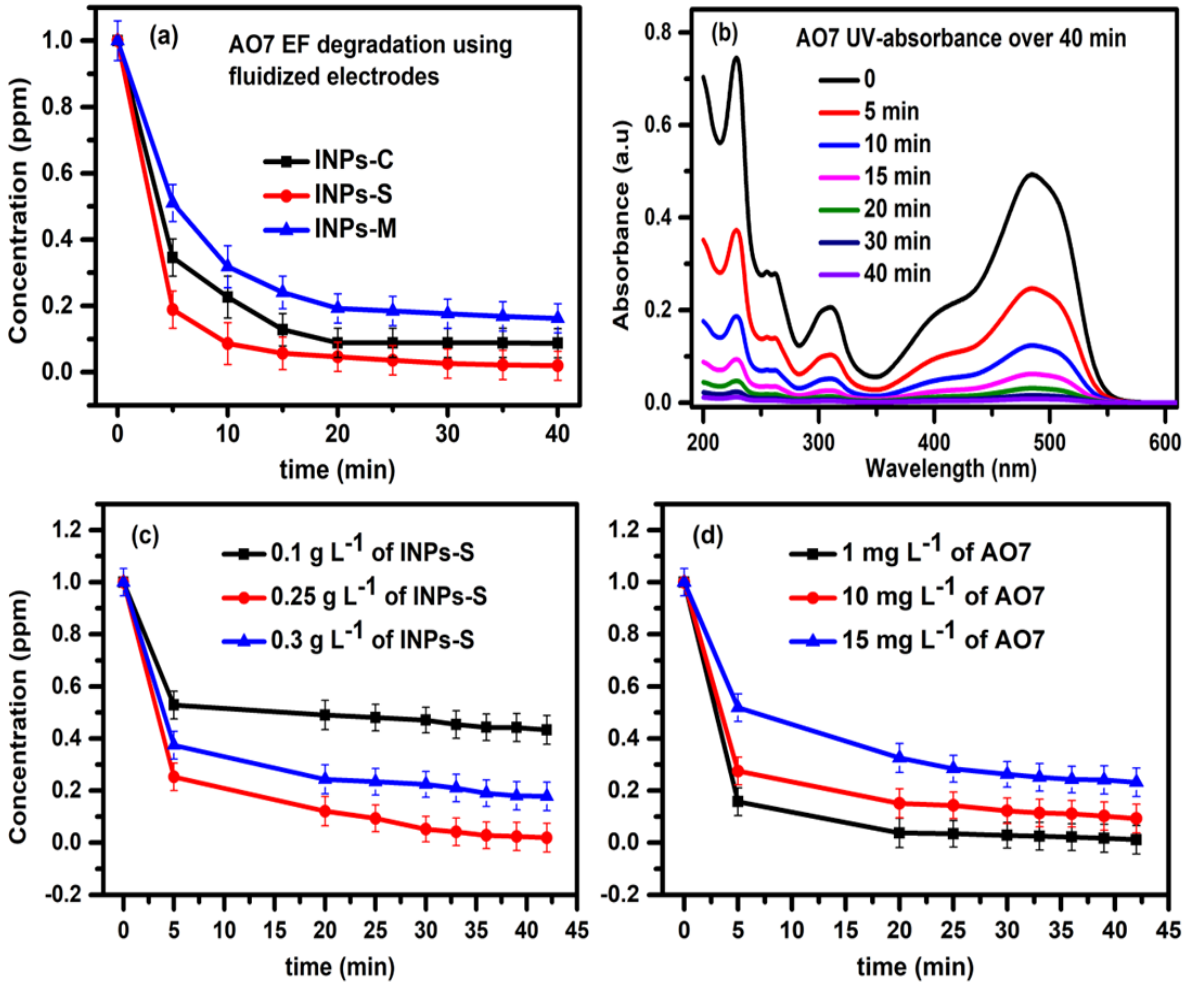

Figure 3.6: *Time dependent AO7 kinetics*

Time dependent AO7 kinetics and spectroscopy analysis before and after EF oxidation: degradation performance of each INPs (a); UV-Vis spectroscopy of AO7 before and after EF oxidation (b); Effect of fluidized INPs-S electrodes (c); and Effect of initial concentration of AO7 on EF degradation (d) at applied voltage of 3 V, pH 3 and electrolyte (Na_2SO_4, 50 mg L^{-1})

3.3.5. Effects of Fluidized INPs-S and Initial AO7 Concentration

Keeping the pH value (pH~3), applied voltage (~3V), initiator H_2O_2 concentration (2.5-mL) and initial AO7 (5 mg L^{-1}) constants, the effect of fluidized INPs-S electrode doses on EF

degradation efficiency was investigated. Fig. 3.6c showed the effect of an addition of INPs-S fluidized electrodes as homogeneous catalyst. The experiment was started by adding 0.1 g L^{-1} of fluidized INPs-S electrodes into the reaction medium and 56.7 ± 1.4% removal efficiency was observed (Fig. 3.6c, black). Increasing the concentration dose of fluidized INPs-S electrodes to 0.15 g L^{-1}, the AO7 removal efficiency increased significantly to 87.8 ± 1.5% and increased to 97.8 ± 1.4% with the further addition of 0.2 g L^{-1} over 40-min (Fig. 3.6c, red). The high concentration dose of fluidized INPs-S electrodes (Fe^{2+}) triggered to increase the oxygen reduction to H_2O_2 which in turn regeneration of ·OH radicals [180,200]. However, increasing the dose of fluidized INPs-S does to 0.3 and 3.5 g L^{-1} into the system, the degradation performance starts to decline to 92.3 ± 1.6 and 82.3 ± 2.1% (Fig. 3.6c, blue) respectively. This was due the inhibition effect of the leached Fe^{2+} that consume the generated ·OH radicals. Similar results were reported by Cui et al. and Suhan *et al.* [174,201].

Similarly, by maintaining the pH value (pH~3), applied voltage constant (~3V), initiator H_2O_2 (2.5-mL) and fluidized INPs-S electrodes (0.2 g L^{-1}) constant, the effect of initial concentration of AO7 on degradation efficiency was investigated. As presented in Fig. 3.6d, when the concentration of AO7 increased from 1 mg L^{-1} (Fig. 3.6d, black) to 10 mg L^{-1} (Fig. 3.6d, red), the removal efficiency remained above 91 ± 2% over 40-min. However, the efficiency dropped to 76.8 ± 1.9% when the AO7 concentration increased to 15 mg L^{-1} (Fig. 3.6d, blue). At lower AO7 concentration, all the AO7 molecules have access to the active surfaces of the fluidized electrodes, hence higher degradation was observed. Whereas at higher concentration, the dye molecules competed for active sites of the fluidized electrodes resulted in declining degradation efficiency [180,200]. The INPs-S fluidized electrodes possess large surface area to volume ration, the probability of collusion between AO7 molecules and INPs-S fluidized electrodes increased, contributing to higher degradation efficiency.

3.3.6. TOC-Removal, Reusability and Stability of Fluidized INPs-S

The degree of mineralization of AO7 was measured by the loss of the total organic carbon (TOC) at the end of oxidation. The TOC values have been related to the total concentration of organic carbon in the AO7 concentration solution. Analysis of TOC at the time (t = 0, 0.5, 1, and 1.5 h) and optimal operating conditions suggested the degree of mineralization of AO7 [202]. As described in Fig. 3.7a, over 40-min of reaction time, an approximate 56.7 ± 1.9% TOC removal as well as 96 ± 2.1% color removal was achieved.

However, increasing the degradation time to 1.5 h, the TOC removal increased to 84.2 ± 3.3% while the color removal was complete indicating that the chromophore bond was easier to break apart than the benzine rings.

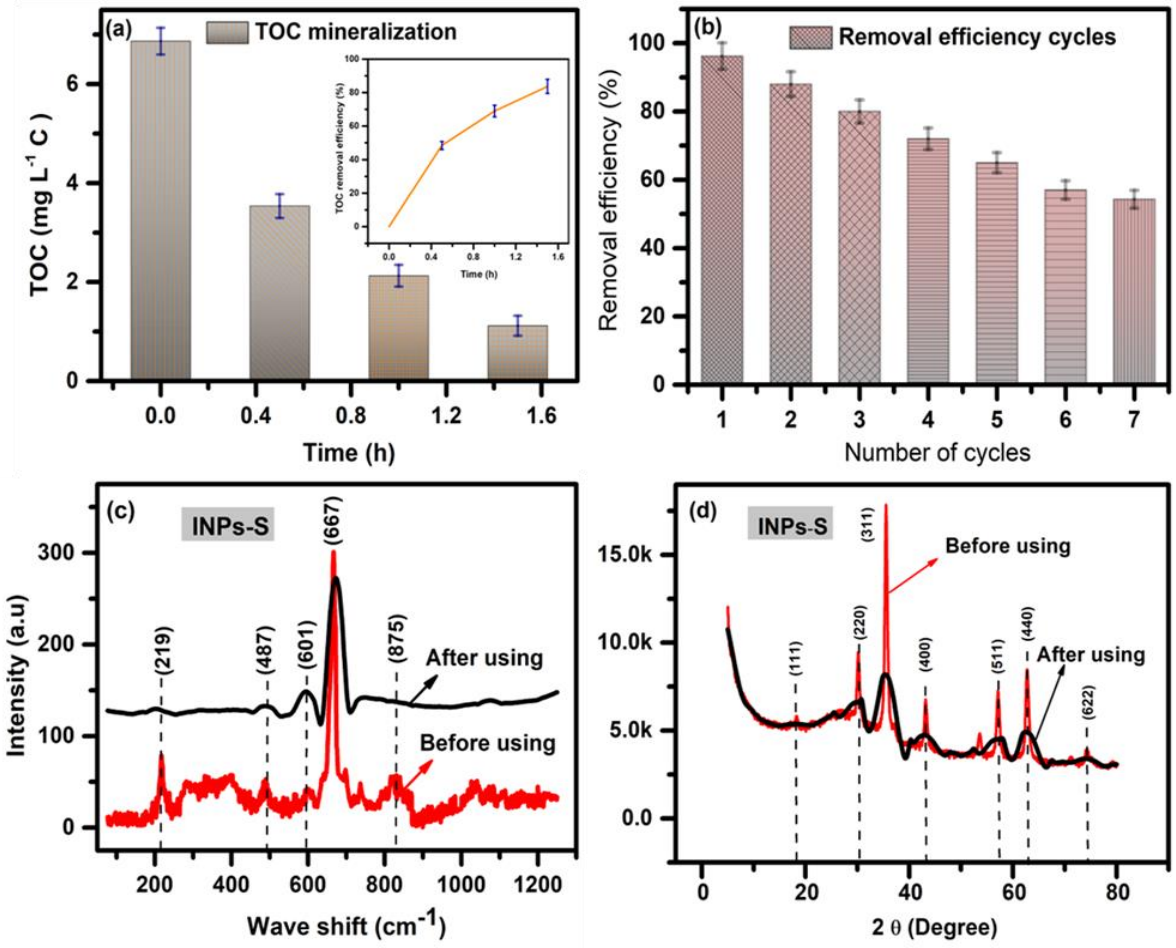

Figure 3.7: *TOC removal, reusability, and stability*

TOC removal, reusability and stability of fluidized INPs-S electrodes: TOC removal of AO7 (a); Reusability of INPs-S (b); Raman spectra of INPs-S before and after EF oxidation of AO7 (c); and XRD spectral patterns of INPs-S before and after EF oxidation of AO7 at operating conditions of applied voltage of 3 V, pH 3, AO7 concentration of 10 mg L^{-1}, INPs-S dose 0.25 mg L^{-1} and electrolyte (Na_2SO_4, 50 mg L^{-1})

Both reusability and stability analysis are the most significant measurements to predict the extent loss of fluidized INPs-S electrode active species over repeated usage. Although the iron-based catalysts have good degradation efficiency, they exhibited less reusability due to the crystalline deformational structure [28]. After seven cycles of EF AO7 degradation, the fluidized INPs-S electrodes were recollected by an external magnet. The presence of leached

iron ions in the solution was determined by ICP-OES analysis and 0.025 mg L^{-1} iron residuals were quantified and compared to 0.25 g initially added (96.4 ± 1.3% recovery). The amount of iron ion residuals in the reacting solution indicated that the magnetic nature of fluidized INPs-S electrodes was not significantly altered. The reusability analysis described in Fig. 3.7b exhibited a gradual decline of AO7 degradation efficiency over seven cycles of INPs-S usability. Thus, after seven cycles of INPs-S usage for EF AO7 degradation, 54.3 ± 2.8% removal efficiency was observed over 40-min under specified operating conditions. This result could be due to the deformation of INPs-S crystalline structure, which was confirmed by comparing the Raman and XRD spectral patterns of INPs-S before and after EF oxidation. Comparing the Raman analysis of INPS-S before and after EF oxidation, some spectral peaks disappeared indicating structural change of the particles as indicated in Fig. 3.7c. Moreover, the major crystalline characteristic peaks of the fluidized INPs-S electrodes disappeared compared to XRD result before degradation as shown by XRD analysis in Fig. 3.7d. Only the major characteristic peaks at around 29.9°, 37.2° and 62.8° that correspond to (220), (311) and (440) lattice planes [203] were remained which confirming crystallite deformation of INPs-S.

3.3.7. Proposed Intermediate Products of AO7

After 40-min of EF AO7 oxidation, the orange color of the solution disappeared, indicating destruction of the chromophore bond [204]. After 1.5 h EF oxidation of AO7, LC-MS and ion exchange chromatography system (ICS) analysis were performed to propose the possible degradation mechanism, at operating conditions of applied voltage of 3 V, pH 3, AO7 concentration of 10 mg L^{-1}, INPs-S dose 0.25 mg L^{-1} and electrolyte (Na_2SO_4, 50 mg L^{-1}). As reported by X. Wang *et.al.*, [205], AO7 could be degraded via two main pathways i.e., cleavage of the chromophore bond and breakage of C-S bond. The cleavage of azo bond resulted in formation of amino benzenesulfonic acid and 1-amino-2-naphthol. The breakage of C-S bond follows formation of nitroso benzine compounds and monocyclic aromatic intermediates. Subsequently, the intermediates were oxidized to H_2O and CO_2. Thus, the dominant reaction intermediate products of AO7 with their chemical structure were presented in Fig. 3.8. Moreover, the LC-MS spectra peaks of the intermediate by-products were listed in Appendix 3.3 and 3.4. Similarly, after 1.5 h EF oxidation of AO7, the anionic oxidation products were identified using ICS, indicating that about 87.4 ± 2.8% of the nitrogen and sulfur elements present in AO7 were converted to NO_3^- and SO_4^{2-} as described in Appendix 3.5.

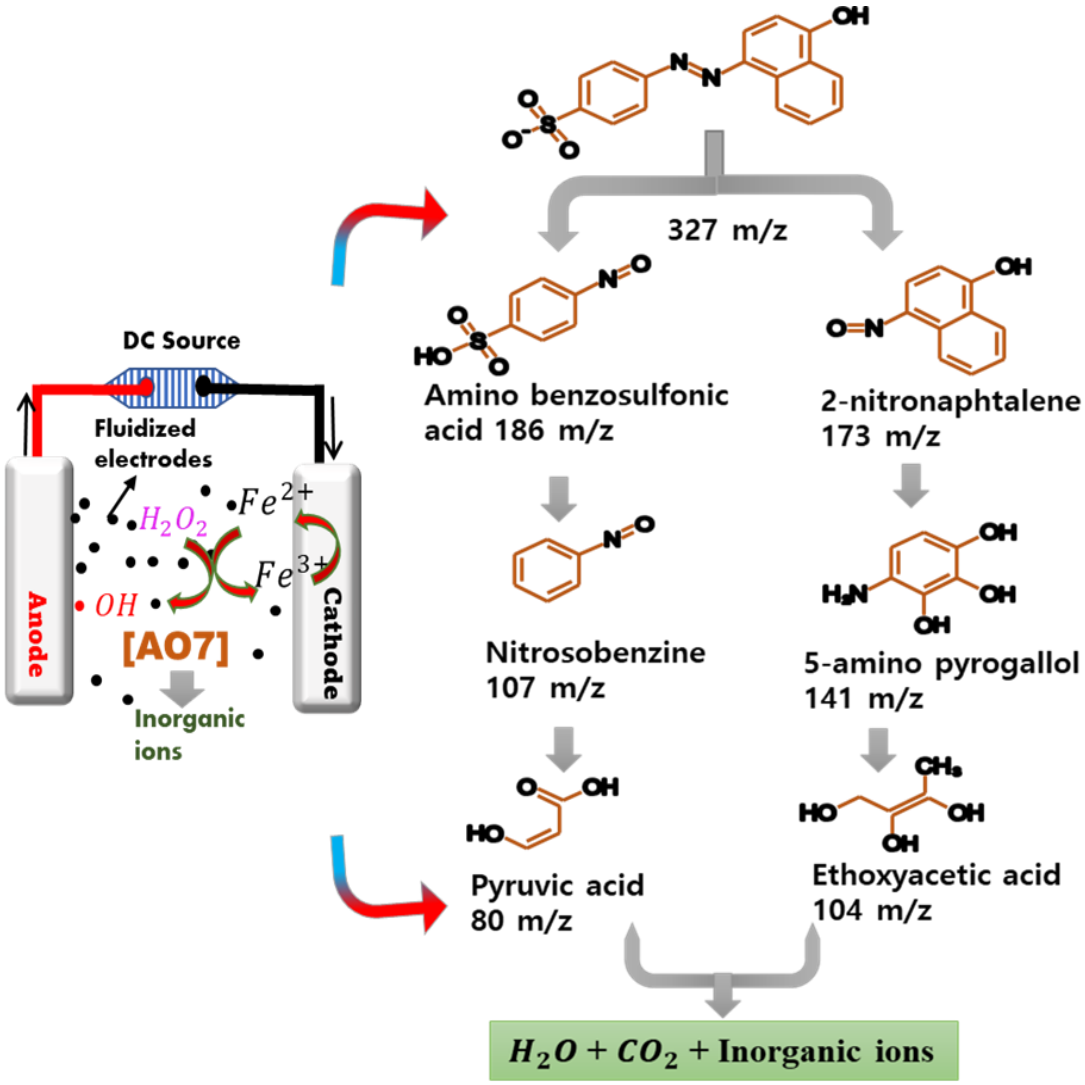

Figure 3.8: *Possible EF degradation pathway of AO7*

Possible EF degradation pathway of AO7 using fluidized INPs-S, at operating conditions (pH, 3), applied potential (3 V), catalyst dose (0.25 g), initial AO7 concentration (10 mg L^{-1}) and electrolyte (Na_2SO_4, 50 mg L^{-1}) over 1.5 h.

3.4. Summery

Easy and cheap co-precipitation procedure was used for INPs synthesis, the degradation was 89.4 ± 1.7%, 93.2 ± 1.5% and 83.7 ± 2.3% for different INPs, mineralization products NO_3^-, NH_4^+ and SO_4^{2-} were identified in degradation and 54.3 ± 2.8% regeneration efficiency was obtained after continuous seven cycles.

CHAPTER 4

4. CARBON FELT COMPOSITE ELECTRODES

4.1. INTRODUCTION

Large amounts of organic dyes are used in industry and then directly discharged into natural water bodies, which is the main cause of environmental color contamination. If dyes are present in water even at a very low level (e.g., < 1 mg L^{-1}), the penetration of sunlight into aquatic systems is blocked to negatively affect the natural photo-degradation process. Traditional biological treatment technologies are insufficient for the removal of organic dyes from water [8,28]. A variety of treatment technologies such as coagulation, adsorption, membrane filtration, etc., have been applied to treat water contaminated with dyes. Since organic dyes are intentionally designed to persist, however, their treatment is still challenging [46,190,206].Recently, advanced oxidation processes (AOPs) are widely employed to degrade various organic dyes (Eqn. 4. 1). The working principle of all AOPs is related to the generation of hydroxyl radical (·OH) [207,208].

Fenton process, in which H_2O_2 reacts with Fe^{2+} to continuously produce ·OH (Eqn. 4. 2), is one of the most widely applied AOPs for degrading organic contaminants in wastewater. However, it requires continuous supply of Fenton's reagents (H_2O_2 and Fe^{2+}) and a lower working pH, while generating large amount of iron-precipitates-containing sludge as a secondary contaminant [209]. In recent years, electro Fenton (EF) process has drawn attention from water engineers as an alternative to the traditional Fenton process since EF overcomes some of the drawback of the latter through the *in-situ* generation of H_2O_2 and the electro-recycling of Fe^{2+}/ Fe^{3+}; consequently, it generates less sludge (Eqn. 4.3). H_2O_2 is continuously generated at the cathode surface via two electron oxygen reduction reaction (2e-ORR) (Eqn. 4.4) and reduced to ·OH radicals by Fe^{2+} ion activation at the cathodic surface. ·OH radicals participate to degrade nearby organic materials [210].

$$Organic\ contaminants + \cdot \mathrm{OH} \rightarrow intermidates \rightarrow CO_2 + 2H_2O \quad (4.1)$$

$$Fe^{2+} + H_2O_2 \rightarrow Fe^{3+} + OH^- + \cdot OH \qquad E^0\,(\text{vs. SHE}) = 2.80\,V \qquad (4.2)$$

$$Fe^{3+} + e^- \rightarrow Fe^{2+} \qquad E^0\,(\text{vs. SHE}) = 0.77\,V \qquad (4.3)$$

$$O_2 + 2H^+ + 2e^- \rightarrow H_2O_2 \qquad E^0\,(\text{vs. SHE}) = 0.547\,V \qquad (4.4)$$

Still in the EF, the rate of H_2O_2 generation is limited due to the low water solubility of oxygen. As a result, gas diffusion electrodes have been employed to enhance oxygen diffusion from bulk solution to electrode surface and subsequently generate of H_2O_2 on the surface [169]. Among the factors affecting H_2O_2 generation in EF for degrading organic pollutants, cathode material is the most essential. Due to its excellent electrolytic capacity, high electrochemical strength, conductivity as well as biocompatibility, carbon electrodes [28,43] and carbon felt (CF) have been used as cathode materials in EF processes [153,211,212]. However, low wettability and electrochemical stability of CF have been an obstacle in adopting in wider CF application [213].

The increasing use of electrochemical technologies in a variety of applications such as synthesis, energy storage and environmental treatment (EF) has been increasing [214]. The utilization of porous materials such as carbon Felt (CF) cathode for wastewater treatment owing to its good electrical conductivity, hydraulic permeability, and durability in strong acid and alkali electrolytes [214,215]. Good electrical conductivity arises from the movement of electrons through the carbon filaments to reach the electrolyte. CF conductivity is determined by the carbon fibers comprising the felt structure and which connect simultaneously to both electrodes. Conductivity is well known to be improved by felt compression. A tremendous amount of research work has been carried out to investigate and measure the properties of CF [214–216].

Therefore, much research has been performed to chemically modify CF surface to overcome its weakness. For example, the interfacial surface electro-activity of CF could be considerably increased if the CF surface were modified to have oxygen-containing functional groups such as carboxyl (-C =O-OH), carbonyl (-C=O) and hydroxyl (-OH) ones. These functional groups act as a site for generation of H_2O_2 at a higher rate. Like Fenton oxidation, EF oxidation requires a low working pH. Consequently, heterogenous EF oxidation based on the catalysts, which are made of magnetite nano-particles (Fe_3O_4), recently attracts increasing attention in the field of dye wastewater treatment since its working pH is wider than conventional EFs [78].

In fact, insoluble MNPs have been proven to be an effective alternative heterogeneous catalyst for water-soluble iron catalysts that are used in homogeneous Fenton oxidation. Prominent attributes, i.e., a large surface area to volume ratio, good biocompatibility [140], and ease of catalyst-recycling, make MNPs promising as a catalyst for oxidizing organic contaminants in wastewater [141,142,217].

The most important types of industrial wastewater caused by chemical products are dyes with the production of more than 7 million tons per year. If dye effluents produced by various industries, including paper, leather industry, cosmetic industries, printing, foodstuffs, etc., discharged into surface and groundwater before purification, causes human and aquatic diseases and deaths in the short or long term, toxicity to ecosystems, and the environmental accumulation of organisms in these environments [218]. CR is one of the most common dyes in the textile industry. High solubility in water, light resistance, and complex chemical structure are features of CR dye. It causes eye stimulation, nausea, vomiting, diarrhea, blood clotting, drowsiness, etc. Accordingly, removing CR from wastewater solution is essential.

Briefly, CR is a brownish-red diazo compound and is high water-soluble (33 g L^{-1}). This anionic air-stable acid dye finds application in diverse fields such as diagnosing amyloidosis, pH indicator, as well as to analyze the concentration of hydrochloric acid in gastric materials. Due to its strong affinity towards cellulose fibers, it has been widely employed in textile industries too. The direct contact of the dyes results in hazardous effects to both humans and animal species that include skin allergy, eye irritation, neurotoxicity and pulmonary diseases [219]. Several methods have been reported to remove dyes from aqueous solutions, which can be referred to as chemical oxidation, coagulation, electrochemical treatment, filtration, photocatalytic process, ozonation, ion exchange, membrane process, and adsorption. Due to their unique properties, such as high saturation magnetization, biocompatibility, and stability, INPs are applied for biomedical applications (i.e., electrochemical sensors, cancer treatment, or medical imaging), catalysis (i.e., in wastewater treatment as Fenton reagent), supercapacitors (energy storage). The electrochemical behavior is thus the first step toward the assessment of the potential material effectiveness.

In this study, different MNPs-synthesizing methods have been reported. The size, shape, and purity of MNPs vary depending on applied synthesis procedures. In fact, the effectiveness of MNPs as a catalyst distinctively depends on their particle size. Magnetite nano-particles with

a smaller size shows higher superparamagnetic behavior [215,220]. Therefore, a large efforts have been exerted to produce MNPs with a smaller size, and the size of MNPs could be determined by iron-salt precursors [153]. MNPs with a well-defined size were synthesized by modifying a classical co-precipitation method; iron sulfate salt precursor was utilized. In addition, CF was chemically activated using a mixture of sulfuric acid and nitric acid to induce the oxygen-containing functional groups on the surface (i.e., carboxyl groups) while removing inorganic contaminants, and to increase its surface area to enhance electrochemical reduction of oxygen to generate H_2O_2. Here, MNPs were added to pull the H_2O_2 generated on the electro active surface of the cathode to the solution where ·OH radicals were generated. Two ACF cathodes and stainless steel (SS) anode in the middle were parallelly connected. Here the role of MNPs was to pull the H_2O_2 generated on the electro active surface of the cathode to the solution where ·OH radicals were generated. Thus, based on generation of ·OH radical and H_2O_2 activation by Fe^{2+}, the EF system was evaluated in degrading Congo red (CR) as a model contaminant. On the system, the influence of the initial pH, the applied potential, catalyst dose and initial CR concentration on the EF performance were investigated. Lastly real textile wastewater was employed for EF oxidation.

4.2.Materials and Methods

4.2.1. Chemicals and Materials

All the chemical reagents used for synthesizing the catalysts and electrodes were analytical grade which had been provided by Samchun Pure Chemicals (Seoul, Korea). Congo red (CR>89%), (Appendix 4.1), ethanol (> 99%), para-benzoquinone (> 98%), *tert*-butanol (> 99.5%), $FeSO_4 \cdot 7H_2O$ (> 98%), $Fe_2(SO_4)_3 \cdot 6H_2O$ (> 99%), Na_2SO_4 (> 99%), ammonia solution (28% w/w) and SS (6 cm × 2.5 cm; Anode Scientific-E160-0032) were purchased from Sigma-Aldrich (Seoul, Korea). Polyacrylonitrile based carbon felt (> 99%, V-07-G-10, thickness: 3 mm, bulk density: 0.11-0.15 g cm^{-3} and tensile strength 0.40 MPa) was provided by Fiber Land Co. (Seoul, Korea). The solution was prepared with high-purity water (resistivity > 18 MΩ cm at 25 °C). During the experiment, 0.1-M H_2SO_4 and 0.1-M NaOH solutions were used to adjust the initial pH of the solutions.

4.2.2. MNPs Synthesis and CF Activation

Following the modified co-precipitation method of our previus report, MNPs were synthesized using 6.87 g $Fe_2(SO4)_3 \cdot 6H_2O$ and 4.73 g $FeSO_4 \cdot 7H_2O$. Briefly, the methods of MNPs synthesis were described in Text S1. To activate chemically, 12 cm^2 (4 cm × 3 cm) surface area of CF was soaked in a solution containing 0.75-mL H_2SO_4 (5% w/w) and 1.75-mL HNO_3 (5% w/w) for 15-min. To remove inorganic impurities from the surface, it was immersed into distilled water for 20-min, washed several times, and dried at 100 °C in a drying oven overnight.

4.2.3. MNPs and ACF Electrodes Characterization

X-ray diffraction (Rigaku, Tokyo, Japan) operated at 40 kV and 40 mA with Cu Kα (λ = 1.541 Å) over the 2θ range of 5º-85º was used to determine the crystallite size of MNPs and CF. The average crystallite size of MNPs was estimated from full width half maximum (FWHM) of the main peak, using the Scherrer's law and the distance between atomic layers of the MNPs crystals was determined using Bragg's law. Fourier transform infrared (FTIR) (Thermos Scientific, Nicolet iN10 mx, Madison, USA) was employed to determine the oxygen containing functional groups on the surface of ACF. The morphological structure of the materials was characterized by field emission scanning electron microscope (FE-SEM, SU8010, Hitachi, Japan) under 15 kV of operational voltage. The elemental composition and mapping of MNPs, and ACF were analyzed using Energy dispersive X-ray (EDX) spectroscopy (Thermo Scientific, Madison, USA).

X-ray photoelectron spectroscopy (XPS) (Scienta-ESCA5500, Shimadzu, Tokyo, Japan) equipped with the high resolution Scienta-ESCA5500 spectrometer was used for ACF cathode analysis. The machine was operated at high power (19 kW) rotating anode monochromate 460 W Al Kα source. Wide scan spectra were measured over a binding energy range of 0-1400 eV and a pass energy of 185.75 eV. The C1s and O1s levels were recorded with a step of 0.05 eV and a pass energy of 12.75 eV. For data acquisition and data analysis, SCIENTA software was used. The binding energy of each element was corrected by C 1s peak (284.8 eV) from residual carbon [169,221]. The magnetic properties were analyzed on the Magnetic Property Measurement System (MPMS-XL-7T, quantum design Inc., San Diego, USA) squid magnetometer in the field of sweeping -7.95k to 7.95 kOe [165]. The electrochemical properties of the electrodes were carried out in a three-electrode system of potentiostat/galvanostat. Cyclic voltammetry (CV, CHI660E, Chenhua, China) and the linear

sweep voltammetry (LSV) were performed under scan rate of 10 mV s^{-1} from -0.2 to 0.2 V (vs. Ag/AgCl). The prepared cathodes were used as a working electrode (1.2 cm × 0.96 cm) while Ag/AgCl (0.82 cm^2) and platinum plate (2.92 cm^2) were used as a reference electrode and counter electrode respectively. The solution pH was adjusted to 4 and the electrolyte was 0.5-mol L^{-1} Na_2SO_4. The average number of electrons transferred (n) for ORR were determined from the slope of graph of reciprocal of limiting current vs the reciprocal square root of the angular speed of the electrode according to Koutecky-Levich plot [169] (Eqn. 4.5).

$$\frac{1}{i_L} = \left(\frac{1}{0.62nAFD^{2/3}C_i\nu^{-1/6}}\right)\omega^{-1/2} \quad (4.5)$$

Where i_L is limiting current (A), n is number of electrons transferred, F is the Faraday constant (96,485.3 $Cmol^{-1}$), D is the diffusion coefficient of oxygen (2.47 × 10^{-5} m^2 s^{-1}), A is the electrode area (1.2 cm × 0.96 cm), ν is the kinematic viscosity of water (1× 10^{-2} m^2 s^{-1}), C is the concentration of oxygen at the electrode surface (1.67 × 10^{-6} mol L^{-1}) and ω is the rotation speed (RPM) of the electrode.

4.2.4. Experimental and Analytical Methods

A cylindrical Pyrex reactor with 500-mL volume (i.e., 300-mL~300 cm^3 active volume) was employed. Initially, 300-mLmin^{-1} of oxygen gas was pumped to the solution for 10-min. Two stacks of cathode-anode-cathode (i.e., ACF-SS-ACF ~ ACF-SS-ACF, 1 cm gap) arranging of SS in the middle were connected parallelly at a distance gap of 2.5 cm (Fig. 6.1). Degradation of 5-30 mg L^{-1} concentration of CR solution at various pH (3-6), various voltages (0.5-6.5 V) and various catalyst dosages (0.1-0.6 g) was conducted. Sample volume of 2-mL was harvested at each 5 min intervals for UV-Vis spectrophotometer (Shimadzu 1800, Kyoto, Japan) analysis and the kinetic degradation efficiency was studied [171] (Eqn. 4.6). Besides TOC decay was determined using TOC-V_{CPH} (Shimadzu, Tokyo, Japan) analyzer and the values were estimated (Eqn. 4.7).

$$Congo\ red\ removal\ (\%) = \frac{C_0 - C_t}{C_0} \times 100 \quad (4.6)$$

$$Congo\ red\ decay(\%) = \frac{\Delta(TOC)_t}{(TOC)_0} \times 100 \quad (4.7)$$

where C_0 is the initial CR concentration, C_t is the CR concentration measured at time t, $(TOC)_o$ and $\Delta(TOC)_t$ are the TOC measured at time 0 and at time t to evaluate the extent of CR mineralization (mg C L^{-1}).

Similarly, the electrochemical energy consumption (EEC) and mineralization current density efficiency (MDCE) were determined (Eqn. 4.8 and 4.9) respectively [46].

$$EEC = \frac{UAIt}{\Delta(TOC)_t V} \quad (4.8)$$

$$MDCE(\%) = \frac{\Delta(TOC)_t nFV}{4.32x10^7\, mjAt} \times 100 \quad (4.9)$$

Where U is the cell voltage (V); n is number of electrons transferred during CR oxidation (178e, Eqn. 4.10), assuming the mineralization products were NO_3^- and SO_4^{2-} ions; F is the Faraday constant ($Cmol^{-1}$); V is the solution volume (cm^{-3}); m is the number of carbon atoms of CR (32 atoms); j is the current density (A); A is the total area of the electrodes and 4.32×10^7 is a conversion factor ($3600\ sh^{-1} \times 12000\ mgCmol^{-1}$).

$$[C_{32}H_{22}N_6O_6S_2]^{-2} + 84H_2O \rightarrow 32CO_2 + 6NO_3^- + 2SO_4^{2-} + 190H^+ + 178e^- \quad (4.10)$$

By assuming the MNPs did not interact with the active species of ACF and the space for CR degradation could be within the volume of the double layer and the only diffusion affect the mass transport. Mathematically the rate of CR degradation was expressed as a function of ·OH radical and CR concentration leading to diffusional mass flux (Eqn. 4.11). The concentration of ·OH radical were assumed at a steady state condition (i.e., the change of ·OH concentration approximated to zero). The apparent rate constant (k_{app}) was determined from Eqn. 4.12.

$$\frac{dC_{CR}}{dt} = -kC_{\cdot OH}C^*_{CR} = -k_D(C^0_{CR} - C^*_{CR}),\ where\ k_D = \frac{D}{\delta} \quad (4.11)$$

$$k_{app}C^*_{CR} = \frac{j}{VnFA} \quad (4.12)$$

Where C_{CR} is the concentration of CR at time t (mol L^{-1}); k is second order rate constant ($mol^{-1}\ cm^3\ min^{-1}$) k_{app} is pseudo second order rate constant ($mol^{-1}\ cm^3\ min^{-1}$); $C_{\cdot OH}$ is concentration of ·OH radicals (mol L^{-1}); C^*_{CR} is concentration of CR at the electrode surface (mol L^{-1}); D is the diffusion coefficient of CR in water ($1.95 \times 10^{-6}\ cm^2s^{-1}$),and δ is thickness of the double layer (2.5×10^{-6} cm); j is measured current density (mA cm^{-2}), n is number of electrons transferred,

F is the Faraday constant (96,485.3 $Cmol^{-1}$), A is the electrode area (2.5 cm × 3.5 cm), V is the reactor volume (300 × cm^3) and C^0 is the initial CR concentration at the electrode surface (15 mg L^{-1}~2.2×10^{-5} mol L^{-1}).

Inductively coupled plasma optical emission spectrometry (ICPE-900, Shimadzu, Tokyo, Japan) was used to quantify the residual iron concentrations existing in the treated solution. Chemical scavenging method was performed to determine the oxygen reactive species involving in degrading CR [162,170]. The CR oxidation intermediates were analyzed by liquid chromatography-mass spectrometry (LC-MS, Shimazu, Kyoto, Japan) and the mineralized inorganic by-products of CR (i.e., NO_3^- and SO_4^{2-} ions) were determined using ion-exchange chromatography (ICS-90, Thermo Fisher Scientific, Borken, Germany). Samples were filtered using a membrane filter of 0.45 μm (PTEF, ADVANTEC, HP045AN) during LC-MS and IC analysis [28].

4.3. Results and Discussion

4.3.1. Characterization of MNPs, CF and ACF

The XRD technique was performed to identify the crystal structure and crystallite size of MNPs and CF cathodes. As described in Fig. 1, different diffraction peaks were displayed at 19.3°, 31.4°, 35.3°, 43.5°, 53.7°, 57.3°, 62.1° and 74.3° which correspond to (111), (220), (311), (400), (422), (511), (440) and (622) lattice plane of MNPs, respectively. all the peaks were according to JCPDS No-19-0629 standard [203]. However, the highest diffraction intensity was identified at 35.3° which corresponds to the (311) lattice plane. The crystallite size and the distance between atomic layers of MNPs were calculated to be 10.73 nm and 2.28 Å, respectively according to Scherrer's and Bragg's law [181]. The characteristic peak location in Fig. 1a (blue) revealed the purity of the synthesized MNPs crystal face of spinel structure [215]. Higher anionic strength of SO_4^{-2} contributed to the small size of MNPs. The crystalline nature of pristine CF and ACF was also analyzed. In the case of pristine CF, two broad hump-shaped peaks near 2θs of 17.5° and 26.9° were detected, which belong to the amorphous carbonization process of CF [222] (Fig. 1a, black). In the case of ACF, the narrow peak was observed at 2θ of 25° (002), which was attributed to the formation of the crystal structure of carbon (Fig. 1a, red, insert). Additional diffraction peaks observed at 2θs of 35.7° and 43.3° were attributed to the disordered graphite layer of amorphous carbon formed during the chemical treatment

process [223]. The additional diffraction peaks observed in ACF indicated that the CF was interfacial activated and oxygen containing functional groups were formed.

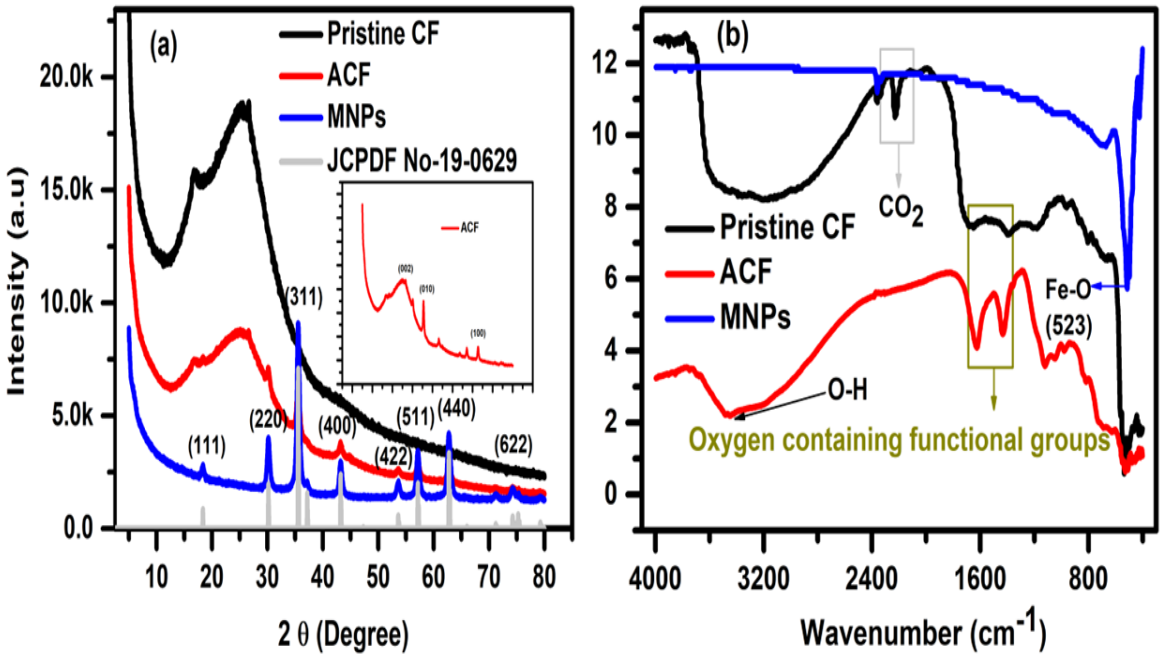

Figure 4.1: XRD diffraction patterns and FT-IR spectral vibrations

XRD diffraction patterns (a) and FT-IR spectral vibrations (b) of pristine CF (black), ACF (red) and MNPs (blue). The insertion in a is ACF to show clear diffraction peaks.

Any functional groups that absorbed at the surface of MNPs and oxygen containing functional groups formed during CF activation were determined using FT-IR analysis. The vibration of the Fe-O was observed within 500-600 cm^{-1} [224]. A strong peak at around 525 cm^{-1} due to Fe-O bonds stretching and vibrational mode. Understanding the spectral range of MNPs which laid between 500-650 cm^{-1} confirmed the purity of the synthesized MNPs [225] (Fig. 1b, blue). In both CF and ACF, the peaks that were observed at around 2920 and 2241 cm^{-1} were due to symmetric and asymmetric expansion vibration of -C-H and bending vibration of adsorbed water (H-O-H), respectively. The peak at around 1643 cm^{-1} was ascribed to -C=C stretching vibration, the peak at around 1326 cm^{-1} and 1164 cm^{-1} were assigned to symmetrical bending vibration of C-H of CF as presented in Fig. 1b (black). Also small peaks were observed at around 1655 and 1554 cm^{-1} of ACF which were assigned to stretching vibrations of carboxyl functional groups (-C=O-OH) [226] and carbonyl functional groups (-C=O) starching modes, respectively and the peaks at 1446 cm^{-1} and 1246 cm^{-1} were mainly indexed to the -N-O groups

and hydroxyl functional groups (-OH) [54] respectively (Fig. 1b, red). However, the peak at 2360 cm^{-1} was due to stretching of adsorbed CO_2 during sample preparation. The presence of new absorption peaks in ACF suggested that the material was successfully activated.

4.3.2. Characterization of ACF

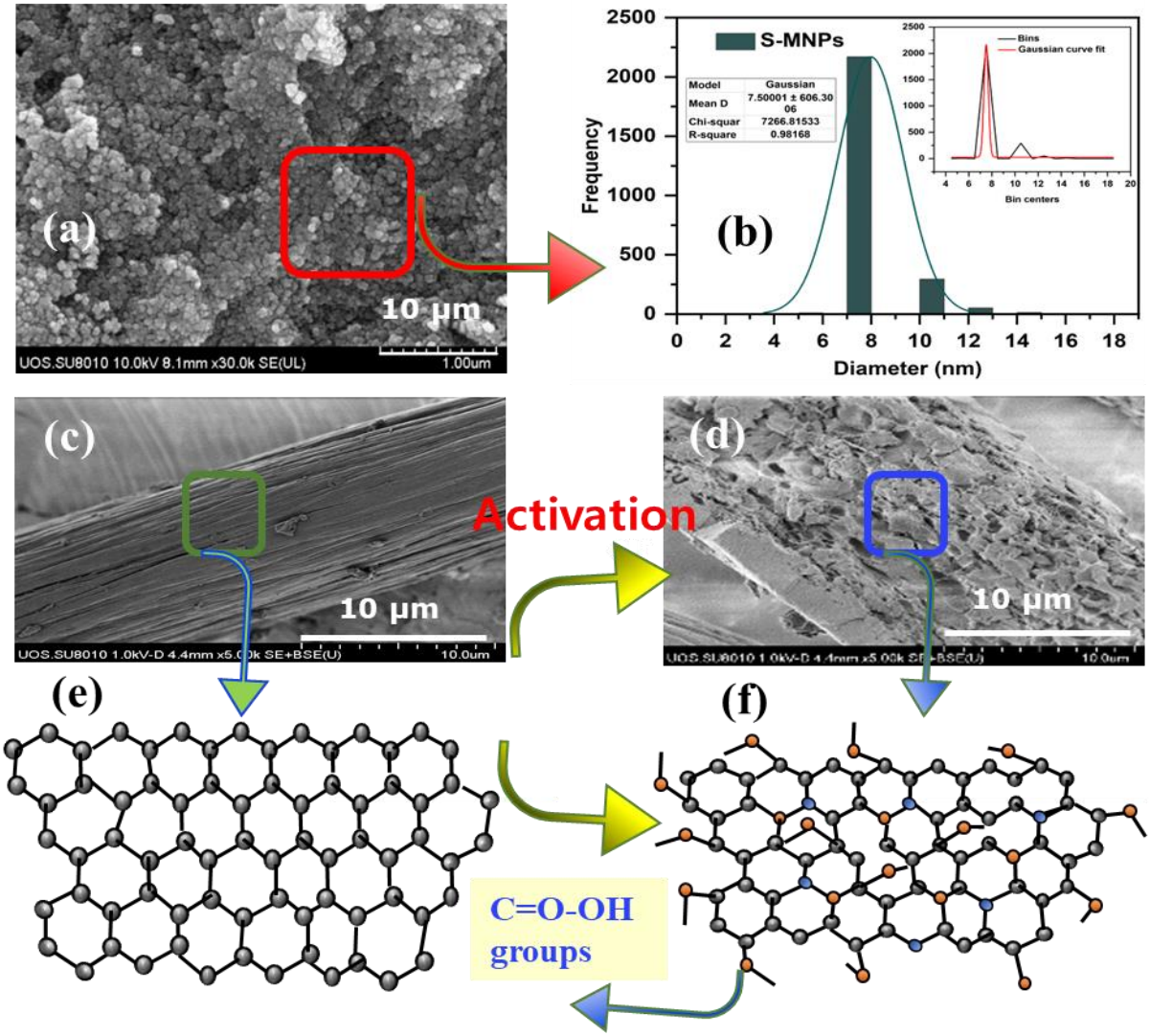

Figure 4.2: Topographical structure of ACF

Topographical structure of MNPs (a), Pristine CF (c) ACF (d) in SEM and the plot of MNPs size distribution (b). The structure in (e) and (f) defined the skeletal arrangement of carbon atom and of pristine CF and ACF respectively.

The morphological structure of MNPs, CF and ACF was determined by FE-SEM. The crystal structures of MNPs were displayed in Fig. 2a, and their mean diameter and their size

distribution were determined using image j software (Fiji is Just) [62,227] (Fig. 2b). Obvious difference was observed between the average crystallite size calculated from XRD (10.71 nm), and the average diameter analyzed from FE-SEM images. It was clear that XRD analysis showed the crystallite size of MNPs not the particles size [186,187]. The difference come from the agglomeration and magnetization of the particles during FE-SEM analysis [174,188]. Since the particles possess high surface energy, they tend to aggregate to minimize the surface energy [162,174]. Comparing the surface roughness of pristine CF (Fig. 2c) to ACF (Fig. 2d), very rough walls of carbon fiber were observed. The scratched and rugged face on the wall of the ACF were formed due to oxygen containing functional groups which served a site for 2e-ORR. The chemical composition of the functional groups on the outer face wall of the pristine CF and ACF were proposed as presented in Fig. 2e & f respectively.

FE-SEM-EDX analysis was performed to determine the elemental composition of the synthesized materials (i.e., MNPs and ACF) as shown in Appendix 4.2. The sharp peaks of Fe and O were incorporated into MNPs. However, other signals that originated from the MNPs storage were also observed, which were according to Dash *et al.* [228] report (Appendix 4.2a). Theoretically, the weight percent of O and Fe in 100% pure Fe_3O_4 were 27.6% and 72.4%, respectively. However, we found 28.3% O and 71.7% Fe, confirming that our synthesized MNPs were within 99.1% purity as described in Appendix 4.2a (Table). Similarly, EDX and elemental mapping analysis were employed to prove the presence of the functional elements on the wall of the ACF. Since the pristine CF was an acrylonitrile compound, soaking in a mixture solution of H_2SO_4 and HNO_3 could change the surface chemistry of the material. As shown in Appendix 4.2b (1-6), the ACF cathode contained carbon, oxygen, nitrogen, and sulfur elements in a uniform elemental distribution (Appendix 4.2b, Table).

The XPS analyses were performed to further confirm the formation of oxygen-containing functional groups, i.e., carboxyl, carbonyl, and hydroxyl groups upon the surface activation of pristine CF to determine the effect of chemical activation on the surface chemistry of ACF cathode. As described in Fig. 3, the C 1s and O 1s spectra peaks of pristine CF and ACF appeared at approximately 285 and 530 eV, respectively. Whereas in CF, these peaks were interpreted as surface oxidation of the carbon film and heteroatom oxygen molecule in the intrinsic pristine CF framework due to waster adsorption [20,59,169,221,229] as described in Fig. 3a. Whereas, the high-resolution of C 1s spectrum on ACF at binding energies of 286. 2, 284.8 and 283.9 eV correspond to carbonyl groups (-C=O) or hydroxyl groups (-C-OH), carboxyl groups (-C=O-OH) and nitro functional groups (-N-O), respectively [90,230] (Fig. 3b). This oxygen containing functional groups indicated the successful activation of the pristine

CF. Furthermore, the O 1s peaks of pristine CF at 532. 5 and 529.9 eV correspond to C-O species (Fig. 3c). To analyze the changes of C-O species after activation of pristine CF; however, a comprehensive deconvolution of the peaks at 533.2, 531.1 and 530.3 eV was carried out as shown in Fig. 3d. These peak binding energy positions correspond to nitro groups (N-C=O), carboxyl groups (-C=O-OH) and carbonyl groups (-C=O) respectively, which suggests that the formation of active oxygen containing functional groups. Generally, the FT-IR, SEM-EDX spectra and XPS data indicated that the CF was successfully activated, and the oxygen-containing functional groups were bonded on the surface of CF without significant structural changes. The N 1s spectra peak of ACF located at around 400.5 eV corresponding to sp^2-hybridized N atoms of -C=N-C [169,221] (Appendix 4.3). The N 1s signal of ACF originated from the pristine CF of acrylonitrile compound and the activation process neither introduce an N atom nor change the chemical position of the existing N atom [169].

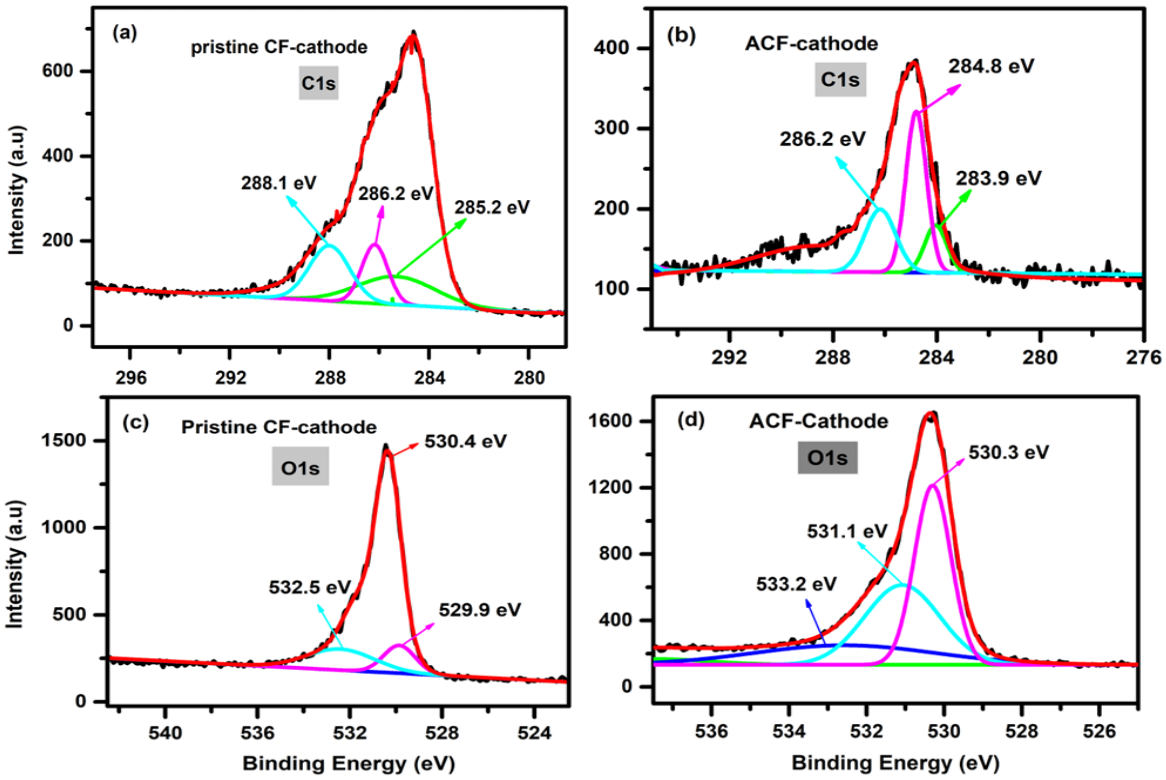

Figure 4.3: *High resolution XPS measurement with its curve fittings*

Pristine CF (a, c) and ACF (b, d); (a) and (b) for C 1s and (a) and (b) for O 1s

Using a VSM device, the magnetic properties of MNPs were measured at room temperature within the sweeping field ranging between -7.95k to 7.95 kOe. The hysteresis curve in Fig.

4.3a indicated that the synthesized MNPs exhibited ferromagnetic characteristics with magnetization saturation (M_S) of 74 $emug^{-1}$ which was in accordance with Gang *et al*. [231]. Since the M_S value is dependent on the phase composition, crystallinity, and size of the synthesized particles [182], MNPs with a larger size presented a higher M_s value than smaller MNPs [190]. The observed VSM result for the synthesized MNPs confirmed that they could be easily separated from the aqueous medium using an external magnet after their use, e.g., in CR oxidation.

The electrochemical functionality of CF and ACF were tested using an electrochemical workstation to test the electrochemical performance of the cathodes (i.e., CF, ACF) in a three-rotating disk electrode system in O_2-saturated solution at 300 RPM rotating rate. As described in the Fig. 4.3b, the electrochemical property of ACF electrode showed higher peak current densities in both oxidation (higher positive value, 6.79 ± 0.17-$mAcm^{-2}$) and reduction (higher negative value, 5.96 ± 0.14-$mAcm^{-2}$) than that of pristine CF electrode, which could be attributed to porous surface chemistry modification of ACF [162,196]. Specifically, the available oxygen containing functional groups (-C=O-OH) as a site for oxidation reduction reaction contributed to higher current density. The higher current density of ACF indicated the best performance of ACF in electrochemical activity in the system. To check oxygen reduction reaction indirectly, the electrochemical analysis was repeated under N_2-saturated solution. Thus, a very limited magnitude of current density (approximately ± 0.15-$mAcm^{-2}$) was observed as described in Appendix 4.4a. The molecular ORR expression in O_2-saturated solution and ORR suppression in N_2-saturated solution confirmed the catalytic activity of ACF. The higher ORR catalytic performance in O_2-saturated solution of ACF was attributed to its high surface area to volume ratio and in turn acted as reservoir for H_2O_2 generation during CR degradation.

During ORR mechanism, both convective limiting current and diffusive limiting current were affected by rotation rate and determined using Koutecky-Levich plot [169,197]. The rotation rate contributed to smaller diffusion layer, high concentration gradient of electroactive species at ACF surface and higher current density. The sigmoidal curve in Fig. 4.3c explained the dependence of limiting current density on rotational rate when the current density was solely controlled by mass transport (i.e., steady-state condition of active species on ACF). The limiting current density is directly related to rotational speed of the disk. The Koutecky-Levich plot (Fig. 4.3d) described the kinetic contribution of electroactive species on ACF, which used

to determine the number of electrons transferred (*n)*. Assuming the faraday constant (F, 96,485.3 $Cmol^{-1}$), diffusion coefficient of oxygen (D, 2.47×10^{-5} $m^2 s^{-1}$), electrode area (A, 1.2 cm × 0.96 cm), kinematic viscosity of water (v, 1×10^{-2} $m^2 s^{-1}$), concentration of oxygen at the electrode surface (C, 1.67×10^{-9} mol L^{-1}) and rotation speed (ω, RPM) at -1.5 V cell potential, the number of electrons transferred were estimated to be 2.1 ± 0.01 [169,198]. The quantity of transferred electrons (2.1 ± 0.01 e) during ORR mechanism confirmed the selectivity of ACF toward 2e-ORR. Based on the slope of Koutecky-Levich plot, the number of transferred electrons could be calculated at various potentials (-0.2 to +0.2 V) (Fig. 4.3e). The 2e-ORR reaction efficiency could be measured directly by percentage of H_2O_2 generated at the surface of ACF [169,199]. The % H_2O_2 produced at different cell potentials (-0.2 to +0.2 V) was plotted as described in the (Fig. 4.3f) and about 89 ± 3.1% H_2O_2 generation was estimated according to Eqn. 4.13.

$$H_2O_2(\%)generation = 200 \times \frac{i_R}{Ni_D + i_R} \qquad (4.13)$$

where *N* is the collection efficiency (27%), and i_R and i_D are the values of the ring and disk current densities at different cell potentials (-0.2 to +0.2 V).

The LSV analysis of pristine CF and ACF in O_2-saturated solution was analyzed as shown in Appendix 4.4b. The current response of pristine CF cathode (3.75 ± 0.54-mA cm^{-2}) was less than that of ACF (more than 10-mA cm^{-2}), confirmed that the electrochemical catalytic activity of ACF was from the contribution of surface modification [211]. The higher ORR in ACF was due to the functional groups formed during activation process which supports the FTIR and XPS spectra results.

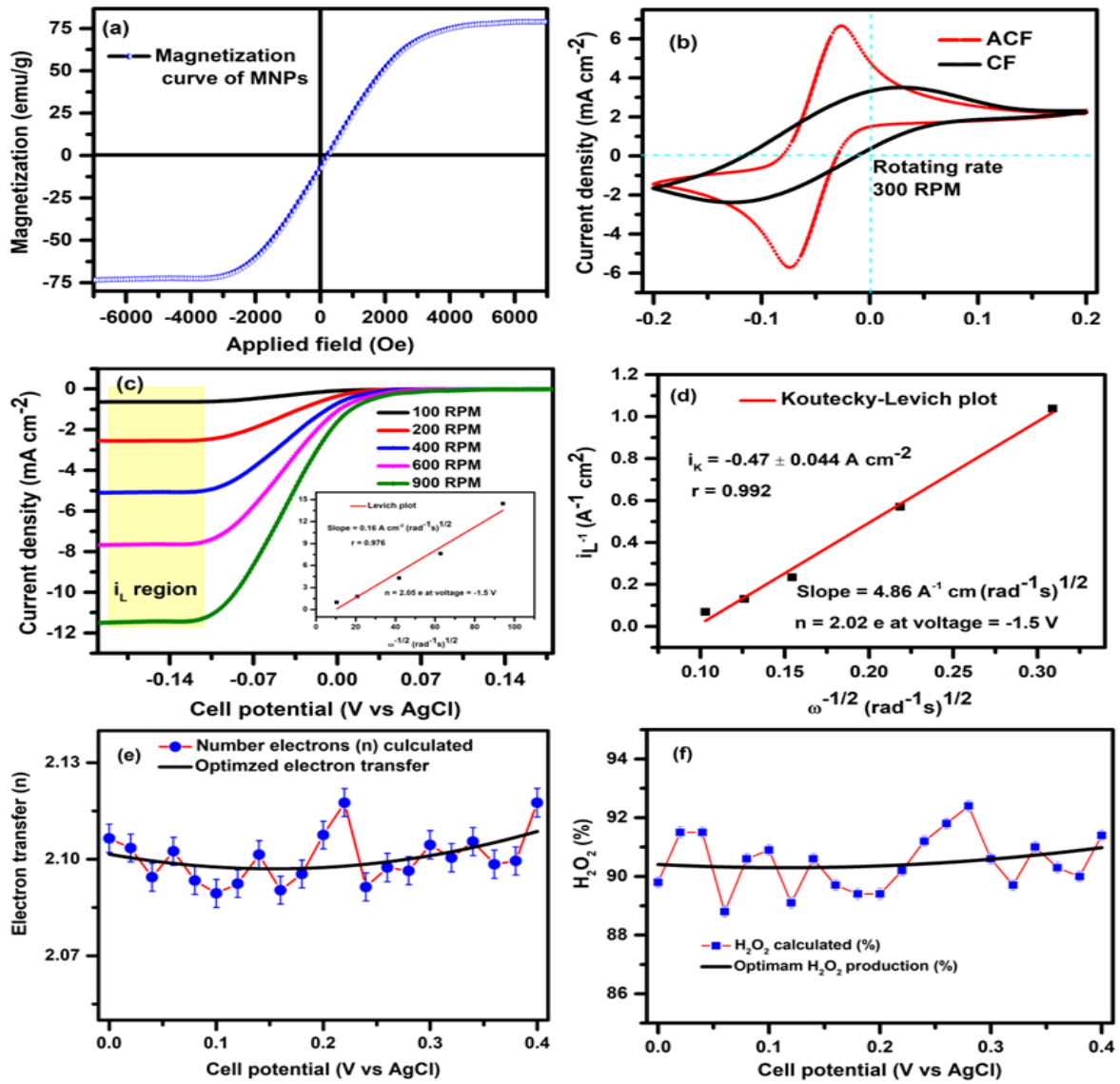

Figure 4.4: *Magnetization and Cyclic voltammetry*

Magnetization property of MNPs (a), Cyclic voltammetry (CV) of pristine CF and ACF (b), Effect of rotating speed of the electrode on ACF (c); Koutecky-Levich plot (d), number of electrons transferred (e) and estimation of percentage H_2O_2 production (f), at scan rate of 10 mVs^{-1}, potential scan of -0.2 to +02 V, pH 4 and electrolyte (Na_2SO_4, 10 mg L^{-1})

4.3.3. EF Oxidation Analysis of CR

The degradation performance of pristine CF and ACF as a cathode and SS as anode were evaluated. The stainless-steel anode could facilitate dissolution of MNPs as homogeneous Fe^{2+} catalyst to the solution and enhance the reaction rates of CR degradation. The reactor with 10 mg L^{-1} of initial CR concentration and 0.2 g of the homogeneous catalyst (MNPs) was adjusted

to pH 3 and operated at applied voltage of 4.5 V. The EF catalytic degradation efficiency of the prepared cathodes for CR degradation were determined based on the change of the maximum absorbance at 485 nm Fig. 4.5. Using UV-Vis analysis, the absorption band of CR continuously decreased with time, and finally the peak disappeared [232]. Fig. 4.5a showed the catalytic (with MNPs) and non-catalytic (without MNPs) degradation of CR using the cathodes (pristine CF and ACF). Over 40-min. of EF reaction, the removal efficiency of non-catalytic, pristine CF and ACF were 16.2 ± 1.8%, 47.5 ± 2.4% and 94.3 ± 1.7% respectively. Fig. 4.5b and d were the EF stack cell experimental setup before CR degradation and after degradation. The removal efficiency of ACF was 2 times higher than pristine CF and 6 times higher than the non-catalyzed CR degradation (Fig. 4.5c).

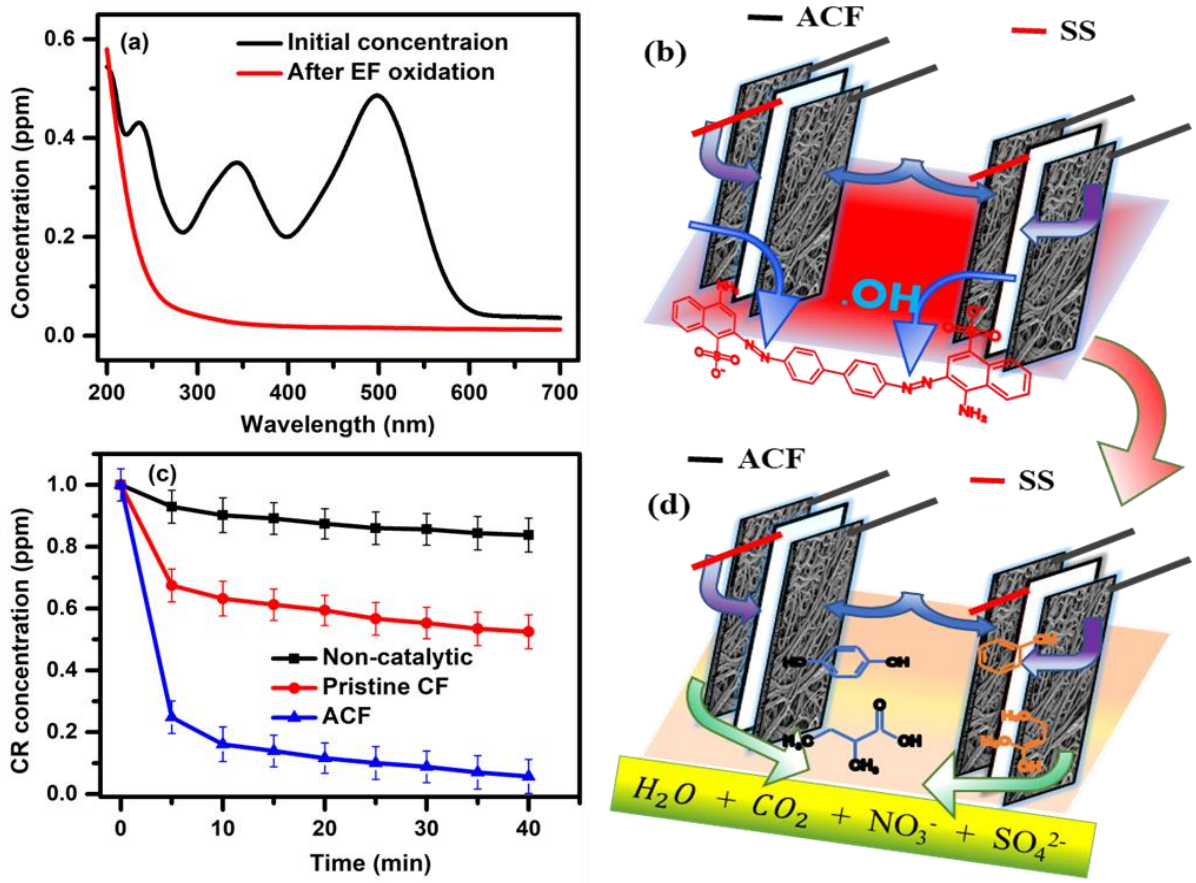

Figure 4.5: *Spectroscopy analysis before and after CR degradation*

Spectroscopy analysis before and after CR degradation (a), degradation kinetics (c), cell configuration before EF (b) and after EF oxidation (d) at operating conditions (pH, 3), applied potential (4.5 V), catalyst dose (0.2 g), initial CR concentration (10 mg L^{-1}) and electrolyte (Na_2SO_4, 10 mg L^{-1}).

The higher degradation efficiency of the ACF cathode could be due to its active species on its surface. These oxygen containing active species facilitate ease transfer of electrons to and from the cathode surface [233]. The ease transfer of electrons to and from the active cathode surface led to higher generation of current density. Similarly, changing the surface chemistry of the material contributes to affinity of wettability that triggers rapid diffusion of dissolved oxygen. The diffusion of oxygen to the surface of ACF facilitate selectively to 2e-ORR and subsequently generate H_2O_2 [229]. Depending on the morphology of the MNPs on the CF or ACF electrode, the EF process showed different performance in CR degradation. In fact, the CR degradation relied on the particle size and iron content of MNPs. The iron content of MNPs is directly related to the amount of iron ions (Fe^{2+}) released into bulk solution, bringing about homogenous EF oxidation which would subsequently produce higher H_2O_2 on the surface of the ACF.

4.3.4. Effects of Operational Parameters on CR Degradation

The interaction between the Fenton's reagent and recycling of Fe^{3+}/Fe^{2+} during EF oxidation are mainly affected by pH values. In fact, at more acidic conditions (pH<3), a lower removal efficiency is expected due to the formation of iron-water ligand complexes reacting with H_2O_2; if H_2O_2 is surrounded by many protons, a stable molecule called oxonium ion can be formed to hinder generation of ·OH radicals by reducing the reactive affinity of H_2O_2 and Fe^{2+} [208]. The highest catalytic degradation of CR (95.3 ± 3.2%) was observed at acidic medium near pH 3. As the pH value was increased to 6, the removal efficiency quickly dropped to 70.0 ± 2.6%. Interestingly, 94.3 ± 2.4% removal efficiency was achieved at pH 4 (Fig. 4.6a). However, at pH value higher than 4, auto-decomposition of H_2O_2 and formation iron precipitates occurred, eventually leading to the excessive sludge generation, which negatively affects the EF oxidation process. These results were also reported by Sheikhmohammadi *et al.* [186]. After comparing the removal efficiencies of CR by the EF oxidation at pH 3 and 4 and the associated chemical cost for pH adjustment, pH 4 was adopted in further experiment. Above 4 pH value the auto-decomposition of H_2O_2 to H_2O and O_2 leading to less oxidation efficiency.

The performance of the EF oxidation process depends on the applied voltage [90] which is the driving force in electron transfer between the electrodes and the bulk aqueous solution. Herein, the effect of applied voltage on CR oxidation was determined by varying the voltage from 0.5 to 6.5 V. As the applied potential step-up increased from0.5 to 3 V, the CR removal rate also

sharply improved from 77.5 ± 2.1 to 95.7 ± 3.2% (Fig. 4.6b). It was hypothesized that application of a higher voltage would enhance the generation of H_2O_2 and the recycling of Fe^{3+} between Fe^{2+} in the system, resulting in higher degradation efficiency. However, when the applied potential was over 5.5 V, an insignificant increase of CR removal rate (94.7 ± 2 to 97.8 ± 1.4%) was observed. This might be associated to scavenging effects of Fe^{2+} and H_2O_2 for ·OH radicals generated [171,234]. Consequently, 2.5 V of applied voltage was identified as optimal voltage for subsequent experiments. Comparing degradation efficiency and electricity consumption cost 2.5 V was more feasible for electro-Fenton oxidation in this experiment.

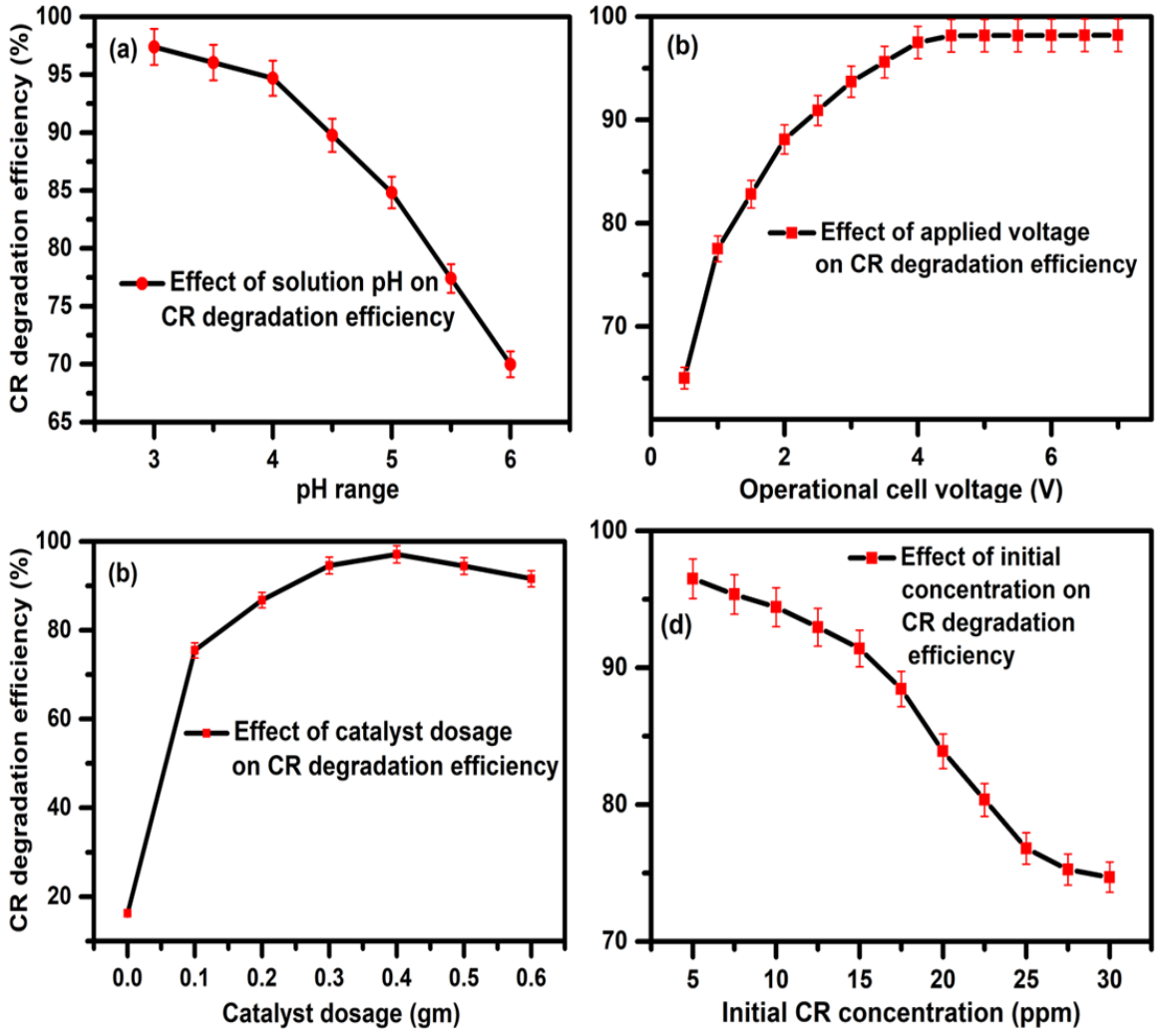

Figure 4.6: *Effect of operational parameters*

Effect of operational parameters on CR degradation: effect of pH (a), effect of applied voltage (b), effect of catalyst dosage (c), and effect of initial CR concentration (d), at electrolyte (Na_2SO_4, 10 mg L^{-1}).

The performance of EF oxidation was also affected by catalyst dosage [180]. The effect of addition of MNPs as homogeneous catalyst into EF system for CR degradation was investigated. When 0.1 g of MNPs was added into the EF system with ACF electrode, the CR removal efficiency dramatically increased to 85.8 ± 1.5% comparing to non-catalyzed system (15.2 ± 1.2%) (Fig. 4.6c). An additional dosage of homogeneous catalyst (0.4 g of MNPs) into the system, the CR degradation efficiency further increased to 96.4 ± 2%. More Fe^{2+} would trigger the rapid generation of H_2O_2 and subsequent ·OH radicals on the cathode surface [200]. The role of homogenous Fe^{2+} ions in the system acted as channel for electron transfer to pull off the H_2O_2 from the active sites of ACF cathode. This pull system contributed for releasing of H_2O_2 to the system and react with Fe^{2+} ion to generate ·OH radicals [200]. However, additional increase of MNPs dose (to 0.5 g or 0.6 g) could not further improve the rate. It was hypothesized that Fe^{2+}, if added excessively, might also consume ·OH radicals (i.e., inhibition effect). The result could also be due to the maximum limit of the active sites of the ACF for H_2O_2 generation. A similar result was also reported [174,201] in the Fenton process for CR degradation. In short, 0.4 g was selected as the optimal dose for MNPs. From the analysis in this study 0.3 g MNPs dosage was enough to facilitate homogeneous EF CR degradation. The degradation of CR relied on particle size and iron content of MNPs as confirmed by FE-SEM and SEM-EDX elemental analysis [165]. Similarly, smaller particles have a higher surface area to volume ratio, which contributed to higher degradation of CR through catalyst-CR molecule interaction.

Lastly, the effect of the initial CR concentration on EF oxidation process was determined. When the initial CR concentration was increased while keeping the other parameters constant, the degradation efficiency declined [91]. As the concentration of CR increased from 5 mg L^{-1} to 20 mg L^{-1}, the degradation efficiency was maintained at above 94 ± 1.5% over 40-min reaction time. However, the removal efficiency deteriorated when the CR concentration was increased to 30 mg L^{-1} (72.7 ± 1.6% removal efficiency) as described in Fig. 4.6d. From the result, it was assumed that all the active sites of MNPs would be occupied if the initial CR concentration was extremely high, resulting in incomplete CR degradation. If it is the case, more MNPs should be added. The EF oxidation process having the operational parameters, which resulted in the CR removal efficiency of > 90% was considered as the optimum. Therefore, 15 mg L^{-1} was used as the initial CR concentration in the subsequent analysis.

4.3.5. Rate Constant and Dominant Oxygen Reactive Species

Using the measured current density (14.5 ± 1.23-mAcm^{-2}) and constants (n (78 e), F (96,485.3 Cmol^{-1}), k_D (0.078 cms^{-1}), A (8.75 cm^2), C^0 (15 mg L^{-1} CR) and V (300 cm^3), the apparent rate constant (k_{app}) at optimal operating conditions (pH, 4), applied potential (2.5 V), catalyst dose (0.3 g) and initial CR concentration (15 mg L^{-1}) was determined (Eqn. 4.14). Therefore, the EF CR degradation followed pseudo-second order rate kinetics with rate constant of 8.78 × 10^{-4} ± 1.72×10^{-5} mol^{-1} cm^3 min^{-1} (0.878 ± 0.017 M^{-1} min^{-1}).

$$k_{app} = \frac{j}{VC^0{}_{CR}nFA - jk_D} \qquad (4.14)$$

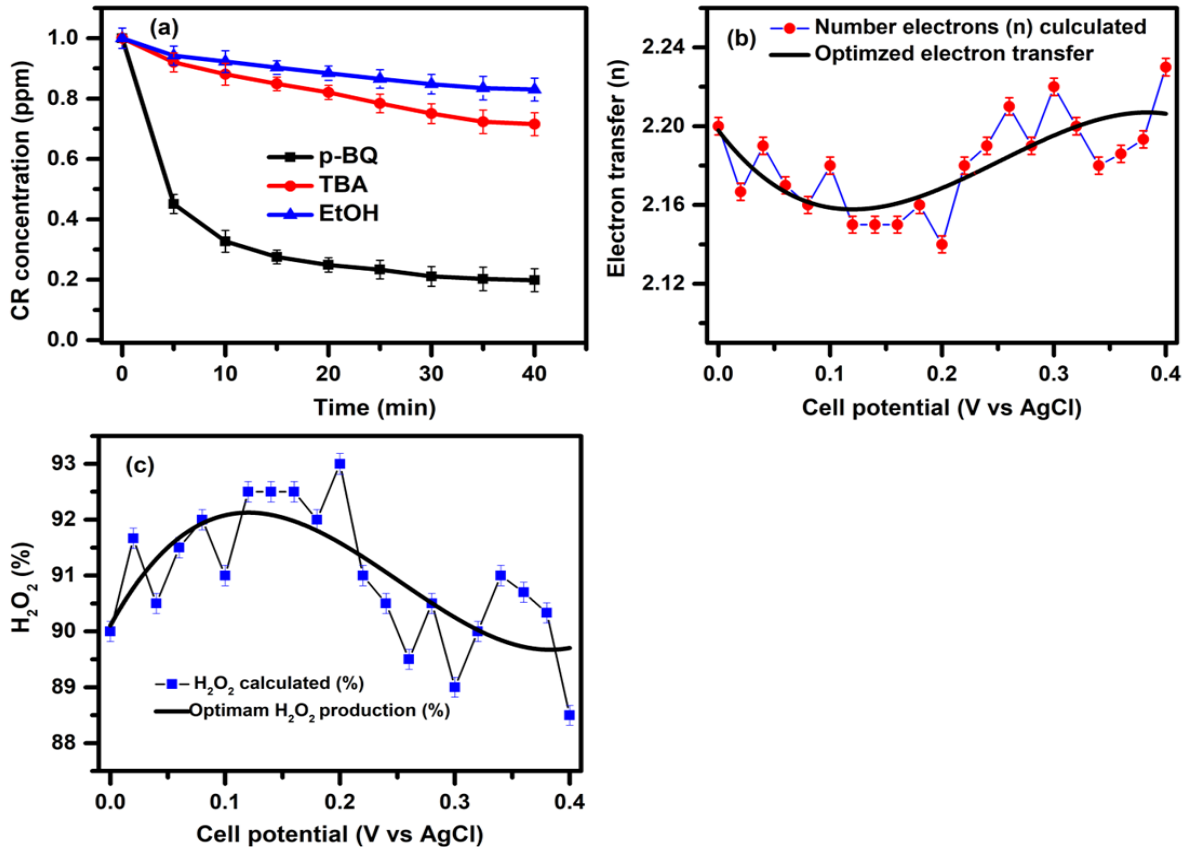

Figure 4.7: *Chemical trapping*

Chemical trapping of ·OH radicals in EF system (a), estimation of average transferred electrons for 2e-ORR (b), estimation of H_2O_2 generation in the system during chemical trapping (c), at operating conditions of chemical quenching (0.25-mol L^{-1}), pH (4), applied potential (2.5 V), catalyst dose (0.3 g), initial CR concentration (15 mg L^{-1}) and electrolyte (Na_2SO_4, 10 mg L^{-1}).

To determine the dominant free reactive oxygen species generated in the system, EF process was applied for oxidizing 15-mg L^{-1} CR in the presence of alcohols and p-benzoquinone (*p*-BQ) for quenching ·OH and superoxide ion ($O_2^{\cdot-}$) radicals, respectively [235,236]. Excess concentration of scavenging chemicals was used to ensure a complete trapping of radials from the bulk solution in the system. As demonstrated in (Fig. 4.7a), the removal efficiency of CR rapidly dropped from 94.3 ± 1.7% to 17 ± 1.2% after the addition of an excess of ethanol concentration (0.25-mol L^{-1}) to the reactor. The 17 ± 1.2% removal efficiency of CR could be attributed to non-radical reaction mechanism such as singlet oxygen, which might generated from the transfer of a single electron through the surface of ACF during EF process [235]. Similarly, an addition of excess concentration of TBA (0.25-mol L^{-1}) to the reacting system, the degradation of CR declined to 28.5% due to less inhibition effect of TBA to ·OH radicals than that of EtOH. The EtOH and TBA quenching analysis indicated that ·OH radicals played a crucial role for CR degradation in EF system.

The number of electrons transferred (2.16 ± 0.02 e) and the approximate H_2O_2 generated (90.0 ± 1.3) were checked in the presence of chemical quenching (Fig. 4.7b & c, respectively), indicating that still the system follows 2e-ORR. However, addition of 0.25-mol L^{-1} of P-BQ to the reacting system resulted in slight change in the CR removal efficiency; 88.3 ± 2.1% was obtained. This result clearly indicates of the role of $O_2^{\cdot-}$ ion radicals would not be significant. Instead, ·OH radicals would be the dominant free reactive oxygen species in the system. Insignificant amounts of superoxide radicals might be formed via the reduction of oxygen on the cathodic surface according to Eqn. 4.15 and 4.16 and consumed for H_2O_2 formation in acidic bulk system (Eqn. 4.17). It was concluded that, the dominant free reactive oxygen species generated in the system were ·OH radicals.

$$O_2 + 2e^- \rightarrow O_2^{\cdot-} \quad (4.15)$$

$$\mathrm{Fe(II)} + O_2 \rightarrow \mathrm{Fe(II)} + O_2^{\cdot-} \quad (4.16)$$

$$O_2^{\cdot-} + 2H^+ \rightarrow H_2O_2 + O_2 \quad (4.17)$$

4.3.6. TOC Removal and Energy Consumption

The extent of CR mineralization was measured based on presence of total organic carbon (TOC) in the treated solution. The values of TOC have been related to the total organic carbon of the CR solution. The TOC analysis at different time intervals indicated the degrees of mineralization [202]. Performing at optimal operating parameters, a reasonable TOC removal of about 54.6 ± 2.3% was observed over 40-min., while the color removal was 94.3 ± 1.7%. However, when the reaction time was increased to 120-min., the mineralization efficiency could reach 82.7 ± 2.8% with the complete color removal, confirming that the chromophore of CR, i.e., azo bond (-N=N-) would be easier to destroy than an aromatic ring (Fig. 4.8a). EF mineralization of high molecular weight dyes such as CR (MW-697 g mol^{-1}) over short time reaction was incapable due to the confinement of a quite stable benzene ring molecules that could not break apart in the system.

The primary cost associated with the EF process is incurred by electricity and its consumption should be analyzed. The degradation rate of CR at different cell potential (0.5-6.5 V) is related to energy consumption ($kWhm^{-3}$) of the system [237]. An innovative and energy efficient EF system was required to minimize the cost. When the highest potential was applied (6.5 V), a satisfactory CR mineralization (i.e., 61 ± 3% TOC removal) could be achieved within over 40-min. However, when the applied potential was lowered to 2.5 V, the extent of the CR mineralization slightly decreased to 55 ± 2.5%. Considering the electrical energy consumption calculation, 37 ± 2 $kWhm^{-3}$ energy consumption of 6.5 V applied potential and 24 ± 1.5 $kWhm^{-3}$ energy consumption of 2.5 V applied potential were determined. Comparing the above applied voltages in terms of their energy consumption and CR mineralization efficiency, the latter (2.5 V) would be considered as the optimal applied cell potential for CR mineralization. Therefore, the applied voltage of 2.5 V was an efficient energy and cost effective to mineralize CR to approximately 82.7 ± 2.8% over 120-min. While CR was degrading at an applied potential of 2.5 V, 14.5 ± 3 $mAcm^{-2}$ current density was measured and the mineralization current density efficiency of about 58 ± 2% was estimated.

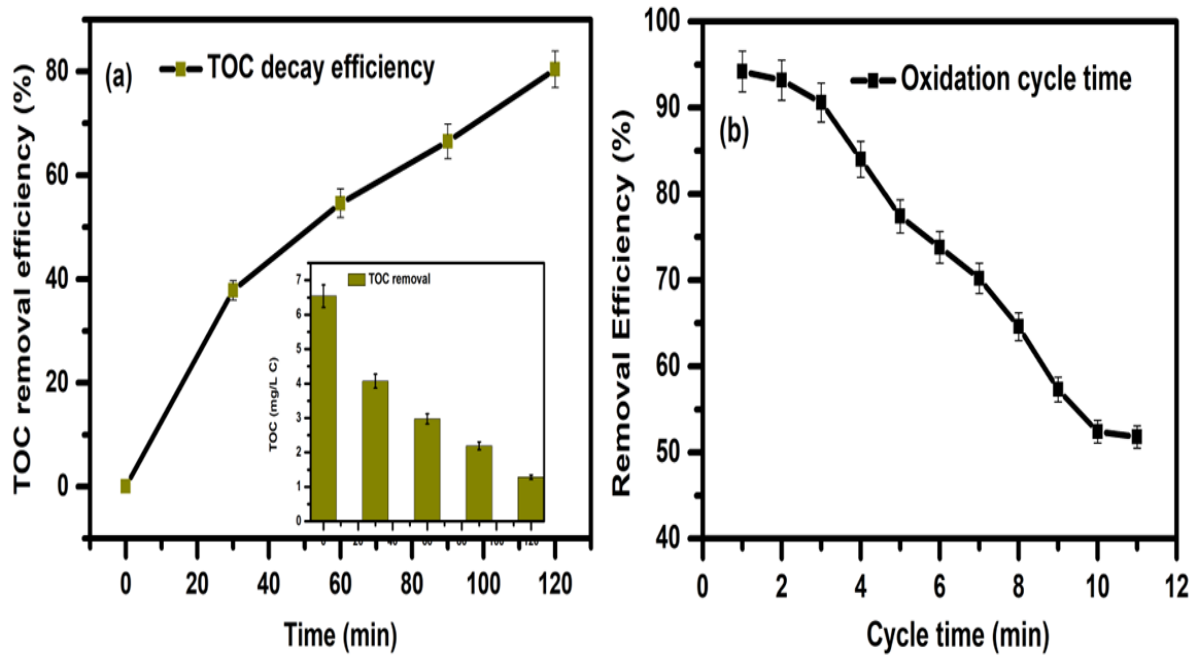

Figure 4.8: *Mineralization efficiency and reusability of the cathode*

CR mineralization efficiency (a), reusability and stability of the cathode as the catalysts (MNPs) for several cycles (b), at optimal operating conditions (pH, 4), applied potential (2.5 V), catalyst dose (0.3 g), initial CR concentration (15 mg L^{-1}) and electrolyte (Na_2SO_4, 10 mg L^{-1}).

4.3.7. Stability and Reusability

Stability and reusability analysis are the most significant measurements to predict the functionality of the materials (i.e., MNPs and ACF) over repeated application (Fig. 4.8b). These parametric analyses were helpful in determining the extent loss of an active species. After ten cycles of EF CR degradation, the catalysts (MNPs) were separated from the solution reaction by an external magnet. To check the dissolved iron quantity in the reaction solution, ICP-OES analysis was performed, and 0.021 mg L^{-1} iron residuals (98.4 ± 1.3% recovery) were quantified which are negligible compared to 0.3 g initially added. Negligible amount of iron residuals in the reacting solution indicated that the magnetic nature of MNPs were not altered and showed stability over ten cycles of EF CR degradation. The crystalline characteristic peaks of MNPs disappeared compared to XRD result before degradation as shown by XRD analysis in Fig. 4.9a (blue). Only the major characteristic peaks at 20.4°, 36.7° and 63.3° that correspond to (111), (311) and (440) lattice planes [203] were determined which indicated the MNPs crystal deformation. Although the Fe-O vibrational mode with smooth curve was observed at

approximately 500-600 cm^{-1}, the FT-IR result of MNPs showed a deformed structure comparing the FT-IR result before used (Fig. 4.9b, blue). Thus, the gradual decline of CR degradation efficiency over 10 cycles (54.3 ± 2.8%), could be due to the deformation crystalline structure of MNPs. Although the iron-based catalysts have good degradation efficiency, they showed poor reusability due to the crystalline structural deformation [28].

After ten cycles of ACF cathode utility, the amorphous nature of carbon at 25.3° was observed, [222] (Fig. 4.9b, red). The narrow peak of the ACF that observed before degradation process were diminished, indicating that the crystal structure of the ACF was altered and the active species (oxygen containing functional groups) were eroded. Besides the FT-IR analysis was performed to locate the pertained oxygen containing functional groups on ACF surface. The functional groups that were at 1655 cm^{-1} (-C=O-OH) and 1554 cm^{-1} (-C=O) on ACF before the experiment were disappeared as seen in Fig. 4.9b (red). The broad and loos absorption peaks of the material suggested that the surface-active groups worn-out through the degradation process. Similarly, the CV curve of ACF showed -1.3 ± 0.36-$mAcm^{-2}$ cathodic peak for 2e-ORR and 0.9 ± 0.037-$mAcm^{-2}$ anodic peak for water oxidation (Fig. 4.9c, red).

The LSV analysis also showed 1.4 ± 0.25-$mAcm^{-2}$ of water oxidation reaction on the system (Fig. 4.9d, red). The results indicated that the ACF cathode activity for 2e-ORR was declined and confirmed the structural change of the cathode (i.e., depletion of active oxygen containing functional groups from the cathode surface). Thus, after ten cycles of CR degradation, 54.3 ± 2.8% efficiency was observed over 40-min. under the optimal operating conditions. Generally, the strong reactive species generated gradually lowering the selectivity of ACF for 2e-ORR.

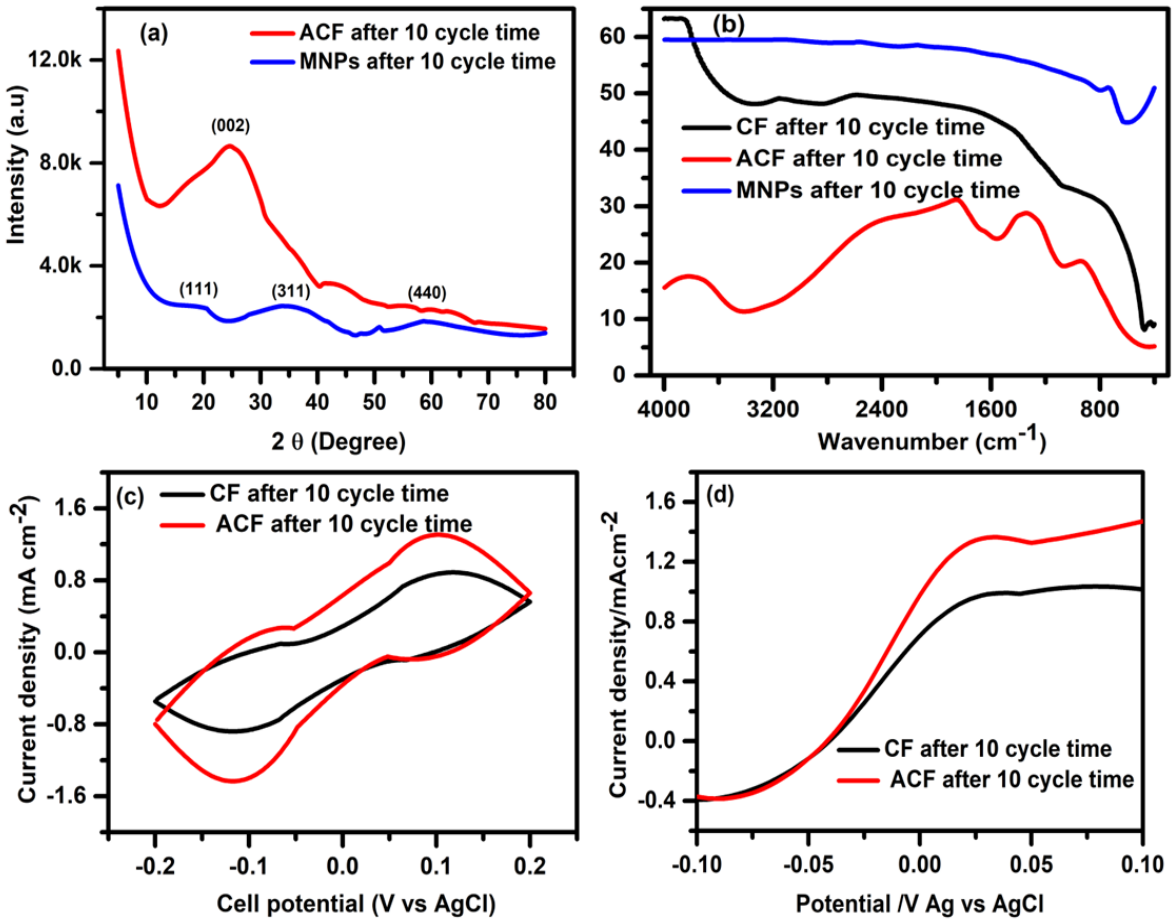

Figure 4.9: *Characterization after usage*

XRD diffraction patterns of ACF (red) and MNPs (blue) (a), FT-IR spectral vibrations of pristine CF (black), ACF (red) and MNPs (blue) (b), CV and LSV of pristine CF (black) and ACF (red) at scan rate of 10 mVs^{-1}, potential scan of -0.2 to +0.2 V, pH 4 and electrolyte (Na_2SO_4, 10 mg L^{-1}). All analyses were performed after ten cycles of analysis.

4.3.8. Degradation Mechanisms and Intermediate Products

As aforementioned, CR could not be completely mineralized by the EF oxidation although the CR color could disappear over 40-min. This indicates destruction of the azo group (-N=N-) of CR and release of the intermediates formed by the ·OH radicals attack on the parent pollutant [204]. However, extending the reaction time to 120-min. contributed to the release of intermediate byproducts. Eventually, the intermediates products were converted to inorganic ions through a continuous exposure to ·OH radicals [46,204]. To understand how the degradation mechanism and the possible degradation pathways of the intermediates in the system, LC-MS and ICS techniques were employed [238]. Noting that the degradation

intermediates might be either aromatic with different substituents or aliphatic organic compounds (Appendix 4.5). Thus, the possible and dominant reaction intermediate products of CR with their chemical structures were proposed in Fig. 4.10. Using LC-MS, the identified reaction products are listed along with their *m/z* values and molecular structures in Appendix 4.6. After 120-min. of EF CR degradation, 6.3 ± 0.2 mg L^{-1} NO_3^- concentration and 3.46 ± 0.1 mg L^{-1} SO_4^{2-} concentration were determined. About 82.7 ± 2.8% of the nitrogen and sulfur atoms contained by CR were oxidized to be released into bulk water as described in Appendix 4.7. The material balance calculations and experimental results of CR degradation were demonstrated in Appendix 4.8.

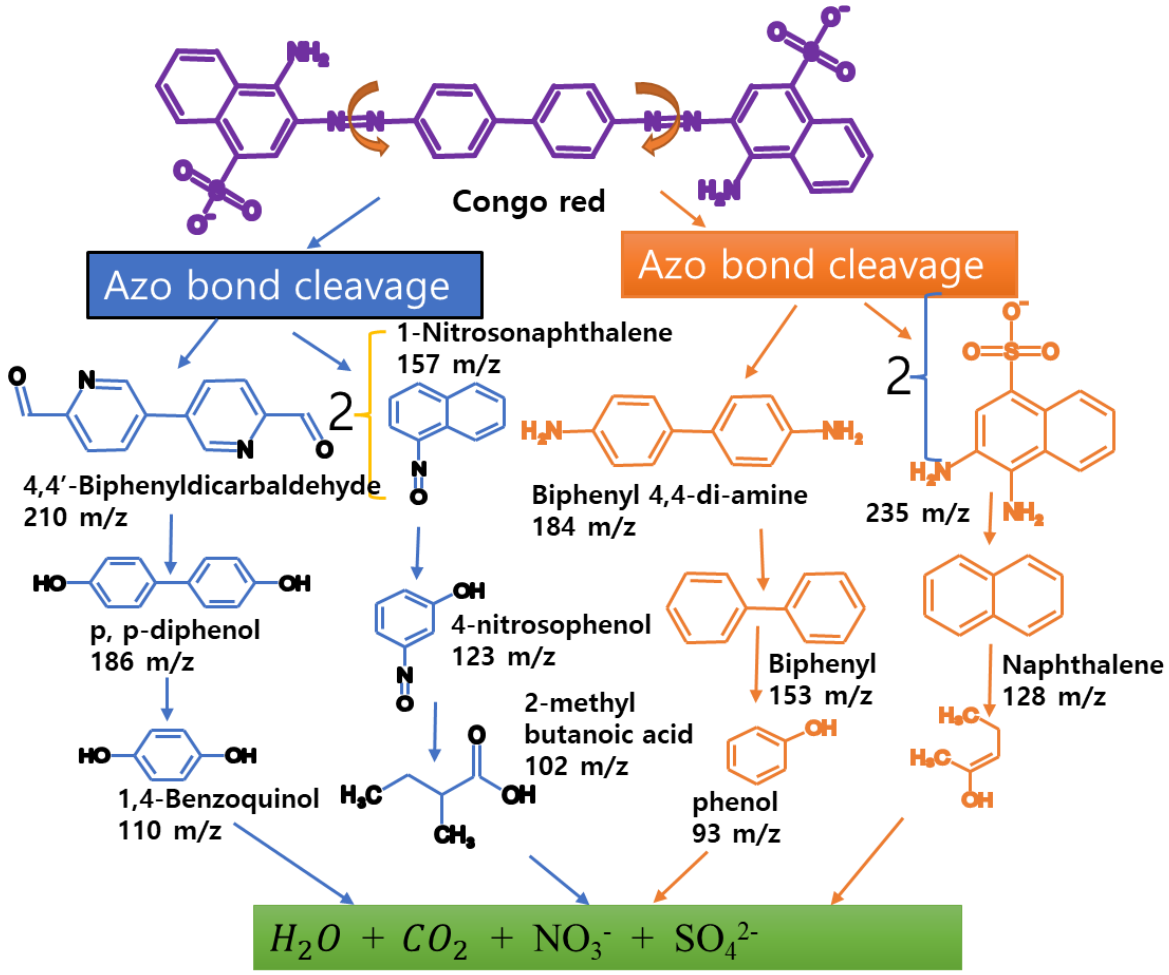

Figure 4.10: *Possible fate of CR degradation*

Possible fate of CR degradation using ACF cathode in EF process, at optimal operating conditions (pH, 4), applied potential (2.5 V), catalyst dose (0.3 g), initial CR concentration (15 mg L^{-1}) and electrolyte (Na_2SO_4, 10 mg L^{-1}) and 120-min.

4.3.9. Assessment the Coupled System for Real Textile Wastewater

Mostly, textile wastewater contains acids, reactive and disperse dyes that are used in the textile industry. The frequently used dyes in textile industry are Congo red (CR), Methylene blue (MB), Acid orange 7 (AO7) and Methyl orange (MO), Table 4.1). To assess the suitability of the coupled system for real textile wastewater, 300 ± 7.5 mL of real sewage wastewater was collected from the effluent of secondary clarifier (Sewage Wastewater Center, Seoul, Korea Table 4.2). After characterization, the solution was diluted 10 times and mixed with CR (15 ± 0.1 mg L^{-1}), MB (15 ± 0.75 mg L^{-1}), and AO7 (10 ± 0.5 mg L^{-1}) solution, the pH was adjusted to 4 and let it to EF degradation for 120-min. 2 mL of the treated wastewater was harvested at the end of EF degradation for further analysis.

EF degradation assessment for different dye containing sewage wastewater was performed to confirm the potential application for real textile wastewater treatment [8,201,206]. Following similar procedures and mechanisms to CR degradation mentioned, two stacks of ACF-SS-ACF in which ACF used as cathode and SS as anode (Fig. 4.11a & b). In real textile wastewater oxidation assessment, the effective working volume of the reactor was 300-mL and adjusted to pH value of 4. The reactor was employed with the applied voltage of 2.5 V, catalyst dosage of 0.3 g and the total dye concentration of 60 mg L^{-1} as optimum operating conditions. As demonstrated in Fig. 4.12a & b, the initial concentration of individual dyes and the mixture of the wastewater was analyzed at their maximum absorbance. However, while mixing with real sewage wastewater, the absorbance peak of each dye was not clear compared to individual absorbance peaks. This could be due to shielding effect of the wastewater matrix on chromophores. After 120-min. EF degradation, 3-mL of samples were taken and filtered for UV-Vis, TOC, LC-Ms and IC analysis. As shown in the Fig. 4.12c, the UV-Vis of absorption peaks of each dye diminished, indicating that the chromophore bonds were broken apart and the maximum degradation efficiency for CR, MB, and AO II were calculated to be 72.3 ± 1.7%, 81.8 ± 2.1% and 92.7 ± 1.8% respectively [203,209,238] and presented in Table 4.3. Increasing the concentration of inorganic ions (NO_3^- and SO_4^{2-}, IC analysis) and decreasing TOC, confirming the mixture of real textile wastewater was degraded into inorganic compounds, CO_2, and H_2O, indicating that the proposed system was capable of degrading and mineralizing complex matrix of textile wastewater.

Table 4.1: Molecular structure and property of CR, MB, AO7 and MO.

Dye	***Molar mass (g mol^{-1})***	***Formula***	***λ_{max} (nm)***
Congo red	696.66	$C_{32}H_{22}N_6Na_2O_6S_2$	492
Methylene blue	319.85	$C_{16}H_{18}ClN_3S$	665
Acid orange II	350.33	$C_{16}H_{11}N_2NaO_4S$	485
Methylene orange	327.34	$C_{14}H_{14}N_3NaO_3S$	510

Table 4.2: Characteristics of real wastewater

Parameter	**Measured values**
pH	6.1 ± 0.5
COD (mg O_2 L^{-1})	3,264 ± 163.2
TOC (mg O_2 L^{-1})	287 ± 14.4
Total Nitrogen (mg L^{-1})	45 ± 2.8
Congo red (mg L^{-1})	15 ± 0.1
Methylene blue (mg L^{-1})	15 ± 0.8
Acid orange 7 (mg L^{-1})	10 ± 0.5
TDS (mg L^{-1})	612 ± 30.6
TSS (mg L^{-1})	246 ± 12.3
NO_3^--N (mg L^{-1})	25 ± 1.3
SO_4^{2-} (mg L^{-1})	105 ± 5.3
NH_4^+-N (mg L^{-1})	22.5 ± 1.1

Table 4.3: Characteristics of real wastewater after EF degradation.

Parameter	Measured values
pH	5.3 ± 0.5
COD (mg O_2 L^{-1})	913 ± 22.8
TOC (mg O_2 L^{-1})	80.36 ± 2
Total Nitrogen (mg L^{-1})	12 ± 0.3
Congo red (mg L^{-1})	5 ± 0.1
Methylene blue (mgL^{-1})	4.2 ± 0.1
Acid orange 7 (mg L^{-1})	3.5 ± 0.1
TDS (mg L^{-1})	171.4 ± 4.3
TSS (mg L^{-1})	68.89 ± 1.7
NO_3^--N (mg L^{-1})	65 ± 3.3
SO_4^{2-} (mg L^{-1})	155 ± 6.5
NH_4^+-N (mg L^{-1})	47.4 ± 2.3

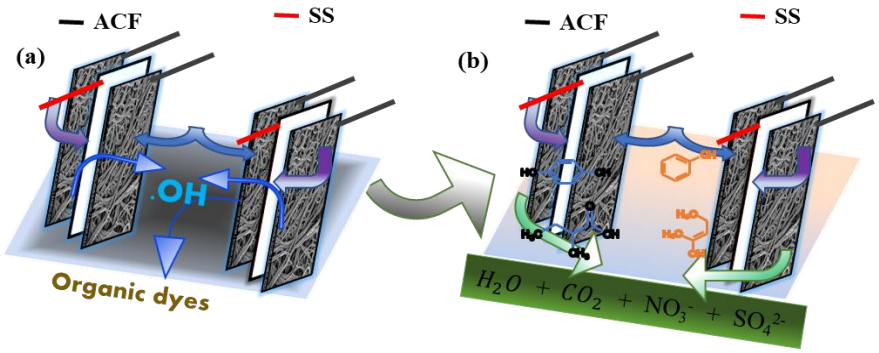

Figure 4.11: *Experimental set-up, cell configuration*

Experimental set-up, cell configuration (ACF-SS-ACF~ACF-SS-ACF) before EF (a) and after EF oxidation (b) at operating conditions (pH, 3), applied potential (4.5 V), catalyst dose (0.2 g), initial CR concentration (10 mg L^{-1}) and electrolyte (Na_2SO_4, 10 mg L^{-1}).

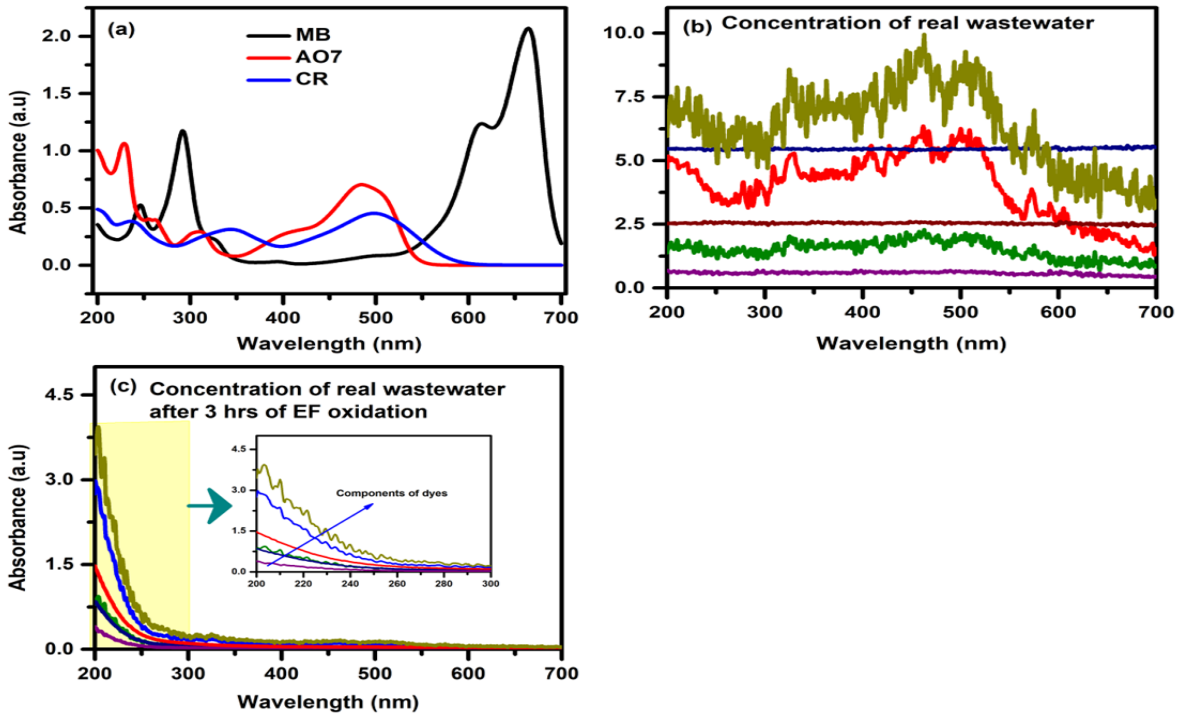

Figure 4.12: *Application on real textile wastewater treatment*

Application of carboxyl group saturated CF cathode and size controlled MNPs EF oxidation for real textile wastewater treatment. Spectroscopic analysis of model contaminants (CR, MB and AO7) (a); Real textile wastewater before oxidation (b) and after oxidation of real textile wastewater (c) at operating conditions of (pH, 4), applied potential (2.5 V), catalyst dose (0.3 g), initial dye concentration (CR = 15 ± 0.10, MB = 15 ± 0.75 and AO7 = 10 ± 0.5 mg L^{-1}) and electrolyte (Na_2SO_4, 10 mg L^{-1}).

4.4. Summery

Chapter 4 concludes that Size-controlled MNPs were synthesized from iron sulfate precursors, carbon felt was activated to form surface carbonyl functional groups (-C =O-OH), employing cathode-anode-cathode stacks of electrodes, electro-Fenton reaction system was developed, 89 ± 3.1% H_2O_2 generation was determined using two electron oxygen reduction reaction and over 40-min, 94.3 ± 1.7% of Congo red was removed with 0.878 ± 0.017 M^{-1} min^{-1} of rate constant.

CHAPTER 5

5. HETEROGENEOUS EF METHYLENE BLUE DEGRADATION

5.1. INTRODUCTION

Significant challenge faced worldwide to ensure adequate water quality status and healthy ecosystems, where the large number of water bodies is contaminated by organic chemicals and pathogens. Most textile industries are water-intensive and produce large amounts of colored wastewater. Colored wastewater is generated due to the use of organic dyes, which are often intentionally designed to resist photochemical and biological processes [46,226]. Treatment of such industrial wastewater is a challenging task since dyes are not easily degradable. Therefore, if discharged into water environment without proper treatment, synthetic dyes may persist in the aquatic environment and result in toxic and mutagenic by-products via auto-oxidation [70,215]. Dyes are colored aromatic organic compounds that absorb light and impart color to the visible region. More than 100,000 commercial dyes have been reported worldwide. Dyes are applied to the substrates to give permanent color, which can resist fading upon exposure to water, light, oxidizing agents, sweat, and microbial attack [239].

Due to these advantages, various dyes are used in different industries such as textiles, food, rubber, printing, cosmetics, medicine, plastic, concrete, and the paper industry for multiple purposes. These industries generate a tremendous amount of wastewater containing carcinogenic and toxic dyes that pollute water, which becomes unfit for human consumption [239,240]. The most common textile dye is methylene blue (MB), which is an aromatic heterocyclic basic dye. it is a well-known cationic and primary thiazine dye with a molecular formula of $C_{16}H_{18}N_3ClS$, having λ_{max} of 663 nm [240]. It is highly water-soluble, and thus forms a stable solution with water at room temperature. MB comes under the class of polymethine dye with an amino autochrome unit and is a positively charged compound which is used for coloring paper, cotton, silk, wool and reported to cause several risks to human health, such as eye, respiratory, digestive, and mental disorders. Iron-based EF for degradation of textile organic dye effluents is an eco-friendly route due to their narrow bandgap and electron

donor behavior. However, the dissolved iron content of these iron-based catalysts is relatively high, which propels the research community to develop alternative materials that are cost-effective and minimize sludge formation. In this regard, carbon felt composite electrodes have attracted much attention owing to their good electrical conductivity, high surface area to volume ratio and outstanding oxygen reduction activity, low bandgap, and excellent durability. They could display by interconversion of Fe^{2+} and Fe^{3+} for the elimination of organic dye effluents through EF treatment.

To minimize the problem, efficient treatments systems are required to treat water and wastewater before discharge into the environment, reuse, or human consumption. In this frame, advanced oxidation processes (AOPs) are often employed to destroy recalcitrant organic dyes using hydroxyl radicals (·OH) and enhance their biodegradability [91,93,208]. Recently, electrochemical advanced oxidation processes (EAOPs) have gained attention for their efficient degradation of recalcitrant organic dye contaminants in industrial wastewaters [69,239,241]. Electro-Fenton (EF) oxidation is an emerging treatment technology for water and wastewater treatment. It is one of the EAOPs that uses *in situ* spontaneously generated hydrogen peroxide using a source of Fenton reagent. The main advantages of these processes are (1) better cost-benefit ratio, requiring less maintenance than other processes; (2) good performance for the degradation of pollutants in synthetic or industrial effluent, (3) consumption of small quantities of chemicals (or none, depending on the water matrix), (4) free of sludge generation, (5) versatility, (6) non-selectivity character, and (7) amenability to automation maintaining high energy efficiency.

In general, the efficiency of EF oxidation is dependent on cathodic material and its surface morphology which determine the electron transfer within the bulk solution [116]. The right choice of cathodic material with appropriate morphology and structure, i.e. high specific surface area, high structural stability and active sites available for reaction [6], is the primary requirements for the system [104,216]. Despite its less wettability and instability in electrochemical degradation, carbon felt (CF) has been used as cathodic material in the EF oxidation process because it has a high specific surface area, good electrical conductivity and biocompatibility and costs less [212]. To enhance the hydrophilicity and electrochemical redox reactivity, the surface of CF has been modified using inorganic materials such as Fe_3O_4 [36,212], $FeVO_4$ [122], $ZnO\text{-}CeO_2$ [242], and $CoFe_2O_4$ [243] or using carbon-based materials, e.g., activated carbon (AC), carbon nanotubes (CNTs) and graphene [197].

Magnetite nanoparticles and CNTs have been widely used as an interfacial modifier for cathodic material due to their high specific surface area, high electrochemical conductivity and pore structure which provides many active sites for electrochemical reactions [244]. Carbon felt is a lightweight and flexible material with multi-porous structure that can serve as a scaffold for CNTs and Fe_3O_4, which has a higher electro-catalytic activity for oxygen reduction reaction (ORR). However, integrating the modifiers onto the CF surface to form stable multi-layered networks [215,245] is challenging. Li *et al*. [246] synthesized CNT/CF hybrid composite by electro-phoretically depositing CNTs on the surface of CFs to enhance wettability and tensile strength of CFs. By modifying CFs with exfoliated graphene oxide (GO), Gao *et al*. [90] could *in situ* generate H_2O_2 and increase the ·OH yield, eventually resulting in the enhancement of the ORR capacity of CF. It seems that the carbon-based surface modifier simultaneously reduces the electron transfer resistance and enhances the catalytic molecular oxygen reduction on the surface of CF [198]. Yu *et al*. [98] developed hierarchically porous-carbon-modified AC fiber (HPC-ACF cathode) for ORR process and could increase H_2O_2 generation from 111.8 mg L^{-1} to 160.4 mg L^{-1} at pH 3 by increasing current density from 16 mA cm^{-2} to 24 mA cm^{-2}. Pristine CF cathode has not been widly applied for the degradation of organic dyes without its surface modification due to its electrochemical instability and low degradation efficiency. Thus, the interfacial surface of CF was modified and then the effects of pH, applied voltage and initial concentration on MB degradation were investigated.

In this study, (1) CF was soaked into acid solution chemically activated and then coated with magnetite (Fe_3O_4) nanoparticles (MNPs) and activated CNTs to form a cross-link channels on the surface. (2) Different cathodes, such as CNT/ACF, Fe_3O_4/ACF and Fe_3O_4/CNT/ACF were, then, synthesized using the activated CF and characterized. to be used later as composite electrodes for methylene blue (MB) degradation in EF system.

5.2. Materials and Methods

5.2.1. Chemicals and Materials

All organic and inorganic chemical reagents used in this study were of analytical grade, purchased from Samchun Pure Chemicals (Seoul, Korea), and used as received, i.e., without further purification. $FeCl_3.6H_2O$ (98% purity), $FeSO_4 \cdot 7H_2O$ (99%), MB (85%, Appendix 5.1), Ajax Scientific-E160-0004 iron electrode strip (65 × 25 mm), and CNTs (content of 93% and specific surface area of 1223.7 m^2g^{-1}) were purchased from Sigma-Aldrich (Seoul, Korea).

Polyacrylonitrile-based CF (V207-G-19, thickness: 3 mm, bulk density: 0.12–0.14 g cm^{-3}, C content: > 99.67%, tensile strength: 0.43 MPa) was obtained from Jin Gu Carbon Material (Seoul, Korea). The solution reagents were prepared with a high-purity water-filtering system (resistivity > 18 MΩ cm at 25 °C; Seoul, Korea). HCl and NaOH solutions were used for initial pH adjustment when an experiment was performed.

5.2.2. Synthesis of MNPs and Cathode Electrodes

Magnetite-nanoparticles were synthesized by a modified co-precipitation method. Briefly, 0.033-mol $FeCl_3 \cdot 6H_2O$ and 0.024-mol $FeSO_4 \cdot 7H_2O$ were dissolved in 50-mL distilled water, respectively, to prepare solution 1 and solution 2. 1-mM HCl and 2-mM NaOH were then added to the prepared solutions 1 and 2, respectively. Each solution was heated to 95 ^{0}C on a hot plate with a magnetic stirrer under an N_2 atmosphere for 30 min. Then, the two solutions were mixed. After the mixture was heated for 30 min, it was added dropwise with NH_4^+ solution (25 mL, 28 wt.%) over a 30-min period to form precipitates. The solution with precipitates was allowed to cool down, and the supernatant was discarded. Then, the remaining was washed several times with distilled water and ethanol. Finally, MNPs were harvested with an external magnet and were dried at 50 ^{0}C overnight.

As proposed by Rahmani *et al*. [222], CF with a surface area of 18 cm^2 (6 × 3 cm^2) was cut and activated in the solution containing 1-mL H_2SO_4 (5% w/w) and 3-mL HNO_3 (5% w/w) in N_2-atmosphere for 30 min. Then, it was soaked in distilled water for 15 min, washed several times, and dried at 105 ^{0}C in an oven overnight to remove inorganic impurities from the surface. Carbon nanotubes of 2 g were purified in 2-M nitric acid using a mechanical stirrer for 16 h. After purification, CNTs were filtered and collected using filter paper, washed several times with DI water until the filtrate pH becomes neutral. Then, the filtered material was dried in an oven at 80 ^{0}C overnight. The dried CNTs (2.5 mg) were mixed with 37.5 mg of polyvinylidene fluoride (15% PVDF (w/w) : 1% CNTs (w/w)) in 20-mL DI water [245,247] and continuously stirred at 80 ^{0}C for 6 h. The resultant CNT/PVDF solution of 5 mL was spread out on the surface of the prepared CF by ultrasound to form CNT/ACF. Besides, 2-mM MNPs were mixed with 10-mL Dimethyl Formamide and continuously stirred at 75 ^{0}C for 5 h. The solution was then dispersed on the surface of ACF and composites of CNT/ACF via ultrasonic treatment for 30 min as described by Xu *et al.* [247]. Finally, the solution was dried in an oven at 105 ^{0}C overnight to form Fe_3O_4/ACF and Fe_3O_4/CNT/ACF.

5.2.3. Characterization of MNPs and Synthesized Electrodes

Powder X-ray diffraction (PXRD, Rigaku (smartlab), Tokyo, Japan) was performed at 40 kV and 30 mA with Cu Kα (λ = 0.154060 nm) radiation over 2θ range of 5–85 with a step of 0.02. Fourier transform-infrared (FT-IR, Thermo Scientific, Nicolet iN10 mx, Madison, USA) in the region of 4000–400 cm^{-1} using KBr pellets and a field emission scanning electron microscope (FE-SEM, SU8010, Hitachi, Japan) with the operating voltage of 15 kV were employed to characterize the surface morphology. Elemental mapping and composition of the synthesized materials were analyzed using energy dispersive X-ray (EDX) spectroscopy (Thermo Scientific, Madison, USA). Electrochemical characterization of CNT/ACF, Fe_3O_4/ACF, and Fe_3O_4/CNT/ACF cathodes were carried out in an electrochemical workstation of cyclic voltammetry (CV, CHI660E, USA) at 25 ^{0}C. The prepared cathodes were used as the working electrode (1.4 × 1 cm^2), while Ag/AgCl and a platinum plate (1 × 4 cm^2) were used as reference electrode and the counter electrode, respectively, in the potentiostat/galvanostat under a potential window of -0.2 to 0.2 V (vs. Ag/AgCl). Further, a scan rate of 10–50 mV s^{-1} and 0.1-M Na_2SO_4 electrolyte with the solution pH of 4 were applied. Similarly, linear sweep voltammetry was applied with a scan range of −0.2 to 0.1 V (vs. Ag/AgCl).

5.2.4. Analytical Methods and Catalytic Performance of Electrodes

Methylene blue degradation was performed in a 400-mL reactor with a working volume of 250-mL. The anode was an iron strip with an effective wettable area of 11.25 cm^2 while the prepared composites were used as cathodes with an effective wettable area of 14 cm^2. The electrodes were separated by 3 cm. The electrodes were washed several times with DI water and ethanol to remove any inorganic contaminant from the surface. The effects of the system pH applied voltage, and initial MB concentration on the degradation performance of the electrodes were investigated in the presence of 10-ppm Na_2SO_4 as electrolyte. Aliquots of samples (4 mL) were taken at a given time interval for UV-spectrophotometry (UV-1800, Shimadzu, Kyoto, Japan) [171] (Eqn. 5.1). The degree of MB mineralization was determined with a TOC-V_{CPH} analyzer (Shimadzu, Kyoto, Japan) and calculated using Eqn. 5.2.

$$Dye\ Removal\ Efficiency\ (\%) = \frac{A_0 - A_t}{A_0} \times 100 \qquad (5.1)$$

$$Mioneralization\ efficiency\ (\%) = \frac{(TOC)_0 - (TOC)_t}{(TOC)_0} \times 100 \qquad (5.2)$$

where A_0 and A_t are the UV absorption measured at time 0 and t, respectively, while $(TOC)_o$ and $(TOC)_t$ are the TOC values (mg C L^{-1}) measured at time 0 and t, respectively.

The residual iron was analyzed by inductively coupled plasma optical emission spectrometry (ICPE-9000, Shimadzu, Kyoto, Japan). The dominant reactive oxygen species were quantified using the chemical quenching method [203]. The intermediates from the MB oxidation were determined by liquid chromatography coupled to mass spectrometry (LC-MS, Shimadzu, Kyoto, Japan), and inorganic by-products of MB were determined using ion chromatography (IC) (ICS-90, Thermo Fisher Scientific, Borken, Germany). Samples were filtered using 0.45-μm filters prior to the LC-MS and IC analyses [28]. Similarly, the mineralization current efficiency (MCE) at a given time t (h) and electrochemical energy consumption (EEC) were calculated using Eqn. 5.3 and Eqn. 5.4 [171] to evaluate the potential cost related with the process.

$$MCE(\%) = \frac{[(TOC)_o - (TOC)_t]\, n\, F\, V}{4.32 \times 10^7\, m\, I\, t} \times 100 \qquad (5.3)$$

$$EEC = \frac{U\, I\, t}{[(TOC)_o - (TOC)_t]V} \qquad (5.4)$$

where n is the stoichiometric number of electrons transferred during mineralization (Eqn. 5.5), provided that the applied electric charge was consumed solely by the mineralization process; F is the Faraday constant (96487 C mol^{-1}); V is the solution volume (L); m is the number of carbon atoms of MB (16); I is the applied current (A); 4.32×10^7 is the conversion factor (3600 s h^{-1} × 12000 mg C mol^{-1}) and U is the cell voltage (V).

$$[C_{16}H_{18}N_3S]^+ + 45\ H_2O \rightarrow 16\ CO_2 + 3\ NO_3^- + SO_4^{2-} + 108\ H^+ + 102e^- \qquad (5.5)$$

Given that the reaction occurred in a batch reactor and the ·OH concentration was maintained constant, the first order and the second order kinetic models were tested using Eqns. 5.6 and 5.7 [40,46,238].

$$ln\left(\frac{A_o}{A_t}\right) = k_1 t \qquad (5.6)$$

$$\frac{1}{A_t} - \frac{1}{Ao} = k_2 t \qquad (5.7)$$

where k_1 (min^{-1}) and k_2 (M^{-1} min^{-1}) are the pseudo-first order and second-order rate constants, respectively. A_0 and A_t are defined above.

5.3. Results and Discussion

Magnetite nanoparticles have been synthesized either from iron chlorides or iron sulfates by co-precipitation method. HCl was added into ferric solution, while NaOH was added into ferrous solutions. Since $Fe(OH)_3$ precipitates in acid (pH~2–4), while $Fe(OH)_2$ precipitates in alkaline condition (pH~7.5–8) [158]. Similarly, the co-precipitation of $Fe(OH)_3$ and $Fe(OH)_2$ in solution, which results in the formation of black crystal precipitates of Fe_3O_4 nanoparticles (i.e., MNPs), is favored at pH ~8–10, which was observed immediately after the addition of concentrate NH_4^+ to the solution. Finally, the MNPs were separated from the solution using an external magnet for further analysis (Fig. 1c, inset). In classical co-precipitation method, the MNPs formation and controlling size of MNPs are challenging. It is because the co-precipitation is performed simply by weighing and mixing of ferrous and ferric salts in a solution and by considering only a few parameters, i.e., ferric to ferrous salt proportion, temperature, mixing rate, and reducing agents [146]. The MNPs nuclei formation and size of MNPs can be controlled by precipitating $Fe(OH)_3$ and $Fe(OH)_2$ in their respective reagents, i.e., HCl and NaOH, respectively, prior to the co-precipitation. Improper preparation of iron salt solution would result in unsought intermediates of $Fe_6(OH)_{12}CO_3$ and a poorly crystalline of $Fe_{10}O_{14}(OH)_2$ [149] that hinder the precipitation process. Besides iron salt precursors and salt precursor charges significantly affect the size of the nanoparticles nuclei formation and precipitation [153,154]. Since the magnetic performance of MNPs depends on the particle size, shape and purity, MNPs of a small size shows clear superparamagnetic behavior [220].

5.3.1. Characterization of MNPs and Composite Cathodes

The crystalline structure and crystallite size of the synthesized MNPs, as shown in Fig. 5.1, were investigated using XRD. Nine distinct diffraction peaks of MNPs were observed at 19.1°, 31.6°, 35.6°, 43.3°, 53.5°, 57.2°, 62.6°, 71.4°, and 74.3°, which were attributed to the (111), (220), (311), (400), (422), (511), (440), (620), and (622) lattice planes, respectively; these peaks correspond to PDF #19–0629 [181]. However, a weak diffraction peak was observed at 2θ of 38.2° representing the (222) lattice plane, and the highest intensity was recorded at 35.6°, which corresponds to the (311) lattice plane.

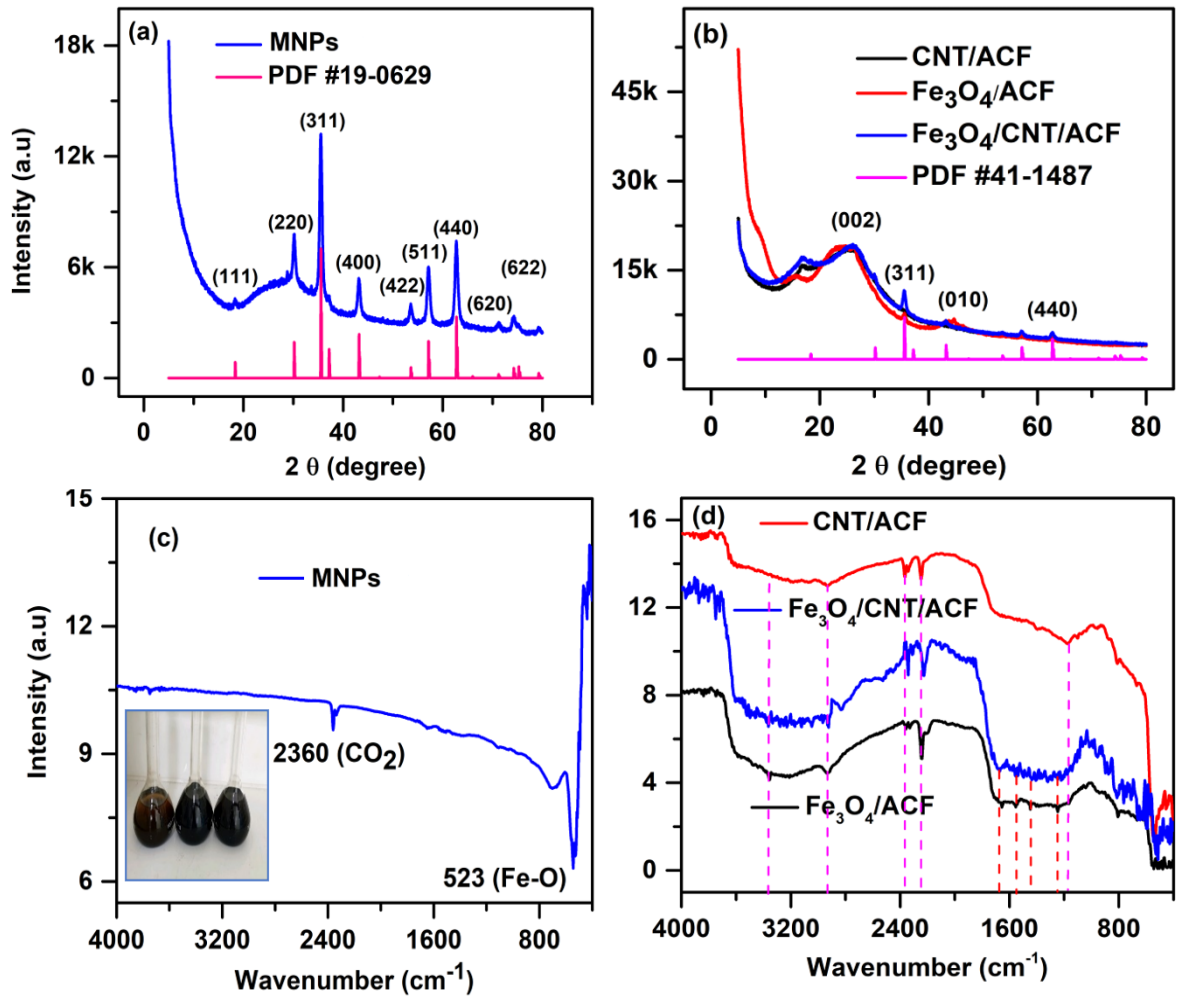

Figure 5.1: *XRD diffraction patterns and FT-IR spectral vibrations*

XRD pattern of MNPs with standard XRD of Fe_3O_4 (a); XRD of three synthesized electrodes (i.e., CNT/ACF, Fe_3O_4/ACF and Fe_3O_4/CNT/ACF) (b); FT-IR spectral vibrations of MNPs (c) and three synthesized electrodes (d). The dot lines represent the position of functional groups formed during the CF activation process.

Using the Debye-Scherrer equation and Bragg's law [248,249], the crystallite size and distance between atomic layers of MNPs were determined to be 10.98 nm and 2.44 Å, respectively, which were in accordance with the standard (PDF #19–0629) [181]. Figure 5.1a confirms the formation of MNPs with a crystal face of spinel structure, and the characteristic peak location reveals a cubic spinel structure of MNPs [215]. The small size of the MNPs can be attributed to the higher anionic strength of SO_4^{2-}. The broad hump peaks near 2θ of 17.5° and 26.7° were due to amorphous graphitic carbon of ACF and CNTs, which was formed during activation processes [222]. The XRD analysis (Fig. 5.1b) showed that the MNP crystallinity was intact in

both the Fe_3O_4/ACF and Fe_3O_4/CNT/ACF precipitates. This might be due to the shielding effect of the interaction between ACF and CNTs and the formation of iron organo-metals. The characteristic diffraction peaks at 35.3° and 62.7° for Fe_3O_4/ACF and Fe_3O_4/CNT/ACF were corresponding to the (311) and (440) crystal planes of Fe_3O_4 with a cubic crystal structure (PDF file #19–0629), respectively [231]. The characteristic diffraction peaks representing the (002) and (010) crystal planes were attributed to the hexagonal graphite structure of CNTs and ACF [250]. This result confirms that MNPs were successfully coated on the surface of the ACF electrodes.

Fourier transform infrared analysis was performed to determine the functional groups present on the surface of MNP-coated electrodes, i.e., Fe_3O_4/ACF, and Fe_3O_4/CNT/ACF. Functional groups such as amine (-NH) and carboxyl (-COOH) groups can enhance the electron transfer by changing the surface properties of the materials [215]. As reported by Mehdizadeh *et al*. [224], the sharp absorption peak observed at approximately 523 cm^{-1} could be assigned to the stretching vibrational mode of the metal-oxygen (Fe-O) bond (Fig. 5.1c). Similarly, the surface activation of CF was confirmed by the appearance of multiple peaks in the distinct ranges of 3016, 1655, 1543, 1246, and 676 cm^{-1}, due to the presence of amines groups (-NH), acrylic acid (C=O), nitro compounds (-NO_2), alcohols (C-OH) and (aliphatic amines) -NH [212,226] respectively, as shown in Fig. 5.1d. The characteristic peaks at 1588–1608 cm^{-1} could be attributed to the C=C stretching vibration of the sp^2 structure of CNTs and ACF [251]. Similarly, the peak at 2240 cm^{-1} for Fe_3O_4/ACF could be due to the bending vibration of H-O-H on the surface of ACF [252]. However, Fe_3O_4/CNT/ACF showed an extra peaks at approximately at 2823, 2449, 2222 and 1670 cm^{-1} which attributed to -CH groups, thiols (S-H), nitriles (C≡N) C=O functional groups, respectively [253]. The peak at 513 cm^{-1} is related to Fe-O vibrations [254], which clearly indicates the successful spreading of Fe_3O_4 on CNTs and ACF. The formation of different functional groups between the valence and conduction bands can facilitate a decrease in the forbidden energy (band) gap for interfacial electron transfer, which allows the synthesis of a suitable functional composite electrode for wastewater treatment.

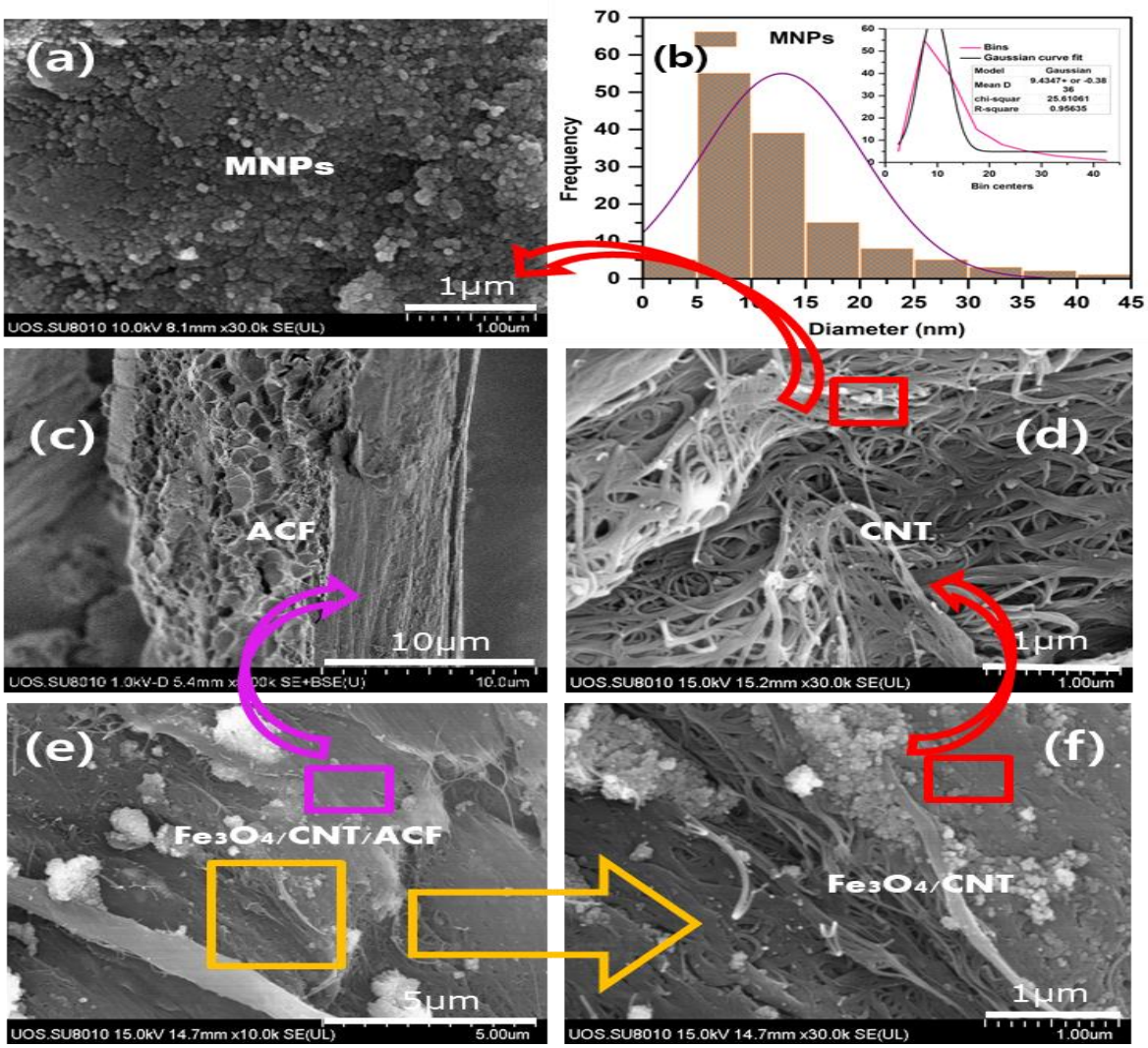

Figure 5.2: *FE-SEM images of MNPs*

FE-SEM images of MNPs (a); Size distribution of MNPs (b); ACF (c); Activated CNT (d); Fe_3O_4/CNT/ACF (e); Fe_3O_4/CNT (f): The starting image of the electrode specified in (e) as Fe_3O_4/CNT/ACF from which Fe_3O_4, CNT and ACF were identified. The rough surface (c) was due to activation of CF.

The morphologies of MNPs and the three synthesized electrodes (i.e., CNT/ACF, Fe_3O_4/ACF, and Fe_3O_4/CNT/ACF) are shown in Fig. 5.2. The average diameter of the MNPs was determined to be 9.43 nm (Fig. 5.2b); the size range of MNPs was 0.2–45 nm. The size distribution could make the surface of the ACF-based electrodes rough and porous during the coating process, and subsequently an excellent two-electron ORR on the surface (Fig. 5.2d). Comparing the surface roughness of the FE-SEM images of pristine CF and CNTs to activated

CF and CNTs in Appendix 5.2, revealed that the surface area of ACF and CNTs was larger than that of CF and CNTs which is crucial for ORR on the surface the electrode.

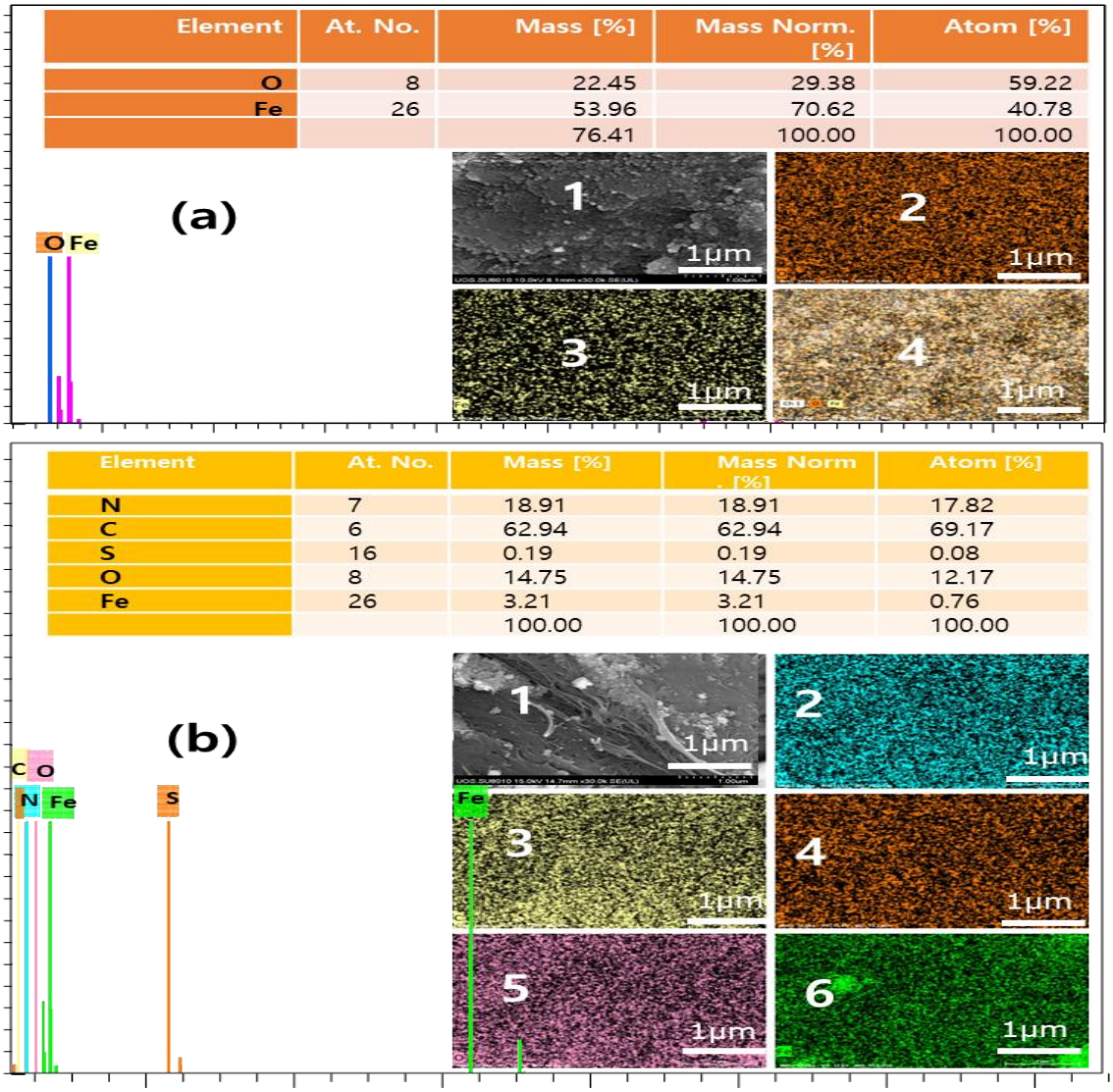

Figure 5.3: *SEM-EDX elemental analysis and mapping*

MNPs (a, 1-4); and Fe_3O_4/CNT/ACF *(b, 1-6) respectively. The elements observed in the analyses are presented in the inset tables. The graph is energy (keV) vs. counts per second (cps/eV).*

The elemental compositions of MNPs and ACF were analyzed using the FE-SEM-EDX technique (Fig. 5.3). The distinctive strong peaks for Fe and O are associated with Fe_3O_4 nanoparticles (Fig. 5.3a). The peaks are consistent with the results reported by Dash *et al*. [228]. As shown in the inset table of Fig. 5.3a, the weight percentages of O and Fe were 25.3% and

74.7%, respectively. In pure MNPs, the weight percentages of O and Fe were 27.6% and 72.4%, respectively, which indicates that the synthesized MNPs were 97.7% pure. Similarly, EDX and elemental mapping analyses also confirmed the presence of the desirable elements on the surface of Fe_3O_4/CNT/ACF. On the surface of CF mainly composed of carbon and nitrogen from acrylonitrile groups, other elements were successfully incorporated during surface activation. As shown in Fig. 5.3b (1–6), N, C, S, O, and Fe were uniformly distributed on the surface, which was confirmed by the FT-IR and XRD results.

5.3.2. Electrochemical Characteristics of Electrodes

The catalytic performance of a cathode is related to its electrochemical characteristics. Cyclic voltammetry and linear sweep voltammetry (LSV) measurements were performed to understand the electrochemical behavior of the three synthesized electrodes in a conventional three-electrode system with O_2-saturated solution or in the one with N_2-saturated solution. The tests were performed with 0.1-M Na_2SO_4 as electrolyte at pH 4 and scan rate of 30 mVs^{-1}. Higher peak values indicated stronger redox activities of the electrodes (anodic and cathodic peaks) (Eqns. 5.8 and 5.9). The cathodes were synthesized to facilitate the path of ORR to be more selective to 2e-ORR than 4e-ORR. Figure 5.4a shows the order of peak current density (mA cm^{-2}) in a reduction reaction at the cathodic surface of the prepared electrodes: CNT/ACF (-6.29 mA cm^{-2}) < Fe_3O_4/ACF (-13.6 mA cm^{-2}) < Fe_3O_4/CNT/ACF (-30 mA cm^{-2}) for the same applied potential range (-0.2 V to + 0.2 V). The higher peak current density of Fe_3O_4/CNT/ACF was attributed to the better electrical conductivity performance of Fe_3O_4 and CNTs. Moreover, higher surface area could be attributed to the highest current density in Fe_3O_4/CNT/ACF, which allowed to expect a good MB degradation by an electro-Fenton system using the cathode.

Anodic reaction $2H_2O \rightarrow O_2 + 2H^+ + 4e^-$ (5.8)

Cathodic reaction $2H^+ + 2e^- + O_2 \rightarrow H_2O_2$ (5.9)

The LSV curve of the prepared cathodes in O_2-saturated solution are presented in Fig. 5.4b. As shown in Fig. 5.4b, the current responses of CNT/ACF and Fe_3O_4/ACF were less than that of Fe_3O_4/CNT/ACF. The highest current response of -30 mA cm^{-2} was achieved by Fe_3O_4/CNT/ACF, indicating that modification of ACF surface by CNTs and Fe_3O_4 together

enhanced the electrochemical activity of the cathode. Moreover, CNTs could provide extra chemical reaction sites which allow the high electrical conductivity of Fe_3O_4 [211].

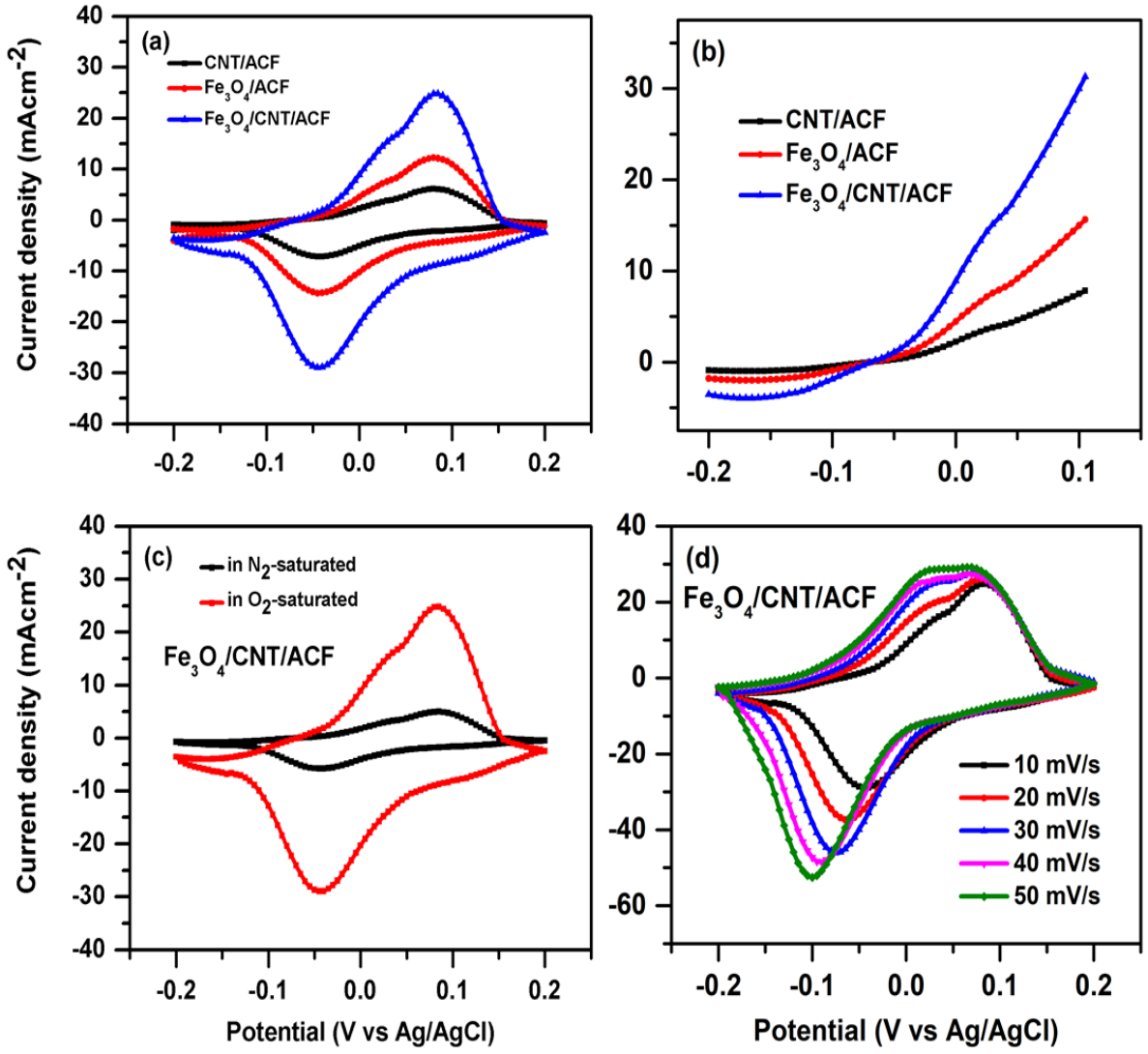

Figure 5.4: *Cyclic voltammogram (CV) (a) and LSV*

Cyclic voltammogram (CV) (a) and LSV (b) of prepared electrodes in O_2-saturated solution; CV of Fe_3O_4/CNT/ACF in N_2- or O_2-saturated solution at scan rate of 30 mV s^{-1} (c); and CV of Fe_3O_4/CNT/ACF in O_2-saturated solution at different scan rates (10-50 mVs^{-1}) (d). Operating conditions: 0.1-M Na_2SO_4 as electrolyte, pH 4 and temperature of 25 °C.

Low current density of Fe_3O_4/CNT/ACF (i.e., about -5 mA cm^{-2}) in N_2-saturated solution (Fig. 5.4c) comparing to that obtained in O_2-saturated solution (Fig. 5.4a) demonstrated that the catalytic reduction of molecular oxygen was achieved by Fe_3O_4/CNT/ACF cathode [90]. Even

if the CV and LSV analysis of the cathodes were insignificant, electron transfer quantity recorded for Fe_3O_4/CNT/ACF was higher than those measured using Fe_3O_4/ACF and CNT/ACF electrodes. This electrical conductivity may affect the MB degradation, which was consistent with degradation results obtained by Fe_3O_4/CNT/ACF. The relationship between the reduction current peak and the scanning rate was described in Fig. 5.4d. As the square root of the scanning rate ($v^{1/2}$) increased from 3.16 $(mVs^{-1})^{1/2}$ to 7.07 $(mVs^{-1})^{1/2}$, the reduction current peak also increased from -6 mA cm^{-2} to -17 mA cm^{-2}. Generally, Fe_3O_4/CNT/ACF cathode showed a higher ORR electro-catalytic activity (i.e., a more positive E_{redox} potential) than other cathodes.

5.3.3. Catalytic Performance of the electrodes on MB Degradation

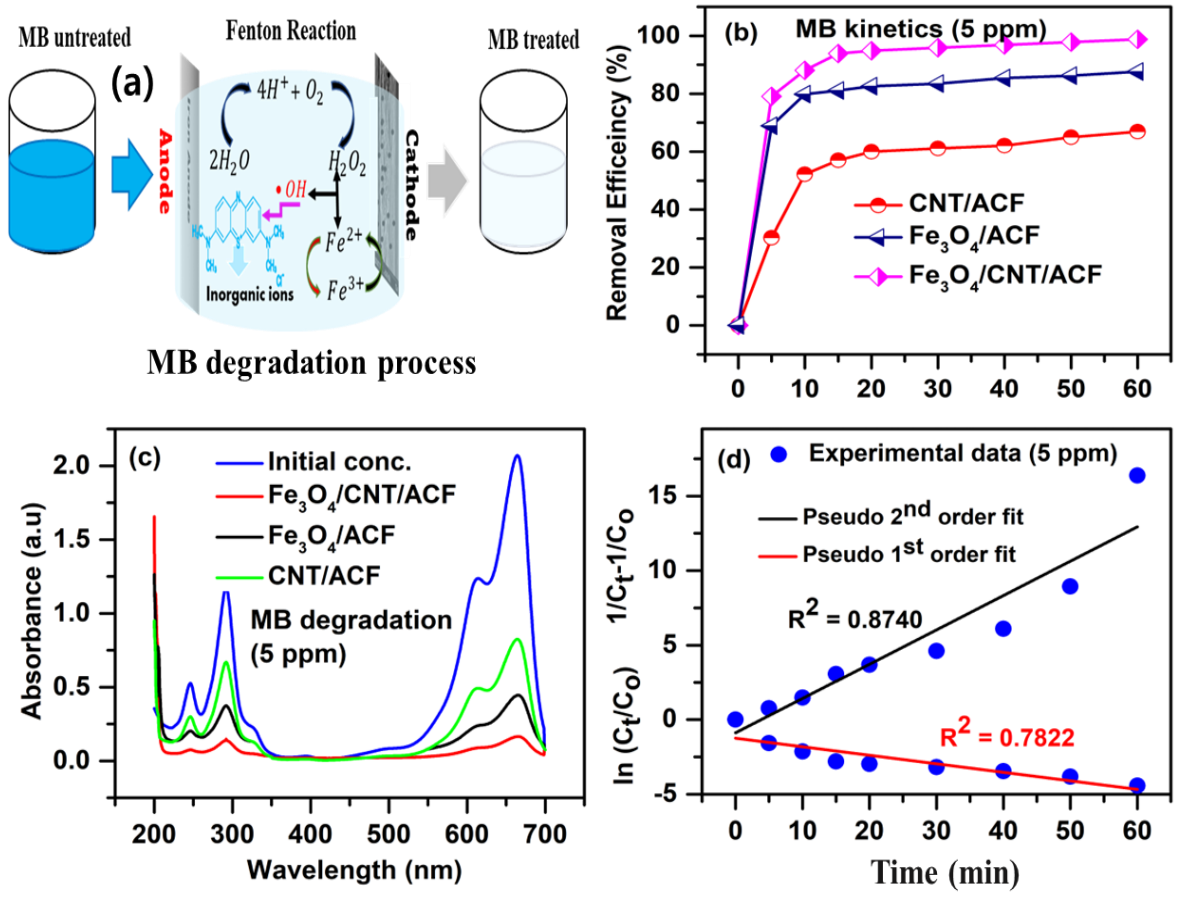

Figure 5.5: *Schematic diagram and removal efficiency of MB*

Schematic diagram of experimental setup (a); removal efficiency of MB by the prepared electrodes (b); UV-Vis absorbance of MB measured at t = 0 and t = 1 h (c); and kinetic model of MB degradation by Fe_3O_4/CNT/ACF system (d). Operating condition: pH = 3, applied

voltage = 4 V, initial MB concentration = 5 ppm, concentration of Na_2SO_4 electrolyte = 10 ppm, and reaction time = 1h. All experiments were performed at 25 °C.

Alternate ACF composites as cathode and iron strip as anode were used in the experimental set up for ORR and oxygen evolution, respectively. Possible redox reactions on the surface of the electrodes were proposed, as illustrated in the schematic representation of the EF process for MB degradation (Fig. 5.5a). The efficiency of all the alternate electrodes in MB degradation was evaluated by measuring the UV-Vis absorbance to select the best electrode for further electrochemical experiments. Two absorbance bands were observed for MB at 292 and 665 nm: one for the π-π^* transition benzene ring and the other for the n-π^* transition functional group (-S-) [255]. For all the three synthesized materials, the absorbance values of MB measured at 665 nm significantly decreased, compared to those measured at 292 nm over 1-hr reaction. (Fig. 5.5c).

Nonetheless, depending on the material coated on the electrode surface, the performance of the cathodes in the MB degradation varied [180]. Figure 5.5b shows the catalytic degradation efficiency of the prepared cathodes. From the experimental results, Fe_3O_4/CNT/ACF (98.8%) showed the highest degradation efficiency compared to Fe_3O_4/ACF (87.6%) and CNT/ACF (67.0%). On the other hand, 64.6% and 46.3% MB degradation efficiencies were observed when ACF and CF were used as the cathode, respectively (Appendix 5.3). From the result, it was hypothesized that the interfacial structural modification of ACF by CNT and Fe_3O_4 would allow the rapid H_2O_2 and ·OH radicals generation on the surface and result in a higher redox potential and enhanced interfacial-electrochemical interaction compared to unmodified ACF [229]. Figure 5.3a shows that the highest redox potential and MB degradation efficiency was observed by Fe_3O_4/CNT/ACF. Multiple components such as CNTs and Fe_3O_4 doped ACF facilitated electron transfer channels to or from the catalytic site [233] and increased the surface wettability of the cathode. As explained in the above section, differently sized MNPs contributed to the rough surface of Fe_3O_4/CNT/ACF, and multiple pores for inherent ORR activity on the surface. The MB degradation followed the pseudo-second-order kinetics (Fig. 5.5d). Regarding the regression values, the degradation rate constants and removal efficiency of CNT/ACF, Fe_3O_4/ACF and Fe_3O_4/CNT/ACF are presented in Appendix 5.4 and 5.5.

5.3.4. Effects of Experimental Parameters on MB Degradation

5.3.4.1. Effect of pH

The reaction using Fenton's reagents during EF is mainly affected by the pH values. It was clear that at lower pH values (< 3), insignificant removal efficiencies were obtained mainly due to the formation of iron-water ligand complex, which could react with H_2O_2; when H_2O_2 is surrounded by protons, a stable molecule called oxonium ion can be formed to hinder the generation of ·OH radicals by reducing the reactive affinity between H_2O_2 and Fe^{2+} [208].

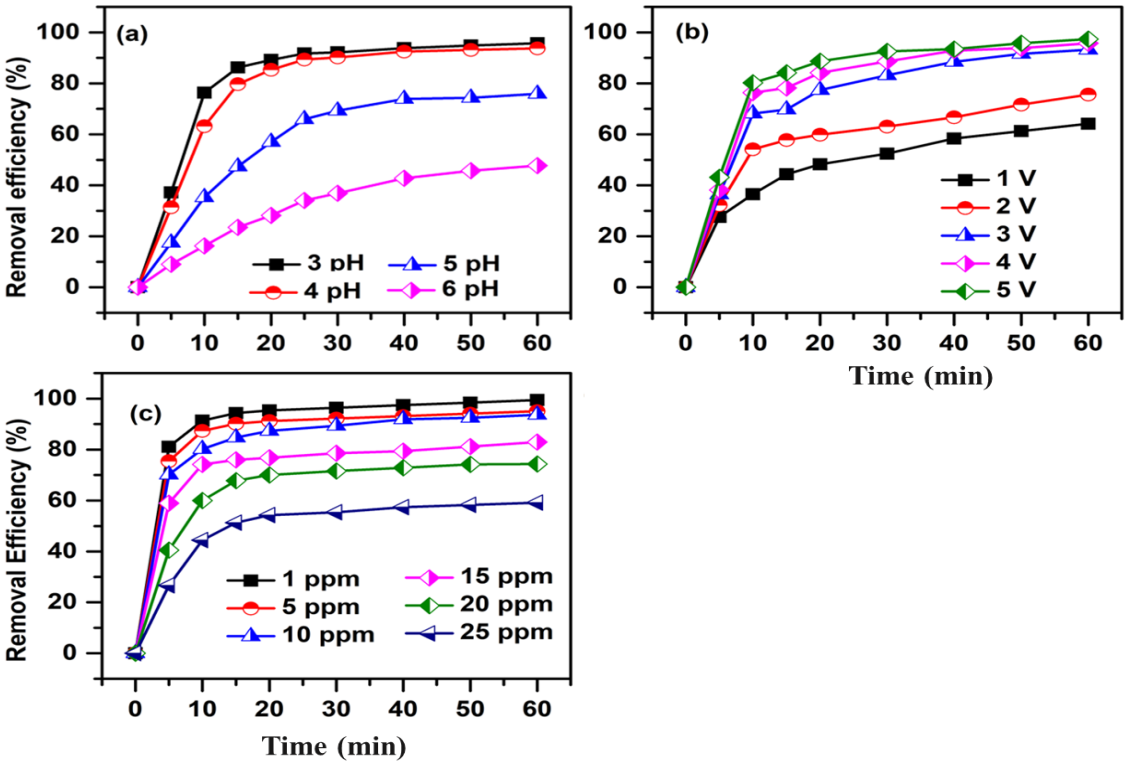

Figure 5.6: *Effect of operating parameters*

Effect of operating parameters on MB degradation by Fe_3O_4/CNT/ACF. Effects of pH variation (a; initial MB concentration = 5 ppm, and applied voltage = 4 V), applied voltage (b; pH = 4, and initial MB concentration = 5 ppm), and initial MB concentration (c; pH = 4, applied voltages = 3 V). All experiments were performed at 10-ppm Na_2SO_4 as electrolyte at 25 °C for 1 h.

As presented in Fig. 5.6a, the highest removal efficiency for MB was observed at pH 3 with the removal efficiency of 97%. As pH value was increased from 3 to 6, the removal efficiency

decreased sharply to 43% within 1 h. It is noteworthy that removal efficiency of 93% was obtained even at pH 4. On the other hand, at a higher solution pH (> 4), decomposition of H_2O_2, detaching of MNPs and precipitation of iron complexes might occur, leading to excessive sludge generation that could eventually hinders MB degradation [186]. Nonetheless, after considering both MB removal efficiency and chemical cost, pH 4 was selected as the system pH for further experiments.

5.3.4.2. Effect of Applied Voltage

Similar to pH, EF is influenced by the applied voltage [90] since the latter is the driving force for electron transfer between the surface of electrodes and the bulk aqueous solution. Herein, the effects of applied voltage on MB degradation were studied. Figure 5.5b shows that the removal efficiency of MB sharply increased from 71% to 94% as the applied potential was increased from 2 V to 3 V; the voltage increase would enhance generation of H_2O_2 and recycling of iron ions in the system. Increasing the applied potential further to 5 V, insignificant improvement of MB degradation was obtained (95.8%), which might be due to scavenging effects of ·OH radicals [171]. Therefore, 3 V was selected as the optimum voltage for further experiments.

5.3.4.3. Effect of Initial Concentration

As the initial MB concentration was increased from 1 ppm to 10 ppm, the MB removal efficiency was not much affected (Fig. 5.5c). However, the removal efficiencies were significantly reduced as the initial MB concentration was further increased to 25 ppm, at which 58% removal efficiency could be observed. As evidenced by a decline in the percentage removal at higher MB concentrations, the dye molecules competed for the active catalytic sites in the surface of the electrode [103,256]. The balance between ·OH radical formation and the ·OH radical reaction with dye molecules on the surface of the cathode may not be able to be matched if the organic compound concentration is too high. Therefore, 10-ppm MB was used as the initial concentration for further MB degradation experiments. Therefore, in an optimized initial pH (pH~4), applied voltage (3 V) and initial concentration (10 ppm), MB degradation followed second order rate kinetics as presented in Table 5.1.

Table 5.1: Summarized results of R^2 and kinetic rate of MB degradation

Pseudo-first order		Pseudo-second order		
R^2	k_1 (min $^{-1}$)	R^2	k_2 ($M^{-1}.min^{-1}$)	Removal Efficiency (%)
0.7414	4.6×10^{-2}	0.976	2.5×10^{-2}	93.7

5.3.5. Dominant Oxygen Reactive Species

A chemical quenching technique was applied to quantify the possible free reactive oxygen species generated during the MB degradation; alcohols (i.e., ethanol (EtOH) and *tert*-butanol (TBA)) and p-benzoquinone (*p*-BQ) were used to quench ·OH and superoxide ion radicals ($O_2^{\cdot-}$), respectively [235,236]. As presented in Fig. 5.7, the removal efficiency of MB rapidly decreased from 94% to 12% after EtOH (150 mM) had been added as a quenching agent into the system. Only 12% of MB could be degraded via non-radical reaction mechanisms, such as singlet oxygen [235].

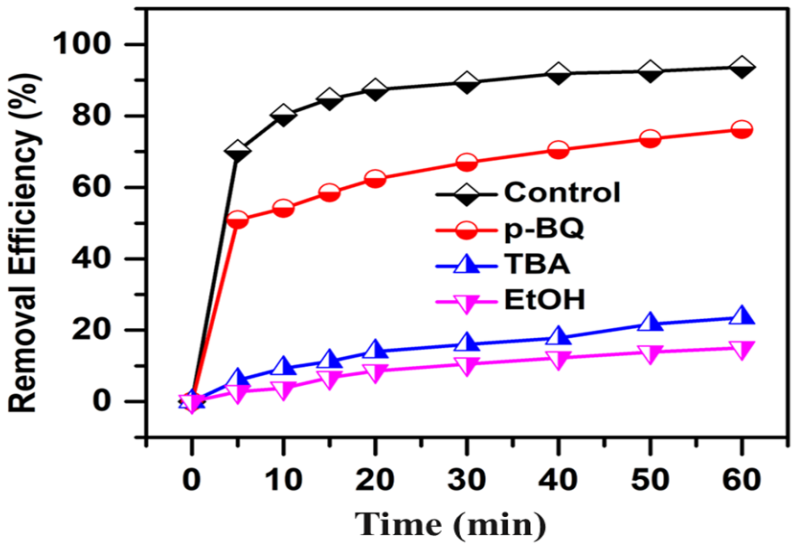

Figure 5.7: *Effects of quenching-agent*

Effects of quenching-agent presence on BM degradation in Fe_3O_4/CNT/ACF system. Quenching agents evaluated: EtOH, TBA, and p-BQ. Amount of quenching agent added =150 mM. Operating condition: pH = 4, applied voltage = 3 V, initial MB concentration = 10 ppm, 10-ppm Na_2SO_4 as electrolyte, and reaction time = 1h. All experiments were performed at 25 °C.

Similarly, the addition of TBA (150 mM) lowered the degradation efficiency down to 23.5%; apparently, ·OH radicals were less inhibited by TBA than by EtOH. The result of the quenching study clearly demonstrated that the ·OH radicals would play a crucial role in the MB degradation. In fact, even when 150-mM *p*-BQ was added as a quenching agent, the MB degradation efficiency decreased to 78.2%. From the result, it was hypothesized that $O_2^{\cdot-}$ also should play a role in degrading MB. Nonetheless, it was clearly demonstrated that ·OH radicals would be the dominant reactive oxygen species.

As shown above, ·OH radicals would play a crucial role in the MB degradation. Therefore, the EF process can be very promising, because it can continuously regenerate H_2O_2 at the cathode surface by the two-electron ORR (Eqn. 5.9) [93] and subsequently split it to ·OH radicals at the cathode interface (Eqn. 5.10). The ·OH radicals are a powerful oxidant (E_0 = 2.8 eV) that non-selectively attacks organic contaminants (Eqn. 5.11). In our system, the catalytic reduction of molecular oxygen at the cathodic surface of Fe_3O_4/CNT/ACF may facilitate the formation of $O_2^{\cdot-}$ radicals according to Eqns. 5.12 and 5.13. The unstable $O_2^{\cdot-}$ radicals also result in the formation of H_2O_2 in the acidic bulk system (Eqn. 5.14). However, the EF process is pH-dependent [171] in the generation of H_2O_2 and oxidation of different organic compounds. The maximum degradation efficiency of the process was reported under an acidic condition at pH 2–4 at which formation of iron precipitates is hindered. However, in an EF oxidation system using heterogeneous catalysts (Fe_3O_4) the working pH can be extended to a higher value [78].

$$Fe^{2+} + H_2O_2 \rightarrow Fe^{3+} + \cdot OH + OH^- \quad (5.10)$$

$$\cdot OH + MB \rightarrow MB(OH) \quad (5.11)$$

$$O_2 + 2e^- \rightarrow O_2^{\cdot-} \quad (5.12)$$

$$Fe^{2+} + O_2 \rightarrow Fe^{3+} + O_2^{\cdot-} \quad (5.13)$$

$$O_2^{\cdot-} + 2H^+ \rightarrow H_2O_2 + O_2 \quad (5.14)$$

5.3.6. TOC-Removal, Energy-Consumption and Reusability of Cathode

To evaluate the extent of mineralization of MB by the synthesized cathode, TOC of the MB solution was measured during the MB oxidation. As shown in Fig. 5.8, the Fe_3O_4/CNT/ACF electrode-based system could achieve TOC removal efficiency of > 87% in 2.5 h. (Fig. 5.8,

inset). To compare the efficiency of Fe_3O_4/CNT/ACF to previous reported carbon-based synthesized electrodes for different organic dye degradation were listed in Table 5.2.

Table 5 2: Previous reported articles

Organic dye	***Electrode material***	***Concentration (mg L^{-1})***	***Color removal/min***	***TOC removal/min***	***Ref.***
Methylene blue	*Fe_3N@NG/NC*	10	92 (60)	--	[257]
Methyl orange	Fe_3O_4@MUS	100	99 (60)	98 (180)	[36]
Methylene blue	Graphite felt	150	90 (120)	50 (120)	[258]
Congo red	*Fe-based heterogeneous*	*200*	*97/150*	*65/90*	[204]
Congo red	*Air-diffusion cathode*	*0.26*	*93 (85)*	*92/360*	[259]
Acid orange II	*Thermally activated carbon cathodes*	*35*	*92.5/15*	*84/120*	[46]
Amoxicillin	Fe_3O_4/Graphite felt	70	98.2 (60)	--	[260]
Sunset Yellow dye	Fe_3O_4/Gas diffusion electrode	100	99 (90)	71(90)	[180]
Metronidazole	*$FePO_4$/GO*	80	--	66 (300)	[261]
Methylene blue	Fe_3O_4/CNT/ACF	10	93.7/60	87/150	[This study]

In terms of cost, electricity consumption is only cost-associated. The MB degradation rates measured at different applied potentials (1–5 V) (Fig. 5.6b) were compared according to their energy efficiencies. Thus, considering EECs measured for applied voltages of 5 V and 3 V (i.e., 39.7 and 25.7 $kWhm^{-3}$, respectively; Eqn. 5.4) and TOC removal efficiencies (i.e., 61.2% and 57.4%, respectively; Eqn. 5.2), it was found that 3 V would be the most favorable for the EF system [237]. Similarly, the MCE ($kWhm^{-3}$) of MB degradation was determined to be 76.3% within 2.5 h. (Eqn. 5.3). To reuse the Fe_3O_4/CNT/ACF cathode, the residual iron ions leaching into the solution must be quantified. Iron-based catalysts have good degradation efficiency but often show poor reusability owing to structural deformation [28]. However, in this study, a satisfactory MB removal efficiency of 78.4% could be achieved even after ten cycles of Fe_3O_4/CNT/ACF cathode. This indicates that detachment of the MNPs from ACF would be negligible; it was confirmed by ICP-OES that only 0.0043-mg iron residue was observed in the treated solution, which were insignificant comparing to 460-mg of the initial concentration of MNPs coated on the surface of ACF. Therefore, it was concluded that Fe_3O_4/CNT/ACF would

have an excellent catalytic ability and can be reusable multiple times, as shown in Appendix 5.6.

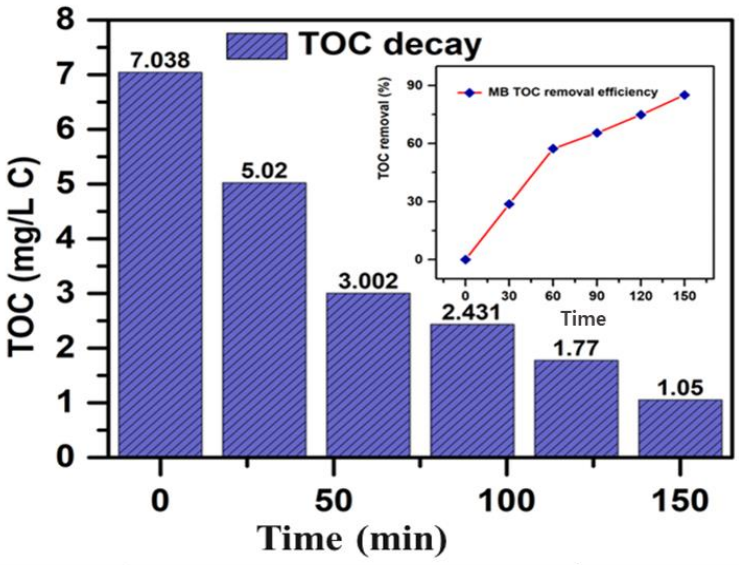

Figure 5.8: *TOC measured during MB degradation.*

TOC measured during MB degradation. Operating condition: pH = 4, applied voltage = 3 V, initial MB concentration = 10 ppm, 10-ppm Na_2SO_4 as electrolyte, and reaction time = 2.5 h. All experiments were performed at 25 °C.

5.3.7. Intermediate Products and Degradation Mechanisms of MB

The color of MB was associated with the chromophore (-S-) in the thiazine ring (C_4H_5NS), which disappeared upon destruction of the ring by ·OH radicals and was degraded to small intermediate molecules. In fact, the functional group would be more easily destroyed than the aromatic rings, which are also the constituents of MB [239,240]. Eventually, the intermediates were degraded to simpler biodegradable by-products and then to CO_2, H_2O, and inorganic ions such as NO_3^- and SO_4^{2-}.

To explore and propose the possible fate of MB degradation, the intermediate products must be determined. LC-MS spectra of MB-containing water treated by the Fe_3O_4/CNT/ACF cathode revealed that MB was degraded to a few fragments through demethylation and hydroxylation processes. One potential pathway of MB degradation is described in Fig. 5.9. Our results are in accordance with those previously reported by others [238]. The dominant

intermediates products of MB degradation were identified at 90, 94, 110, 116, 173 and 240 *m/z*, which was attributed to demethylation reactions as presented in Appendix 5.7 and 5.8. After 2.5-h reaction for MB degradation, the anionic products generated were analyzed using the ICS technique. A gradient elution of the mixture solutions of 3 mM Na_2CO_3 and 1 mM $NaHCO_3$ was used. Three inorganic anions were detected, i.e., Cl^-, NO_3^-, and SO_4^{2-} at the concentrations of 1.645, 0.713, and 3.531 ppm, respectively Fig. Appendix 5.9. This indicates that a majority of MB was oxidized to inorganic ions. As presented in Table Appendix 5.10, the concentrations of NO_3^- were very low compared to Cl^- and SO_4^{2-}. This is because HCl was added for pH adjustment and Na_2SO_4 was used as the electrolyte (2.253 ppm of sulfur).

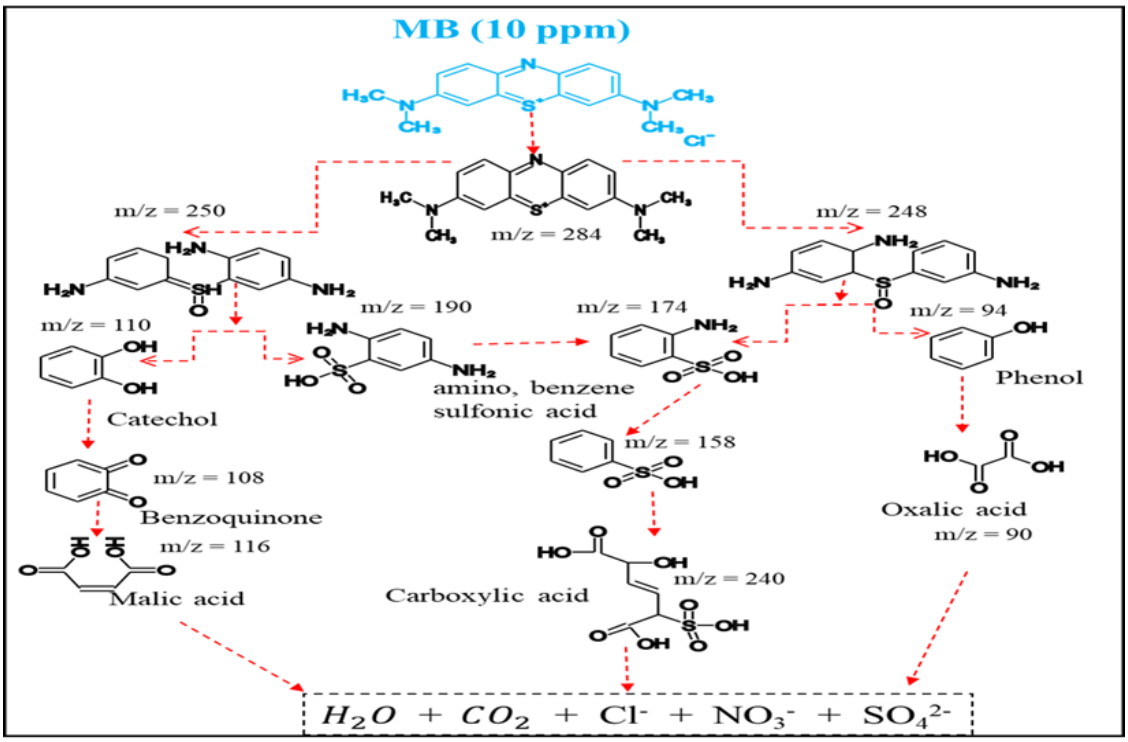

Figure 5.9: *Possible fate of MB degradation*

Possible fate of MB degradation by Fe_3O_4/CNT/ACF electrode in EF process. Operating conditions: pH = 4, applied voltage = 3 V, MB concentration = 10 ppm, 10-ppm Na_2SO_4 as electrolyte and reaction time = 2.5 h. All experiments were performed at 25 °C.

5.4. Summery

Chapter 5 concludes that Higher degradation rate of MB was observed by Fe_3O_4/CNT/ACF cathode and Final degradation products CO_2, H_2O, NO_3^- and SO_4^{2-} etc. were formed.

CHAPTER 6

6. COUPLED BIO ELECTRO FENTON FOR DYE OXIDATION

6.1. INTRODUCTION

Textile industries are among the most environmentally polluting industries by discharging a large amount of non-biodegradable organic compounds containing wastewater into nearby rivers. This wastewater demands an innovative and environmentally friendly wastewater treatment system with efficient energy consumption and less sludge generation [92]. Advanced oxidation processes (AOPs) are a group of emerging technologies that have been widely developed as efficient and effective wastewater treatment methods to degrade refractory organic compounds into more biodegradable by-products [3,79,262]. Recently, electrochemical advance oxidation processes (EAOPs) have gained increasing attention as water and wastewater treatment technologies due to stable performance, easy control, less chemical demand and environmental friendliness [259,263]. To enhance pollutant oxidation efficiency and minimize energy consumption, coupled EAOP systems such as Electro Fenton (EF) were utilized. EF system is a coupled system of Fenton oxidation and electrochemical (EC) system which is widely employed in wastewater treatment through in-situ H_2O_2 generation and recycling of ferrous ions (Fe^{2+}) [7,264] *(*Eqn. 6.1). However, for commercial use, EF systems are energy intensive processes which make them inefficient for emerging pollutant oxidation [262,263].

Despite high retention time, temperature sensitivity and inability to degrade recalcitrant organics, biological wastewater treatment systems were used for many years due to less sludge production and less energy requirements [265]. Sequential coupling of the biological-electrochemical processes has been utilized depending on treatment purposes. Carboneras et al. [116] coupled with a biological system as a pretreatment for an electrochemical advanced oxidation process to remove oxyfluorfen [266]. The BEF systems are complexly interlinked compartments, which utilize microorganisms in the anodic compartments to facilitate redox processes by releasing or capturing electrons [2,116]. As mentioned earlier, biological systems

require a longer time for recalcitrant organic oxidation compared to EF oxidation as reported by Zou et al. [103], Yong et al. [267] and P. Xu et al. [117] for different dye oxidation.

An anodic compartment contains anaerobic electrogenic microflora that generate electrons by oxidizing biodegradable substrates (acetate or glucose) [268]. Then electrons are transferred to the cathode compartment by an external wire. As a result, continuous regeneration of H_2O_2 takes place on the cathodic surface. Eventually, ·OH radicals are generated through Fenton's reaction mechanism to drive Fenton's process [93,94]. The type and nature of the cathode is one of the determinant factors to favor two-electron oxygen reduction reaction (2e-ORR, Eqn. 6.2) over four electron oxygen reduction reaction (4e-ORR, Eqn. 6.3) in the cathodic compartment while designing a successful and functional BEF system [90]. Most metal-based electrocatalysts follow 4e-ORR to produce H_2O instead of H_2O_2 while carbonaceous cathodes support the 2e-ORR pathway leading to the generation of H_2O_2 [269]. Having Fe species impregnated on the cathode surface makes the cathode favorable for Fenton oxidation to occur. In contrast, H_2O_2 is continuously produced in situ, while Fe is either added externally or impregnated on the cathode surface. Fe-based composite cathode catalysts were used to enhance H_2O_2 generation in BEF systems such as Fe-Mn-Mg/carbon fiber [270], powdered activated carbon-Fe_3O_4-CF [271], Fe@Fe_2O_3/ACF [272], and Fe_2O_3/graphite felt [267].

Bio-electrochemical system (BES) is a coupled method of biological and electrochemical systems that can transform the biological energy of recyclable organic substances with the help of microbes to generate power [269,273]. However, the BEF system involves the integration of half-cells of an EF and BES [266]. In BEF, oxidation of pollutants takes place in a cathodic chamber equipped with a carbonaceous cathode capable of following 2e-ORR such as activated carbon felt [274], carbon felt [275], carbon brush [276], cubic graphite plate [277], carbon plate [278]. The rapid development of the materials has led to the invention of functional electrodes that are potentially employed in the BEF system.

$$Fe^{2+} + H_2O_2 \rightarrow Fe^{3+} + \cdot OH + OH^- \quad (6.1)$$

$$O_2 + 2H^+ + 2e^- \rightarrow H_2O_2 \quad (6.2)$$

$$O_2 + 4H^+ + 4e^- \rightarrow 2H_2O \quad (6.3)$$

The electron transfer performance of the BEF process depends on biofilm formation on the anodic surface [69,279] in the anode compartment. This is a complex flora of microorganisms containing over 90% w/w bacteria [280]. Biofilm formation follows a sequential process of transport of microbes to the anode surface, initial attachment to the surface, irreversible attachment, and biofilm maturation. The most studied electro-active microorganisms used for the BEF system are Geobacter species [57], Shewanella species [281] and activated sludge [282]. Biofilm could be formed when the electrode reached a stable negative potential.

The BEF is regarded as a promising green system for emerging contaminants oxidation in wastewater treatment due to its energy and cost-effectiveness, environmental friendliness, and strong coupling opportunities with other systems. In this study, coupled bio-electro Fenton (CBEF) systems were developed as integrated systems for EF and biological wastewater treatment systems. This system compensates for the energy consumption by the EF system and significantly reduces the long retention time of the biological system. (1) functional Fe-based carbon electrodes were fabricated, (2) the BES system was developed using activated sludge inoculum and carbonaceous electrodes, (3) the BES was coupled with a previously established EF system, (4) the oxidation performance of the coupled system was evaluated based on the removal efficiency of azo dye (Methyl orange) and the system was evaluated on actual textile wastewater. The results showed that the coupled BES-EFS system achieved a satisfactory azo dye oxidation efficiency, indicating the synergistic effect of combining these two systems. Overall, the BES-EFS system demonstrated a great potential for efficient and sustainable wastewater treatment, and further research could focus on optimizing the system for large-scale industrial applications and exploring its potential for treating other types of contaminants.

6.2. Materials and Methods

6.2.1. Chemical and Materials

In this study, all chemical reagents used were analytical grade and supplied by Samchun pure chemicals (Seoul, South Korea). $Fe_2(SO_4)_3.6H_2O$ (99%), Methyl orange (MO > 89%), and Acid orange 7 (AO7 > 85%), Na_2SO_4 (> 99%), ammonia solution (28% w/w) and iron electrode (Ajax scientific-E160-004, 5 × 2.4 cm^2) were purchased from Sigma-Aldrich (Seoul, Korea). Polyacrylonitrile-based carbon felts (CF) (V207-G-19, thickness: 3 mm, Bulk density: 0.12-0.14 g cm^{-3}, Carbon content: > 99.67%, strength of extension: 0.43 MPa) were provided by Jin Gu Carbon Material Co. Ltd, Korea. Solutions and reagents were prepared in a high-purity

water-filtered system (resistivity > 18 MΩ cm at 25 ℃). HCl and NaOH solutions were used for initial pH adjustment during the experiment and the pH was determined using pH meter (Eutech Instruments Pte, Ltd, 6plus pH meter, Singapore).

6.2.2. Wet Phase Activation of CF and Immobilization of Fe_3O_4 on ACF

Carbon felts (CF) with a surface area of 15.0 cm^2 (5 cm $\times$ 3 cm) were cut and immersed in 10 mL of 5 wt.% hot (65 ℃) HNO_3 at room temperature for 15 minutes to generate oxygen-containing surface functional groups [40]. After 15 min of acid treatment, it was again soaked in distilled water for 30 minutes, washed several times and dried at 105 ℃ in a drying oven overnight. This was done to remove inorganic impurities from the surface of the material. Moreover, a ferric sulfate solution was prepared by dissolving 22.77 g of $Fe_2(SO4)_3.6H_2O$ into 150 mL of distilled water. The solution was heated to 90 ℃ in a magnetic stirrer under an N_2 atmosphere for 30 min to form black Fe_3O_4 (MNPs) according to a previous study [162]. After 30 min, the acid-treated CF was completely soaked into the solution and NH_3 solution (15 mL, 28 wt. %) was added in a drop-wise manner over a 30 min period over it using a dropping funnel until a black precipitate deposition on the surface of the ACF was observed. Finally, the solution together with ACF was sonicated for 10 min to facilitate uniform deposition of MNPs on ACF and allowed to dry for 2 h. The deposited ACF was washed with ethanol and distilled water several times to remove any loosely attached residual Fe_3O_4 and dried at 60 ℃ overnight to form an immobilized Fe_3O_4@ACF electrode.

6.2.3. Electrode Characterization

The X-ray diffraction (XRD) pattern of ACF and immobilized Fe_3O_4@ACF electrodes were examined by an X-ray diffractometer (Rigaku, Tokyo, Japan) which is equipped with Cu Kα (λ = 0.1541 nm) radiation over the 2θ interval of 5-85 at a scan rate of 0.2 per step at 40 kV and 30 mA. Fourier transforming infrared (FT-IR) (Thermos Scientific, Nicolet iN10 mX, Madison, USA) was employed to identify oxygen-containing functional groups on the surface of the electrodes. The surface morphology of the electrodes was analyzed through a field emission scanning electron microscope (FE-SEM, SU8010, Hitachi, Japan) at an operating voltage of 10 KV. The elemental composition and mapping of the electrodes were determined by energy dispersive X-ray (EDX). To determine the elemental oxidation states of the electrodes, X-ray photoelectron spectroscopy (XPS) (Scienta-ESCA5500, Shimadzu, Tokyo, Japan) equipped with the high-resolution Scienta-ESCA5500 spectrometer was used.

For all electrochemical experiments, a standard three-electrode mode electrochemical workstation CHI660A system (CHI606E, Austin, USA) was used. Before all chemistry-based measurements, dissolved oxygen was removed by bubbling argon through the electrolyte solution at 30 mL min^{-1}. The electrochemical performance of the electrodes was determined with electrochemical impedance spectroscopy (EIS), linear sweep voltammetry (LSV) and cyclic voltammetry (CV). The cathodes (ACF and immobilized Fe_3O_4@ACF) were applied as working electrodes, while Ag/AgCl and platinum electrodes were employed as reference and counter electrodes respectively. The analysis of EIS was performed over a frequency range from 10^{-5} to 10^5 Hz with an AC signal of 10 mV amplitude at the open circuit voltage (OCV) of the cathodes. The Nyquist plot was used to estimate solution resistance (R_s), charge transfer resistance (R_{ct}), and diffusion resistance (W). Moreover, CV and LSV analyses were performed in three-electrode mode, where the cathodes were used as working electrodes in the presence of a platinum sheet (1 cm × 1 cm) and Ag/AgCl as counter and reference electrodes respectively. The potential was scanned from -0.2 V to +0.2 V at a scan rate of 25 mV s^{-1}.

6.2.4. Development of Bio-electro Fenton System

A coupled bio-electro-Fenton system (CBEF) of bio-electrochemical (BES) and Electro-Fenton (EF) systems was developed. The coupled system consists of two identical cylindrical chambers with a working volume of 250 mL each. In BES, iron strips and ACF were used as bio-anodes and bio-cathodes respectively. Similarly, an iron strip was used as an anode and Fe_3O_4@ACF was utilized as a cathode in EFS. The electrodes are related to titanium wire (99.9% pure grade 1 TA1 0.1 mm). The BES was fed with 230 mL of general media which was composed of 4.44 g L^{-1} Na_2HPO_4, 10.5 g L^{-1} $NaH_2PO_4 \cdot H_2O$, 0.47 g L^{-1} NH_4Cl, 0.2 g L^{-1} KCl, trace vitamins (17.0 mg L^{-1}) and minerals (30 mg L^{-1}) [104]. Sodium acetate (1.5 g L^{-1}) was used as a carbon source. Then it was inoculated with 20 mL of prefiltered (sieve size 0.5 mm) activated sludge from Jungnang sewage treatment plant (J-STP), Seoul, Korea.

To achieve maximum and stable voltage output, the system was fed continuously every 24 hours until the output reached a maximum and stable for 25 days. After the output voltage of the BES reached maximum and stable value, the BES was coupled to EFS. Here, BES was used as an energy source for the EF system. 25 mL of sewage wastewater with characteristics listed in Appendix 6.1 was used to feed the BES. On the other hand, the EF chamber was filled with 0.5 mg L^{-1} Na_2SO_4 electrolyte solution including the model contaminant of azo dye (MO:

20 mg L^{-1}) and purged with air at a flow rate of 400 mL min^{-1} and the pH was adjusted to 3. The polarization curves of BES were drawn by varying the external resistance from 10 to 1,000 Ω at 30 min intervals after the OCV was stabilized. The voltage drops (V, mV) was measured using a bench digital multimeter (GDM-8342, Jiangsu, China). The current flow (I, mA) and power (P, W) outputs were calculated according to Ohm's law of Eqn. 6.4 and 6.5 respectively. To obtain current and power densities, the current and power outputs were normalized to the surface area of the cathode (15.0 cm^2) [283].

$$Current\ flow\ (I, mA) = \frac{V}{R} \qquad (6.4)$$

$$Power\ output\ (P, W) = I \times V \qquad (6.5)$$

Where I represent a flowing current (mA) and P represents the power output (W) of the BES.

6.2.5. Analytical Methods

The H_2O_2 generation in the EFS chamber was measured by spectrophotometric analysis using the iodide method at 352 nm [284]. The model contaminant dye oxidation was determined using a UV-spectrophotometer (UV-1800, Shimadzu, Japan) [285] (Eqn. 6.6). TOC decay of the azo dyes was detected with a TOC-V_{CPH} (Shimadzu, Japan) analyzer (Eqn. 6.7). The residual iron ions were determined by inductively coupled plasma optical emission spectrometry (ICPOES-9000, Shimadzu, Japan). The intermediate oxidation by-products were quantified by liquid chromatography-mass spectrometry (LC-MS, Shimadzu, Japan) and inorganic by-product ions were quantified using an ion-exchange chromatography system (ICS-90, Thermo Fisher Scientific, USA). Before LC-MS and IC analysis, the samples were filtered using 0.45 μm filters [28].

$$Color\ Removal\ Efficiency\ (\%) = \frac{C_0 - C_t}{C_0} \times 100 \qquad (6.6)$$

$$Dyes\ mineralization\ (\%) = \frac{(TOC)_0 - (TOC)_t}{(TOC)_0} \times 100 \qquad (6.7)$$

Where C_t and $(TOC)_t$ are the concentration of dyes (mg L^{-1}) and TOC (mg carbon L^{-1}) at electrolysis time t and C_0 and $(TOC)_0$ are the concentration of dyes and TOC before treatment.

6.3. Results and Discussion

Following the wet phase activation process of CF using HNO_3, ACF was obtained. The detailed activation process was described in section 2.2 in which oxygen-containing functional groups were formed. Soaking pristine CF into hot HNO_3 could produce a higher amount of phenolic and carboxyl (acrylic acid) with relatively few amounts of hydroxyl, carbonyl, and ethoxy functional groups on its surface. However, wet-phase activation of CF with HNO_3 leads to the formation of a large amount of carboxyl and carbonyl functional groups on the surface [286]. After the formation of oxygen-containing functional groups, the ACF was further treated with ammonia solution to generate nitrogen-containing functional groups such as amide, imide, amine and pyrrolic functional groups by reacting with previously formed oxygen-containing functional groups. Further, when the ACF was soaked in the ferric solution and NH_3 was added, the oxygen-containing functional groups were replaced by amine groups. Then, the amine groups irreversibly interacted with Fe_3O_4 particles to form immobilized Fe_3O_4@ACF [287]. The overall activation of CF and impregnation of Fe_3O_4 particles on the surface of ACF was described in Fig. 6.1. Overall, the activation and functionalization of CF through a multi-step process provides a promising avenue for the development of highly functionalized and versatile materials with a wide range of potential applications in various fields. Further research on the optimization of this process and exploration of new functionalization strategies could lead to even more advanced materials with enhanced properties and even broader application potential. Moreover, the development of such functionalized materials can contribute significantly to advancing sustainable and environmentally friendly technologies, as ACF can be derived from renewable biomass sources and can serve as a more sustainable alternative to traditional carbon-based materials derived from non-renewable sources such as petroleum. Furthermore, the ability to control the types and amounts of functional groups on the surface of ACF allows for tailoring the properties of the material to specific applications and further enhances its potential usefulness. In addition, the scalability of this process should also be investigated to assess its potential for large-scale production and commercialization.

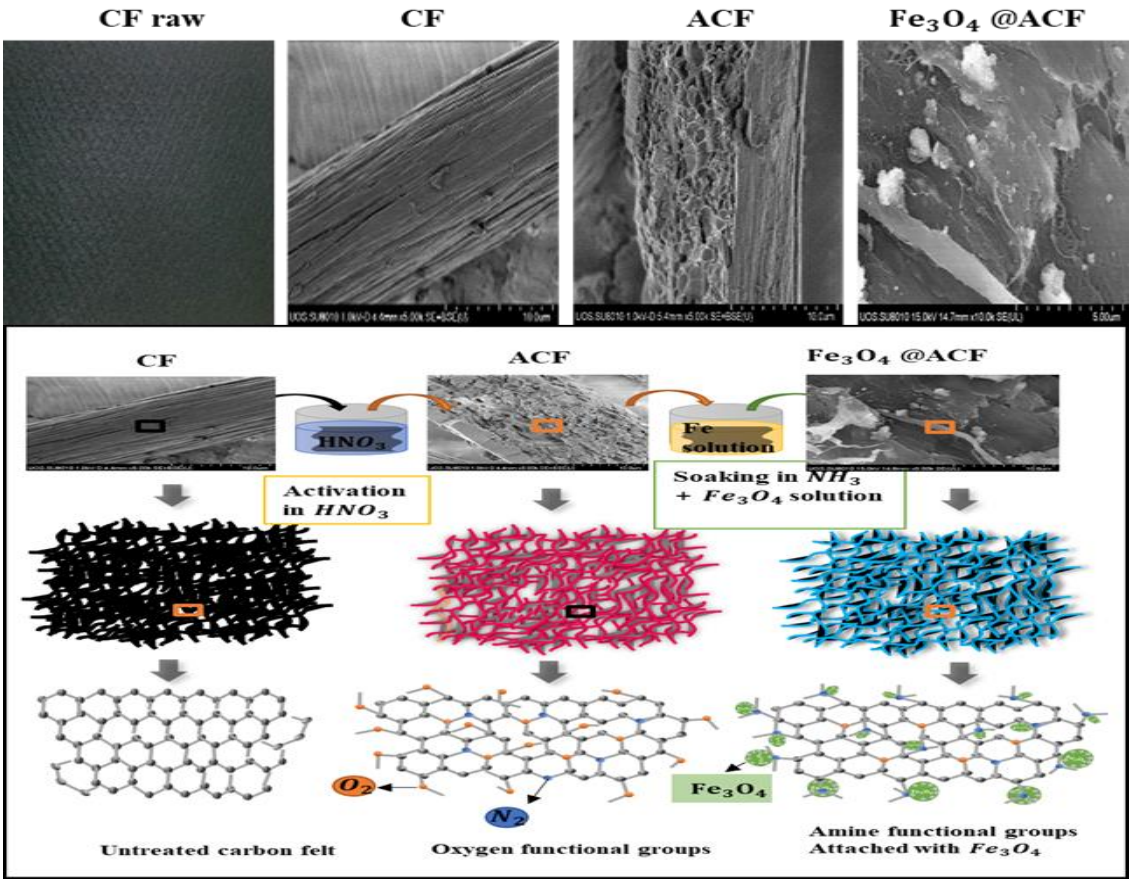

Figure 6.1: CF activation and Fe_3O_4 deposition on ACF

Process description of CF activation and deposition of Fe_3O_4 on ACF to from Fe_3O_4@ACF functional cathode. After suitable size of pristine CF was cut, wet phase activation was followed using HNO_3. The process could produce hydroxyl, carbonyl, carboxyl and ethoxy functional groups on its surface. The ammonia solution was added to generate nitrogen-containing functional groups to attach with Fe_3O_4 particles to form immobilized Fe_3O_4@ACF.

6.3.1. Characterization of Cathodes

XRD technique was used to identify the crystal structure and crystallite size of MNPs presented in Fig. 6.2. The broad hump peak at 2θ of 25.6^0 corresponding to the lattice plane (002) of the carbon atom of ACF was observed. The pattern peak was due to the amorphous graphite carbon of ACF which was formed by the acid treatment process [222]. Moreover, a narrow peak at around 45.3^0 was assigned to the (010) lattice plane of the carbon atom in ACF Fig. 6.2a (red). Similarly, apart from the diffraction peaks observed on ACF, additional peaks were also observed on the Fe_3O_4@ACF cathode [222]. The major diffraction peak patterns corresponding

to lattice plane of (311), (311), and (311) at 36.2°, 57.3° and 71.8° respectively were due to Fe_3O_4 impregnated on the surface of ACF Fig. 6.2a (blue). The additional XRD diffraction peaks and crystal planes of Fe_3O_4 in Fe_3O_4@ACF confirmed the successful impregnation of Fe_3O_4 particles on the surface of the ACF cathode [250]. The FTIR analysis was performed to determine any functional groups that formed during the activation process of CF as described in Fig. 6.2b. Similar absorption peaks at around 1655 and 1543 cm^{-1} on both ACF and Fe_3O_4@ACF were observed which were assigned to stretching vibrations of carbonyl (C=O) and carboxyl (C-OOH) functional groups respectively [226]. However, the short and narrow absorption peaks in Fe_3O_4@ACF could be due to complex organometallic interactions [54]. The peak at around 529 cm^{-1} could be assigned to the vibrational mode of the metal-oxygen (Fe-O) bond (Fig. 6.2b (blue)) [224].

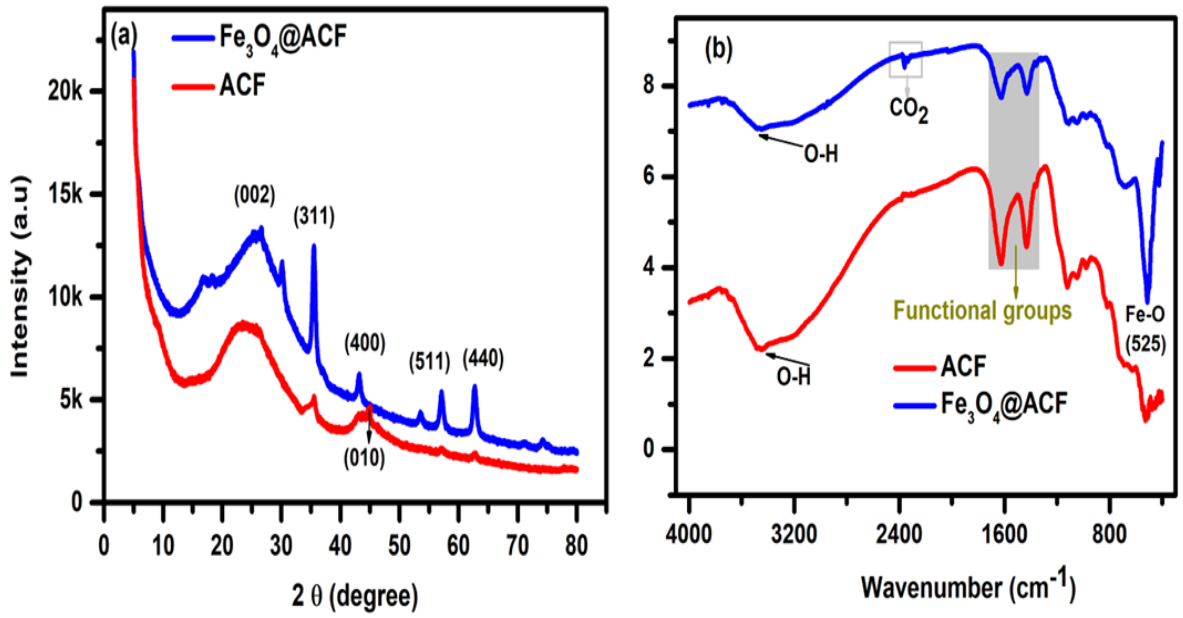

Figure 6.2: XRD diffraction and FT-IR spectral vibrations

XRD diffraction patterns (a) and FTIR spectral vibrations (b) of ACF and Fe_3O_4@ACF respectively

The surface analysis study of pristine CF, ACF and Fe_3O_4@ACF was performed using FE-SEM as described in Fig. 6.3. Comparing the morphology of ACF to pristine CF (Fig. 6.3a), the surface morphology of the ACF was rough as seen from the images (Fig. 6.3b). This was due to the formation of oxygen-containing functional groups on the surface of ACF because of the immersion of pristine CF into hot HNO_3 which could contribute to biofilm formation. The

functional groups were detected using FT-IR and XPS. The immobilization of Fe_3O_4 on ACF was performed further soaking of ACF in ferric solution and the Fe_3O_4 particles were observed on the surface of ACF (Fig. 6.3c). The roughest surface was seen on Fe_3O_4@ACF which was due to the presence of Fe_3O_4 particles. This surface roughness could also contribute to 2e-ORR.

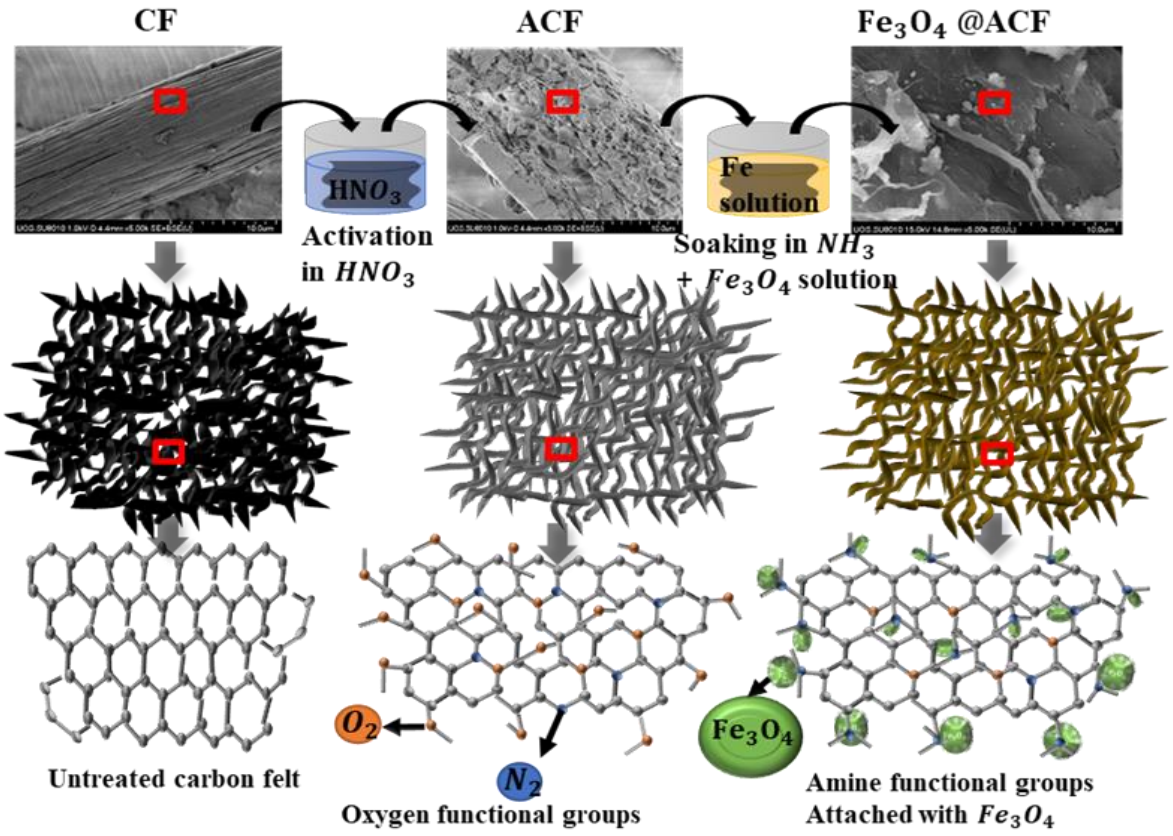

Figure 6.3: SEM image of CF, ACF and Fe_3O_4@ACF

FE-SEM images of CF, ACF and Fe_3O_4@ACF with process description of functional group formation. Wet phase activation was followed using HNO_3. The process could produce hydroxyl, carbonyl, carboxyl and ethoxy functional groups on its surface. The ammonia solution was added to generate nitrogen-containing functional groups to attach with Fe_3O_4 particles to form immobilized Fe_3O_4@ACF.

The chemical composition formed on Fe_3O_4@ACF cathode was examined by EDX and the data obtained are given in Fig. 6.4. The main elements determined from EDX analysis are provided in the table form in the same figure. The obtained data indicate that Fe_3O_4@ACF cathode is composed of hetero compounds bearing N, C, S, O and Fe were represented by

distinctive strong peaks [228]. The presence of Fe and oxygen-containing functional groups on the surface of Fe_3O_4@ACF were the indication of the successful impregnation of the Fe element and activation of pristine CF. These elements were an active center for ORR and dye oxidation process.

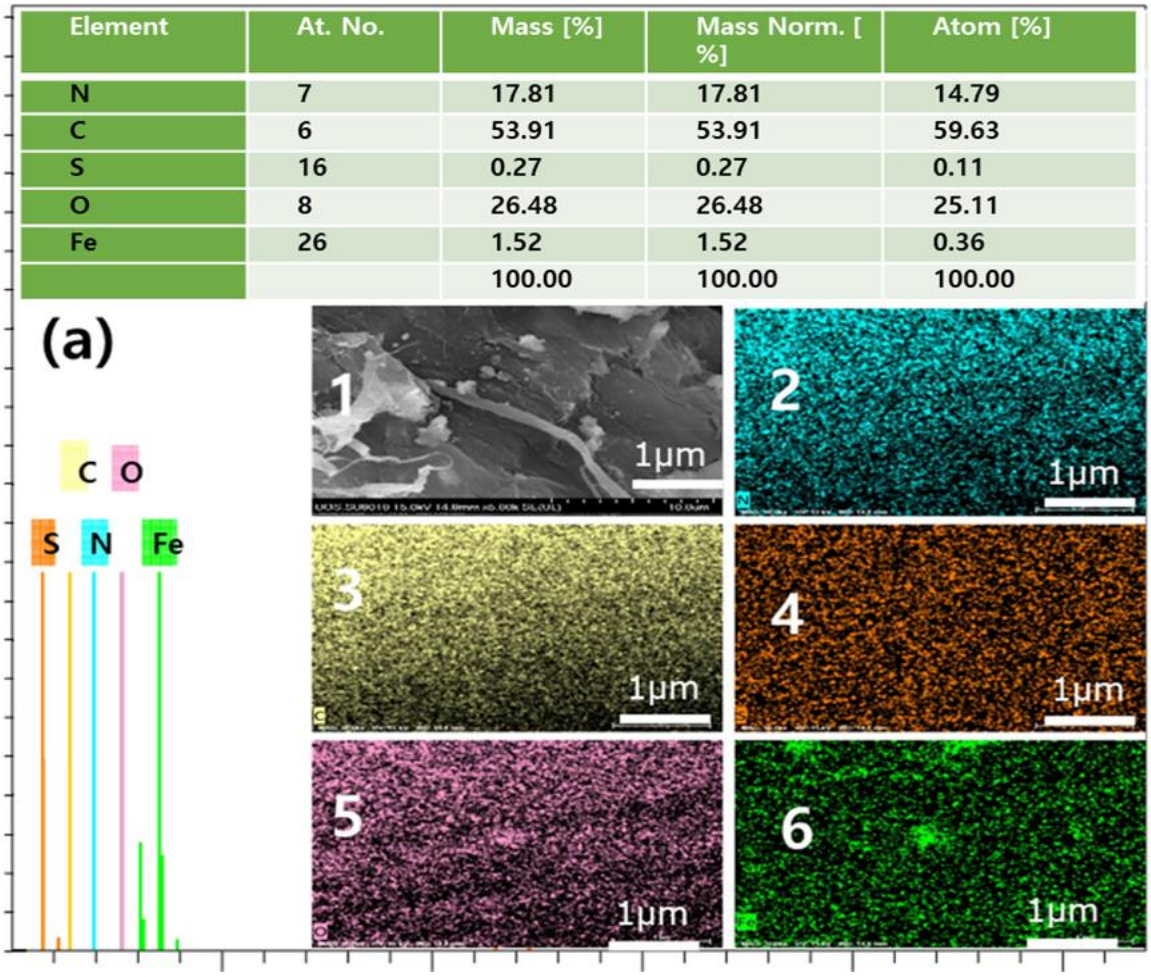

Figure 6.4: SEM-EDX elemental mapping

SEM-EDX elemental analysis and mapping of Fe_3O_4@ACF with the elemental composition and the graph is energy (keV) vs counts per second (cps/eV).

The interaction between ACF and Fe_3O_4, as well as the composition and valence state of n-Fe_3O_4@ACF was further characterized by X-ray photoelectron spectroscopy (XPS) [40,90]. The coexistence of Fe, C, N and O in immobilized Fe_3O_4@ACF was described in Fig. 6.5. Fig. 6.5a presented four distinct spectra peaks were detected in n-Fe_3O_4@ACF that corresponded to Fe2p, C1s, O1s and N1s spectrum comparing to CF and ACF spectrums [39]. The sp2 orbital hybridization of ACF in immobilized Fe_3O_4@ACF was assigned to three deconvoluted

characteristic peaks of carbon atom, C = C at 284.82 eV, C = O at 286.01 eV, and O–C–O at 289.22 eV, respectively. Fig. 6.5b presented the deconvoluted peaks of C1s core level spectrum for ACF in immobilized Fe_3O_4@ACF. The peak spectrum centered at the binding energy at 284.82 eV assigned to the sp2-hybridized defect of carbon atoms in ACF.

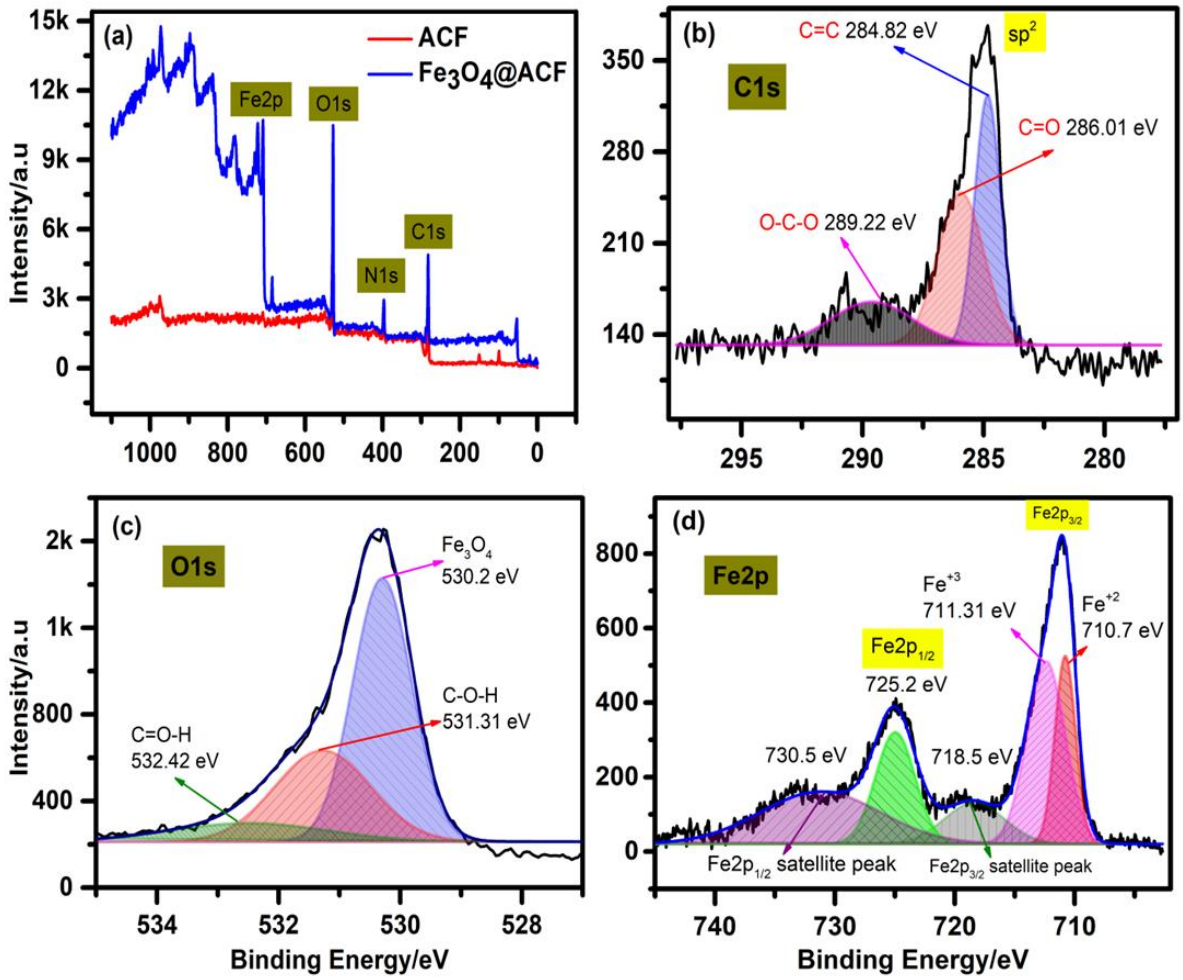

Figure 6.5: X-ray photoelectron spectroscopy (XPS)

High resolution XPS measurement of ACF and Fe_3O_4@ACF (a) and curve fittings of Fe_3O_4@ACF for C 1s (b), O 1s (c) and Fe2p (d)

Moreover, Fig. 6.5c shows the high-resolution spectrum with curve fittings of O1s in immobilized Fe_3O_4@ACF, and the three characteristic peaks at around 532.42 eV, 531.31 eV, and 530.2 eV were assigned to C = O, C–O, and Fe–O of Fe_3O_4, respectively which demonstrated the presence of Fe_3O_4 [235]. The above results verified that the as-prepared sample was modified ACF with Fe_3O_4 nanoparticles. Fig. 6.5d presented $Fe2p_{3/2}$ and $Fe2p_{1/2}$ spectra peaks, which corresponded to the Fe2p spin-orbit of Fe_3O_4. The deconvoluted spectra

peaks at 711.31 eV and 710.7 eV could be assigned to $Fe2p_{3/2}$, and the spectra peak at 725.2 eV was attributed to $Fe2p_{1/2}$ [57]. Moreover, satellite spectra peaks at around 718.5 eV and 730.5 eV were assigned to $Fe2p_{3/2}$ and $Fe2p_{1/2}$ respectively [39,40,90]. The satellite peaks could be assigned to Fe^{3+} in Fe_2O_3 which indicated the oxidation of Fe_3O_4 to Fe_2O_3. The oxidation state of Fe (Fe^{2+} and Fe^{3+}) was determined from the spectra peaks of $Fe2p_{3/2}$ and $Fe2p_{1/2}$ [229,288]. XPS results reconfirmed the findings of XRD, FTIR and SEM. The overall characterization revealed that the immobilized Fe_3O_4@ACF composite electrode was successfully synthesized for textile wastewater treatment application in BEF.

Electrochemical impedance spectroscopy (EIS) was employed to estimate the electron conductivity of ACF and immobilized Fe_3O_4@ACF electrodes in the BEF system. The solution resistance (Rs), charge transfer resistance (Rct), double layer capacitance (Cdl) and Warburg element (W) were represented by an equivalent circuit described in Fig. 6.6a (insert). The real and imaginary components of the impedance in the equivalent circuit were calculated according to Eqn. 6.8 and 6.9 respectively. The semicircle portion represents the charge-transfer resistance (Rct) and the linear portion represents the diffusion resistance (W) of the pristine CF, ACF and immobilized Fe_3O_4@ACF electrodes [90]. The ohmic resistance of the cathodes in the Nyquist plot (Fig. 6.6a) was associated with a high frequency intercept to the *x*-axis. At high and low impulse frequencies, the ohmic resistance and the surface charge transfer resistance of the Fe_3O_4@ACF composite cathode were 4.26 and 3.85 Ω which were significantly smaller than that of the ACF cathode (12.66 and 5.49 Ω) [28,90]. Similarly, EIS also explained in terms of frequency domain (Bode plot), i.e., the magnitude of the impedance as a function of frequency (10^{-5} to 10^{5} Hz) as described in Fig. 6.6b.

$$z' = \lim_{\omega \to 0 \text{ and } \omega \to \infty} \left(R_{\Omega} + \frac{R_{ct} + \sigma\omega^{-1/2}}{\left(\sigma\omega^{1/2}C_d + 1\right)^2 + \omega^2 C_d{}^2 \left(R_{ct} + \sigma\omega^{-1/2}\right)^2} \right) \tag{6.8}$$

$$z'' = \lim_{\omega \to 0 \text{ and } \omega \to \infty} \left(\frac{\omega C_d \left(R_{ct} + \sigma\omega^{-1/2}\right)^2 + \sigma^2 C_d + \sigma\omega^{-1/2}}{\left(\sigma\omega^{1/2}C_d + 1\right)^2 + \omega^2 C_d{}^2 \left(R_{ct} + \sigma\omega^{-1/2}\right)^2} \right) \tag{6.9}$$

where, z' and z'' are real and imaginary impedances of the electrodes, ω is frequency, C_d is double layer capacitance, R_{ct} is charge transfer resistance and σ is the ratio of ω^2 to C_d or the $\omega^2 \times (R_s - R_{ct})$

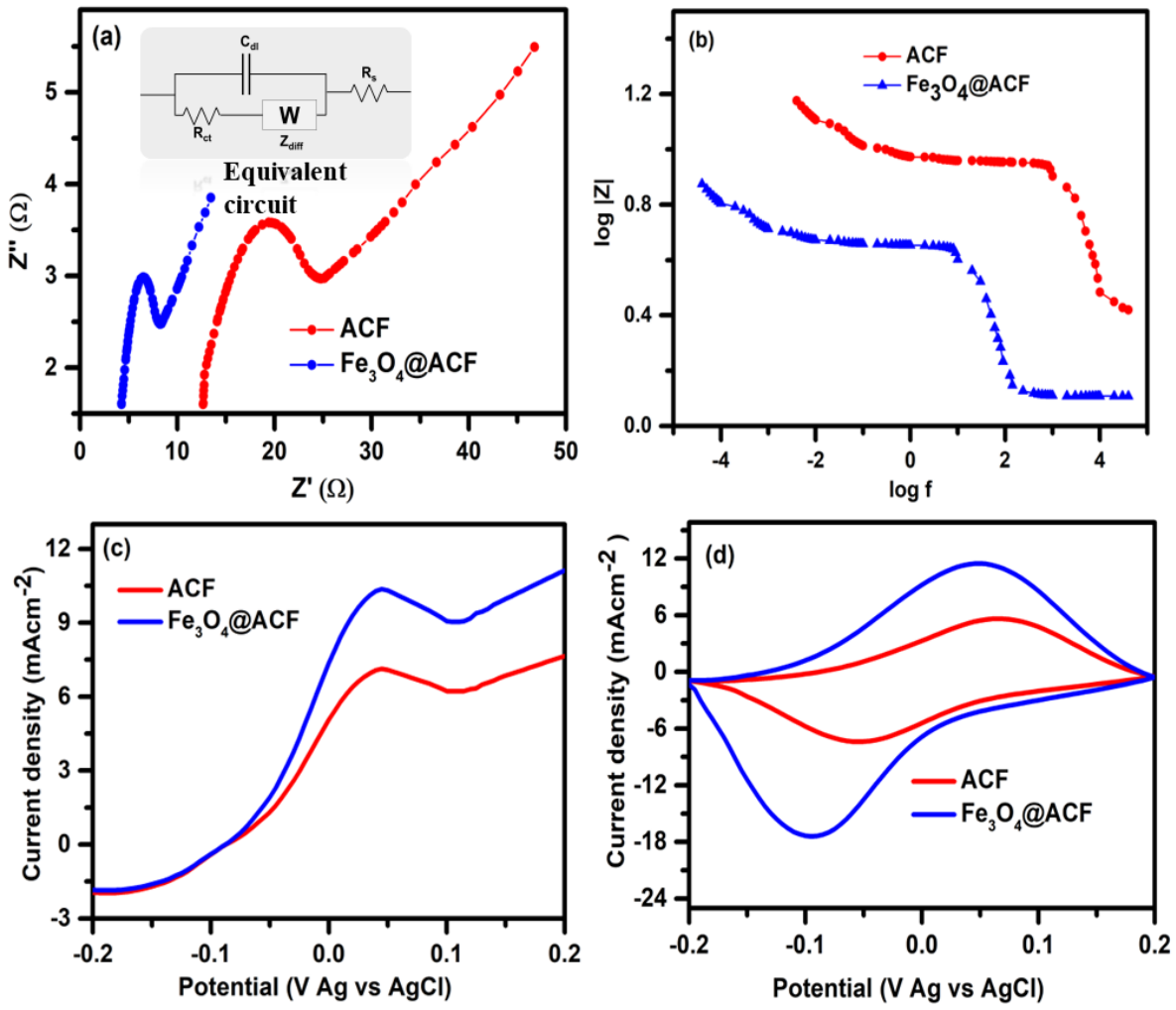

Figure 6.6: Electrochemical characterization

Nyquist plot (a) and Bode plot (b) *of* ACF and Fe_3O_4@ACF *electrodes* at 10^{-5} *to* 10^{5} *Hz and AC signal of 10 mV, LSV (c) and CV (d) of* ACF and Fe_3O_4@ACF *electrodes in* O_2 *saturated solution at a scan rate of 25 mV* s^{-1} *and 0.5 mg* L^{-1} Na_2SO_4

The result suggested that the remarkable decrease in interfacial resistance of Fe_3O_4@ACF was attributed to the impregnated Fe_3O_4 particles on the surface of ACF. Moreover, the significant decrease in the magnitude of the Nyquist arc in the Fe_3O_4@ACF cathode suggested a decrease in the electron transfer resistance. These results demonstrate that the Fe_3O_4@ACF could decrease the cathodic ohmic resistance and facilitate the kinetics of BEF reactions [101,121]. Here, it is proposed that the active electron transfer in the Fe_3O_4@ACF cathode was possibly attributed to the increased specific surface area as well as the fast and reversible redox reactions between the oxidation states of Fe^{+2} and Fe^{+3} in each potential range. Thus, minimizing the value of Rct is essential to maximize power delivery efficiency. The difference between the

origin to the initial start of the semicircle gives the solution resistance (Rs) [289]. The Rs values were influenced by electrolyte type, the pore size of the electrode, and initial concentration of the contaminant. LSV analysis was performed in some oxygen saturated Na_2SO_4 solution to confirm further the EIS results. As described in Fig. 6.6c, the Fe_3O_4@ACF cathode exhibited a stronger current response of 10.36 mA at 0.045 V, which was 31.2% higher than that of ACF (7.13 mA). In this case, 0.045 V was the reduction peak of Fe_3O_4@ACF where a molecular ORR took place on the surface of ACF. As a result, about 217.2 μmol L^{-1} H_2O_2 generation was observed as described in Appendix 6.1, which was much higher than that of H_2O_2 generated using ACF cathode alone [55,290].

The overall electrochemical analysis suggested that Fe_3O_4@ACF was an excellent electron transport facilitator from the Fe (Fe^{2+} and Fe^{3+}) electron channel to the ACF surface to stimulate more electrons to pass through the low-resistance gap of Fe_3O_4 [283,290]. Therefore, the Fe_3O_4@ACF cathode was utilized in the EF system for enhancement of H_2O_2 generation from the molecular reduction reaction of oxygen on its surface. Compared to the ACF cathode electrode, a higher amount of H_2O_2 generation was observed, which rapidly converted to ·OH radicals through a continuous interaction with active site of Fe_3O_4@ACF on the interface of the Fe_3O_4@ACF cathode. Cyclic voltammetry analysis was performed to further illustrate the mechanism of H_2O_2 generation and dyes oxidation using Fe_3O_4@ACF cathode in an oxygen saturated Na_2SO_4 solution. As shown in Fig. 6.6d, higher redox peaks were observed on Fe_3O_4@ACF cathode compared to ACF. The higher redox peaks in the Fe_3O_4@ACF cathode were due recycling of Fe_3O_4@ACF and $(Fe_3O_4@ACF)^+$ reactions which was a crucial step for the EF process for in situ H_2O_2 generation. In contrast, weak redox peaks were observed in the ACF cathode which could significantly reduce the electrochemical performance of the CBEF system for dye oxidation.

6.3.2. Catalytic Performance of BEF System

In most BEF studies, a proton exchange membrane was used to separate the anodic BES compartment from the cathodic EF compartment [276]. However, in this study, both BES and EF systems were prepared separately, and four electrodes were utilized to connect the two systems without a proton exchange membrane. An iron strip of bio-anode from BES was connected to the Fe_3O_4@ACF cathode of EFS and ACF of bio-cathode from BES was connected to the iron anode of EFS. To compare the performance of Fe_3O_4@ACF cathode to

ACF in EFS, independent tests were conducted for Fe_3O_4@ACF and ACF cathodes as Fe_3O_4@ACF-EFS and ACF-EFS respectively.

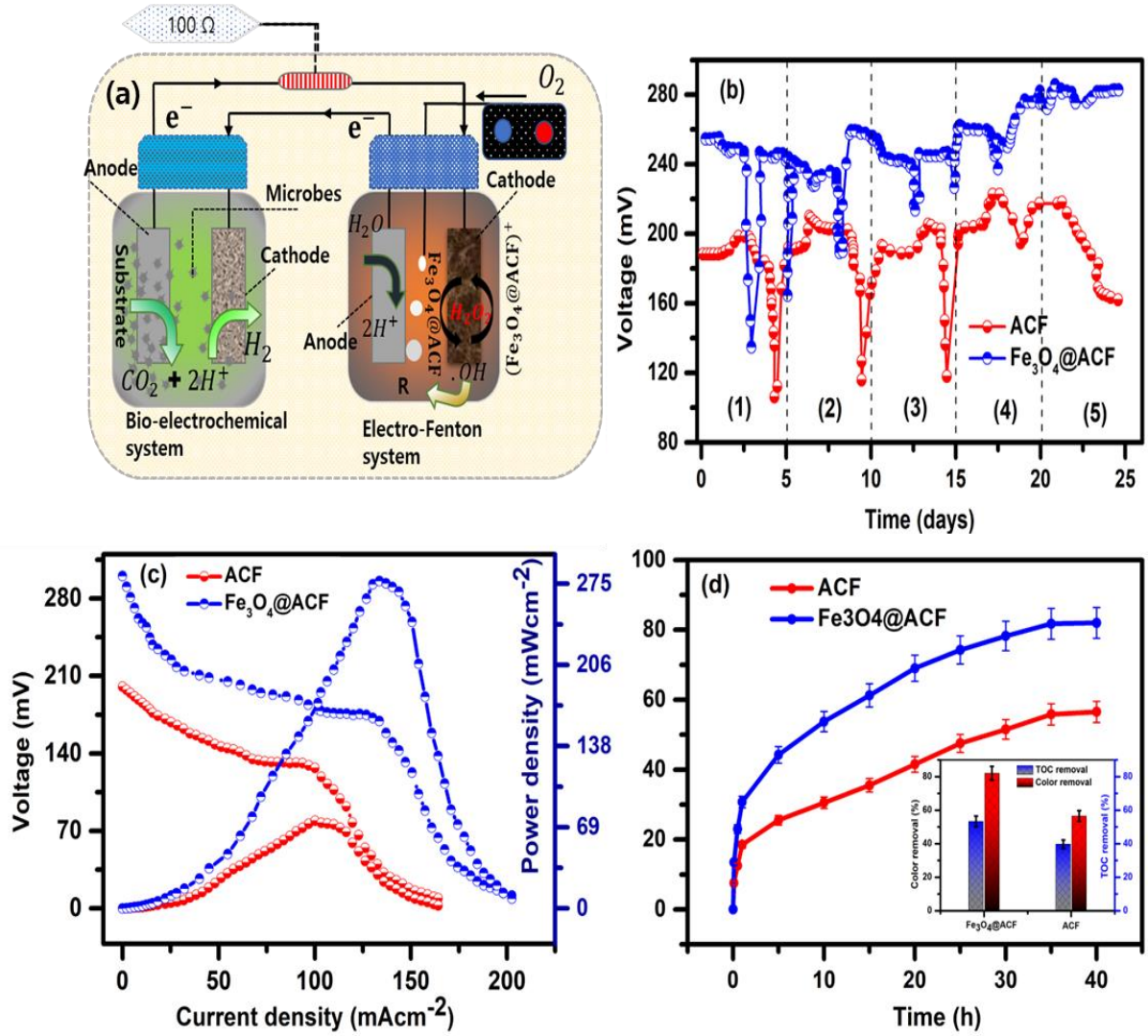

Figure 6.7: BEF configuration and MO oxidation

CBEF system configuration (a), Voltage-drop and power generation stabilization during opens circuit voltage of microbial metabolism over 25 days (b), Polarization curves (current density vs voltage drop and power density) (c) and simultaneous BES and EFS removal efficiency at pH 3, aeration rate 400 mL min^{-1}, external resistance 10 Ω, MO concentration 20 mg L^{-1}, operating time 40 h and 0.5 mg L^{-1} Na_2SO_4 (d) using ACF and Fe_3O_4@ACF *electrodes.*

The overall configuration of BES and EFS is described in Fig. 6.7a. In five phases, the open circuit voltage analysis of the BES was conducted for a period of 25 days. During the early start-up phase, the open circuit voltage was near 165 mV. The voltage was unstable and dependent on the microbial metabolism of the BES. In the late phases the microorganisms

adapted to their environment. Consequently, the open circuit voltage values of the BES unsteadily grew as seen in Fig. 6.7b. After the 5th phase, however, the open circuit voltage of the system became stable and maximum (near 280 mV). After the attainment of a steady state and a maximum open circuit voltage, the BES was connected to the EFS. Here, the BES was used as a source of energy for EF oxidation in the EFS. When the BES was connected to the EFS, the voltage started to decrease. The power density was tested using polarization curves and the maximum power density obtained with Fe_3O_4@ACF cathode was 275.2 ± 9.4 mW cm^{-2}, i.e., 75 ± 3.4% higher than that of ACF (68.93 ± 2.7 mW cm^{-2}) as shown in Fig. 6.7c. The reason for enhanced power density in Fe_3O_4@ACF was due to the use of highly conductive and nanosized Fe_3O_4 as a cathodic catalyst. This has improved the cathodic molecular ORR.

To determine the oxidation capability of the microbes for real sewage wastewater in the BES, the time-dependent oxidation of various water quality parameters such as TOC, COD, and NH_4^+-N was investigated. As shown in Appendix 6.2 the organic pollutants which could be a source of energy for microbes were oxidized in the anode solution. EFS oxidation of dye by EF was observed in parallel with sewage wastewater oxidation for TOC, COD and NH_4^+-N removal efficiency of 65.8%, 72.1%, and 68.4%, respectively. The enhancement of sewage wastewater oxidation in BES could be due to high electron and proton generation which corresponds to an increased 2e-ORR at EFS [291]. The use of Fe anodes positively contributed to better electrochemical sewage treatment owing to higher electron exchange. This resulted in enhanced anode potential that was conducive to enhanced microbial metabolism. Similarly, the time-dependent oxidation performance of EFS on MO EF oxidation was evaluated using Fe_3O_4@ACF and ACF cathodes. With a MO concentration of 20 mg L^{-1} and a retention time of 40 h, Fe_3O_4@ACF and ACF removed 82.1% and 56.5% MO, respectively, respectively (Fig. 6.7d). However, 53.3% and 39.7% of TOC removal were obtained using Fe_3O_4@ACF and ACF respectively as depicted in Fig. 6.7d (insert). Moreover, the internal resistance to electron flux in Fe_3O_4@ACF was 1.7 folds lower than ACF, which provides better electrical performance. The overall analysis indicated that the application of Fe_3O_4@ACF was not only used to initiate EF oxidation at EFS but also used to harvest electrons that were generated in BES due to microbial activities.

6.3.3. Effect of Operational Parameters

6.3.3.1. Effect of pH

As explained above, the molecular ORR and the function of H_2O_2 were affected by the pH value in EFS. To generate sufficient ·OH radicals, the ideal pH value should be higher than 2.8. However, at higher pH values (greater than 4) the formation of ·OH radicals were reduced due to the decomposition of H_2O_2 into H_2O and O_2. While, at a lower pH value, the generated ·OH radicals could be consumed by H^+ ions, leading to the formation of oxonium ions. The oxonium ion is a stable molecule that could hinder the formation of ·OH radicals [208]. As indicated in Fig. 6.8a, the rate of *MO* removal increased when the pH jumped from 2 to 3 but the oxidation efficiency fell as the pH continued to rise from 3 to 4 [186]. During the first 15 h, the *MO* oxidation efficiency was higher (62 ± 4.4%) at a pH value of 3.5 and subsequently underwent a similar trend to that of pH 3. Over 40 h contact time, the maximum *MO* oxidation efficiency at the pH values of 2.5, 3, 3.5 and 4 were 38.02 ± 3.5%, 82.2 ± 3.2%, 81.4 ± 2.8% and 60.8 ± 3% respectively.

6.3.3.2. Effect of External Resistance

The removal efficiency of *MO* was affected by varying the external resistance of the CBEF system. Keeping the *MO* concentration in the catholyte constant, the higher removal efficiency was observed at lower external resistances over 36 h contact time. While at higher external resistances, the removal efficiency of *MO* was dropped, i.e., at 10 Ω, the *MO* removal efficiency was 86.6 ± 3.2%, which was 30 ± 1.5% times higher than that of 10,000 Ω within 40 h. When the external resistance of the circuit was reduced, an increased number of electrons could travel from the BES to the EFS via the external circuit. This might cause the coupled system to generate a significant amount of current, and 2e-ORR could occur quickly at the surface of Fe_3O_4@ACF [292]. The *MO* oxidation efficiency at all external resistances after 40 h was above 60%. H_2O_2 is a Fenton reagent that is the source of ·OH formation. The correlation between external resistance and the generation of H_2O_2 was well documented by Sathe *et al.* [291]. Moreover, at higher external resistances, a significant potential drop occurred which affects the sewage wastewater oxidation. Consequently, the system could build a higher number of electrons favorable to methanogenic biofilm formation than exo-electrogenic microflora that interfere with electron transfer. This may also affect the generation of H_2O_2 at EFS and then the *MO* oxidation declined as shown in Fig. 6.8b.

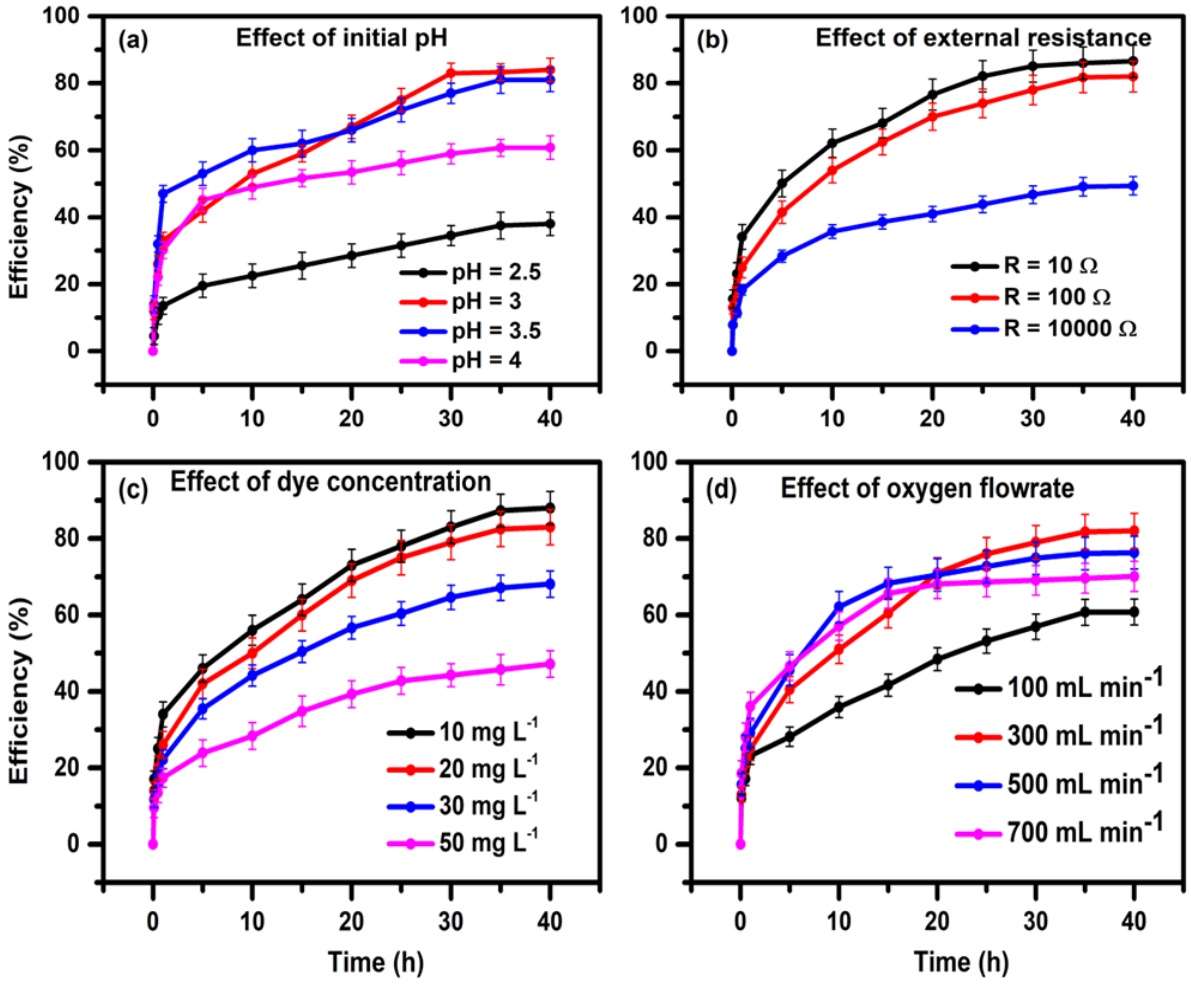

Figure 6.8: Effect of operational parameters on MO degradation

Effect of operational parameters on MO oxidation in CBEF system: effect of initial pH (a), effect of external resistance (b) effect of initial MO concentration (c) and effect of oxygen flowrate (d) at 0.5 mg L^{-1} Na_2SO_4, operating time 40 h and at different experimental conditions with ACF and Fe_3O_4@ACF *electrodes*

6.3.3.3. Effect Initial Dye Concentration

The amount of H_2O_2 that was produced on the electrode surface of Fe_3O_4@ACF was practically the same when all other parameters were kept constant or under optimal operating conditions [229]. As the initial *MO* concentration increased, the relative proportion of generation of ·OH in EFS was decreased, leading to a decline in the rate of organic dye oxidation [292]. The adaptability and performance of the coupled system were tested at various starting *MO* concentrations. As presented in Fig. 6.8c, the MO oxidation rate was nearly the same when the beginning dose of *MO* was between 10 mg L^{-1} (88 ± 4.3%) and 20 mg L^{-1} (84 ± 3.7%). At lower initial *MO* concentration doses (10 mg L^{-1}), the generated ·OH radicals were vigorous enough

to oxidize the recalcitrant organic dye quickly. However, the *MO* oxidation efficiency was significantly affected when the concentration exceeded 50 mg L^{-1} at which 47.2 ± 3.1% removal efficiency was observed over 40 h contact time. The possible explanation was that at low initial *MO* doses, the resulting ·OH radicals were sufficient to oxidize the *MO* molecules. However, at a higher *MO* dose, the generated ·OH radicals could reach the saturation point resulting in a slower oxidation rate. Therefore, the *MO* oxidation rate was maximum (88 ± 4.3%) at starting concentrations of 10 mg L^{-1}, and when the contact time was extended above 40 h, the oxidation rate did not vary significantly.

6.3.3.4. Effect Oxygen Flowrate

The two dominant molecular ORR are 2e-ORR and 4e-ORR. Depending on the cathodic material, molecular O_2 undergoes either 2e-ORR (Eqn. 6.10) to generate H_2O_2 or 4e-ORR (Eqn. 6.11) to produce H_2O at the cathodic surface. For this case, Fe_3O_4@ACF cathode was synthesized to favor in 2e-ORR mechanism than 4e-ORR.

$$O_2 + 2H^+ + 2e^- \rightarrow H_2O_2 \qquad E^0\ (\text{vs. SHE}) = 0.547\ V \qquad (6.10)$$

$$O_2 + 4H^+ + 4e^- \rightarrow H_2O \qquad E^0\ (\text{vs. SHE}) = 1.29\ V \qquad (6.11)$$

Moreover, the rate of H_2O_2 generation was determined by the rate at which O_2 undergoes a reduction by 2e-ORR on the cathode surface of Fe_3O_4@ACF. Hence, the rate of oxidation of MO was studied at various oxygen flow rates, i.e., 100 mL min^{-1}, 300 mL min^{-1}, 500 mL min^{-1} and 700 mL min^{-1}. At a lower aeration rate, the rate of oxygen transfer was slower. As a result, insufficient generation of H_2O_2 was observed on EFS and a slow rate of *MO* oxidation was recorded. On the contrary, an excessive aeration rate could decrease the amount of H_2O_2 generation, thereby decreasing the regeneration of ·OH radicals. Besides, the excess oxygen molecule could inhibit the active site of the *MO* molecule from being accessed by ·OH radicals. This could result in inefficient energy consumption for the air pump transfer operation [292]. As shown in Fig. 6.8d, within the first 5 h of contact time, higher *MO* oxidation efficiencies were observed at higher oxygen flow rates, i.e., 45.6 ± 4.1% and 48.4 ± 3.7% corresponding to 500 mL min^{-1} and 700 mL min^{-1} oxygen flow rates. However, after 20 h, higher *MO* oxidation efficiencies were recorded at lower oxygen flow rates. Thus, the oxidation efficiency of an initial *MO* concentration of 20 mg L^{-1} reached 82.5 ± 4.3% at a flow rate of 300 mL min^{-1} in EFS over 40 h.

Table 6.1: *Previously reported different cathode supported bio-electro-Fenton systems.*

Cathode	Source of inoculum	Oxidation efficiency (experimental condition)	Contaminants concentration	Ref
$Fe@Fe_2O_3$/ ACF	Anaerobic sludge	95% (pH 3, reaction time of 160 h, external resistance of 120 Ω, and aeration rate of 0.3 L min^{-1})	Rhodamine B (10 mg L^{-1})	[272]
Iron coated Carbon felt	-	85% (neutral pH, reaction time of 3 h, external resistance of 10 Ω) and reactor volume of 75 mL	Sodium dodecyl sulphate (20 mg L^{-1})	[291]
Graphite felt	Activated sludge	75% (pH 3, reaction time of 36 h, external resistance 100 Ω, aeration rate of 13.5 L min^{-1}) and reactor volume of 500 mL	Levofloxacin (20 mg L^{-1})	[292]
CNT/γ-FeOOH/stainless-steel-mesh	Activated sludge	95% (external resistance of 1000 Ω, aeration rate of 20 mL min^{-1}) and reactor volume of 28 mL	Sulfamethoxazole (25 mg L^{-1})	[121]
$FeVO_4$/CF	Wastewater	85% (8.8 mg L^{-1} TOC, 32.5 mg L^{-1} COD and 4.5 mg L^{-1} BOD concentrations) and reactor volume of 200 mL	Coal gasification wastewater	[122]
Fe_2O_3@ACF	Sewage wastewater	82.4% (pH 3.5, external resistance of 100 Ω, aeration rate of 300 L min^{-1}) and reactor volume of 250 mL	Methyl orange (20 mg L^{-1})	[This work]

Overall, these results demonstrate the importance of optimizing the pH, external resistance initial concentration and oxygen flow rate to achieve maximum oxidation efficiency in BES-EFS using a polarizable Fe_3O_4@ACF cathode. Furthermore, the study highlights the significance of understanding the underlying mechanisms involved in electro-Fenton systems to enhance their efficiency and potential application in wastewater treatment and other environmental remediation processes. Further research could explore the optimization of other parameters such as temperature, electrode materials, and catholyte concentration for enhancing the overall performance of BES-EFS in removing various types of organic pollutants from

wastewater. For comparison, different oxidation performances of BEF were listed in Table 6.1. Therefore, the CBEF system exhibited an acceptable oxidation performance in an acceptable oxidation range.

6.3.4. Stability of BEF and Reusability of the Cathode

The electron-generating capability of the activated sludge in the BES could limit the performance of *MO* oxidation in the EFS. To determine the stability performance of the coupled system, different experimental trials were conducted at pH 3.5, external resistance 100 Ω, initial *MO* dose 20 mg L^{-1} and oxygen flowrate 300 mL min^{-1}. Here, both the electrolyte solution of the EFS and the Cathode with Fe_3O_4@ACF have been replaced by a new electrolyte solution and the Fe_3O_4@ACF cathode at every 12 h. As presented in Fig. 6.9a, 79.5% *MO* oxidation efficiency was obtained at the end of the second cycle of EF oxidation and the efficiency of TOC removal was nearly 56.4%. During several cycles of *MO* oxidation, however, the oxidation efficiency steadily decreased and approximately 37.4% of *MO* was removed at the end of the fifth cycle and the percentage of TOC removed was nearly 28.6% (Fig. 6.9b). The main factor for decreasing the rate of *MO* oxidation at the fifth cycle was attributed to insufficient power generation of the BES due to depletion of nutrition. This was confirmed by refreshing the BES with a nutritional solution after 48 h. The system reassumed the power output and the oxidation rate of *MO* was fully recovered. As explained in numerous studies, the highest rate of oxidation in CBEF system was obtained by changing the nutrient solution every 48 h [291,292]. Therefore, over 48 h, the maximum microbial oxidation of the sewage wastewater in the BES in terms of TOC, COD and NH_4^+-N was determined to be 67.4 ± 3.6%, 71.2 ± 3.8% and 69.3 ± 3.7% respectively and presented in Fig. 6.9c. Within 48 hours, EFS had the highest MO oxidation rate and the maximum microbial metabolism and bio-oxidation efficiency.

Moreover, the stability of the electron conductivity of the electrode was another factor in *MO* oxidation. To examine the durability of the electrode (Fe_3O_4@ACF), different *MO* oxidation cycles were conducted every 48 h in the EFS at pH 3.5, external resistance 100 Ω, initial *MO* dose 20 mg L^{-1} and oxygen flowrate 300 mL min^{-1}.

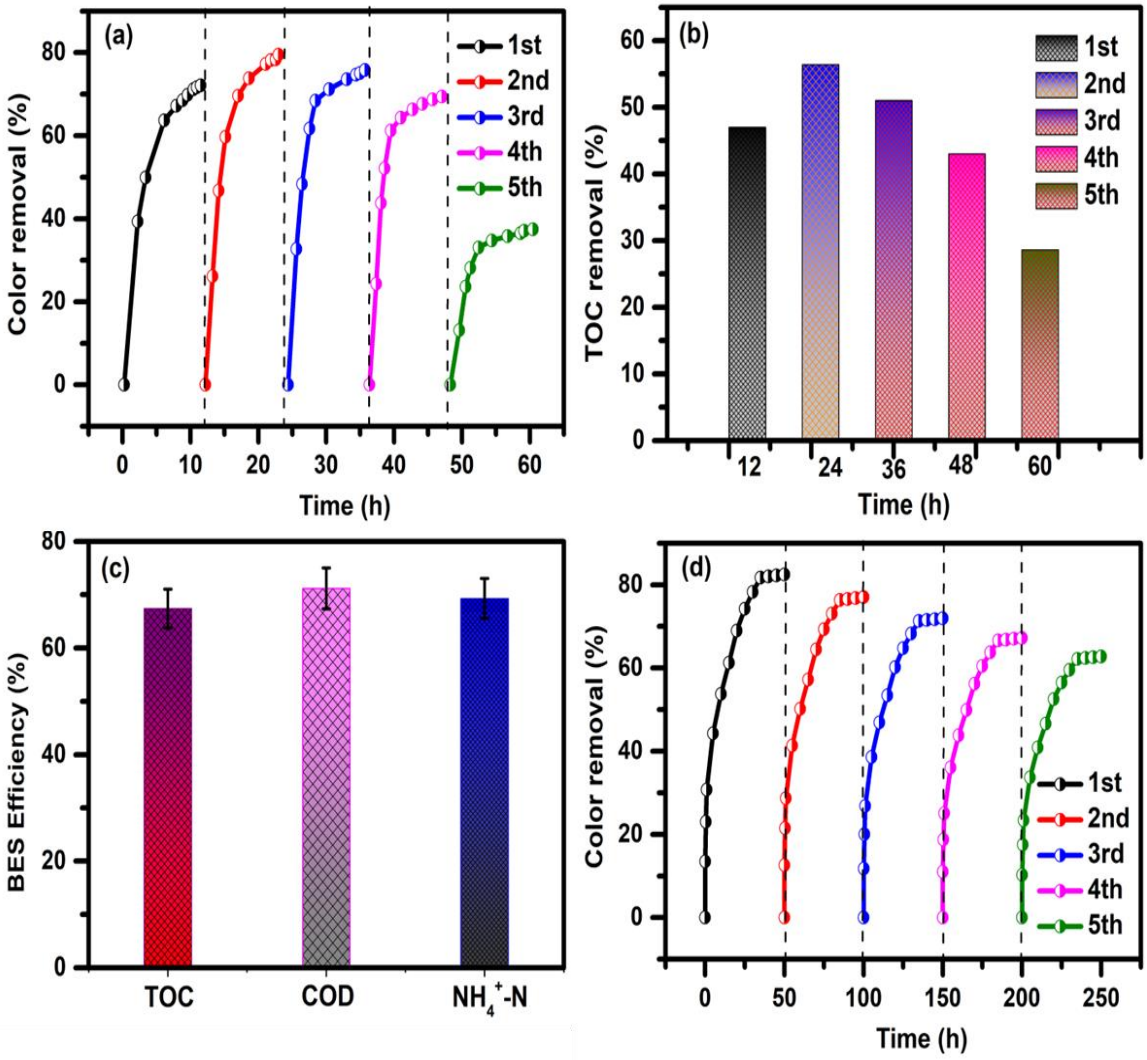

Figure 6.9: Stability of BEF and reusability of cathode

Stability of the CBEF system in terms of MO removal (a) and TOC removal at operating time of 40 h (b), sewage wastewater oxidation efficiency of BES in terms of TOC, COD and NH_4^+*-N (c) and reusability test of* Fe_3O_4@ACF *electrode* for five consecutive cycles over 40 h each (d) *at pH 3.5, aeration rate 300 mL* min^{-1}*, external resistance 100 Ω, MO concentration 20 mg* L^{-1}*, and 0.5 mg* L^{-1} Na_2SO_4

Here, the polarizable Fe_3O_4@ACF cathode was not changed but the electrolyte solution of the EFS and the nutritional media of the BES were replaced by a fresh nutrition every 48 h. Five experimental trials were conducted to explore the durability of the Fe_3O_4@ACF. The maximum *MO* oxidation (82.5 ± 3.2%) was obtained in the first cycle and then gradually reduced the functionality of the cathode. At the end of the fifth cycle 62.8 ± 2.8% removal efficiency was achieved over 48 h as described in Fig. 6.9d. Again, to check the detachment of the functional

iron from the surface of the electrodes, iron residue in the treated solution was quantified using ICP-OES and insignificant iron residues (1×10^{-4} g L^{-1}) were detected indicating that the Fe_3O_4@ACF cathode was stable and underwent limited iron leaching during the reaction. Thus, the experimental analysis conducted repeatedly revealed that the coupled BEF system was capable of oxidizing sewage wastewater and textile wastewater simultaneously in BES and EFS respectively. In addition, the stability of the system and functionality of the Fe_3O_4@ACF were evaluated, and the cathode was found to be an efficient tool for the treatment of industrial wastewater application.

6.3.5. Oxidation Pathway of MO

Direct EF oxidation and indirect oxidation are examples of reactive oxygen species (ROS) mediated electrochemical oxidation. In this study, indirect oxidation was considered and investigated using a chemical scavenger. 50 mL of 5 mmol L^{-1} isopropyl alcohol (IPA) was added to the coupled system to trap ·OH radicals and 50 mL of 5 mmol L^{-1} para-benzoquinone (*p*-BQ) was used to capture superoxide ion radical ($O_2^{\cdot-}$) [293]. As illustrated in Fig. 6.10a, when IPA was added, the removal rate of MO decreased from 83.5% to 27.8%, suggesting that the MO was oxidized largely by ·OH radicals in the EFS. However, 69.2% MO efficiency was obtained upon the addition of *p*-BQ, indicating that $O_2^{\cdot-}$ radicals were produced. Even though, H_2O_2 could be generated following the 2e-ORR mechanism (Eqn. 6.12), the direct oxidation of MO by H_2O_2 could be insufficient and demanded an activation step to generate ·OH radicals [209]. In the absence of activation, the generated H_2O_2 could dissociate to H_2O in the solution (Eqn. 6.13). The active site of the Fe_3O_4@ACF cathode was used to activate the H_2O_2 to regenerate ·OH radicals through Fe_3O_4@ACF-complexation, a Fenton-like reaction (Eqn. 6.14). The rate of H_2O_2 activation on the Fe_3O_4@ACF surface was proportional to the surface area of the Fe_3O_4@ACF cathode and the H_2O_2 concentration generated through 2e-ORR. The active site of the Fe_3O_4@ACF cathode continuously regenerated when enough H_2O_2 concentration was generated according to Eqn. 6.15.

Besides, H_2O_2 may dissociate to O_2 and H_2O at the surface of the Fe_3O_4@ACF and the efficiency of H_2O_2 was affected. However, the consumption of ·OH by MO could induce the activation of H_2O_2. The oxidation mechanism of MO was controlled by diffusion-based kinetics depending on adsorption, surface oxidation and desorption processes. Moreover, the

polarized Fe_3O_4@ACF cathode could enhance the removal rate of MO by enhancing the direct electro-oxidation due to the high electrical conductivity of iron particles [294].

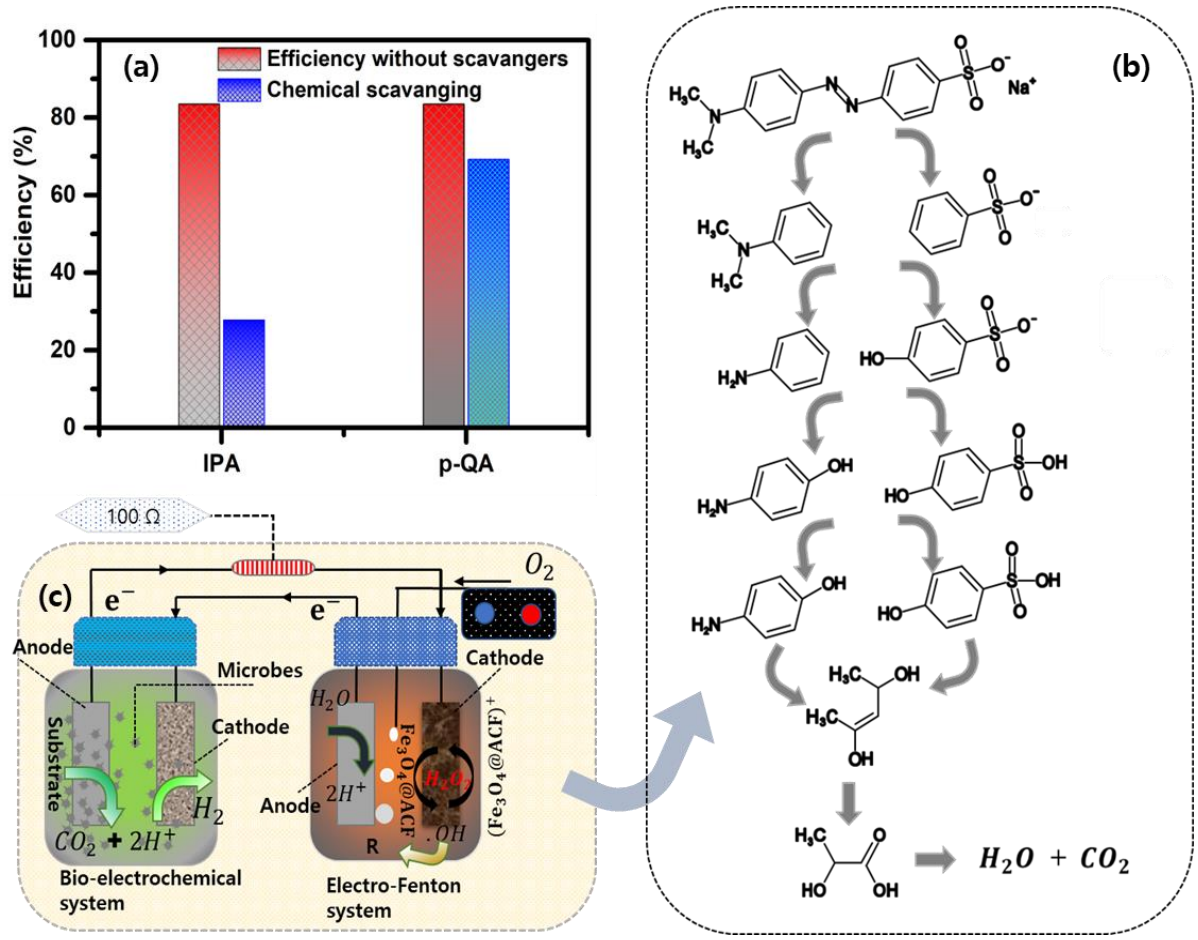

Figure 6.10: Chemical quenching of free radicals

Chemical quenching of free radicals in CBEF system at pH 3.5, aeration rate 300 mL min^{-1}, external resistance 100 Ω, MO concentration 20 mg L^{-1}, and 0.5 mg L^{-1} Na_2SO_4 (a), possible oxidation pathway of MO in the coupled system (b) and experimental set up (c)

Initially, the MO was transformed to organic radical by free radicals (·OH, $O_2^{\cdot-}$ and $HO_2^{\cdot}$), and further oxidized to carboxylic acids, aldehydes, ketose, or alcohols and eventually to inorganic ions, H_2O and CO_2 (Eqn. 6.16). The color of MO was associated with -N=N- which could be terminated when the bond was attacked by ·OH radicals. The azo bond (-N=N-) of MO was the first target for ·OH radicals attack [295]. If ·OH radicals exist in the reaction, hydroperoxyl radicals ($HO_2^{\cdot}$) and $O_2^{\cdot-}$ could also be generated by the active site of Fe_3O_4@ACF cathode using the surface-complex reaction (Eqn. 6.15). Additionally, $HO_2^{\cdot}$ was formed when the concentration of MO was insufficient to trap all the generated ·OH radicals (Eqn. 6.17). Eqn.

6.18 represented the acid-base conjugates of $HO_2^{\cdot}$ and $O_2^{\cdot -}$. These radicals are less reactive than ·OH and meanwhile reduced to H_2O_2, or oxidized to O_2 according to Eqn. 6.19 [22]. The biochemical oxidation mechanism of sewage wastewater in BES was described using the general expression for all organic compounds (Eqn. 6.20).

$$O_2 + 2H^+ + 2e^- \rightarrow H_2O_2 \quad (6.12)$$

$$H_2O_2 + 2H^+ + 2e^- \rightarrow 2H_2O \quad (6.13)$$

$$Fe_3O_4@ACF + H_2O_2 \rightarrow (Fe_3O_4@ACF)^+ + \cdot OH + OH^- \quad (6.14)$$

$$(Fe_3O_4@ACF)^+ + H_2O_2 \rightarrow Fe_3O_4@ACF + H^+ + HO_2^{\cdot} \quad (6.15)$$

$$\cdot OH + MO \rightarrow \text{inorganic ions} + H_2O + CO_2 \quad (6.16)$$

$$\cdot OH + H_2O_2 \rightarrow HO_2^{\cdot} + H_2O \quad (6.17)$$

$$HO_2^{\cdot} \leftrightarrow H^+ + O_2^{\cdot -} \quad (6.18)$$

$$\cdot OH + HO_2^{\cdot} \rightarrow H_2O + O_2 \quad (6.19)$$

$$C_xH_yO_z + (2x - z)H_2O \rightarrow xCO_2 + (y + 4x - 2z)H^+ + (y + 4x - 2z)e^- \quad (6.20)$$

The intermediate organic fragments and inorganic ions (NO_3^- and SO_4^{2-}) of MO were quantified using LC-MS and ICS respectively and presented in TableS1. According to the reaction mechanisms, LC-MS, and ICS results (Fig.6.11), a possible oxidation pathway of MO was proposed and described in Fig. 6.10b and Fig. 6.10c is the configuration of the coupled system.

One of the most energy-efficient approaches to oxidizing highly polluted wastewater is bio-electrochemical technology [266]. Even though combining one system with another wastewater treatment system was challenging, the coupled bio-electro-Fenton (BEF) system was configured using a polarizable Fe_3O_4@ACF functional cathode to oxidize MO. The coupled system generated about 275.2 ± 9.4 mW cm^{-2} power density and about 280 mV over 25 days. Keeping the MO concentration at 20 mg L^{-1} at 100 Ω external resistance, a pH value of 3.5 and an aeration rate of 300 mL min^{-1}, 82.5 ± 4.3% efficiency was achieved over 40 h. The Fe_3O_4@ACF cathode was demonstrated to be stable and durable. Based on electron transfer mechanisms and LC-MS analysis, a potential MO oxidation mechanism was proposed.

Apart from the MO oxidation in EFS, simultaneous sewage and wastewater oxidation was observed accompanied by TOC, COD and NH_4^+-N removal efficiency of 67.4 ± 3.6%, 71.2 ± 3.8% and 69.3 ± 3.7% respectively. The results showed that the coupled BES-EFS system achieved a satisfactory azo dye oxidation efficiency, indicating the synergistic effect of combining these two systems. Overall, the BES-EFS system demonstrated great potential for efficient and sustainable wastewater treatment, and further research could focus on optimizing the system for large-scale industrial applications and exploring its potential for treating other types of contaminants.

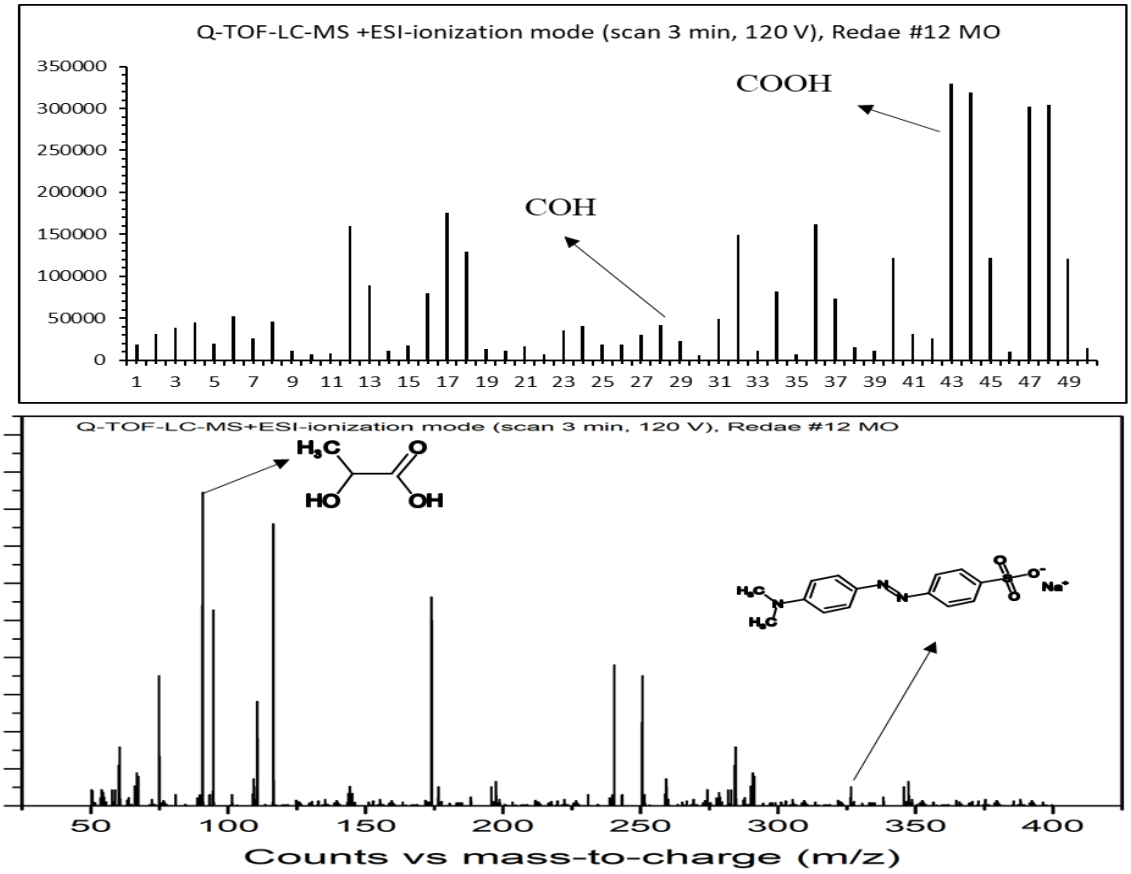

Figure 6.11: LC-MS analysis of MO oxidation

LC-MS analysis of MO that has been oxidized in CBEF with Fe_3O_4@ACF cathode at pH 3.5, aeration rate 300 mL min^{-1}, external resistance 100 Ω, MO concentration 20 mg L^{-1}, and 0.5 mg L^{-1} Na_2SO_4

6.4. Summery

Polarizable Fe_3O_4@ACF supported bio-electro-Fenton system was synthesized to generate 280 mV voltage and 275.2 ± 9.3 mW cm^{-2} power density.

CHAPTER 7

7. CONCLUSION AND RECOMMENDATION

7.1. Conclusion

As a conclusion, the dissertation has focused on the effectiveness of combining hetero-Fenton oxidation with bio-electro oxidation processes to treat textile wastewater, offering a new and sustainable way to deal with the environmental issues related to effluents from the textile industry. The goal of the study was to use the combined impacts of chemical and biological oxidation processes to improve wastewater treatment efficiency. The results of the study highlight the capability of the coupled bio-electro hetero-Fenton system to treat different types of organic pollutants found in textile wastewater. The coupled hetero-Fenton oxidation and biological processes showed higher treatment efficiency and increased organic pollutant degradation. The synergistic effects of coupled systems demonstrate the potential of this strategy as an effective and long-lasting way to remediate industrial wastewater. Additionally, the study of the critical factors affecting treatment effectiveness, such as pH, temperature, and electrode composition, offers insightful information for improving the architecture and functionality of coupled system.

The detailed analysis of the degradation kinetics and the identification of intermediate products contribute to understanding the basic principles underlying the treatment process. The findings of the study and environmental effect assessment demonstrate that the treated toxicity of the wastewater and pollutant levels have dramatically dropped, suggesting that the coupled bio-electro hetero-Fenton system may be used to meet stringent environmental regulations. The findings of this dissertation contribute to the growing corpus of research on wastewater treatment as we move toward a more sustainable future. In addition to lessening the environmental impact of textile wastewater, the effective application of this novel strategy may open the door for the establishment of integrated, environmentally responsible treatment plans for other industrial effluents. To sum up, by bridging the gap between biological and chemical treatment techniques, coupled bio-electro hetero-Fenton oxidation processes offer a viable

alternative for the sustainable treatment of textile wastewater. The knowledge acquired from this study aids in the continuous attempts to create effective, economical, and ecologically friendly wastewater treatment technologies.

7.2. Recommendation

Textile wastewater is an extremely complex matrix of salinity and alkalinity with a low BOD/COD ratio and the presence of hazardous chemicals. Optimizing the operational parameters could be the focus of future study and experimentation if the coupled system is to be deployed in an industrial level of wastewater treatment. This entails examining the impacts of various pH, temperature, electrode material, and initial contamination concentrations. Designing more reliable and effective treatment systems will be made easier with a full grasp of these parameters. Extended investigations to evaluate the robustness and stability of the coupled bio-electro hetero-Fenton system could be required. long-term performance of the coupled system should be examined to be used consistently and effectively in real-world situations. To determine whether the coupled system can be used on an industrial scale, scale-up experiments are recommended. The scalability, prospective upscaling challenges, and the financial impact of the technology on implementation must be considered. A comprehensive cost-benefit analysis should be performed to determine the economic viability of the recommended treatment choice. It is crucial to balance the costs of materials, energy, and maintenance with the benefits of improved wastewater treatment efficiency and compliance with environmental regulations.

It is appropriate to prolong the environmental impact assessment to analyze the overall ecological footprint of the treatment process. It is important to consider not only the immediate consequences on water quality but also any possible implications on soil, air, and the larger ecosystem. It is necessary to design strong monitoring and control mechanisms for the coupled system. It is recommended to use sensors and automation to provide real-time parameter monitoring, which will allow for adaptive control and treatment process optimization. It is advisable to look for potential partnerships in industry, academic institutions, and environmental organizations. Working together can result in the creation of creative solutions and make it easier to put the research findings into practice. The coupled system can help develop understanding of the field and make it easier to put the research on sustainable textile wastewater treatment into practice if these suggestions are taken into consideration.

REFERENCES

[1] Y. Jiang, W. Cai, P. Du, W. Pan, C. Wang, Virtual water in interprovincial trade with implications for China ' s water policy, J. Clean. Prod. 87 (2015) 655–665. https://doi.org/10.1016/j.jclepro.2014.10.074.

[2] M. Kahoush, N. Behary, V. Nierstrasz, Title page Bio-Fenton and Bio-electro-Fenton as sustainable methods for degrading organic pollutants in wastewater, (2017). https://doi.org/10.1016/j.procbio.2017.10.003.

[3] K. Paździor, L. Bilińska, S. Ledakowicz, A review of the existing and emerging technologies in the combination of AOPs and biological processes in industrial textile wastewater treatment, Chem. Eng. J. 376 (2019) 120597. https://doi.org/10.1016/j.cej.2018.12.057.

[4] F. Cnt, C. Cathode, Enhancement of Electrical Properties by a Composite Microbial Fuel Cell System, (2020) 3252–3257. https://doi.org/10.1166/jnn.2020.17372.

[5] A. Mosbah, I. Hadda, Recent advances in textile wastewater treatment using microbial consortia, 5 (2019) 134–146. https://doi.org/10.15406/jteft.2019.05.00194.

[6] Y. Chen, Y. Cheng, X. Gu, Y. Liu, J. Nie, C. Li, A Rapid Fenton treatment of bio-treated dyeing and finishing wastewater at second-scale intervals : kinetics by stopped-flow technique and application in a full-scale plant, (2019) 1–11. https://doi.org/10.1038/s41598-019-45948-9.

[7] Q. Dai, S. Zhang, H. Liu, J. Huang, L. Li, Bioelectrochemistry Sul fi de-mediated azo dye degradation and microbial community analysis in a single-chamber air cathode microbial fuel cell, 131 (2020). https://doi.org/10.1016/j.bioelechem.2019.107349.

[8] P.H. Nakhate, K.K. Moradiya, H.G. Patil, K. V Marathe, G.D. Yadav, Case study on sustainability of textile wastewater treatment plant based on lifecycle assessment approach, J. Clean. Prod. 245 (2020) 118929. https://doi.org/10.1016/j.jclepro.2019.118929.

[9] Y. Yoon, Y. Hwang, M. Kwon, Y. Jung, T. Hwang, J. Kang, Journal of Industrial and Engineering Chemistry Application of O 3 and O 3 / H 2 O 2 as post-treatment processes for color removal in swine wastewater from a membrane filtration system, 20 (2014) 2801–2805.

[10] Y.J. Jung, B.S. Oh, M. Koga, R. Shinohara, The degradation of diethyl phthalate (DEP) during ozonation : Oxidation by- products study ozonation : oxidation by-products study, (2010). https://doi.org/10.2166/wh.2009.301.

[11] J.F. Pérez, J. Llanos, C. Sáez, C. López, P. Cañizares, M.A. Rodrigo, Separation and Puri fi cation Technology On the design of a jet-aerated micro fl uidic fl ow-through reactor for wastewater treatment by electro-Fenton, Sep. Purif. Technol. 208 (2019) 123–129. https://doi.org/10.1016/j.seppur.2018.04.021.

[12] R. Carafa, L. Faggiano, A. Munné, A. Ginebreda, H. Guasch, M. Flo, L. Tirapu, P. Carsten, V. Der Ohe, Science of the Total Environment Water toxicity assessment and spatial pollution patterns identi fi cation in a Mediterranean River Basin District . Tools for water management and risk analysis, Sci. Total Environ. 409 (2011) 4269–4279. https://doi.org/10.1016/j.scitotenv.2011.06.053.

[13] M. Irfan, J. Kim, Fluorographite-co-polydimethylsiloxane coated polyvinylidene- fl uoride membrane for desalination of highly saline water with humic acid in direct contact membrane distillation, Environ. Res. 167 (2018) 255–266. https://doi.org/10.1016/j.envres.2018.07.029.

[14] J. Park, G. Moon, K. Shin, J. Kim, through ligand-to-metal charge transfer under visible light, Chem. Eng. J. 343 (2018) 689–698. https://doi.org/10.1016/j.cej.2018.01.078.

[15] J. Chaichanawong, T. Yamamoto, T. Ohmori, Enhancement effect of carbon adsorbent on ozonation of aqueous phenol, 175 (2010) 673–679. https://doi.org/10.1016/j.jhazmat.2009.10.062.

[16] J. Shim, H. Na, A. Jha, W. Jang, D. Jeong, I. Wook, Effect of preparation method on the oxygen vacancy concentration of, Chem. Eng. J. 306 (2016) 908–915. https://doi.org/10.1016/j.cej.2016.08.030.

[17] T. Lins, P. Dantas, H.J. José, R. De Fátima, P. Muniz, Fenton and Photo-Fenton oxidation of tannery wastewater, (2003). https://doi.org/10.4025/actascitechnol.v25i1.2254.

[18] E. Kusvuran, O. Gulnaz, A. Samil, M. Erbil, Detection of double bond-ozone stoichiometry by an iodimetric method during ozonation processes, 175 (2010) 410–416. https://doi.org/10.1016/j.jhazmat.2009.10.021.

[19] S. Venkateswarlu, M. Yoon, M.J. Kim, An environmentally benign synthesis of Fe3O4 nanoparticles to Fe3O4 nanoclusters: Rapid separation and removal of Hg(II) from an aqueous medium, Chemosphere. 286 (2022) 131673. https://doi.org/10.1016/j.chemosphere.2021.131673.

[20] W. Guo, Z. Fu, Z. Zhang, H. Wang, S. Liu, W. Feng, X. Zhao, J.P. Giesy, Synthesis of Fe3O4 magnetic nanoparticles coated with cationic surfactants and their applications in Sb(V) removal from water, Sci. Total Environ. 710 (2020) 136302. https://doi.org/10.1016/j.scitotenv.2019.136302.

[21] T. Yue, W. Sun, Y. Hu, Z. Xu, Mechanism of Goethite Precipitation on Magnetite and Maghemite Nanoparticles Studied by Surface Complexation/Precipitation Modeling, Langmuir. 34 (2018) 15134–15142. https://doi.org/10.1021/acs.langmuir.8b02571.

[22] S. Shukla, R. Khan, A. Daverey, Synthesis and characterization of magnetic nanoparticles, and their applications in wastewater treatment: A review, Environ. Technol. Innov. 24 (2021) 101924. https://doi.org/10.1016/j.eti.2021.101924.

[23] M. V. Arularasu, J. Devakumar, T. V. Rajendran, An innovative approach for green synthesis of iron oxide nanoparticles: Characterization and its photocatalytic activity, Polyhedron. 156 (2018) 279–290. https://doi.org/10.1016/j.poly.2018.09.036.

[24] M. Zhu, Y. Dai, Y. Wu, K. Liu, X. Qi, Y. Sun, Bandgap control of α-Fe2O3 nanozymes and their superior visible light promoted peroxidase-like catalytic activity, Nanotechnology. 29 (2018). https://doi.org/10.1088/1361-6528/aaddc2.

[25] K. Hamidian, A. Najafidoust, A. Miri, M. Sarani, Photocatalytic performance on degradation of Acid Orange 7 dye using biosynthesized un-doped and Co doped CeO2 nanoparticles, Mater. Res. Bull. 138 (2021) 111206. https://doi.org/10.1016/j.materresbull.2021.111206.

[26] H. Qiu, H. Yu, L. Wang, X. Zhu, M. Chen, L. Zhou, The burden of overall and cause-speci fi c respiratory morbidity due to ambient air pollution in Sichuan Basin , China : A multi-city time-series analysis, Environ. Res. 167 (2018) 428–436. https://doi.org/10.1016/j.envres.2018.08.011.

[27] S.S.U. Rahman, M.T. Qureshi, K. Sultana, W. Rehman, M.Y. Khan, M.H. Asif, M. Farooq, N. Sultana, Single step growth of iron oxide nanoparticles and their use as glucose biosensor, Results Phys. 7 (2017) 4451–4456. https://doi.org/10.1016/j.rinp.2017.11.001.

[28] M. Zuo, S. Yi, J. Choi, Excellent dye degradation performance of FeSiBP amorphous alloys by Fenton-like process, J. Environ. Sci. (China). 105 (2021) 116–127. https://doi.org/10.1016/j.jes.2020.12.032.

[29] W. Wang, Z. Xu, X. Zhang, A. Wimmer, E. Shi, Y. Qin, Rapid and e ffi cient removal of organic micropollutants from environmental water using a magnetic nanoparticles-attached fl uorographene-based sorbent, Chem. Eng. J. 343 (2018) 61–68. https://doi.org/10.1016/j.cej.2018.02.101.

[30] M. Pera-titus, V. Garc, M.A. Baños, J. Giménez, S. Esplugas, Degradation of chlorophenols by means of advanced oxidation processes : a general review, 47 (2004) 219–256. https://doi.org/10.1016/j.apcatb.2003.09.010.

[31] S.D.I. Scienze, Analysis of chemical degradation of caffeine in aqueous solution using an advanced oxidation process : Fenton ' s reagent and UV radiation, (2018).

[32] L. Baloo, M.H. Isa, N. Bin Sapari, A.H. Jagaba, L.J. Wei, S. Yavari, R. Razali, R. Vasu, Adsorptive removal of methylene blue and acid orange 10 dyes from aqueous solutions using oil palm wastes-derived activated carbons, Alexandria Eng. J. 60 (2021) 5611–5629. https://doi.org/10.1016/j.aej.2021.04.044.

[33] Z. Es'haghzade, E. Pajootan, H. Bahrami, M. Arami, Facile synthesis of Fe3O4 nanoparticles via aqueous based electro chemical route for heterogeneous electro-Fenton removal of azo dyes, J. Taiwan Inst. Chem. Eng. 71 (2017) 91–105. https://doi.org/10.1016/j.jtice.2016.11.015.

[34] L.J. Xu, W. Chu, N. Graham, Atrazine degradation using chemical-free process of USUV : Analysis of the micro-heterogeneous environments and the degradation mechanisms, 275 (2014) 166–174. https://doi.org/10.1016/j.jhazmat.2014.05.007.

[35] M. Kahoush, N. Behary, J. Guan, A. Cayla, B. Mutel, V. Nierstrasz, Genipin-mediated immobilization of glucose oxidase enzyme on carbon felt for use as heterogeneous catalyst in sustainable wastewater treatment, J. Environ. Chem. Eng. 9 (2021) 0–2. https://doi.org/10.1016/j.jece.2021.105633.

[36] M.A. Barakat, R. Kumar, E.C. Lima, M.K. Seliem, Facile synthesis of muscovite–supported Fe3O4 nanoparticles as an adsorbent and heterogeneous catalyst for effective removal of methyl orange: Characterisation, modelling, and mechanism, J. Taiwan Inst. Chem. Eng. 119 (2021) 146–157. https://doi.org/10.1016/j.jtice.2021.01.025.

[37] M. Chang, Y. hsin Shih, Synthesis and application of magnetic iron oxide nanoparticles on the removal of Reactive Black 5: Reaction mechanism, temperature and pH effects, J. Environ. Manage. 224 (2018) 235–242. https://doi.org/10.1016/j.jenvman.2018.07.021.

[38] V.A. Sakkas, A. Islam, C. Stalikas, T.A. Albanis, Photocatalytic degradation using design of experiments : A review and example of the Congo red degradation, 175 (2010) 33–44. https://doi.org/10.1016/j.jhazmat.2009.10.050.

[39] H.K. Sharma, S.K. Sharma, K. Vemula, A.R. Koirala, H.M. Yadav, B.P. Singh, CNT facilitated interfacial charge transfer of TiO2 nanocomposite for controlling the electron-hole recombination, Solid State Sci. 112 (2021) 106492. https://doi.org/10.1016/j.solidstatesciences.2020.106492.

[40] N. Nadeem, M. Yaseen, Z.A. Rehan, M. Zahid, R.A. Shakoor, A. Jilani, J. Iqbal, S. Rasul, I. Shahid, Coal fly ash supported CoFe2O4 nanocomposites: Synergetic Fenton-like and photocatalytic degradation of methylene blue, Environ. Res. 206 (2022) 112280. https://doi.org/10.1016/j.envres.2021.112280.

[41] Y. Lu, J. Wang, L. Wang, D. Zhao, S. Song, Construction of 3D carbon fiber/carbon nanotube/silicone rubber nanocomposites for stretchable conductors through interface host-guest dendrimers, Compos. Sci. Technol. 205 (2021) 108692. https://doi.org/10.1016/j.compscitech.2021.108692.

[42] A. Ding, D. Zhao, F. Ding, S. Du, H. Lu, M. Zhang, P. Zheng, E ff ect of inocula on performance of bio-cathode denitri fi cation and its microbial mechanism, 343 (2018) 399–407. https://doi.org/10.1016/j.cej.2018.02.119.

[43] T.X. Huong Le, M. Bechelany, M. Cretin, Carbon felt based-electrodes for energy and environmental applications: A review, Carbon N. Y. 122 (2017) 564–591. https://doi.org/10.1016/j.carbon.2017.06.078.

[44] S. Kanrar, S. Debnath, P. De, K. Parashar, K. Pillay, P. Sasikumar, Preparation , characterization and evaluation of fluoride adsorption efficiency from water of iron-

aluminium oxide-graphene oxide composite material, Chem. Eng. J. 306 (2016) 269–279. https://doi.org/10.1016/j.cej.2016.07.037.

[45] I. Sirés, E. Brillas, Upgrading and expanding the electro-Fenton and related processes, Curr. Opin. Electrochem. 27 (2021) 100686. https://doi.org/10.1016/j.coelec.2020.100686.

[46] B.T. Ergan, E. Gengec, Dye degradation and kinetics of online Electro-Fenton system with thermally activated carbon fiber cathodes, J. Environ. Chem. Eng. 8 (2020) 104217. https://doi.org/10.1016/j.jece.2020.104217.

[47] N. Saeidi, F.D. Kopinke, A. Georgi, Controlling adsorption of perfluoroalkyl acids on activated carbon felt by means of electrical potentials, Chem. Eng. J. 416 (2021) 129070. https://doi.org/10.1016/j.cej.2021.129070.

[48] Y. Zhang, N. Wang, P. Xue, Y. Liu, B. Tang, Z. Bai, Co 9 S 8 @ carbon nanospheres as high-performance anodes for sodium ion battery, Chem. Eng. J. 343 (2018) 512–519. https://doi.org/10.1016/j.cej.2018.03.048.

[49] E.S.J. Harris, S. Cao, B.A. Little, J.A. Craycroft, R. Scholten, T. Kaptchuk, Y. Fu, W. Wang, Y. Liu, H. Chen, Z. Zhao, J. Clardy, A.D. Woolf, D.M. Eisenberg, Science of the Total Environment Heavy metal and pesticide content in commonly prescribed individual raw Chinese Herbal Medicines, 409 (2011) 4297–4305. https://doi.org/10.1016/j.scitotenv.2011.07.032.

[50] J. Hou, J. Luo, Z. Hu, Y. Li, M. Mao, S. Song, Q. Liao, Q. Li, Tremendous effect of oxygen vacancy defects on the oxidation of arsenite to arsenate on cryptomelane-type manganese oxide, Chem. Eng. J. 306 (2016) 597–606. https://doi.org/10.1016/j.cej.2016.07.072.

[51] S.R. Nayak, K.N.S. Mohana, M.B. Hegde, K. Rajitha, A.M. Madhusudhana, S.R. Naik, Functionalized multi-walled carbon nanotube/polyindole incorporated epoxy: An effective anti-corrosion coating material for mild steel, J. Alloys Compd. 856 (2021). https://doi.org/10.1016/j.jallcom.2020.158057.

[52] E. Benetto, C. Jury, E. Igos, J. Carton, P. Hild, Using atmospheric plasma to design multilayer fi lm from polylactic acid and thermoplastic starch : a screening Life Cycle Assessment, 87 (2015) 953–960. https://doi.org/10.1016/j.jclepro.2014.10.056.

[53] M.M. Smarr, K. Kannan, L. Sun, M. Honda, W. Wang, R. Karthikraj, Z. Chen, J. Weck, G.M. Buck, Preconception seminal plasma concentrations of endocrine disrupting chemicals in relation to semen quality parameters among male partners planning for pregnancy, Environ. Res. 167 (2018) 78–86. https://doi.org/10.1016/j.envres.2018.07.004.

[54] M. Kim, Y.E. Song, J.Q. Xiong, K.Y. Kim, M. Jang, B.H. Jeon, J.R. Kim, Electrochemical detection and simultaneous removal of endocrine disruptor, bisphenol A using a carbon felt electrode, J. Electroanal. Chem. 880 (2021) 114907. https://doi.org/10.1016/j.jelechem.2020.114907.

[55] B. Li, Z.Y. Yan, X.N. Liu, C. Tang, J. Zhou, X.Y. Wu, P. Wei, H.H. Jia, X.Y. Yong, Enhanced Bio-Electro-Fenton degradation of phenolic compounds based on a novel Fe–Mn/Graphite felt composite cathode, Chemosphere. 234 (2019) 260–268. https://doi.org/10.1016/j.chemosphere.2019.06.054.

[56] I. Koyuncu, D. Topacik, E. Yuksel, Reuse of reactive dyehouse wastewater by nanofiltration : process water quality and economical implications, 36 (2004) 77–85. https://doi.org/10.1016/S1383-5866(03)00154-0.

[57] J. Ali, L. Wang, H. Waseem, R. Djellabi, N.A. Oladoja, G. Pan, FeS @ rGO nanocomposites as electrocatalysts for enhanced chromium removal and clean energy generation by microbial fuel cell, Chem. Eng. J. 384 (2020) 123335. https://doi.org/10.1016/j.cej.2019.123335.

[58] Q. Yang, F. Yao, Y. Zhong, D. Wang, F. Chen, J. Sun, S. Hua, S. Li, X. Li, Catalytic and electrocatalytic reduction of perchlorate in water – A review, Chem. Eng. J. 306 (2016) 1081–1091. https://doi.org/10.1016/j.cej.2016.08.041.

[59] C. Liu, Y. Liu, Z. Dang, S. Zeng, C. Li, Enhancement of heterogeneous photo-Fenton performance of core-shell structured boron-doped reduced graphene oxide wrapped magnetical Fe3O4 nanoparticles: Fe(II)/Fe(III) redox and mechanism, Appl. Surf. Sci. 544 (2021) 148886. https://doi.org/10.1016/j.apsusc.2020.148886.

[60] B. Tserengombo, H. Jeong, A. Delgado, E. Dolgor, S. Kim, The alkaline synthesizing method for improved thermal characteristics of CNT/alumina nanocomposite, Diam. Relat. Mater. 109 (2020) 108082. https://doi.org/10.1016/j.diamond.2020.108082.

[61] T. Guo, J. Du, J. Wu, S. Wang, J. Li, Structure and kinetic investigations of surface-stepped CeO 2 -supported Pd catalysts for low-concentration methane oxidation, Chem. Eng. J. 306 (2016) 745–753. https://doi.org/10.1016/j.cej.2016.08.020.

[62] Z. Izadiyan, K. Shameli, M. Miyake, H. Hara, S.E.B. Mohamad, K. Kalantari, S.H.M. Taib, E. Rasouli, Cytotoxicity assay of plant-mediated synthesized iron oxide nanoparticles using Juglans regia green husk extract, Arab. J. Chem. 13 (2020) 2011–2023. https://doi.org/10.1016/j.arabjc.2018.02.019.

[63] C. Santhosh, V. Velmurugan, G. Jacob, S. Kwan, A. Nirmala, A. Bhatnagar, Role of nanomaterials in water treatment applications : A review, Chem. Eng. J. 306 (2016) 1116–1137. https://doi.org/10.1016/j.cej.2016.08.053.

[64] A. Asghar, A. Aziz, A. Raman, W. Mohd, A. Wan, Advanced oxidation processes for in-situ production of hydrogen peroxide / hydroxyl radical for textile wastewater treatment : a review, J. Clean. Prod. 87 (2015) 826–838. https://doi.org/10.1016/j.jclepro.2014.09.010.

[65] X. Li, X. Jin, N. Zhao, I. Angelidaki, Y. Zhang, Novel bio-electro-Fenton technology for azo dye wastewater treatment using microbial reverse-electrodialysis electrolysis cell, Bioresour. Technol. 228 (2017) 322–329. https://doi.org/10.1016/j.biortech.2016.12.114.

[66] G.G. Gelebo, F.E. Ahmed, Removal of direct and reactive dyes from textile wastewater using Moringa stenopetala seed extract, 5 (2019) 184–191. https://doi.org/10.15406/jteft.2019.05.00200.

[67] J.R.S. Carvalho, F.M. Amaral, L. Florencio, M.T. Kato, T.P. Delforno, S. Gavazza, Chemosphere Microaerated UASB reactor treating textile wastewater : The core microbiome and removal of azo dye Direct Black 22, Chemosphere. 242 (2020) 125157. https://doi.org/10.1016/j.chemosphere.2019.125157.

[68] A.K. Pathak, R. Kothari, V. V Tyagi, S. Anand, ScienceDirect Integrated approach for textile industry wastewater for efficient hydrogen production and treatment through solar PV electrolysis, Int. J. Hydrogen Energy. (2020). https://doi.org/10.1016/j.ijhydene.2020.03.079.

[69] I. Chakraborty, S.M. Sathe, C.N. Khuman, M.M. Ghangrekar, Materials Science for Energy Technologies Bioelectrochemically powered remediation of xenobiotic compounds and heavy metal toxicity using microbial fuel cell and microbial electrolysis cell, Mater. Sci. Energy Technol. 3 (2020) 104–115. https://doi.org/10.1016/j.mset.2019.09.011.

[70] R. Changotra, H. Rajput, A. Dhir, Journal of Photochemistry & Photobiology A : Chemistry Treatment of real pharmaceutical wastewater using combined approach of Fenton applications and aerobic biological treatment, J. Photochem. Photobiol. A Chem. 376 (2019) 175–184. https://doi.org/10.1016/j.jphotochem.2019.02.029.

[71] L. Lai, J. Yan, J. Li, B. Lai, Co / Al 2 O 3 -EPM as peroxymonosulfate activator for sulfamethoxazole removal : Performance , biotoxicity , degradation pathways and mechanism, Chem. Eng. J. 343 (2018) 676–688. https://doi.org/10.1016/j.cej.2018.01.035.

[72] A.A. Ahmad, B.H. Hameed, Fixed-bed adsorption of reactive azo dye onto granular activated carbon prepared from waste, 175 (2010) 298–303. https://doi.org/10.1016/j.jhazmat.2009.10.003.

[73] L. Garavaglia, S.B. Cerdeira, D.L. Vullo, Chromium (VI) biotransformation by □ - and □ -Proteobacteria from natural polluted environments : A combined biological and chemical treatment for industrial wastes, 175 (2010) 104–110. https://doi.org/10.1016/j.jhazmat.2009.09.134.

[74] K.Y. Foo, B.H. Hameed, Detoxification of pesticide waste via activated carbon adsorption process, 175 (2010) 1–11. https://doi.org/10.1016/j.jhazmat.2009.10.014.

[75] A.L. Ahmad, S. Sumathi, B.H. Hameed, Coagulation of residue oil and suspended solid in palm oil mill effluent by chitosan , alum and PAC, 118 (2006) 99–105. https://doi.org/10.1016/j.cej.2006.02.001.

[76] C. Liu, Y. Guo, X. Wei, C. Wang, M. Qu, D.W. Schubert, An outstanding antichlorine and antibacterial membrane with quaternary ammonium salts of alkenes via in situ polymerization for textile wastewater treatment, Chem. Eng. J. 384 (2020) 123306. https://doi.org/10.1016/j.cej.2019.123306.

[77] M. Hassan, N. Pous, B. Xie, J. Colprim, M.D. Balaguer, S. Puig, Influence of iron species on integrated microbial fuel cell and electro-Fenton LEQUiA , Institute of the Environment , University of Girona , C / Maria Aurelia Type of contribution : Research article, Chem. Eng. J. (2017). https://doi.org/10.1016/j.cej.2017.07.025.

[78] M.M. Bello, A.A. Abdul Raman, A. Asghar, A review on approaches for addressing the limitations of Fenton oxidation for recalcitrant wastewater treatment, Process Saf. Environ. Prot. 126 (2019) 119–140. https://doi.org/10.1016/j.psep.2019.03.028.

[79] L. Bilińska, M. Gmurek, S. Ledakowicz, L. Bilin, Comparison between industrial and simulated textile wastewater treatment by AOPs – Biodegradability , toxicity and cost assessment, Chem. Eng. J. 306 (2016) 550–559. https://doi.org/10.1016/j.cej.2016.07.100.

[80] A. Yurtsever, E. Sahinkaya, Ç. Özer, Journal of Water Process Engineering Performance and foulant characteristics of an anaerobic membrane bioreactor treating real textile wastewater, 33 (2020). https://doi.org/10.1016/j.jwpe.2019.101088.

[81] T.B. Tafesse, A. Kassa, The Physico-Chemical Studies of Wastewater in Hawassa Textile Industry The Physico-Chemical Studies of Wastewater in Hawassa Textile Industry, (2015). https://doi.org/10.4172/2380-2391.

[82] T.B. Tafesse, A.K. Yetemegne, S. Kumar, Journal of Environmental Analytical The Physico-Chemical Studies of Wastewater in Hawassa Textile Industry, 2 (2015) 2–7. https://doi.org/10.4172/2380-2391.

[83] J. Luo, Y. Wang, D. Cao, K. Xiao, T. Guo, X. Zhao, Enhanced photoelectrocatalytic degradation of 2 , 4-dichlorophenol by TiO 2 /, 343 (2018) 69–77. https://doi.org/10.1016/j.cej.2018.02.120.

[84] H. Nadais, X. Li, N. Alves, C. Couras, H. Rasmus, Bio-electro-Fenton process for the degradation of Non-Steroidal Anti- In fl ammatory Drugs in wastewater, Chem. Eng. J. 338 (2018) 401–410. https://doi.org/10.1016/j.cej.2018.01.014.

[85] A. Sharma, J. Ahmad, S.J.S. Flora, Application of advanced oxidation processes and toxicity assessment of transformation products, Environ. Res. 167 (2018) 223–233. https://doi.org/10.1016/j.envres.2018.07.010.

[86] D.B. Miklos, C. Remy, M. Jekel, K.G. Linden, U. Hübner, Evaluation of advanced oxidation processes for water and wastewater treatment e A critical review, 139 (2018) 118–131. https://doi.org/10.1016/j.watres.2018.03.042.

[87] G.D. Bhowmick, I. Chakraborty, M.M. Ghangrekar, A. Mitra, Bioresource Technology Reports TiO 2 / Activated carbon photo cathode catalyst exposed to ultraviolet radiation to enhance the e ffi cacy of integrated microbial fuel cell-membrane bioreactor, Bioresour. Technol. Reports. 7 (2019) 100303. https://doi.org/10.1016/j.biteb.2019.100303.

[88] H.J. Jos, A.E. Rodrigues, R.F.P.M. Moreira, Treatment of textile wastewater by heterogeneous Fenton process using a new composite Fe 2 O 3 / carbon, 118 (2006) 77–82. https://doi.org/10.1016/j.cej.2006.01.016.

[89] L. Zhang, H. Tao, Bioelectro-Fenton System for Environmental Pollutant Degradation, (2019). https://doi.org/10.1007/978-981-10-8542-0.

[90] Y. Gao, W. Zhu, C. Wang, X. Zhao, M. Shu, J. Zhang, H. Bai, Enhancement of oxygen reduction on a newly fabricated cathode and its application in the electro-Fenton process, Electrochim. Acta. 330 (2020) 135206. https://doi.org/10.1016/j.electacta.2019.135206.

[91] F. Sun, H. Liu, H. Wang, D. Shu, T. Chen, X. Zou, F. Huang, D. Chen, Science of the Total Environment A novel discovery of a heterogeneous Fenton-like system based on natural siderite : A wide range of pH values from 3 to 9, Sci. Total Environ. 698 (2020) 134293. https://doi.org/10.1016/j.scitotenv.2019.134293.

[92] H. Olvera-vargas, B. Zhang, M. Hassan, H. Olvera-vargas, X. Zhu, B. Zhang, Y. He, Microbial electro-Fenton : An emerging and energy-efficient platform for environmental remediation Microbial electro-Fenton : An emerging and energy-efficient platform for environmental remediation, J. Power Sources. 424 (2019) 220–244. https://doi.org/10.1016/j.jpowsour.2019.03.112.

[93] S. V Niveditha, R. Gandhimathi, Chemosphere Flyash augmented Fe 3 O 4 as a heterogeneous catalyst for degradation of stabilized land fi ll leachate in Fenton process, Chemosphere. 242 (2020) 125189. https://doi.org/10.1016/j.chemosphere.2019.125189.

[94] S. Thor, L. Ho, S. Ong, N. Nordin, Y. Ong, Explicating the Importance of Aeration and pH for Amaranth Degradation and Electricity Generation in a Viable Hybrid System of Photocatalytic Fuel Cell and Electro-Fenton Process, Sep. Purif. Technol. (2020) 116535. https://doi.org/10.1016/j.seppur.2020.116535.

[95] G. Matyszczak, S. Agata, Dyes and Pigments Comparative degradation of Metanil Yellow in the electro-Fenton process with different catalysts : A simplified kinetic model study, 174 (2020) 3–8. https://doi.org/10.1016/j.dyepig.2019.108076.

[96] Y. Jiang, L. Soon, C. Lim, C. Pan, W. Jern, Bioresource Technology Reports E ff ect of free ammonia inhibition on process recovery of partial nitritation in a membrane bioreactor, Bioresour. Technol. Reports. 6 (2019) 152–158. https://doi.org/10.1016/j.biteb.2019.02.014.

[97] J. Lim, M.R. Ho, Substrate oxidation enhances the electrochemical production of hydrogen peroxide, 374 (2019) 958–964. https://doi.org/10.1016/j.cej.2019.05.165.

[98] F. Yu, Y. Wang, H. Ma, Enhancing the yield of H 2 O 2 from oxygen reduction reaction performance by hierarchically porous carbon modified active carbon fiber as an effective cathode used in electro-Fenton, J. Electroanal. Chem. 838 (2019) 57–65. https://doi.org/10.1016/j.jelechem.2019.02.036.

[99] W. Zhou, L. Rajic, L. Chen, K. Kou, Y. Ding, X. Meng, Y. Wang, B. Mulaw, J. Gao, Y. Qin, A.N. Alshawabkeh, Electrochimica Acta Activated carbon as effective cathode material in iron-free Electro-Fenton process : Integrated H 2 O 2 electrogeneration ,

activation , and pollutants adsorption, Electrochim. Acta. 296 (2019) 317–326. https://doi.org/10.1016/j.electacta.2018.11.052.

[100] S. Cho, A. Jang, P.L. Bishop, S. Moon, Kinetics determination of electrogenerated hydrogen peroxide (H 2 O 2) using carbon fiber microelectrode in electroenzymatic degradation of phenolic compounds, 175 (2010) 253–257. https://doi.org/10.1016/j.jhazmat.2009.09.157.

[101] P. Cao, X. Quan, K. Zhao, S. Chen, H. Yu, J. Niu, Selective electrochemical H 2 O 2 generation and activation on a bifunctional catalyst for heterogeneous electro-Fenton catalysis, J. Hazard. Mater. 382 (2020) 121102. https://doi.org/10.1016/j.jhazmat.2019.121102.

[102] S.O. Ganiyu, M. Zhou, C.A. Martínez-huitle, Paper submitted to Applied Catalysis B : Environmental for consideration SC, "Applied Catal. B, Environ. (2018). https://doi.org/10.1016/j.apcatb.2018.04.044.

[103] R. Zou, I. Angelidaki, B. Jin, Y. Zhang, Feasibility and applicability of the scaling-up of bio-electro-Fenton system for textile wastewater treatment, Environ. Int. 134 (2020) 105352. https://doi.org/10.1016/j.envint.2019.105352.

[104] M. Hassan, H. Olvera-vargas, X. Zhu, B. Zhang, Y. He, Microbial electro-Fenton : An emerging and energy-e ffi cient platform for environmental remediation, 424 (2019) 220–244. https://doi.org/10.1016/j.jpowsour.2019.03.112.

[105] D. Yuan, C. Zhang, S. Tang, X. Li, J. Tang, Y. Rao, Z. Wang, Enhancing CaO 2 fenton-like process by Fe (II) -oxalic acid complexation for organic wastewater treatment, Water Res. 163 (2019) 114861. https://doi.org/10.1016/j.watres.2019.114861.

[106] S.Y. Guvenc, Optimization of COD removal from leachate nanofiltration concentrate using H 2 O 2 / Fe + 2 / heat – Activated persulfate oxidation processes, Process Saf. Environ. Prot. 126 (2019) 7–17. https://doi.org/10.1016/j.psep.2019.03.034.

[107] Y. Liu, K. Li, W. Xu, B. Du, Q. Wei, B. Liu, D. Wei, Science of the Total Environment GO / PEDOT : NaPSS modified cathode as heterogeneous electro-Fenton pretreatment and subsequently aerobic granular sludge biological degradation for dye wastewater treatment, Sci. Total Environ. 700 (2020) 134536. https://doi.org/10.1016/j.scitotenv.2019.134536.

[108] G. Eshaq, S. Wang, H. Sun, M. Sillanpää, Separation and Puri fi cation Technology Core / shell FeVO 4 @ BiOCl heterojunction as a durable heterogeneous Fenton catalyst for the e ffi cient sonophotocatalytic degradation of p-nitrophenol, Sep. Purif. Technol. 231 (2020) 115915. https://doi.org/10.1016/j.seppur.2019.115915.

[109] S. Jor, S. Pourfadakari, B. Kakavandi, A new approach in sono-photocatalytic degradation of recalcitrant textile wastewater using MgO @ Zeolite nanostructure under UVA irradiation, 343 (2018) 95–107. https://doi.org/10.1016/j.cej.2018.02.067.

[110] A.P.M. Alves, Chemosphere Vermiculite as heterogeneous catalyst in electrochemical Fenton- based processes : Application to the oxidation of Ponceau SS dye, 240 (2020). https://doi.org/10.1016/j.chemosphere.2019.124838.

[111] Y. Liu, H. Guo, Y. Zhang, W. Tang, X. Cheng, W. Li, Heterogeneous activation of peroxymonosulfate by sillenite Bi 25 FeO 40 : Singlet oxygen generation and degradation for aquatic levo fl oxacin, Chem. Eng. J. 343 (2018) 128–137. https://doi.org/10.1016/j.cej.2018.02.125.

[112] A. Xu, B. He, H. Yu, W. Han, J. Li, J. Shen, X. Sun, L. Wang, Electrochimica Acta A facile solution to mature cathode modi fi ed by hydrophobic dimethyl silicon oil (DMS) layer for electro-Fenton processes : Water proof and enhanced oxygen transport, Electrochim. Acta. 308 (2019) 158–166. https://doi.org/10.1016/j.electacta.2019.04.047.

[113] N. Xu, Y. Zhang, H. Tao, S. Zhou, Y. Zeng, Bioresource Technology Bio-electro-Fenton system for enhanced estrogens degradation, Bioresour. Technol. 138 (2013) 136–140. https://doi.org/10.1016/j.biortech.2013.03.157.

[114] M. Hassan, G.A. Ashraf, B. Zhang, Y. He, G. Shen, S. Hu, Energy-efficient degradation of antibiotics in microbial electro-Fenton system catalysed by M-type strontium hexaferrite nanoparticles, Chem. Eng. J. 380 (2020) 122483. https://doi.org/10.1016/j.cej.2019.122483.

[115] H. Olvera-vargas, Bio- electro-Fenton : A New Combined Process . Principles and Applications . Bio-electro-Fenton : A New Combined Process – Principles and Applications, (2017). https://doi.org/10.1007/698.

[116] M.B. Carboneras, M.A. Rodrigo, P. Canizares, J. Villasenor, Chemosphere Removal of oxy fl uorfen from polluted ef fl uents by combined bio- electro processes, 240 (2020). https://doi.org/10.1016/j.chemosphere.2019.124912.

[117] P. Xu, D. Zheng, Z. Xie, J. Ma, J. Yu, B. Hou, Separation and Puri fi cation Technology The mechanism and oxidation e ffi ciency of bio-electro-Fenton system with Fe @ Fe 2 O 3 / ACF composite cathode, Sep. Purif. Technol. 234 (2020) 116103. https://doi.org/10.1016/j.seppur.2019.116103.

[118] R. Tajdid, S. Aber, K. Nofouzi, Efficient improvement of microbial fuel cell performance by the modification of graphite cathode via electrophoretic deposition of CuO / ZnO, Mater. Chem. Phys. 240 (2020) 122208. https://doi.org/10.1016/j.matchemphys.2019.122208.

[119] G. Eshaq, S. Wang, H. Sun, M. Sillanpaa, Superior performance of FeVO 4 @ CeO 2 uniform core-shell nanostructures in heterogeneous Fenton-sonophotocatalytic degradation of 4-nitrophenol, J. Hazard. Mater. 382 (2020) 121059. https://doi.org/10.1016/j.jhazmat.2019.121059.

[120] M. Hassan, N. Pous, B. Xie, J. Colprim, M.D. Balaguer, S. Puig, M. Dolors, S. Puig, Influence of iron species on integrated microbial fuel cell and electro-Fenton process

treating landfill leachate, Chem. Eng. J. 328 (2017) 57–65. https://doi.org/10.1016/j.cej.2017.07.025.

[121] S. Li, T. Hua, C. Yuan, B. Li, X. Zhu, F. Li, Bioresource Technology Degradation pathways , microbial community and electricity properties analysis of antibiotic sulfamethoxazole by bio-electro-Fenton system, Bioresour. Technol. 298 (2020) 122501. https://doi.org/10.1016/j.biortech.2019.122501.

[122] P. Xu, H. Xu, Z. Shi, Separation and Puri fi cation Technology Short Communication A novel bio-electro-Fenton process with FeVO 4 / CF cathode on advanced treatment of coal gasi fi cation wastewater, Sep. Purif. Technol. 194 (2018) 457–461. https://doi.org/10.1016/j.seppur.2017.11.073.

[123] G.D. Bhowmick, S. Das, K. Adhikary, M.M. Ghangrekar, A. Mitra, ScienceDirect Using rhodium as a cathode catalyst for enhancing performance of microbial fuel cell, Int. J. Hydrogen Energy. 44 (2019) 22218–22222. https://doi.org/10.1016/j.ijhydene.2019.06.063.

[124] G. Yadav, I. Sharma, M. Ghangrekar, R. Sen, A live bio-cathode to enhance power output steered by bacteria-microalgae synergistic metabolism in microbial fuel cell, J. Power Sources. (2019) 227560. https://doi.org/10.1016/j.jpowsour.2019.227560.

[125] K. Guo, Y. Shang, B. Gao, X. Xu, S. Lu, Q. Qi, Study on the treatment of soybean protein wastewater by a pilot-scale IC-A / O coupling reactor, Chem. Eng. J. 343 (2018) 189–197. https://doi.org/10.1016/j.cej.2018.02.128.

[126] A. Almatouq, A.O. Babatunde, M. Khajah, G. Webster, Journal of Water Process Engineering Microbial community structure of anode electrodes in microbial fuel cells and microbial electrolysis cells, J. Water Process Eng. 34 (2020) 101140. https://doi.org/10.1016/j.jwpe.2020.101140.

[127] L. Zhang, X. Yin, S. Fong, Y. Li, Bio-electrochemical degradation of paracetamol in a microbial fuel cell-Fenton system, Chem. Eng. J. 276 (2015) 185–192. https://doi.org/10.1016/j.cej.2015.04.065.

[128] Y. Deng, X. Zhao, J. Luo, Z. Wang, J. Tang, Magnetic recyclable CoFe 2 O 4 @ PPy prepared by in situ Fenton oxidization polymerization with, 4 (2020) 1858–1869. https://doi.org/10.1039/c9ra09191b.

[129] H. Mai, X. Li, Bio-Electro-Fenton Process Driven by Microbial Fuel Cell for Wastewater Treatment, 44 (2010) 1875–1880. https://doi.org/10.1021/es9032925.

[130] V. V Patil, P.R. Gogate, A.P. Bhat, P.K. Ghosh, Treatment of laundry wastewater containing residual surfactants using combined approaches based on ozone, catalyst and cavitation, Sep. Purif. Technol. (2020) 116594. https://doi.org/10.1016/j.seppur.2020.116594.

[131] M.A. Hassaan, A. El Nemr, Advanced Oxidation Processes for Textile Wastewater Treatment Advanced Oxidation Processes for Textile Wastewater Treatment, (2017). https://doi.org/10.11648/j.ijpp.20170203.13.

[132] S. Yuan, M. Wang, J. Liu, B. Guo, Recent advances of SBA-15-based composites as the heterogeneous catalysts in water decontamination : A mini-review, J. Environ. Manage. 254 (2020) 109787. https://doi.org/10.1016/j.jenvman.2019.109787.

[133] Y. Jung, E. Hong, M. Kwon, J. Kang, A kinetic study of ozone decay and bromine formation in saltwater ozonation : Effect of O3 dose , salinity , pH , and Temperature A kinetic study of ozone decay and bromine formation in saltwater ozonation : Effect of O 3 dose , salinity , pH , and temper, Chem. Eng. J. 312 (2016) 30–38. https://doi.org/10.1016/j.cej.2016.11.113.

[134] C.A. Somensi, E.L. Simionatto, S.L. Bertoli, A. Wisniewski, C.M. Radetski, Use of ozone in a pilot-scale plant for textile wastewater pre-treatment : Physico-chemical efficiency , degradation by-products identification and environmental toxicity of treated wastewater, 175 (2010) 235–240. https://doi.org/10.1016/j.jhazmat.2009.09.154.

[135] S. Zhou, L. Bu, Z. Shi, C. Bi, Q. Yi, A novel advanced oxidation process using iron electrodes and ozone in atrazine degradation : Performance and mechanism, Chem. Eng. J. 306 (2016) 719–725. https://doi.org/10.1016/j.cej.2016.08.001.

[136] M.M. Hassan, C.J. Hawkyard, Decolourisation of aqueous dyes by sequential oxidation treatment with ozone and Fenton ’ s reagent, 841 (2002). https://doi.org/10.1002/jctb.641.

[137] M. Coca, M. Pe, G. Gonz, Kinetic study of ozonation of molasses fermentation wastewater, 149 (2007) 364–370. https://doi.org/10.1016/j.jhazmat.2007.04.006.

[138] Y. Waktole, B. Yan, T. Li, V. Jegatheesan, Chemosphere Treatment of anthraquinone dye textile wastewater using anaerobic dynamic membrane bioreactor : Performance and microbial dynamics, Chemosphere. 238 (2020) 124539. https://doi.org/10.1016/j.chemosphere.2019.124539.

[139] Y. Su, X. Wang, S. Dong, S. Fu, D. Zhou, Key Lab of Groundwater Resources and Environment , Ministry of Education , Jilin Jilin Provincial Key Laboratory of Water Resources and Environment , Jilin Engineering Lab for Water Pollution Control and Resources Recovery , School of Biodesign Swette Cen, Bioresour. Technol. (2020) 123009. https://doi.org/10.1016/j.biortech.2020.123009.

[140] I.E. Medina-ramírez, C.E.D. De León-macias, G. Pedroza-herrera, R. Gonzáles-segovia, J. Antonio, J.L. Rodríguez-lópez, Evaluation of the biocompatibility and growth inhibition of bacterial bio fi lms by ZnO , Fe 3 O 4 and ZnO @ Fe 3 O 4 photocatalytic magnetic materials, Ceram. Int. (2019) 0–1. https://doi.org/10.1016/j.ceramint.2019.12.145.

[141] Y. Shi, B. Wang, S. Ye, Y. Zhang, B. Wang, Y. Feng, W. Han, C. Liu, C. Shen, Applied Surface Science Magnetic , superelastic and superhydrophobic porous thermoplastic polyurethane monolith with nano-Fe 3 O 4 coating for highly selective and easy-recycling oil / water separation, Appl. Surf. Sci. 535 (2021) 147690. https://doi.org/10.1016/j.apsusc.2020.147690.

[142] M. Hachemaoui, A. Mokhtar, A. Mekki, F. Zaoui, S. Abdelkrim, S. Hacini, B. Boukoussa, International Journal of Biological Macromolecules Composites beads based on Fe 3 O 4 @ MCM-41 and calcium alginate for enhanced catalytic reduction of organic dyes, Int. J. Biol. Macromol. 164 (2020) 468–479. https://doi.org/10.1016/j.ijbiomac.2020.07.128.

[143] C. Wroblewski, T. Volford, B. Martos, J. Samoluk, P. Martos, High yield synthesis and application of magnetite nanoparticles (Fe3 o4), Magnetochemistry. 6 (2020) 1–14. https://doi.org/10.3390/magnetochemistry6020022.

[144] I. Gasmi, K. Kerboua, N. Haddour, O. Hamdaoui, A. Alghyamah, F. Buret, The Galvano-Fenton process: Experimental insights and numerical mechanistic investigation applied to the degradation of acid orange 7, Electrochim. Acta. 373 (2021). https://doi.org/10.1016/j.electacta.2021.137897.

[145] S. Liu, B. Yu, S. Wang, Y. Shen, H. Cong, Preparation, surface functionalization and application of Fe3O4 magnetic nanoparticles, Adv. Colloid Interface Sci. 281 (2020) 102165. https://doi.org/10.1016/j.cis.2020.102165.

[146] M. Jafari Eskandari, I. Hasanzadeh, M. Jafari, I. Hasanzadeh, M. Jafari Eskandari, I. Hasanzadeh, Size-controlled synthesis of Fe3O4 magnetic nanoparticles via an alternating magnetic field and ultrasonic-assisted chemical co-precipitation, Mater. Sci. Eng. B Solid-State Mater. Adv. Technol. 266 (2021) 115050. https://doi.org/10.1016/j.mseb.2021.115050.

[147] W.N.A. Aziz, A. Bumajdad, F. Al Sagheer, M. Madkour, Selective synthesis and characterization of iron oxide nanoparticles via PVA / PVP polymer blend as structure-directing agent, Mater. Chem. Phys. 249 (2020) 122927. https://doi.org/10.1016/j.matchemphys.2020.122927.

[148] P. Gnanamozhi, G. Rajivgandhi, N.S. Alharbi, S. Kadaikunnan, J.M. Khaled, T.N. Almanaa, V. Pandiyan, W.J. Li, Enhanced antibacterial and photocatalytic degradation of reactive red 120 using lead substituted ZnO nanoparticles prepared by ultrasonic-assisted co-precipitation method, Ceram. Int. 46 (2020) 19593–19599. https://doi.org/10.1016/j.ceramint.2020.05.020.

[149] M.O. Besenhard, A.P. LaGrow, A. Hodzic, M. Kriechbaum, L. Panariello, G. Bais, K. Loizou, S. Damilos, M. Margarida Cruz, N.T.K. Thanh, A. Gavriilidis, Co-precipitation synthesis of stable iron oxide nanoparticles with NaOH: New insights and continuous production via flow chemistry, Chem. Eng. J. 399 (2020) 125740. https://doi.org/10.1016/j.cej.2020.125740.

[150] A. Hajnorouzi, N. Modaresi, Journal of Magnetism and Magnetic Materials Direct sono electrochemical method for synthesizing Fe 3 O 4 nanoparticles, J. Magn. Magn. Mater. 505 (2020) 166732. https://doi.org/10.1016/j.jmmm.2020.166732.

[151] A. Benhammada, D. Trache, M. Kesraoui, A. Fouzi, Thermochimica Acta Synthesis and characterization of α-Fe 2 O 3 nanoparticles from different precursors and their catalytic effect on the thermal decomposition of nitrocellulose, Thermochim. Acta. 686 (2020) 178570. https://doi.org/10.1016/j.tca.2020.178570.

[152] C. Zhang, F.M. Allioux, M.A. Rahim, J. Han, J. Tang, M.B. Ghasemian, S.Y. Tang, M. Mayyas, T. Daeneke, P. Le-Clech, R.B. Kaner, D. Esrafilzadeh, K. Kalantar-Zadeh, Nucleation and Growth of Polyaniline Nanofibers onto Liquid Metal Nanoparticles, Chem. Mater. 32 (2020) 4808–4819. https://doi.org/10.1021/acs.chemmater.0c01615.

[153] P. Bhavani, C.H. Rajababu, M.D. Arif, I.V. Subba, N.R. Reddy, Synthesis of high saturation magnetic iron oxide nanomaterials via low temperature hydrothermal method, J. Magn. Magn. Mater. 426 (2017) 459–466. https://doi.org/10.1016/j.jmmm.2016.09.049.

[154] F. Yazdani, M. Seddigh, Magnetite nanoparticles synthesized by co-precipitation method: The effects of various iron anions on specifications, Mater. Chem. Phys. 184 (2016) 318–323. https://doi.org/10.1016/j.matchemphys.2016.09.058.

[155] T. Saragi, B.L. Depi, S. Butarbutar, B. Permana, Risdiana, The impact of synthesis temperature on magnetite nanoparticles size synthesized by co-precipitation method, J. Phys. Conf. Ser. 1013 (2018). https://doi.org/10.1088/1742-6596/1013/1/012190.

[156] N. Rahimdad, A. Khalaj, G. Azarian, D. Nematollahi, Electrochemical Device for the Synthesis of Fe 3 O 4 Magnetic Nanoparticles , J. Electrochem. Soc. 166 (2019) E1–E6. https://doi.org/10.1149/2.0231902jes.

[157] O.Y. Golubeva, E.Y. Brazovskaya, N.Y. Ul'yanova, Y.A. Morozova, Development of Approaches for Designing and Preparing Magnetic Nanocomposites Based on Zeolite Beta and Magnetite Nanoparticles under Hydrothermal Conditions, Glas. Phys. Chem. 44 (2018) 108–114. https://doi.org/10.1134/S1087659618020049.

[158] G. Zanchettin, G. da S. Falk, S.Y.G. González, D. Hotza, High performance magnetically recoverable Fe3O4 nanocatalysts: fast microwave synthesis and photo-fenton catalysis under visible-light, Chem. Eng. Process. - Process Intensif. 166 (2021). https://doi.org/10.1016/j.cep.2021.108438.

[159] I. Persson, Ferric Chloride Complexes in Aqueous Solution: An EXAFS Study, J. Solution Chem. 47 (2018) 797–805. https://doi.org/10.1007/s10953-018-0756-6.

[160] F. Zhang, X. Guo, D.K. Qian, T. Sun, W. Zhang, K. Dai, R.J. Zeng, Decolorization of Acid Orange 7 by extreme-thermophilic mixed culture, Bioresour. Technol. 291 (2019) 121875. https://doi.org/10.1016/j.biortech.2019.121875.

[161] T.J. Al-Musawi, P. Rajiv, N. Mengelizadeh, I.A. Mohammed, D. Balarak, Development of sonophotocatalytic process for degradation of acid orange 7 dye by using titanium dioxide nanoparticles/graphene oxide nanocomposite as a catalyst, J. Environ. Manage. 292 (2021) 112777. https://doi.org/10.1016/j.jenvman.2021.112777.

[162] R.N. Berhe, S.K. Kassahun, J.W. Kang, M. Verma, H. Kim, Synthesis of Fe3O4/CNT/ACF Cathode-based Electro-Fenton System for Efficient Mineralization of Methylene Blue Dye: Kinetics and Mechanism, J. Environ. Chem. Eng. 10 (2022) 108672. https://doi.org/10.1016/j.jece.2022.108672.

[163] A. Elsaidy, J.P. Vallejo, V. Salgueiriño, L. Lugo, Tuning the thermal properties of aqueous nanofluids by taking advantage of size-customized clusters of iron oxide

nanoparticles, J. Mol. Liq. 344 (2021) 117727. https://doi.org/10.1016/j.molliq.2021.117727.

[164] Á. de J. Ruíz-Baltazar, Sonochemical activation-assisted biosynthesis of Au/Fe3O4 nanoparticles and sonocatalytic degradation of methyl orange, Ultrason. Sonochem. 73 (2021). https://doi.org/10.1016/j.ultsonch.2021.105521.

[165] A. Boutemedjet, S. Djerad, L. Tifouti, K. Bachari, Effect of Fe0 content on the effectiveness of Fe0/Fe3O4 catalyst in Fenton process, J. Water Process Eng. 41 (2021) 102079. https://doi.org/10.1016/j.jwpe.2021.102079.

[166] P.R. Jubu, O.S. Obaseki, A. Nathan-Abutu, F.K. Yam, Y. Yusof, M.B. Ochang, Dispensability of the conventional Tauc's plot for accurate bandgap determination from UV–vis optical diffuse reflectance data, Results Opt. 9 (2022) 100273. https://doi.org/10.1016/j.rio.2022.100273.

[167] S. Landi, Comment on "Photocatalytic degradation of RhB from an aqueous solution using Ag3PO4/N-TiO2 heterostructure" and "Evaluation of the effect of dose change of Fe3O4 nanoparticles on electrochemical biosensor compatibility using hydrogels as an experimental l, J. Mol. Liq. 338 (2021) 116635. https://doi.org/10.1016/j.molliq.2021.116635.

[168] P. Anigrahawati, M.R. Sahar, E.S. Sazali, Physical, structural and spectroscopic analysis of tellurite glass containing natural magnetite Fe3O4 nanoparticles, Mater. Chem. Phys. 286 (2022) 126183. https://doi.org/10.1016/j.matchemphys.2022.126183.

[169] Q. Hu, Y. Dong, K. Ma, X. Meng, Y. Ding, Amidation crosslinking of polymeric carbon nitride for boosting photocatalytic hydrogen peroxide production, J. Catal. 413 (2022) 321–330. https://doi.org/10.1016/j.jcat.2022.06.042.

[170] Y. Guo, J. Long, J. Huang, G. Yu, Y. Wang, Can the commonly used quenching method really evaluate the role of reactive oxygen species in pollutant abatement during catalytic ozonation?, Water Res. 215 (2022) 118275. https://doi.org/10.1016/j.watres.2022.118275.

[171] P. Menon, T.S. Anantha Singh, N. Pani, P. V. Nidheesh, Electro-Fenton assisted sonication for removal of ammoniacal nitrogen and organic matter from dye intermediate industrial wastewater, Chemosphere. 269 (2021) 128739. https://doi.org/10.1016/j.chemosphere.2020.128739.

[172] X. Liu, J. Lu, X. Fang, J. Zhou, Q. Chen, Complexation modelling and oxidation mechanism of organic pollutants in cotton pulp black liquor during iron salt precipitation and electrochemical treatment, Chemosphere. 308 (2022) 136374. https://doi.org/10.1016/j.chemosphere.2022.136374.

[173] K.W. Borth, C.W. Galdino, V. de C. Teixeira, F.J. Anaissi, Iron oxide nanoparticles obtained from steel waste recycling as a green alternative for Congo red dye fast adsorption, Appl. Surf. Sci. 546 (2021). https://doi.org/10.1016/j.apsusc.2021.149126.

[174] X. Cui, S.-S. Zhang, Y. Gen, J. Zhen, J. Zhan, C. Cao, S.-Q. Ni, Synergistic catalysis by Fe3O4-biochar/peroxymonosulfate system for the removal of bisphenol a, Sep. Purif. Technol. 276 (2021) 119351. https://doi.org/10.1016/j.seppur.2021.119351.

[175] Á. de J. Ruíz-Baltazar, Green synthesis assisted by sonochemical activation of Fe3O4-Ag nano-alloys: Structural characterization and studies of sorption of cationic dyes, Inorg. Chem. Commun. 120 (2020) 108148. https://doi.org/10.1016/j.inoche.2020.108148.

[176] J.A. Flood-Garibay, M.A. Méndez-Rojas, Synthesis and characterization of magnetic wrinkled mesoporous silica nanocomposites containing Fe3O4 or CoFe2O4 nanoparticles for potential biomedical applications, Colloids Surfaces A Physicochem. Eng. Asp. 615 (2021). https://doi.org/10.1016/j.colsurfa.2021.126236.

[177] Q. Sun, C. Wu, X. Fang, D. Zhang, M. Zhu, D. Zhao, C. Zhen, L. Ma, D. Hou, Modulation on the magnetic and electrical properties of Fe3O4 thin films through strain relaxation, J. Magn. Magn. Mater. 536 (2021) 1–6. https://doi.org/10.1016/j.jmmm.2021.168128.

[178] Z.Y. Chen, A. Gupta, S. Chattopadhyay, Detection of mercury in spiked cosmetics by surface enhanced Raman spectroscopy using silver shelled iron oxide nanoparticles, Sensors Actuators, B Chem. 337 (2021) 129788. https://doi.org/10.1016/j.snb.2021.129788.

[179] Q. Wang, T. Chen, P. Bai, J. Lyu, X. Guo, Fe3O4-loaded ion exchange resin for chromatographic separation of boron isotopes: Experiment and numerical simulation, Chem. Eng. Res. Des. 171 (2021) 358–366. https://doi.org/10.1016/j.cherd.2021.05.023.

[180] A.C.N. Pinheiro, T.S. Bernardino, F.E.B. Junior, M.R.V. Lanza, W.R.P. Barros, Enhanced electrodegradation of the Sunset Yellow dye in acid media by heterogeneous Photoelectro-Fenton process using Fe3O4 nanoparticles as a catalyst, J. Environ. Chem. Eng. 8 (2020) 103621. https://doi.org/10.1016/j.jece.2019.103621.

[181] S. Jiang, K. Qian, K. Yu, H. Zhou, Y. Weng, Z. Zhang, Study on ultralight and flexible Fe3O4/melamine derived carbon foam composites for high-efficiency microwave absorption, Chem. Phys. Lett. 779 (2021) 138873. https://doi.org/10.1016/j.cplett.2021.138873.

[182] H. Aali, N.J. Baygi, S. Mollazadeh, J.V. Khaki, Improving the physicochemical properties of NaCl-assisted solution combustion synthesized iron oxide nanoparticles by controlling the thermodynamics of the process, Ceram. Int. 47 (2021) 19315–19327. https://doi.org/10.1016/j.ceramint.2021.03.233.

[183] S. Han, J. Choi, J. Kim, H.N. Han, H.J. Choi, Y. Seo, Porous Fe3O4 submicron particles for use in magnetorheological fluids, Colloids Surfaces A Physicochem. Eng. Asp. 613 (2021) 126066. https://doi.org/10.1016/j.colsurfa.2020.126066.

[184] H. Ye, X. Cui, X. Li, H. Cui, B. Zhang, H. Li, Y. Pan, R. Feng, Y. Wu, X. Liu, Jo u l P, J. Alloys Compd. (2021) 161117. https://doi.org/10.1016/j.mtcomm.2021.102695.

[185] J. Shebha Anandhi, G. Antilen Jacob, R. Justin Joseyphus, Factors affecting the heating efficiency of Mn-doped Fe3O4 nanoparticles, J. Magn. Magn. Mater. 512 (2020) 166992. https://doi.org/10.1016/j.jmmm.2020.166992.

[186] A. Sheikhmohammadi, E. Asgari, H. Nourmoradi, M.M. Fazli, M. Yeganeh, Ultrasound-assisted decomposition of metronidazole by synthesized TiO2/Fe3O4 nanocatalyst: Influencing factors and mechanisms, J. Environ. Chem. Eng. 9 (2021) 105844. https://doi.org/10.1016/j.jece.2021.105844.

[187] A. Tavousi, E. Ahmadi, L. Mohammadi-Behzad, V. Riahifar, F. Maghemi, Sensitive electrochemical sensor using polypyrrole-coated Fe3O4 core-shell nanoparticles/multiwall carbon nanotubes modified graphite electrode for atorvastatin analysis, Microchem. J. 158 (2020) 105159. https://doi.org/10.1016/j.microc.2020.105159.

[188] M.A. Mohammadi, S. Asghari, B. Aslibeiki, Surface modified Fe3O4 nanoparticles: A cross-linked polyethylene glycol coating using plasma treatment, Surfaces and Interfaces. 25 (2021) 101271. https://doi.org/10.1016/j.surfin.2021.101271.

[189] A. Taufiq, A. Nikmah, A. Hidayat, S. Sunaryono, N. Mufti, N. Hidayat, H. Susanto, Synthesis of magnetite/silica nanocomposites from natural sand to create a drug delivery vehicle, Heliyon. 6 (2020). https://doi.org/10.1016/j.heliyon.2020.e03784.

[190] C.J. Perecin, B.M. Tirich, L.C.C.M. Nagamine, G. Porto, F. V. Rocha, N.N.P. Cerize, L.C. Varanda, Aqueous synthesis of magnetite nanoparticles for magnetic hyperthermia: Formation mechanism approach, high water-dispersity and stability, Colloids Surfaces A Physicochem. Eng. Asp. 627 (2021). https://doi.org/10.1016/j.colsurfa.2021.127169.

[191] R. Pelalak, Z. Heidari, S.M. Khatami, T.A. Kurniawan, A. Marjani, S. Shirazian, Oak wood ash/GO/Fe3O4 adsorption efficiencies for cadmium and lead removal from aqueous solution: Kinetics, equilibrium and thermodynamic evaluation, Arab. J. Chem. 14 (2021) 102991. https://doi.org/10.1016/j.arabjc.2021.102991.

[192] P.M. Kouotou, A. El Kasmi, L.N. Wu, M. Waqas, Z.Y. Tian, Particle size-band gap energy-catalytic properties relationship of PSE-CVD-derived Fe3O4 thin films, J. Taiwan Inst. Chem. Eng. 93 (2018) 427–435. https://doi.org/10.1016/j.jtice.2018.08.014.

[193] Y. Hong, J. Li, W. Wu, Y. Wu, H. Bai, K. Shi, Q. Meng, Z. Zhou, D. Jia, Structure, electricity, and bandgap modulation in Fe2O3–doped potassium sodium niobate ceramics, Ceram. Int. 44 (2018) 16069–16075. https://doi.org/10.1016/j.ceramint.2018.05.174.

[194] A. Bahadur, A. Saeed, M. Shoaib, S. Iqbal, M.I. Bashir, M. Waqas, M.N. Hussain, N. Abbas, Eco-friendly synthesis of magnetite (Fe3O4) nanoparticles with tunable size: Dielectric, magnetic, thermal and optical studies, Mater. Chem. Phys. 198 (2017) 229–235. https://doi.org/10.1016/j.matchemphys.2017.05.061.

[195] A.J. Carmona-Carmona, M.A. Palomino-Ovando, O. Hernández-Cristobal, E. Sánchez-Mora, M. Toledo-Solano, Synthesis and characterization of magnetic opal/Fe3O4 colloidal crystal, J. Cryst. Growth. 462 (2017) 6–11. https://doi.org/10.1016/j.jcrysgro.2016.12.105.

[196] M. Cecchetti, M. Messaggi, A. Donazzi, A. Facibeni, V. Russo, C.S. Casari, A.L. Bassi, A. Casalegno, M. Zago, A combined morphological and electrochemical characterization of carbon electrodes in vanadium redox flow batteries: Insights into positive and negative electrode performance, Electrochim. Acta. 329 (2020) 135143. https://doi.org/10.1016/j.electacta.2019.135143.

[197] Y. Xia, H. Shang, Q. Zhang, Y. Zhou, X. Hu, Electrogeneration of hydrogen peroxide using phosphorus-doped carbon nanotubes gas diffusion electrodes and its application in electro-Fenton, J. Electroanal. Chem. 840 (2019) 400–408. https://doi.org/10.1016/j.jelechem.2019.04.009.

[198] Y. Gao, W. Zhu, Y. Li, J. Li, S. Yun, T. Huang, Novel porous carbon felt cathode modified by cyclic voltammetric electrodeposited polypyrrole and anthraquinone 2-sulfonate for an efficient electro-Fenton process, Int. J. Hydrogen Energy. 46 (2021) 9707–9717. https://doi.org/10.1016/j.ijhydene.2020.04.197.

[199] M. Campos, W. Siriwatcharapiboon, R.J. Potter, S.L. Horswell, Selectivity of cobalt-based catalysts towards hydrogen peroxide formation during the reduction of oxygen, Catal. Today. 202 (2013) 135–143. https://doi.org/10.1016/j.cattod.2012.05.015.

[200] N. Nordin, L. Ho, S. Ong, A. Haqi, A. Latif, A. Rani, S. Lee, Y. Ong, Chemosphere Hydroxyl radical formation in the hybrid system of photocatalytic fuel cell and peroxi-coagulation process affected by iron plate and UV light, Chemosphere. 244 (2020) 125459. https://doi.org/10.1016/j.chemosphere.2019.125459.

[201] M.B.K. Suhan, S.B. Shuchi, A. Anis, Z. Haque, M.S. Islam, Comparative degradation study of remazol black B dye using electro-coagulation and electro-Fenton process: Kinetics and cost analysis, Environ. Nanotechnology, Monit. Manag. 14 (2020) 100335. https://doi.org/10.1016/j.enmm.2020.100335.

[202] I. Dalponte Dallabona, Á.L. Mathias, R.M.M. Jorge, A new green floating photocatalyst with Brazilian bentonite into TiO2/alginate beads for dye removal, Colloids Surfaces A Physicochem. Eng. Asp. 627 (2021). https://doi.org/10.1016/j.colsurfa.2021.127159.

[203] H. Cai, J. Zou, J. Lin, J. Li, Y. Huang, S. Zhang, B. Yuan, J. Ma, Sodium hydroxide-enhanced acetaminophen elimination in heat/peroxymonosulfate system: Production of singlet oxygen and hydroxyl radical, Chem. Eng. J. 429 (2022) 132438. https://doi.org/10.1016/j.cej.2021.132438.

[204] A.A. Zahrani, B. Ayati, Improving Fe-based heterogeneous Electro-Fenton nano catalyst using transition metals in a novel orbiting electrodes reactor, Chemosphere. 256 (2020) 127049. https://doi.org/10.1016/j.chemosphere.2020.127049.

[205] X. Wang, G. Xu, Y. Tu, D. Wu, A. Li, X. Xie, BiOBr/PBCD-B-D dual-function catalyst with oxygen vacancies for Acid Orange 7 removal: Evaluation of adsorption-photocatalysis performance and synergy mechanism, Chem. Eng. J. 411 (2021) 128456. https://doi.org/10.1016/j.cej.2021.128456.

[206] V. Chandanshive, S. Kadam, N. Rane, B.H. Jeon, J. Jadhav, S. Govindwar, In situ textile wastewater treatment in high rate transpiration system furrows planted with aquatic macrophytes and floating phytobeds, Chemosphere. 252 (2020) 126513. https://doi.org/10.1016/j.chemosphere.2020.126513.

[207] W.H. Glaze, J.W. Kang, D.H. Chapin, The chemistry of water treatment processes involving ozone, hydrogen peroxide and ultraviolet radiation, Ozone Sci. Eng. 9 (1987) 335–352. https://doi.org/10.1080/01919518708552148.

[208] S. Hussain, E. Aneggi, S. Briguglio, M. Mattiussi, V. Gelao, I. Cabras, L. Zorzenon, A. Trovarelli, D. Goi, Journal of Environmental Chemical Engineering Enhanced ibuprofen removal by heterogeneous-Fenton process over Cu / ZrO 2 and Fe / ZrO 2 catalysts, 8 (2020). https://doi.org/10.1016/j.jece.2019.103586.

[209] Y. Jiao, L. Ma, Y. Tian, M. Zhou, A flow-through electro-Fenton process using modified activated carbon fiber cathode for orange II removal, Chemosphere. 252 (2020) 126483. https://doi.org/10.1016/j.chemosphere.2020.126483.

[210] X. Li, C. Xiao, X. Ruan, Y. Hu, C. Zhang, J. Cheng, Y. Chen, Enrofloxacin degradation in a heterogeneous electro-Fenton system using a tri-metal-carbon nanofibers composite cathode, Chem. Eng. J. 427 (2021) 130927. https://doi.org/10.1016/j.cej.2021.130927.

[211] W.M. Qian, M.H. Vahid, Y.L. Sun, A. Heidari, R. Barbaz-Isfahani, S. Saber-Samandari, A. Khandan, D. Toghraie, Investigation on the effect of functionalization of single-walled carbon nanotubes on the mechanical properties of epoxy glass composites: Experimental and molecular dynamics simulation, J. Mater. Res. Technol. 12 (2021) 1931–1945. https://doi.org/10.1016/j.jmrt.2021.03.104.

[212] B. Yao, Z. Luo, J. Yang, D. Zhi, Y. Zhou, FeIIFeIII layered double hydroxide modified carbon felt cathode for removal of ciprofloxacin in electro-Fenton process, Environ. Res. 197 (2021) 111144. https://doi.org/10.1016/j.envres.2021.111144.

[213] F. Xu, Y. Cui, D. Bao, D. Lin, S. Yuan, X. Wang, H. Wang, Y. Sun, A 3D interconnected Cu network supported by carbon felt skeleton for highly thermally conductive epoxy composites, Chem. Eng. J. 388 (2020) 124287. https://doi.org/10.1016/j.cej.2020.124287.

[214] A. Wang, Y. Zhang, S. Han, C. Guo, Z. Wen, X. Tian, J. Li, Electro-Fenton oxidation of a β-lactam antibiotic cefoperazone: Mineralization, biodegradability and degradation mechanism, Chemosphere. 270 (2021) 129486. https://doi.org/10.1016/j.chemosphere.2020.129486.

[215] H. Liu, Y. Zhang, Y. Zhou, Z. Chen, E. Lichtfouse, Self-provided microbial electricity enhanced wastewater treatment using carbon felt anode coated with amino-

functionalized Fe3O4, J. Water Process Eng. 38 (2020) 101649. https://doi.org/10.1016/j.jwpe.2020.101649.

[216] Q. Qin, N. Qiao, Y. Liu, X. Wu, Spongelike porous CuO as an efficient peroxymonosulfate activator for degradation of Acid Orange 7, Appl. Surf. Sci. 521 (2020) 146479. https://doi.org/10.1016/j.apsusc.2020.146479.

[217] S. Shi, C. Xu, Q. Dong, Y. Wang, S. Zhu, X. Zhang, Y. Tak Chow, X. Wang, L. Zhu, G. Zhang, D. Xu, High saturation magnetization MnO2/PDA/Fe3O4 fibers for efficient Pb(II) adsorption and rapid magnetic separation, Appl. Surf. Sci. 541 (2021) 148379. https://doi.org/10.1016/j.apsusc.2020.148379.

[218] P. Koohi, A. Rahbar-kelishami, H. Shayesteh, Efficient removal of congo red dye using Fe3O4/NiO nanocomposite: Synthesis and characterization, Environ. Technol. Innov. 23 (2021) 101559. https://doi.org/10.1016/j.eti.2021.101559.

[219] K. Karuppasamy, P. Santhoshkumar, T. Hussain, D. Vikraman, C.J. Yim, S. Hussain, P. Shanmugam, A. Alfantazi, S. Manickam, H.S. Kim, Influence of selenium precursors on the formation of iron selenide nanostructures (FeSe2): Efficient Electro-Fenton catalysts for detoxification of harmful organic dyestuffs, Chemosphere. 272 (2021). https://doi.org/10.1016/j.chemosphere.2021.129639.

[220] S. Ali, S.A. Khan, Z.H. Yamani, M.T. Qamar, M.A. Morsy, S. Sarfraz, Shape- and size-controlled superparamagnetic iron oxide nanoparticles using various reducing agents and their relaxometric properties by Xigo acorn area, Appl. Nanosci. 9 (2019) 479–489. https://doi.org/10.1007/s13204-018-0907-5.

[221] G. Greczynski, L. Hultman, X-ray photoelectron spectroscopy: Towards reliable binding energy referencing, Prog. Mater. Sci. 107 (2020) 100591. https://doi.org/10.1016/j.pmatsci.2019.100591.

[222] A. Rahmani, A. Seid-mohammadi, M. Leili, A. Shabanloo, A. Ansari, S. Alizadeh, D. Nematollahi, Electrocatalytic degradation of diuron herbicide using three-dimensional carbon felt/β-PbO2 anode as a highly porous electrode: Influencing factors and degradation mechanisms, Chemosphere. 276 (2021) 130141. https://doi.org/10.1016/j.chemosphere.2021.130141.

[223] C.R. Jang, J.M. Ji, J.H. Yu, Applicability of CNT as support candidate for thiophene hydrodesulfurization and 1-octene hydrogenation catalyst, Inorg. Chem. Commun. 129 (2021) 108615. https://doi.org/10.1016/j.inoche.2021.108615.

[224] P. Mehdizadeh, M. Masjedi-Arani, O. Amiri, M. Salavati-Niasari, Rapid microwave fabrication of new nanocomposites based on Tb-Fe-O nanostructures for electrochemical hydrogen storage application, Fuel. 304 (2021) 121412. https://doi.org/10.1016/j.fuel.2021.121412.

[225] M. Magro, S. Molinari, A. Venerando, D. Baratella, G. Zoppellaro, G. Salviulo, R. Zboril, F. Vianello, Applied Surface Science Colloidal maghemite nanoparticles with oxyhydroxide-like interface and chiroptical properties, Appl. Surf. Sci. 534 (2020) 147567. https://doi.org/10.1016/j.apsusc.2020.147567.

[226] A. Hassan, T. Tzedakis, Facile chemical activation of graphite felt by KMnO4 acidic solution for vanadium redox flow batteries, Appl. Surf. Sci. 528 (2020) 146808. https://doi.org/10.1016/j.apsusc.2020.146808.

[227] D. Aksu Demirezen, Y.Ş. Yıldız, D. Demirezen Yılmaz, Amoxicillin degradation using green synthesized iron oxide nanoparticles: Kinetics and mechanism analysis, Environ. Nanotechnology, Monit. Manag. 11 (2019). https://doi.org/10.1016/j.enmm.2019.100219.

[228] A. Dash, M.T. Ahmed, R. Selvaraj, Mesoporous magnetite nanoparticles synthesis using the Peltophorum pterocarpum pod extract, their antibacterial efficacy against pathogens and ability to remove a pollutant dye, J. Mol. Struct. 1178 (2019) 268–273. https://doi.org/10.1016/j.molstruc.2018.10.042.

[229] D.R. Chen, P.K. Adusei, M. Chitranshi, Y. Fang, K. Johnson, M. Schulz, V. Shanov, Electrochemical activation to enhance the volumetric performance of carbon nanotube electrodes, Appl. Surf. Sci. 541 (2021) 148448. https://doi.org/10.1016/j.apsusc.2020.148448.

[230] S. Kwon, Y. Suharto, K.J. Kim, Facile preparation of an oxygen-functionalized carbon felt electrode to improve VO2+/VO2+ redox chemistry in vanadium redox flow batteries, J. Ind. Eng. Chem. 98 (2021) 231–236. https://doi.org/10.1016/j.jiec.2021.03.049.

[231] Q. Gang, M. Niaz Akhtar, R. Boudaghi, Development of high-efficient double layer microwave absorber based on Fe3O4/carbon fiber and Fe3O4/rGO, J. Magn. Magn. Mater. 537 (2021) 168181. https://doi.org/10.1016/j.jmmm.2021.168181.

[232] P. Santhoshkumar, S. Hussain, D. Vikraman, K. Karuppasamy, T. Hussain, S. Ramesh, H.S.H.S. Kim, H.S.H.S. Kim, Bifunctional iron molybdate as highly effective heterogeneous electro-Fenton catalyst and Li-ion battery anode, Chemosphere. 286 (2022) 131846. https://doi.org/10.1016/j.chemosphere.2021.131846.

[233] X. Xing, R. Liu, M. Anjass, K. Cao, U. Kaiser, G. Zhang, C. Streb, Bimetallic manganese-vanadium functionalized N,S-doped carbon nanotubes as efficient oxygen evolution and oxygen reduction electrocatalysts, Appl. Catal. B Environ. 277 (2020) 119195. https://doi.org/10.1016/j.apcatb.2020.119195.

[234] R. Zou, I. Angelidaki, X. Yang, K. Tang, H.R. Andersen, Y. Zhang, Degradation of pharmaceuticals from wastewater in a 20-L continuous flow bio-electro-Fenton (BEF) system, Sci. Total Environ. 727 (2020) 138684. https://doi.org/10.1016/j.scitotenv.2020.138684.

[235] Y. Fan, Y. Zhou, L. Zhang, Y. Feng, K. Shih, Highly efficient catalysts of phytic acid-derivative cobalt phosphide encapsulated in N, P-codoped carbon for activation of peroxymonosulfate in norfloxacin degradation, Sep. Purif. Technol. 264 (2021) 118367. https://doi.org/10.1016/j.seppur.2021.118367.

[236] Y. Chen, X. Bai, Y. Ji, T. Shen, Reduced graphene oxide-supported hollow Co3O4@N-doped porous carbon as peroxymonosulfate activator for sulfamethoxazole

degradation, Chem. Eng. J. 430 (2021) 132951. https://doi.org/10.1016/j.cej.2021.132951.

[237] C. Thamaraiselvan, D. Bandyopadhyay, C.D. Powell, C.J. Arnusch, Electrochemical degradation of emerging pollutants via laser-induced graphene electrodes, Chem. Eng. J. Adv. 8 (2021) 100195. https://doi.org/10.1016/j.ceja.2021.100195.

[238] T. de Oliveira Guidolin, N.M. Possolli, M.B. Polla, T.B. Wermuth, T. Franco de Oliveira, S. Eller, O.R. Klegues Montedo, S. Arcaro, M.A.P. Cechinel, Photocatalytic pathway on the degradation of methylene blue from aqueous solutions using magnetite nanoparticles, J. Clean. Prod. 318 (2021). https://doi.org/10.1016/j.jclepro.2021.128556.

[239] M.I. Din, R. Khalid, J. Najeeb, Z. Hussain, Fundamentals and photocatalysis of methylene blue dye using various nanocatalytic assemblies- a critical review, J. Clean. Prod. 298 (2021) 126567. https://doi.org/10.1016/j.jclepro.2021.126567.

[240] F. Mashkoor, A. Nasar, Magsorbents: Potential candidates in wastewater treatment technology – A review on the removal of methylene blue dye, J. Magn. Magn. Mater. 500 (2020) 166408. https://doi.org/10.1016/j.jmmm.2020.166408.

[241] V.M. Vasconcelos, G.O.S. Santos, K.I.B. Eguiluz, G.R. Salazar-Banda, I. de Fatima Gimenez, Recent advances on modified reticulated vitreous carbon for water and wastewater treatment – A mini-review, Chemosphere. 286 (2022). https://doi.org/10.1016/j.chemosphere.2021.131573.

[242] X. Liu, L. Xie, Y. Liu, P. Zhao, Y. Han, S. Cheng, X. Bai, Y. Li, Rapid preparation of highly stable ZnO-CeO2/CF cathode by one-step electro-deposition for efficient degradation of ciprofloxacin in electro-Fenton system, Catal. Today. 355 (2020) 458–465. https://doi.org/10.1016/j.cattod.2019.07.005.

[243] N.T. Dung, L.T. Duong, N.T. Hoa, V.D. Thao, L.V. Ngan, N.N. Huy, A comprehensive study on the heterogeneous electro-Fenton degradation of tartrazine in water using CoFe2O4/carbon felt cathode, Chemosphere. 287 (2022). https://doi.org/10.1016/j.chemosphere.2021.132141.

[244] I. Felhősi, Z. Keresztes, T. Marek, T. Pajkossy, Properties of electrochemical double-layer capacitors with carbon-nanotubes-on-carbon-fiber-felt electrodes, Electrochim. Acta. 334 (2020). https://doi.org/10.1016/j.electacta.2019.135548.

[245] D. Zhang, T. Liu, K. Yin, C. Liu, Y. Wei, Selective H2O2 production on N-doped porous carbon from direct carbonization of metal organic frameworks for electro-Fenton mineralization of antibiotics, Chem. Eng. J. 383 (2020) 123184. https://doi.org/10.1016/j.cej.2019.123184.

[246] L. Li, W. Liu, F. Yang, W. Jiao, L. Hao, R. Wang, Interfacial reinforcement of hybrid composite by electrophoretic deposition for vertically aligned carbon nanotubes on carbon fiber, Compos. Sci. Technol. 187 (2020) 107946. https://doi.org/10.1016/j.compscitech.2019.107946.

[247] C. Xu, Y. Jiang, J. Yang, W. Wu, X. Qian, L. Hou, Co-Fe-MoS x hollow nanoboxes as high-performance counter electrode catalysts for Pt-free dye-sensitized solar cells, Chem. Eng. J. 343 (2018) 86–94. https://doi.org/10.1016/j.cej.2018.02.121.

[248] E. Paulson, M. Jothibas, Significance of thermal interfacing in hematite (α-Fe2O3) nanoparticles synthesized by sol-gel method and its characteristics properties, Surfaces and Interfaces. 26 (2021) 101432. https://doi.org/10.1016/j.surfin.2021.101432.

[249] H. Mahajan, S.K. Godara, A.K. Srivastava, Synthesis and investigation of structural, morphological, and magnetic properties of the manganese doped cobalt-zinc spinel ferrite, J. Alloys Compd. 896 (2022) 162966. https://doi.org/10.1016/j.jallcom.2021.162966.

[250] B. Liu, W. Song, W. Zhang, X. Zhang, S. Pan, H. Wu, Y. Sun, Y. Xu, Fe3O4@CNT as a high-effective and steady chainmail catalyst for tetracycline degradation with peroxydisulfate activation: Performance and mechanism, Sep. Purif. Technol. 273 (2021) 118705. https://doi.org/10.1016/j.seppur.2021.118705.

[251] F. Ali, N. Ishfaq, A. Said, Z. Nawaz, Z. Ali, N. Ali, A. Afzal, M. Bilal, Fabrication, characterization, morphological and thermal investigations of functionalized multi-walled carbon nanotubes reinforced epoxy nanocomposites, Prog. Org. Coatings. 150 (2021) 105962. https://doi.org/10.1016/j.porgcoat.2020.105962.

[252] C.D. Zeinalipour-Yazdi, E.Z. Loizidou, An experimental FTIR-ATR and computational study of H-bonding in ethanol/water mixtures, Chem. Phys. 550 (2021) 111295. https://doi.org/10.1016/j.chemphys.2021.111295.

[253] L. Jiang, J. Chen, Y. An, D. Han, S. Chang, Y. Liu, R. Yang, Enhanced electrochemical performance by nickel-iron layered double hydroxides (LDH) coated on Fe3O4 as a cathode catalyst for single-chamber microbial fuel cells, Sci. Total Environ. 745 (2020) 141163. https://doi.org/10.1016/j.scitotenv.2020.141163.

[254] A. Yildiz, D. Vatansever Bayramol, R. Atav, A.Ö. Ağirgan, M. Aydin Kurç, U. Ergünay, C. Mayer, R.L. Hadimani, Synthesis and characterization of Fe3O4@Cs@Ag nanocomposite and its use in the production of magnetic and antibacterial nanofibrous membranes, Appl. Surf. Sci. 521 (2020). https://doi.org/10.1016/j.apsusc.2020.146332.

[255] M.T. Islam, M.M. Hasan, M.F. Shabik, F. Islam, Y. Nagao, M.A. Hasnat, Electroless deposition of gold nanoparticles on a glassy carbon surface to attain methylene blue degradation via oxygen reduction reactions, Electrochim. Acta. 360 (2020) 136966. https://doi.org/10.1016/j.electacta.2020.136966.

[256] D. Song, J. Li, Z. Wang, C. Zhao, Performance of graphite felt as anodes in the electro-Fenton oxidation systems: Changes in catalysis, conductivity and adsorption properties, Appl. Surf. Sci. 532 (2020) 147450. https://doi.org/10.1016/j.apsusc.2020.147450.

[257] J. Xiao, J. Chen, Z. Ou, J. Lai, T. Yu, Y. Wang, N-doped carbon-coated Fe3N composite as heterogeneous electro-Fenton catalyst for efficient degradation of

organics, Chinese J. Catal. 42 (2021) 953–962. https://doi.org/10.1016/S1872-2067(20)63719-6.

[258] L. Ma, M. Zhou, G. Ren, W. Yang, L. Liang, A highly energy-efficient flow-through electro-Fenton process for organic pollutants degradation, Electrochim. Acta. 200 (2016) 222–230. https://doi.org/10.1016/j.electacta.2016.03.181.

[259] A.M.S. Solano, S. Garcia-Segura, C.A. Martínez-Huitle, E. Brillas, Degradation of acidic aqueous solutions of the diazo dye Congo Red by photo-assisted electrochemical processes based on Fenton's reaction chemistry, Appl. Catal. B Environ. 168–169 (2015) 559–571. https://doi.org/10.1016/j.apcatb.2015.01.019.

[260] R.R. Kalantary, M. Farzadkia, M. Kermani, M. Rahmatinia, Heterogeneous electro-Fenton process by Nano-Fe3O4 for catalytic degradation of amoxicillin: Process optimization using response surface methodology, J. Environ. Chem. Eng. 6 (2018) 4644–4652. https://doi.org/10.1016/j.jece.2018.06.043.

[261] Ö. Görmez, F. Görmez, B. Gözmen, Comparison of the heterogeneous GO-FePO4/electro-Fenton against the homogeneous Fe(II) ion and Fe(III)-oxalate complex/electro-Fenton for the degradation of metronidazole, J. Water Process Eng. 43 (2021) 1–11. https://doi.org/10.1016/j.jwpe.2021.102265.

[262] S.O. Ganiyu, C.A. Martínez-Huitle, M.A. Oturan, Electrochemical advanced oxidation processes for wastewater treatment: Advances in formation and detection of reactive species and mechanisms, Curr. Opin. Electrochem. 27 (2021) 100678. https://doi.org/10.1016/j.coelec.2020.100678.

[263] Z. Pan, C. Song, L. Li, H. Wang, Y. Pan, C. Wang, J. Li, T. Wang, X. Feng, Membrane technology coupled with electrochemical advanced oxidation processes for organic wastewater treatment: Recent advances and future prospects, Chem. Eng. J. 376 (2019) 120909. https://doi.org/10.1016/j.cej.2019.01.188.

[264] T. Van Tran, D. Thi, C. Nguyen, H.T.N. Le, D.N. Vo, S. Nanda, T.D. Nguyen, ScienceDirect and role of surface functional groups on graphene oxide-based nanocomposite towards diclofenac drug, J. Environ. Sci. (2020) 1–14. https://doi.org/10.1016/j.jes.2020.02.007.

[265] A. Aziz, F. Basheer, A. Sengar, Irfanullah, S.U. Khan, I.H. Farooqi, Biological wastewater treatment (anaerobic-aerobic) technologies for safe discharge of treated slaughterhouse and meat processing wastewater, Sci. Total Environ. 686 (2019) 681–708. https://doi.org/10.1016/j.scitotenv.2019.05.295.

[266] E. Mousset, C. Trellu, H. Olvera-Vargas, Y. Pechaud, F. Fourcade, M.A. Oturan, Electrochemical technologies coupled with biological treatments, Curr. Opin. Electrochem. 26 (2021) 100668. https://doi.org/10.1016/j.coelec.2020.100668.

[267] X.Y. Yong, D.Y. Gu, Y.D. Wu, Z.Y. Yan, J. Zhou, X.Y. Wu, P. Wei, H.H. Jia, T. Zheng, Y.C. Yong, Bio-Electron-Fenton (BEF) process driven by microbial fuel cells for triphenyltin chloride (TPTC) degradation, J. Hazard. Mater. 324 (2017) 178–183. https://doi.org/10.1016/j.jhazmat.2016.10.047.

[268] H. Dai, H. He, C. Lai, Z. Xu, X. Zheng, G. Yu, B. Huang, X. Pan, D.D. Dionysiou, Modified humic acids mediate efficient mineralization in a photo-bio-electro-Fenton process, Water Res. 190 (2021) 116740. https://doi.org/10.1016/j.watres.2020.116740.

[269] B. Saba, B. V. Kjellerup, A.D. Christy, Eco-friendly bio-electro-degradation of textile dyes wastewater, Bioresour. Technol. Reports. 15 (2021) 100734. https://doi.org/10.1016/j.biteb.2021.100734.

[270] W. Wang, Q. Zhao, J. Ding, K. Wang, J. Jiang, Development of an MFC-powered BEF system with novel Fe–Mn–Mg/CF composite cathode to degrade refractory pollutants, J. Clean. Prod. 326 (2021) 129348. https://doi.org/10.1016/j.jclepro.2021.129348.

[271] S.M. Sathe, I. Chakraborty, V.R. Sankar Cheela, S. Chowdhury, B.K. Dubey, M.M. Ghangrekar, A novel bio-electro-Fenton process for eliminating sodium dodecyl sulphate from wastewater using dual chamber microbial fuel cell, Bioresour. Technol. 341 (2021) 125850. https://doi.org/10.1016/j.biortech.2021.125850.

[272] P. Xu, D. Zheng, Z. Xie, J. Ma, J. Yu, B. Hou, The mechanism and oxidation efficiency of bio-electro-Fenton system with Fe@Fe2O3/ACF composite cathode, Sep. Purif. Technol. 234 (2020) 116103. https://doi.org/10.1016/j.seppur.2019.116103.

[273] S.S. Siwal, Q. Zhang, A.K. Saini, V.K. Gupta, D. Roberts, V. Saini, F. Coulon, B. Pareek, V.K. Thakur, Recent advances in bio-electrochemical system analysis in biorefineries, J. Environ. Chem. Eng. 9 (2021) 105982. https://doi.org/10.1016/j.jece.2021.105982.

[274] H. Zhao, Q. Zhang, Performance of electro-Fenton process coupling with microbial fuel cell for simultaneous removal of herbicide mesotrione, Bioresour. Technol. 319 (2021) 124244. https://doi.org/10.1016/j.biortech.2020.124244.

[275] S.M. Sathe, I. Chakraborty, B.K. Dubey, M.M. Ghangrekar, Microbial fuel cell coupled Fenton oxidation for the cathodic degradation of emerging contaminants from wastewater: Applications and challenges, Environ. Res. 204 (2022) 112135. https://doi.org/10.1016/j.envres.2021.112135.

[276] X. Song, C.H. Jo, M. Zhou, Enhanced electricity generation and tetracycline removal of bioelectro-Fenton with electroactive biofilm induced by multi external resistance, Chemosphere. 289 (2022) 133070. https://doi.org/10.1016/j.chemosphere.2021.133070.

[277] Z. Yang, S. Wu, H. Sun, S. Gyebi, V.G. Papadakis, M.A. Goula, G. Liu, Y. Zhang, L. Zhou, W. Wang, Efficient degradation of organic compounds in landfill leachate via developing bio-electro-Fenton process, J. Environ. Manage. 319 (2022) 115719. https://doi.org/10.1016/j.jenvman.2022.115719.

[278] S.H. Thor, L.N. Ho, S.A. Ong, C.Z.A. Abidin, C.Y. Heah, N. Nordin, Y.P. Ong, K.L. Yap, Discovering the roles of electrode distance and configuration in dye degradation and electricity generation in photocatalytic fuel cell integrated electro-Fenton process, Sep. Purif. Technol. 278 (2022) 119652. https://doi.org/10.1016/j.seppur.2021.119652.

[279] S. Song, L. Zhan, Z. He, L. Lin, J. Tu, Z. Zhang, J. Chen, L. Xu, Mechanism of the anodic oxidation of 4-chloro-3-methyl phenol in aqueous solution using Ti / SnO 2 – Sb / PbO 2 electrodes, 175 (2010) 614–621. https://doi.org/10.1016/j.jhazmat.2009.10.051.

[280] J. Zhao, J. Huang, M. Guan, Y. Zhao, G. Chen, X. Tian, Mathematical simulating the process of aerobic granular sludge treating high carbon and nitrogen concentration wastewater, Chem. Eng. J. 306 (2016) 676–684. https://doi.org/10.1016/j.cej.2016.07.098.

[281] B. Mishra, S. Varjani, G. Kumar, M.K. Awasthi, S.K. Awasthi, R. Sindhu, Microbial approaches for remediation of pollutants : Innovations , future outlook , and challenges, (2020) 1–30. https://doi.org/10.1177/0958305X19896781.

[282] N.K. Rathinam, M. Bibra, D.R. Salem, R.K. Sani, Bioresource Technology Bioelectrochemical approach for enhancing lignocellulose degradation and bio fi lm formation in Geobacillus strain WSUCF1, Bioresour. Technol. 295 (2020) 122271. https://doi.org/10.1016/j.biortech.2019.122271.

[283] T. Rashid, F. Sher, A. Hazafa, R.Q. Hashmi, A. Zafar, T. Rasheed, S. Hussain, Design and feasibility study of novel paraboloid graphite based microbial fuel cell for bioelectrogenesis and pharmaceutical wastewater treatment, J. Environ. Chem. Eng. 9 (2021) 104502. https://doi.org/10.1016/j.jece.2020.104502.

[284] J. Li, P. Wang, D. Wu, D. Chen, Separation and Puri fi cation Technology Numerical study of opposing pulsed-jet cleaning for pleated fi lter cartridges, Sep. Purif. Technol. 234 (2020) 116086. https://doi.org/10.1016/j.seppur.2019.116086.

[285] D.A. Acosta, E. Gilpavas, S. Correa-s, Using scrap zero valent iron to replace dissolved iron in the Fenton process for textile wastewater treatment : Optimization and assessment of toxicity and biodegradability *, 252 (2019). https://doi.org/10.1016/j.envpol.2019.06.104.

[286] A.A. Abdulrasheed, A.A. Jalil, S. Triwahyono, M.A.A. Zaini, Y. Gambo, M. Ibrahim, Surface modification of activated carbon for adsorption of SO2 and NOX: A review of existing and emerging technologies, Renew. Sustain. Energy Rev. 94 (2018) 1067–1085. https://doi.org/10.1016/j.rser.2018.07.011.

[287] Z. Zhang, H. Liu, L. Wu, H. Lan, J. Qu, Preparation of amino-Fe(III) functionalized mesoporous silica for synergistic adsorption of tetracycline and copper, Chemosphere. 138 (2015) 625–632. https://doi.org/10.1016/j.chemosphere.2015.07.014.

[288] Y. Ren, Y. Yan, Y. Wang, H. Zhang, X. Li, Thermally treated candle soot as a novel catalyst for hydrogen peroxide in-situ production enhancement in the bio-electro-Fenton system, Chemosphere. 262 (2021) 127839. https://doi.org/10.1016/j.chemosphere.2020.127839.

[289] B.R. Tiwari, T. Noori, M.M. Ghangrekar, A novel low cost polyvinyl alcohol-Na fi on-borosilicate membrane separator for microbial fuel cell, Mater. Chem. Phys. 182 (2016) 86–93. https://doi.org/10.1016/j.matchemphys.2016.07.008.

[290] M. Li, M. Sun, H. Dong, J. Zhang, Y. Su, Z. Qiang, Enhancement of micropollutant degradation in UV/H2O2 process via iron-containing coagulants, Water Res. (2020) 115497. https://doi.org/10.1016/j.watres.2020.115497.

[291] S.M. Sathe, I. Chakraborty, M.M. Doki, B.K. Dubey, M.M. Ghangrekar, Waste-derived iron catalyzed bio-electro-Fenton process for the cathodic degradation of surfactants, Environ. Res. 212 (2022) 113141. https://doi.org/10.1016/j.envres.2022.113141.

[292] X. Jia, C. Li, X. Zhao, M. Xu, Y. Cai, T. Wu, J. Huang, The Electrical Generation and Oxidation Efficiency of a Novel Bio-Electro-Fenton System, Process Saf. Environ. Prot. 171 (2023) 794–802. https://doi.org/10.1016/j.psep.2023.01.037.

[293] T. Cen, L. Chen, X. Zhang, Y. Tian, X. Fan, A novel fiber-shaped asymmetric supercapacitor prepared by twisting carbon fiber/carbon nanotube/MnO2 and carbon fiber/carbon nanotube/polypyrrole electrodes+, Electrochim. Acta. 367 (2021). https://doi.org/10.1016/j.electacta.2020.137488.

[294] X. Liu, Z. Chen, W. Du, P. Liu, L. Zhang, F. Shi, Treatment of wastewater containing methyl orange dye by fluidized three dimensional electrochemical oxidation process integrated with chemical oxidation and adsorption, J. Environ. Manage. 311 (2022) 114775. https://doi.org/10.1016/j.jenvman.2022.114775.

[295] F. Yu, Y. Wang, H. Ma, M. Zhou, Hydrothermal synthesis of FeS2 as a highly efficient heterogeneous electro-Fenton catalyst to degrade diclofenac via molecular oxygen effects for Fe(II)/Fe(III) cycle, Sep. Purif. Technol. 248 (2020). https://doi.org/10.1016/j.seppur.2020.117022.

APPENDIXES

Appendix 3.1: Molecular structure of AO7

Dye	*Molar mass (mg L^{-1})*	*Formula*	*Molecular structure*	*λ_{max} (nm)*
Acid orange 7	350.33	$C_{16}H_{11}N_2NaO_4S$	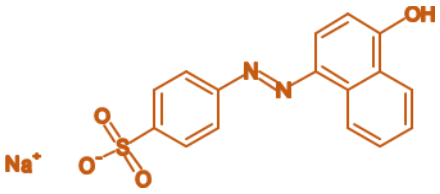	485

Appendix 3.2: Electrochemical characterization of INPs-S

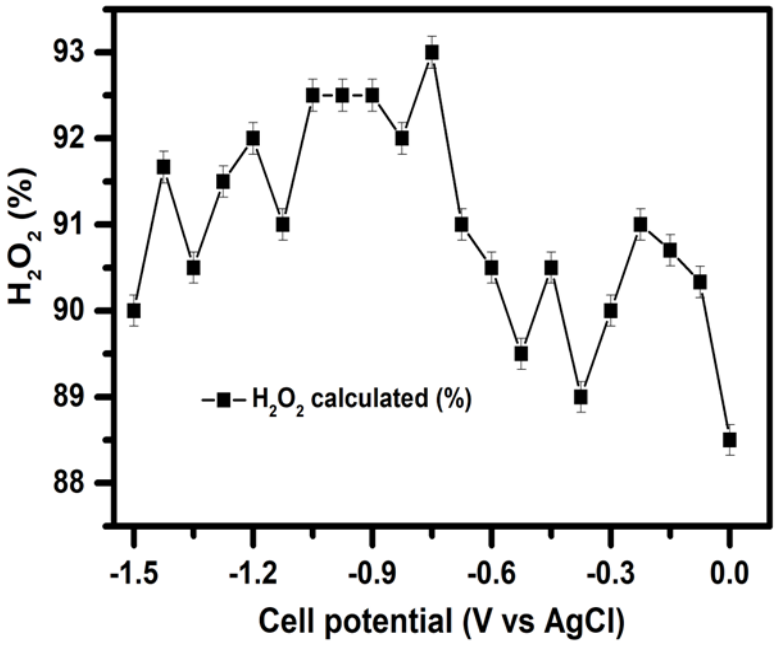

Estimation of percentage of H_2O_2 production; at scan rate of 25 mV s^{-1}, potential scan of -1.5 V to 0 vs Ag/AgCl, pH 3 and electrolyte (Na_2SO_4, 50 mg L^{-1})

Appendix 3.3: LC-MS analysis of AO7 EF oxidation

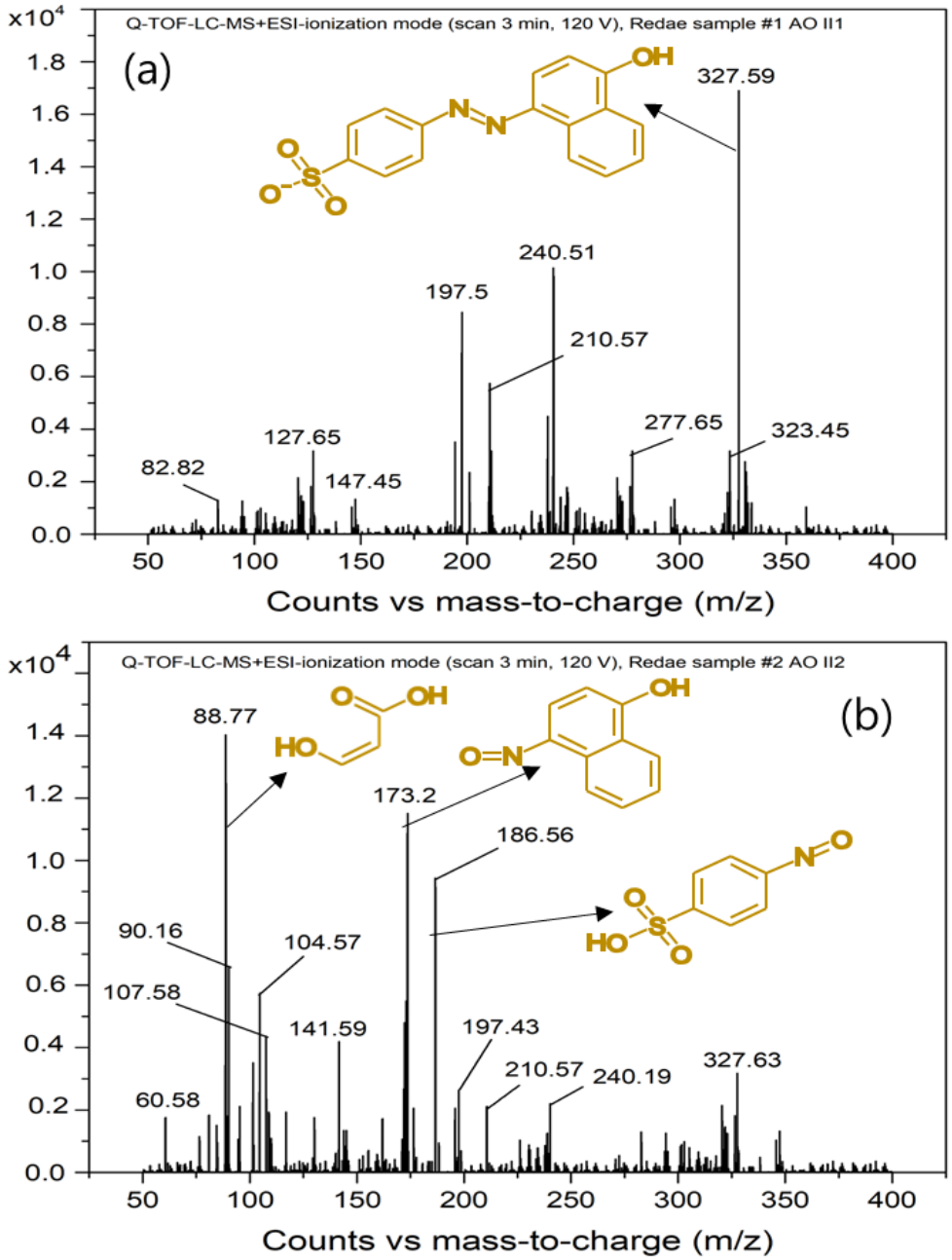

LC-MS analysis of AO7 EF oxidation: After 5 *minutes AO7 oxidation (a) and after 1.5 h of AO7 EF oxidation at* operating conditions of applied voltage of 3 V, pH 3, AO7 concentration of 10 mg L^{-1}, INPs-S dose 0.25 mg L^{-1} and electrolyte (Na_2SO_4, 50 mg L^{-1})

Appendix 3.4: LC-MS detected intermediate products of AO7 EF oxidation using INPs-S fluidized electrodes.

Intermediate products	Mass m z^{-1}	Elemental formula	Molecular structure
IP_1	87.863	$C_3H_4O_3$	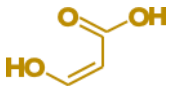
IP_2	103.729	$C_4H_8O_3$	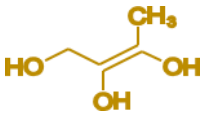
IP_3	107.103	C_6H_5NO	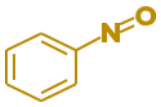
IP_4	141.074	$C_6H_7NO_3$	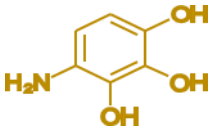
IP_5	173.034	$C_{10}H_7NO_2$	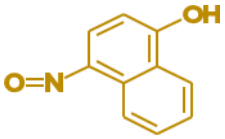
IP_6	185.853	$C_6H_4NO_4S$	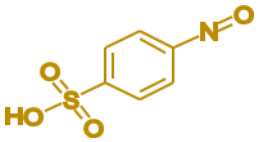
IP_7	327.128	$C_{16}H_{11}N_2O_4S$	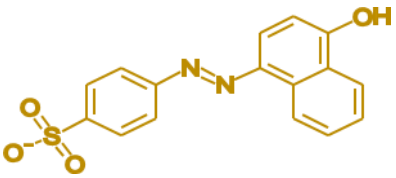

Appendix 3.5: ICS detected anions after 1.5 h EF oxidation of AO7 using INPs-S fluidized electrodes.

Dyes	*Inorganic Anions*	*Concentration (ppm)*			*Retention time (min)*
		Theoretically calculated	**Experimental obtained**	**Difference**	
AO7	Cl^-	0	1.693	+1.693	3.91
	NO_3^-	0.80	0.674	-0.126	6.37
	SO_4^{2-}	0.91	3.510	+2.600	7.32

Appendix 4.1: Molecular structure and property of CR

Dye	*Molar mass (g/mol)*	*Formula*	*Molecular structure*	λ_{max} *(nm)*
Congo red	696.66	$C_{32}H_{22}N_6Na_2O_6S_2$	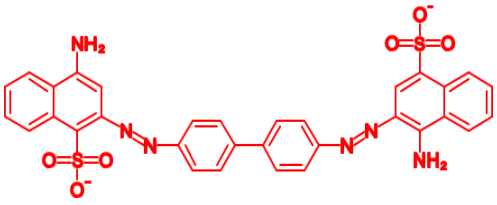	492

Appendix 4.2: Elemental analysis and mapping (SEM-EDX)

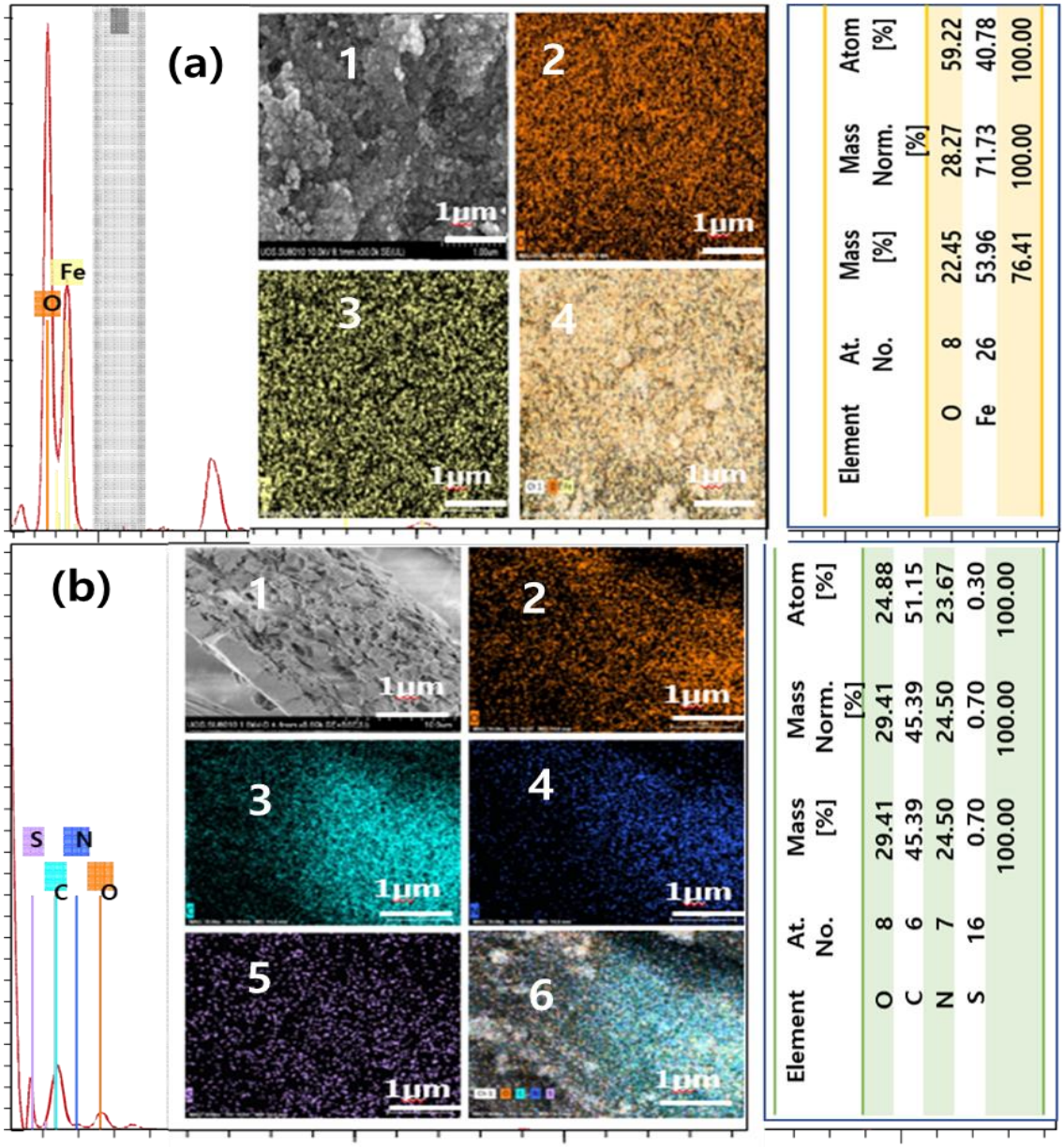

Elemental analysis and mapping (SEM-EDX) of the synthesized MNPs (a) and ACF (b) with respective elemental analysis in table form.

Appendix 4.3: High resolution XPS measurement

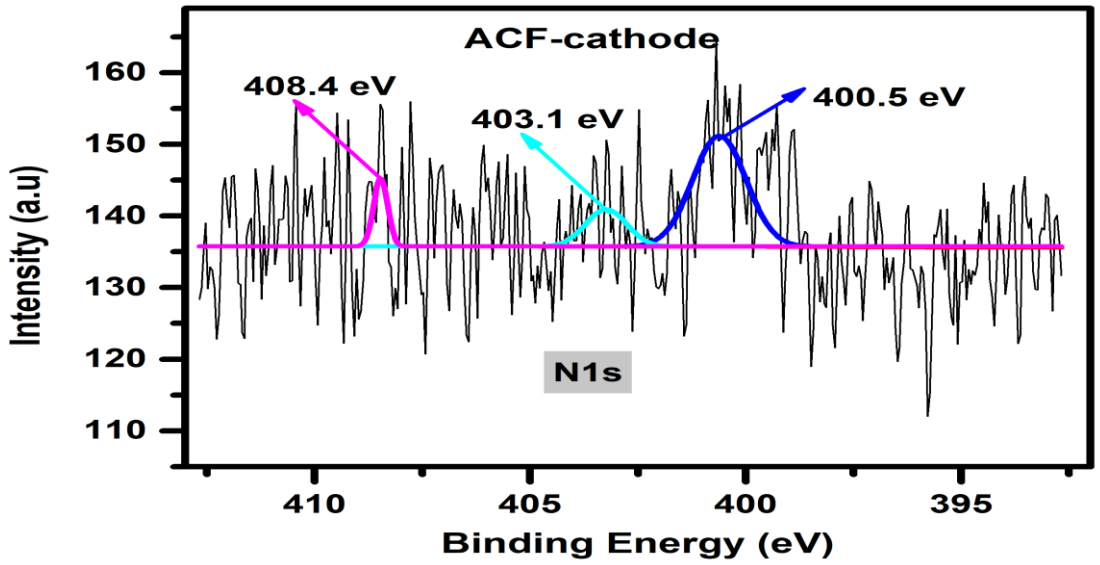

High resolution XPS measurement with its curve fittings of ACF for N 1s

Appendix 4.4: Cyclic voltammetry (CV) and LSV

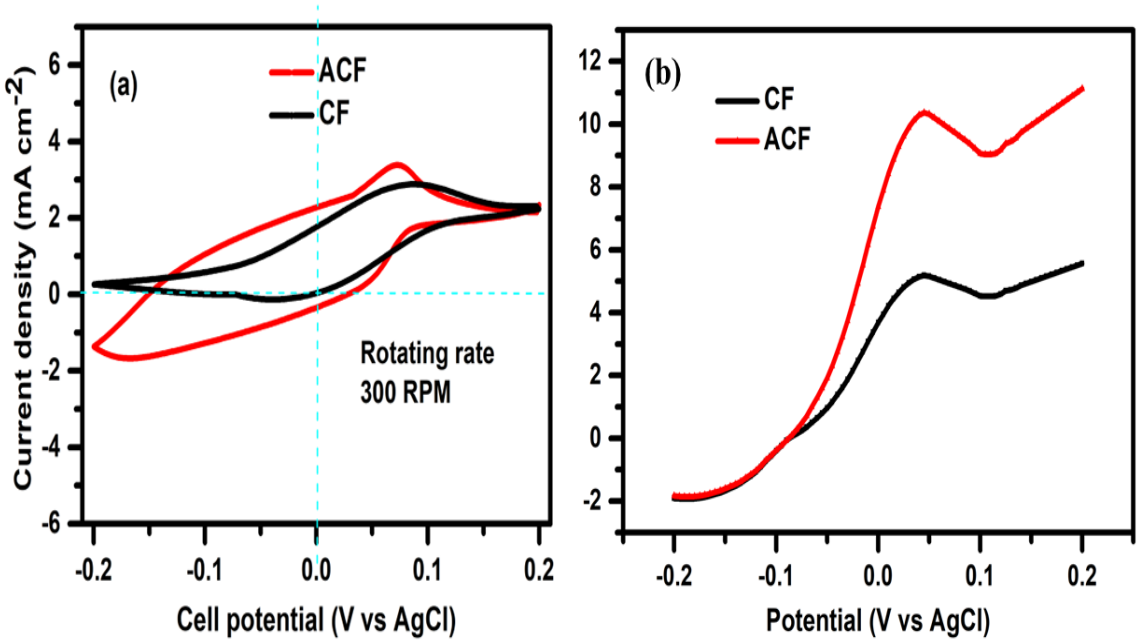

(CV (a) and LSV (b) of pristine CF and ACF over N_2-saturated solution at scan rate of 10 mV s^{-1}, potential scan of -0.2 to +02 V, pH 4 and electrolyte (Na_2SO_4, 10 mg L^{-1})

Appendix 4.5: LC-MS analysis

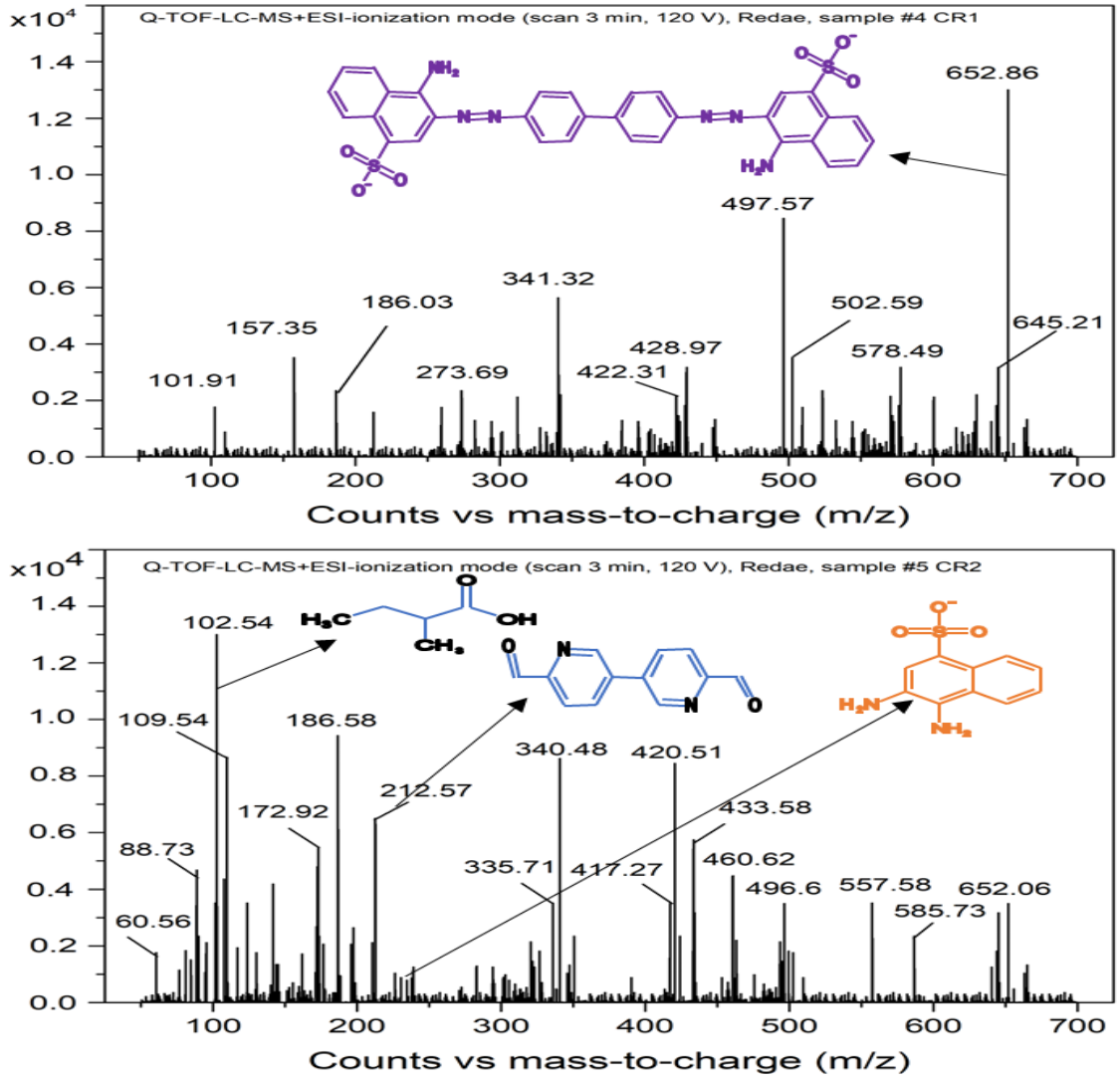

LC-MS analysis in catalytic EF process using ACF cathode after 5 minutes, and after 120-min. of CR degradation, at optimal operating conditions (pH, 4), applied potential (2.5 V), catalyst dose (0.3 g), initial CR concentration (15 mg L^{-1}) and electrolyte (Na_2SO_4, 10 mg L^{-1}) and 120-min.

Appendix 4.6: Identified intermediates products of CR degradation by LC-MS using catalytic ACF cathode in EF oxidation over 120-min.

Intermediate products	Mass m z^{-1}	Elemental formula	Molecular structure
IP_1	101.973	$C_5H_{10}O_2$	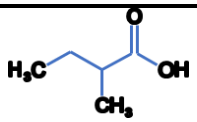
IP_2	109.561	$C_6H_6O_2$	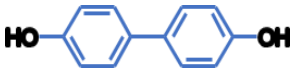
IP_3	123.092	$C_6H_5NO_2$	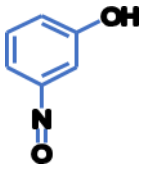
IP_4	157.157	$C_{10}H_7NO$	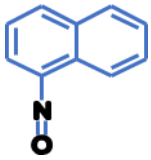
IP_5	186.164	$C_{12}H_{10}O_2$	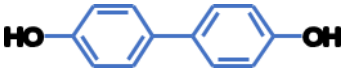
IP_6	211.853	$C_{12}H_8N_2O_2$	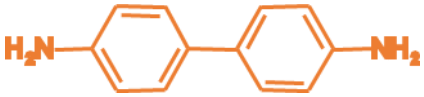
IP_7	339.841	$C_{22}H_{20}N_4$	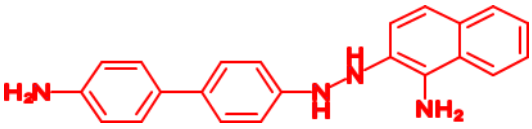
IP_8	496.438	$C_{32}H_{28}N_6$	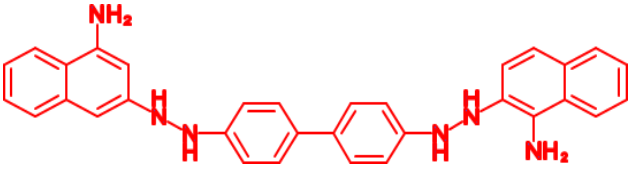
IP_9	651.976	$C_{32}H_{22}N_6O_6S_2$	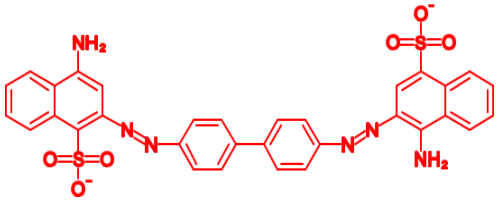

Appendix 4.7: ICS analysis

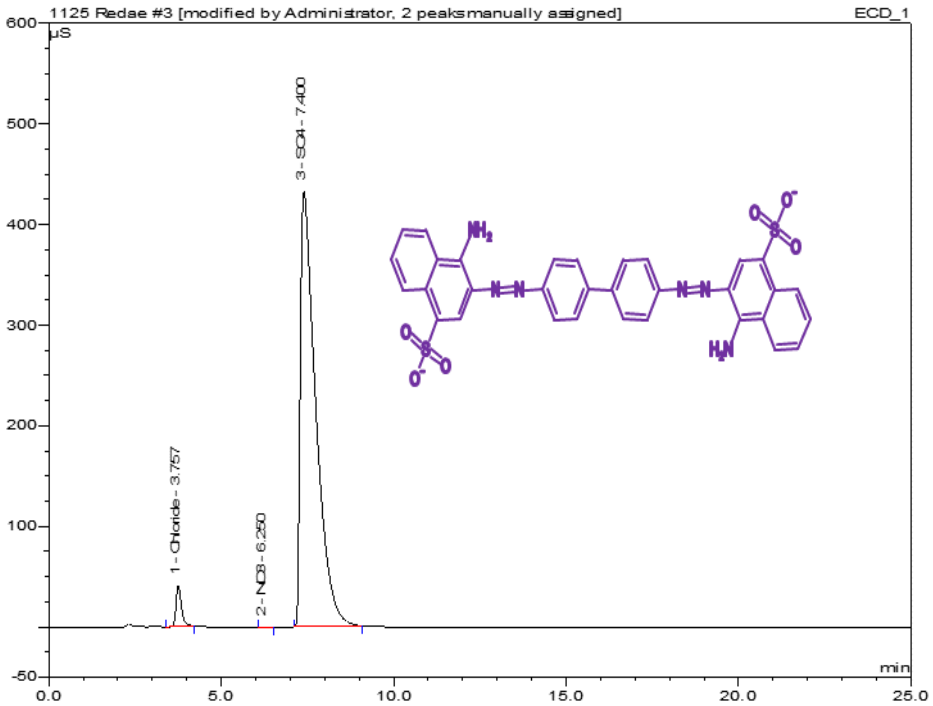

ICS analysis of degraded CR using ACF cathode electrode in EF process, at optimal operating conditions (pH, 4), applied potential (2.5 V), catalyst dose (0.3 g), initial CR concentration (15 mg L^{-1}) and electrolyte (Na_2SO_4, 10 mg L^{-1}) and 120-min.

Appendix 4.8: Theoretically calculated and experimentally obtained anions from ICS analysis after 120-min. of CR degradation using catalytic ACF cathode.

Dyes	***Inorganic Anions***	***Concentration (mg L^{-1})***			***Retention time (min)***
		Theoretically calculated	Experimental obtained	Difference	
CR	Cl^-	0	1.70 ± 0.14	-1.70 ± 0.14	3.82
	NO_3^-	8.03 ± 0.21	6.3 ± 0.17	+1.73 ± 0.04	6.23
	SO_4^{2-}	5.9 ± 0.67	3.46 ± 0.1	+2.44 ± 0.57	7.38

Appendix 5.1: Properties of MB

Dye	*Molar mass (mg L^{-1})*	*Formula*	*Molecular structure*	*λ_{max} (nm)*
Methylene blue	319.85	$C_{16}H_{18}ClN_3S$	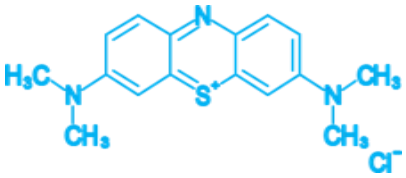	665

Appendix 5.2: SEM images of pristine CF and CNT vs ACF and ACNT

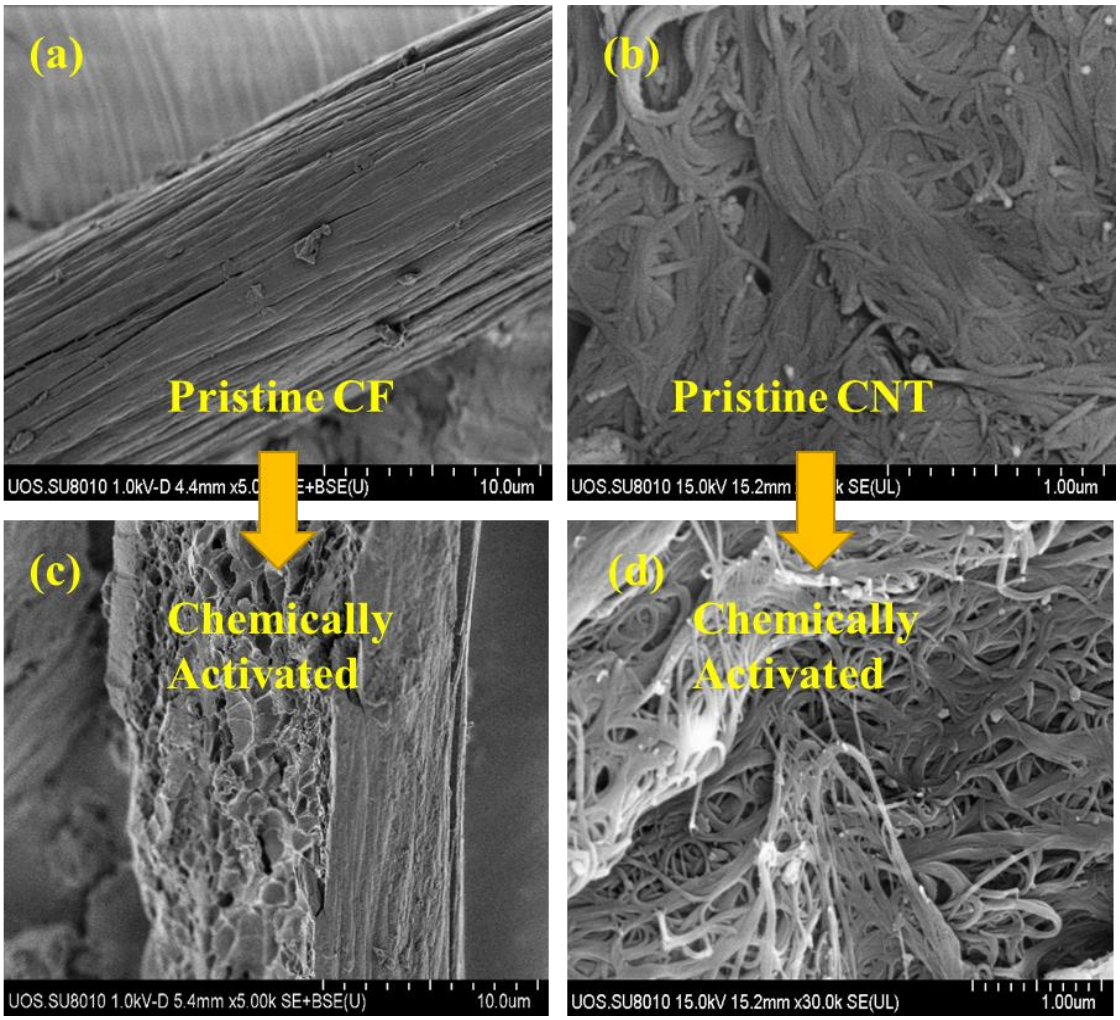

Pristine CF (a); Pristine CNT (b); Activated (ACF) (c); Activated CNT (d)

Appendix 5.3: MB removal efficiency of CF and ACF

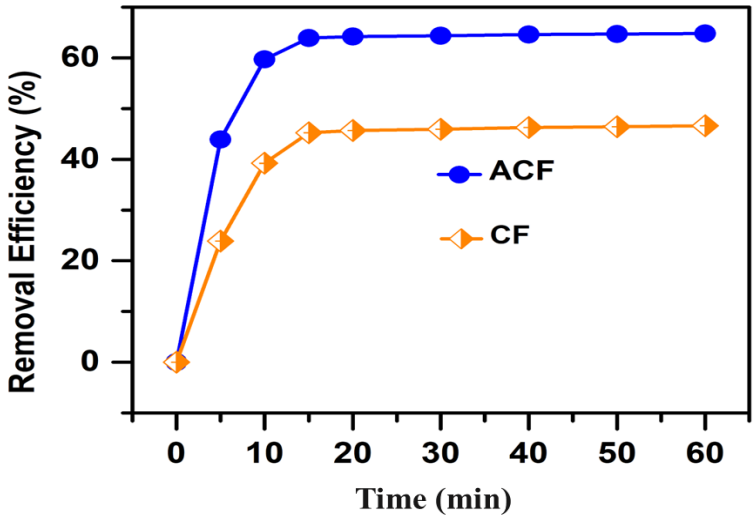

Removal efficiency of MB by ACF versus the pristine CF. Operating condition: pH = 3, applied voltage = 4 V, MB concentration = 5 ppm, concentration of $Na2SO_4$ electrolyte = 10 ppm and reaction time = 1h. All experiments were performed at 25 °C.

Appendix 5.4: Summarized results of R^2 and kinetic rates

Electrodes	***Pseudo-First Order***		***Pseudo-Second Order***		***Removal Efficiency (%)***
	R^2 value	**k_1 (min^{-1})**	**R^2 value**	**k_2 ($M^{-1}.min^{-1}$)**	
CNT/ACF	0.61	1.8×10^{-2}	0.7401	0.7×10^{-2}	66.9
Fe_3O_4/ACF	0.59	3.5×10^{-2}	0.7803	2.4×10^{-2}	87.6
Fe_3O_4/CNT/ACF	0.78	7.4×10^{-2}	0.8740	2.73×10^{-2}	98.8

Appendix 5.5: Kinetic models of MB degradation

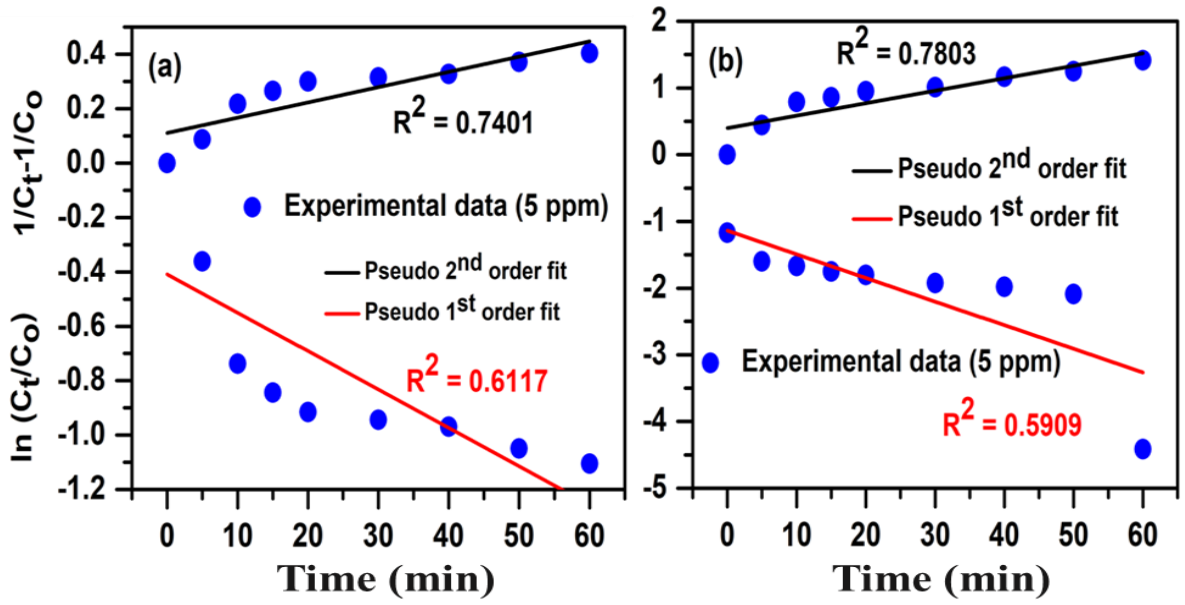

Kinetic models of MB degradation by CNT/ACF system (a) Fe_3O_4/ACF system (b). Operating condition: pH = 3, applied voltage = 4 V, MB concentration = 5 ppm, concentration of Na2SO4 electrolyte = 10 ppm and reaction time = 1h. All experiments were performed at 25 °C.

Appendix 5.6: Reusability of Fe_3O_4/CNT/ACF

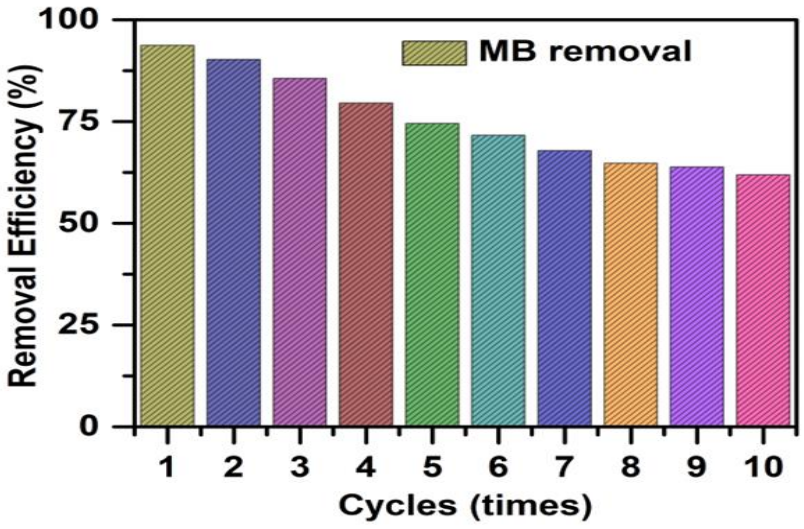

Reusability of Fe_3O_4/CNT/ACF in EF process at 1 h. Operating conditions: pH = 4, applied voltage = 3 V, MB concentration = 10 ppm and concentration of Na2SO4 electrolyte = 10 ppm. All experiments were performed at 25 °C.

Appendix 5.7: LC-MS analysis for MB degradation

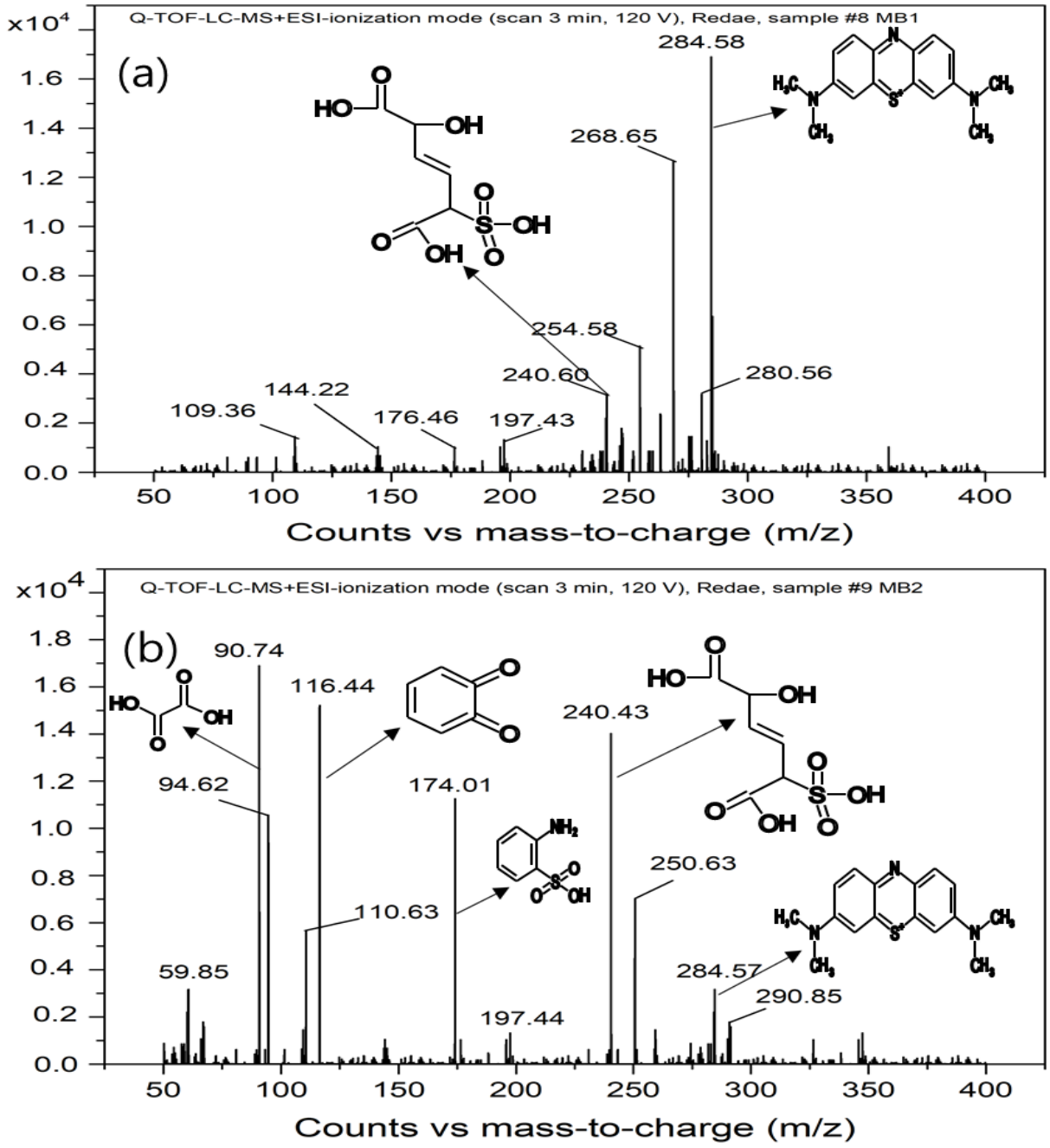

LC-MS analysis for MB degradation in EF system by Fe_3O_4/CNT/ACF cathode system (a) after 30 min and (b) after 2.5 h. Operating condition: pH = 4, applied voltage = 3 V, MB concentration = 10 ppm, and concentration of Na2SO4 electrolyte = 10 ppm. All experiments were performed at 25 °C.

Appendix 5.8: Identified intermediates products of MB degradation.

Intermediate products	Mass m z^{-1}	Elemental formula	Molecular structure
IP_1	90.743	$C_2H_2O_4$	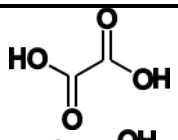
IP_2	94.621	C_6H_6O	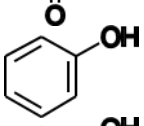
IP_3	110.630	$C_6H_6O_2$	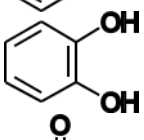
IP_4	116.440	$C_4H_4O_4$	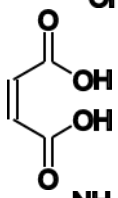
IP_5	174.011	$C_6H_7NO_3S$	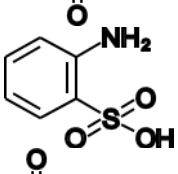
IP_6	240.431	$C_6H_8O_8S$	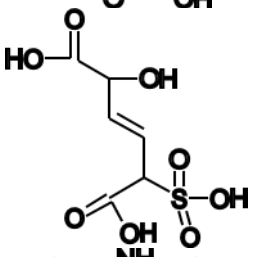
IP_7	247.921	$C_{12}H_{14}N_3OS$	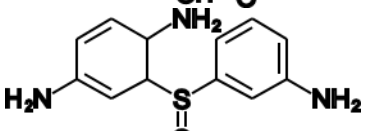
IP_8	250.633	$C_{12}H_{15}N_3OS$	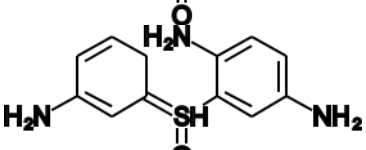
IP_9	284.583	$C_{16}H_{18}N_3S$	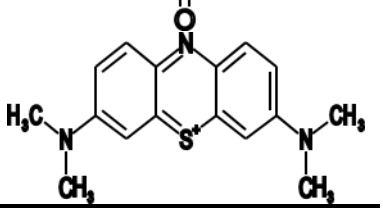

Appendix 5.9: Ion-exchange chromatography analysis

Inorganic Anions	*Concentration (ppm)*			*Retention time (min)*
	Theoretically calculated	**Experimentally obtained**	**Difference**	
Cl^-	1.11	1.645	+0.535	3.76
NO_3^-	1.31	0.713	-0.597	6.27
SO_4^{2-}	1.00	3.531	+2.531	7.36

Appendix 5.10: Ion-exchange chromatography analysis of treated MB

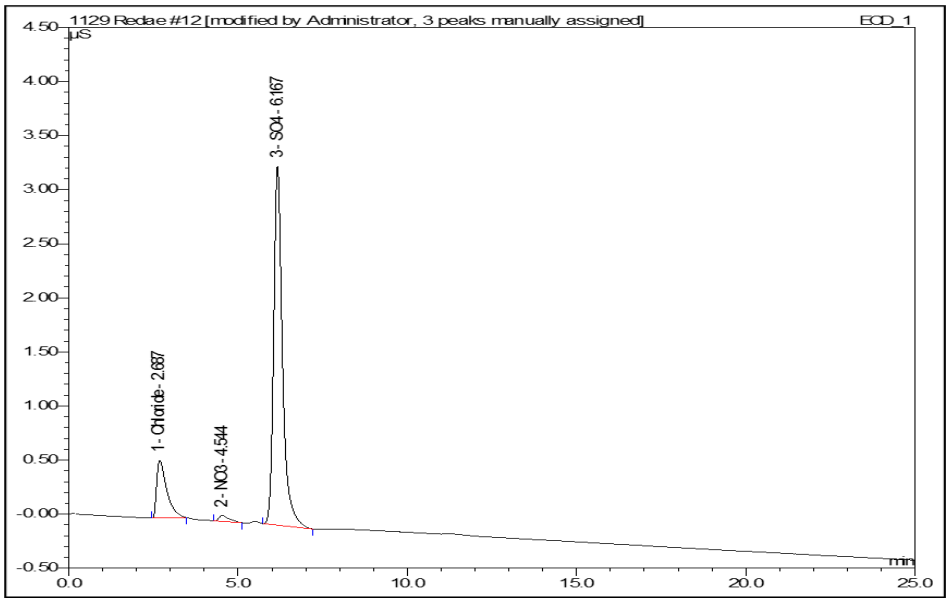

Ion-exchange chromatography analysis of treated MB by Fe_3O_4/CNT/ACF cathode electrode in EF process. Operating condition: pH = 4, applied voltage = 3 V, MB concentration = 10 ppm, concentration of Na2SO4 electrolyte = 10 ppm and reaction time = 2.5 h. All experiments were performed at 25 °C.

Appendix 6.1: H2O2 generation using ACF and Fe_3O_4@ACF

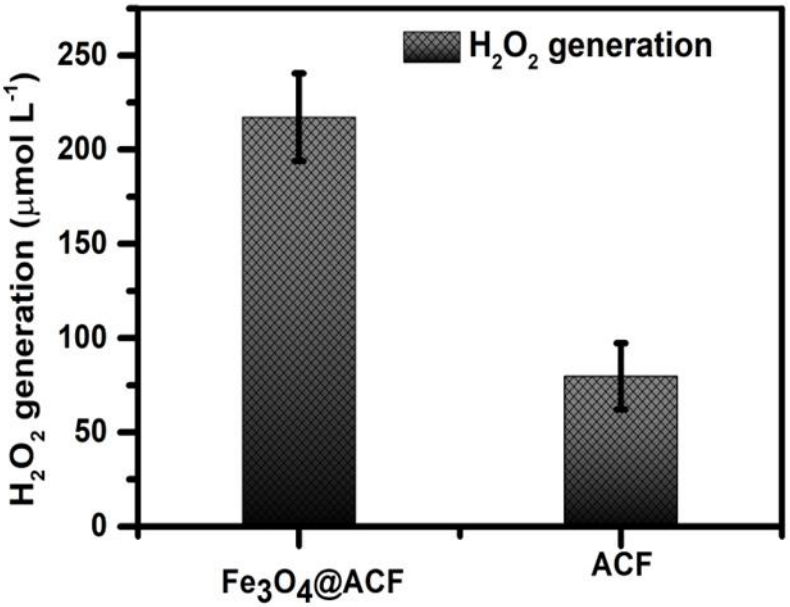

Appendix 6.2: BES efficiency for sewage treatment

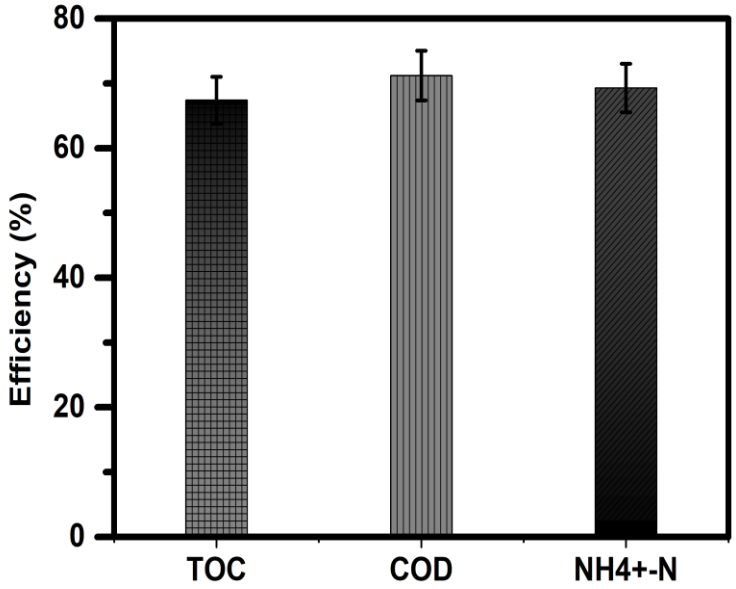

Appendix 6.3: Oxidation intermediates products of MO identified based on LC-MS analysis.

Intermediate products	Mass **m/z**	Elemental formula	Molecular structure
IP_1	90.103	$C_2H_2O_4$	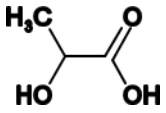
IP_2	102.162	$C_5H_{10}O_2$	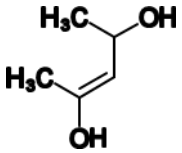
IP_3	92.060	C_6H_6N	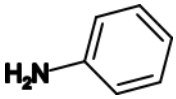
IP_4	109.140	C_6H_7NO	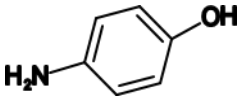
IP_5	173.011	$C_6H_5O_4S$	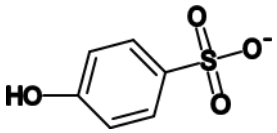
IP_6	174.282	$C_6H_6O_4S$	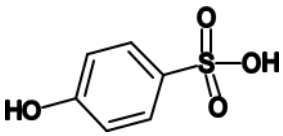
IP_7	121.221	$C_8H_{11}N$	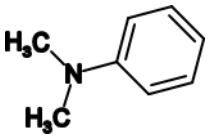
IP_8	284.583	$C_{14}H_{14}N_3NaO_3S$